High Accuracy Tracking of Space-Borne Non-Cooperative Targets

Pedersen, David Arge Klevang

Publication date:
2015

Document Version
Publisher's PDF, also known as Version of record

DTU Space
National Space Institute

High Accuracy Tracking of Space-Borne Non-cooperative Targets

PhD thesis at the Technical University of Denmark - DTU

David Arge Klevang Pedersen

December 14th 2015

Printed at:
Department of Measurement & Instrumentation Systems
DTU Space, National Space Institute
Technical University of Denmark
Elektrovej 327
2800 Kongens Lyngby
Denmark

ISBN: 978-87-91694-29-5

Abstract

This dissertation is focussed on the subject of tracking non-cooperative targets, by the use of a vision based sensor. With the main goal of navigating a spacecraft or a rover. The main objective of the dissertation is to apply image processing methods to facilitate accurate and robust measurements for the spacecraft to navigate safely and autonomously towards the target. These methods are applied on three distinct study cases, which are based on the platform of the microASC instrument.

In relation to the Mars2020 rover, a structured light system is used to navigate the PIXL instrument towards the Martian surface, whose objective is to seek evidence of ancient life in the form of chemical biosignatures. The structured light is a subsystem of the PIXL instrument consisting of two active lasers and an imager. The structured light makes use of active triangulation to support a safe approach towards the surface and to enhance the PIXL instrument's capabilities with highly accurate distance measurements.

Optical observations of planetary bodies and satellites are utilized to determine the inertial position of a spacecraft. A software module is developed, tested and verified by both ground based and in-flight observations, where the performance over the complete operational envelope is characterized by simulations. The in-flight observations were captured onboard Juno, during the Earth flyby, by the microASC instrument, operating as an inertially controlled imager. The involvement in Juno's Earth Fly By operational team and processing of the captured data was recognized with two Group Achievement Awards from the National Aeronautics and Space Administration.

With today's advancement in autonomy, the focus is set on in-flight tracking of a non-cooperative artificial satellite with the end goal of capturing the target. The objective is to facilitate a sensor technology that enables fully autonomous relative navigation between a target and chaser. A novel method is designed, tested and verified to comply with the requirements for the final phase of a rendezvous scenario, applicable to servicing and sample return missions.

Project supervisor:
Head of Department, Professor John Leif Jørgensen,
Measurement and Instrumentation Systems, DTU Space

Resumé

Denne afhandling er rettet mod sporing af passive objekter i rummet ved brug af en billed sensor, hvis hovedformål er at levere målinger til et rumfartøj eller en rover. Således at der kan navigeres selvstændigt, sikkert og autonomt frem mod den ønskede destination. Anvendelsen og sammensætningen af billedbehandlings metoder, samt deres virkemidler, er kernen i denne afhandling, hvorpå disse metoder anvendes på tre forskellige studier.

Brugen af struktureret lys er undersøgt til anvendelse på Mars2020, NASA's kommende Mars rover. Dette system anvendes til at navigere instrumentet PIXL mod Mars' overflade, hvis formål er at finde tegn på tidligere liv i form af såkaldte biosignaturer. Ved brug af aktiv triangulering måles afstanden til overfladen yderst nøjagtigt for både at muliggøre en sikker tilnærmelse mod den nærstuderede overflade, samt at optimere PIXL instrumentets videnskabelige målinger. Dette arbejde er udført på Jet Propulsion Laboratory, California Institute of Technology, i tæt samarbejde med instrumentets arbejdsgruppe.

Optiske observationer af planeter og satellitter anvendes til at bestemme et rumfartøjs position i rummet. En metode er udviklet til at måle retningen og afstanden til sådanne legemer således at rumfartøjets position kan bestemmes lokalt ombord på rumfartøjet. Metodens evne til at positionere rumfartøjet er testet ved brug af observationer fra både Jorden og rummet, hvor dens evner over hele arbejdsområdet er karakteriseret ved brug af simuleringer. Observationerne fra rummet er udført ombord rumsonden Juno. Undervejs dens forbiflyvning om Jorden blev microASC'en kommanderet til at tage billeder af Jord-Måne systemet. Deltagelsen i Juno's operationelle team og databehandlingen af observationerne er anerkendt med to Group Achievement Awards fra NASA.

Med disse tiders fremgang i autonome systemer, er fokuset også sat på at spore et passivt rumfartøj, med det formål at gribe, eller indfange, fartøjet. Målet er at udvikle metoder til billedbehandling, der muliggør en komplet selvstændig og robust navigering mellem to rumfartøjer. En ny metode er udviklet, hvor realistiske tests har vist at kravene til at navigere to rumfartøjer er overholdt. Denne metode ses anvendt til servicering at satellitter i rummet samt såkaldte sample-return missioner.

Projektvejleder:
Sektionsleder, Professor John Leif Jørgensen,
Måling og Instrumentering, DTU Space

Acknowledgements

During my time at the DTU Space and Jet Propulsion Laboratory, I have had the pleasure to work with researchers who excel in their knowledge and understanding the challenges facing continued exploration of the world we reside in. It has been a journey of great learning and I'm grateful for the opportunity to participate in such exciting projects.

I owe a sincere thanks to my supervisor John Leif Jørgensen, whom without this endeavour would not be possible. Your guidance and council is greatly appreciated. Naturally, my thanks go also the whole group of Measurement and Instrumentation for the support and aid during my studies. Each of you have always shown a willingness to generously share your expertise. In particular, I want to thank my office mate Andreas Härstedt Jørgensen for sharing his expertise and insights. I have enjoyed our discussions and collaboration throughout this project. Also thanks to Paulius Ribakovas for assistance in revising this thesis.

The half a year I spent with the PIXL instrumentation group at Jet Propulsion Laboratory has provided many rich experiences. I am honoured to have worked with such knowledgable researchers. My sincere thanks to my hosts Robert Sharrow, Lawrence Wade, and especially Carl Christian Liebe, whose mentorship has not only matured my skills as a researcher but also heightened my belief in my professional future. I especially appreciate the encouraging and uplifting talks. I want to thank Arnoud Prost, Nacer Chahat, Erik Boettcher, Johan Nilson, Matthew Hesse and Jens Schmidt for valued friendship and making me feel at home in California. In addition, I am grateful to the Otto Mønsted Fond for contributing to the expenses for the external research stay.

I want to thank my parents Gunnleyg and Børge, dearest sisters Heidi and Annilisa, and my partner in life, Anna, for their support and encouragement and for having my back when in rough seas.

Finally, this thesis is dedicated to my father, to whom I am ever grateful for promoting curiosity and a love of learning. He always left me inspired to explore further. The time spent stargazing on the snow-covered Atlantic islands, on the lookout for the Big Dipper and North Star are some of my most cherished memories.

David Arge Klevang Pedersen
December 2015, Kongens Lyngby, Denmark

Preface

This thesis is submitted in partial fulfilment of the requirements for achieving the PhD degree at the Technical University of Denmark - DTU. The work described herein has been conducted in cooperation with the Measurement and Instrumentation Systems Group (MIS) at DTU Space, Technical University of Denmark and the Instrumentation Group at Jet Propulsion Laboratory (JPL), California Institute of Technology.

List of Publications

As part of the thesis the following publications have been authored and co-authored. Papers 1 to 4 are contained within this thesis, where each paper constitutes a section in the study cases. Paper 5 and 6 are attached in the appendix as supporting information to the main line of study. Papers 1 to 5 are published or submitted to peer-review journals, while paper 6 is a conference paper.

1. D. A. K. Pedersen, C. C. Liebe, J. L. Jørgensen, "Structured Light System for Positioning Mars Rover Robotic Arm" in *Submitted to IEEE Transactions of Aerospace and Electronic Systems.*
2. D. A. K. Pedersen, A. H. Jørgensen, M. Benn, T. Denver, P. S. Jørgensen, J. B. Bjarnø, A. Massaro, J. L. Jørgensen "MicroASC Instrument Onboard Juno Spacecraft Utilizing Inertially Controlled Imaging" in *Acta Astronautica*, Volume 118. pp. 308-315, 2016.
3. D. A. K. Pedersen, A. H. Jørgensen, J. L. Jørgensen, "Characterization of Optical Observations for Deep Space Navigation" in *Submitted to IEEE Transactions on Aerospace and Electronic Systems.*
4. A. H. Jørgensen, D. A. K. Pedersen, P. Brauer, J. L. Jørgensen, "Semi-Autonomous Optical Observations for Deep Space Navigation", *Submitted to Acta Astronautica.*
5. D. Rössler, D. A. K. Pedersen, M. Benn, J. L. Jørgensen, "Optical stimulator for vision-based sensors", *Advanced Optical Technologies*, 2014 Volume 3, Issue 2, pp. 199-207
6. V. Barrena, P. Colmenarejo, M. Suatoni, D. Rössler, D. A. K. Pedersen, F. Ankersen, "Use of in-flight data to validate Mars sample return autonomous RVD GNC", *Proceedings of the International Astronautical Congress, IAC*, 2012, Volume 10, pp. 8461-8469.

Contents

Acronyms and abbreviations

The following list contains acronyms and abbreviations used throughout the thesis.

ADC	Analog to Digital Converter
BBO	Big Bright Object
BDRF	Bi-Directional Reflectance Function
CAD	Computer Aided Design
CCD	Charge-Coupled Device
CHU	Camera Head Unit
CLS	Coarse Lateral Sensor
DPU	Digital Processing Unit
DN	Digital Number
DOF	Degrees of Freedom
DSN	Deep Space Network
DTU	Technical University of Denmark
ESA	European Space Agency
FLLS	Fine Lateral Longitudinal Sensor
FOV	Field Of View
FW	Full Well
FWHM	Full Width Half Maximum
GEO	Geostationary Orbit
GNC	Guidance, Navigation and Control
GPS	Global Positioning System
GRACE	Gravity Recovery and Climate Experiment

HARVD High-integrity, Autonomous, multi-range RVD

HEOMD Human Exploration and Operations Mission Directorate

ISS International Space Station

ISRU In-Situ Resource Utilization

JPL Jet Propulsion Laboratory

LED Light Emitting Diode

LEO Low Earth Orbit

LOS Line of Sight

LHLV Local Horizontal Local Vertical

LSQ Least Square

microASC micro Advanced Stellar Compass

MAG Magnetic Field Experiment

MAHLI Mars Hand Lens Imager

MARS2020 Mars rover planned for launch in year 2020

MEDA Mars Environment dynamics Analyzer

MEP Mars Exploration Program

MGS Mars Global Surveyor

MIS Measurement and Instrumentation Systems

MLI Multi Layer Insulation

MMS Magnetospheric Multiscale

MOXIE Mars Oxygen ISRU Experiment

MSL Mars Science Laboratory

MSR Mars Sample Return

NASA National Aeronautics & Space Administration

NEA Noise Equivalent Angle

NIR Near Infrared

NSO Non-Stellar Objects

OFS Optical Fiducial System

PIXL	Planetary Instrument for X-ray Lithochemistry
PRISMA	Prototype Research Instruments and Space Mission technology Advancement
PROBA	Project for On Orbit Autonomy
RIMFAX	Radar Imager for Mars's Subsurface Exploration
RGPS	Relative GPS
RME	Relative Measurement Error
ROI	Region Of Interest
RVD	Rendezvous and Docking
RVX	Rendezvous Experiment
SHERLOC	Scanning Habitable Environments with Raman & Luminescence for Organics and Chemicals
SKG	Science Knowledge Gap
SSC	Swedish Space Corporation
STP	Space Technology Program
TOF	Time of Flight
UV	Ultraviolet
ViSOS	Vision Based Sensor Optical Stimulator
VBS	Vision Based Sensor

1 Introduction

This chapter will introduce the line of study dealt with in this PhD thesis. The scope and limitations of the thesis are given together with an overview of the following chapters.

Over the course of my studies at the Technical University of Denmark and California Institute of Technology I have had the opportunity to work on three distinct research projects within space technology. The projects are independent but all revolve within the frame of image analysis and tracking of non-cooperative space borne targets, natural as well as man-made. The technology advancements seek to improve the scientific yield from space explorations by utilizing instruments that facilitate autonomous navigation procedures.

Since the beginning of space exploration in the late 1950's, manned and unmanned landers have explored our closest celestial neighbours and probes have explored the outskirts of our solar system. Today, high priority quests are to find evidence of water and ancient life on Mars and to further understand the beginnings of our solar system. These are executed both by unmanned landers, orbiters and far reaching probes. Besides the advanced systems and instruments, all vehicles have a high level of autonomy with the purpose of maximizing the return of the investment, namely the scientific outcome.

The ability to navigate such vehicles is of essence, as it is to any explorer or traveller. Early navigators were clever to use heavenly objects as beacons to make their way to the destination. Besides the compass, effective tools like the sextant aided navigators in estimating their position or bering when no land markers were in sight. With the advancement of technology, radiometric and radar based navigation made their way to the navigators toolkit. These days global satellite navigation systems from various space agencies encompass a huge aid in daily navigation of various kinds of land, marine and airborne vehicles.

A space probe's ability to navigate as it travels to distant planets, relies on ra-

diometric principles offered by the National Aeronautics & Space Administrations (NASA) Deep Space Network (DSN). The key principals are based on temporal measurements of the doppler shift and time of flight. These navigational procedures are cumbersome and costly to a missions budget as they encompass large infrastructures scattered around the Earth [1]. If navigation procedures could be done onboard the probe while in orbit, the extensive involvement of large ground segments can be reduced, making the navigational procedures more effective. Which in return ultimately reduces the mission costs and optimizing the scientific yield.

For missions operating at large distances the communication bandwidth is limited and imposes an undesirable latency. To realize a Mars Sample Return (MSR) mission the relative navigation, between an orbiter and a sample canister, must rely on a fully automated rendezvous and capture procedure, due to the round-trip communication latency. Depending on the orbital alignments of Earth and Mars, the round-trip communication latency will be 40 minutes at when in orbital conjunctions and 8 minutes when in orbital opposites[1]. The latency is simply too long for a ground segment to intervene in the case of navigation parameters falling outside nominal values.

An Exploration rover on Mars typically receives it's operational instructions at Martian dawn, ready to execute when the environmental conditions reach operational levels. At the end of the Martian day the status and scientific results are reported back to the ground control segment on Earth. Engineers and operators will evaluate the status and scientists the outcome of the performed experiments. Equipped with hazard avoidance cameras and sensors for safe maneuvering and positioning of instruments, the rover is sought to perform the commanded instructions with a high level of autonomy, reducing the need for intervention from operators during the operational cycle of a sol[2]. The capability of navigating autonomously towards a desired target, decreases the turn-around time of maneuvering the rover and increases the time spent on actual measurements. Again, optimising the scientific yield of the mission.

[1]Orbital opposition between Earth and Mars is defined to the instance when Mars and the Sun are seen at opposite directions from the Earth's viewpoint. Meaning that the distance between Earth and Mars is at a minimum. Orbital conjunctions occurs when the planets are positioned on either side of the Sun, meaning that the distance between the planets is at a maximum.

[2]Sol is one Martian day, 24 hours and 37 minutes

1.1 Scope of thesis

The studies described in this dissemination have the focus of developing image processing technologies based on a visual sensor specifically targeted for space applications. The targets being tracked will vary from natural celestial objects to man-made space borne targets, but common to the targets is:

The tracked target is of a non-cooperative nature. In the sense that no information is actively transmitted from the target to the visual sensor.

This thesis will present a general approach for target tracking using a visual sensor and apply these principles on three distinct study cases. The cases are all related to space technology and in-situ measurements for relative navigation. The targets will vary from abraded Martian surface, to natural and man made satellites. The cases will be presented in order of increasing complexity of the image processing and operational envelope of the application at hand.

Thesis Outline

Chapter 2 This chapter describes the general principles of approach for the image analysis, processing and implementation on an system onboard a spacecraft.

Chapter 3 The first study case is presented where a structured light system is utilized to position a rover instrument relative to a targeted surface. The structured light is a part of the Planetary Instrument for X-ray Lithochemistry (PIXL), which is to investigate the small scale structure and chemical composition of the Martian rocks. The instrument is mounted on the robotic arm of the next NASA rover, Mars2020. To position the instrument accurately and safely relative to the targeted surface a structured light system is utilised. This chapter presents the approach and corresponding analysis together with the performance on real world samples.

Chapter 4 The second study targets natural celestial satellites for cis-lunar and interplanetary navigation. As a supplement to current external references from the ground segment of a mission, an onboard system can continually perform measurements to an absolute reference keeping the bias of an inertial reference unit from drifting. The processing of the data captured during Juno's

Earth Fly By[3] is described in detail. These images also serve as excellent data to test an implementation for cis-lunar and interplanetary navigation module. Therefore the chapter also presents the approach for tracking a planet or satellite resolving a spacecrafts position in an inertial reference frame.

Chapter 5 The last case study is about tracking spacecrafts with the end goal of rendezvous and docking. Most planned systems will fly in a cooperative configuration, both to enhance the accuracy but also the robustness. However, this study targets missions like Mars Sample and Return (MSR) where the canister being returned might not have the budget allowing for a cooperative implementation. Also this study targets servicing missions where spacecrafts either need re-fueling or general servicing when malfunctioning. This chapter presents a thorough study of a viable solution for actual implementation. The chapter also describes the test and corresponding results leading to an assessment of the expected performance.

Chapter 6 The last chapter contains concluding comments of the work described in the thesis.

[3]Juno performed a gravity assist maneuver with Earth on the 9th of October 2013

2 Target Tracking

This chapter presents a general overview of tracking a target by the means of an optical sensor and introduces the hardware of the optical instrument used throughout the studies.

2.1 Overview of General Approach

The process of target tracking can be divided into three general classes of procedures: *Feature Extraction*, *Feature Matching* and *Output Estimate*. This classification holds for most applications and is an effective way to structure the approach of target tracking [2]. All procedures are highly customized to the application at hand and thus a scene analysis is essential for an effective approach. A short overview of the procedures will be given in the following where a more detailed analysis of the approach, relevant to the study at hand, will be given in the corresponding chapters.

2.1.1 Scene

It is essential to fully comprehend the scene in which the object is to be tracked. Not only does it describe the operational constraints and lighting conditions but it sets the foundation of defining the approach for the three processes. A general scene analysis will typically addresses the following issues:

Operational Envelope: Determine the distance, position and orientation of the optical sensor relative to the target. Determine if the target is static or in motion relative to the optical sensor and define any operational constraints.

Lighting Conditions: Determine the light sources present in the scene and their characteristics, e.g. power and spectral composition. Determine the geometrical relation between the light sources, tracked object and optical sensor.

Environment Determine if any other objects are present in the scene, either in the foreground or background.

2.1.2 Feature Extraction

This procedure deals with detecting a feature of the object in the image captured by the optical sensor. The procedure is highly customized to the appearance of the object and naturally constrained to the scene in which the object is found. Some general concerns in determining which features to extract are given in the following:

Target Characteristics Determine the geometry that best describes the shape of the target body to be tracked. Define the surface properties and texture of the object, e.g. rough or smooth surface. Definition of the reflective properties describing how light is reflected of the surface, e.g. specular or diffuse reflection. Also a the albedo of the target may vary, depending on the surface properties. These characteristics give a general description of the objects appearance.

Labelling Based on the scene analysis and the targets characteristics, strong features are chosen to be tracked. First and foremost the features must constitute a clear and distinct signal detectable in the image data. Secondly, the signal in the image data should be fairly constant within the operational envelope. The signals are represented by an intensity level, a gradient or the second derivative, typically detected by thresholding, peak detection or zero crossings. The pixels in the image where a signal is detected are labelled, and sorted, corresponding to individual features.

Grouping Having identified the pixels containing the signal being searched for, these coordinates need to be sorted appropriately. For instance, if multiple objects are to be tracked or a single target constitutes as complex spacial pattern in the image.

Feature From a two dimensional distribution of the grouped pixel coordinates a geometric descriptor is used to describe a feature, ultimately describing the shape of the object's feature to be tracked. A feature can vary substantially depending on the target, scene, and the needed output of the application. Typical features are: centroids, circles, ellipses, lines, corners, polygons etc. For an accurate measure of the coordinate of the feature, a model of the targets appearance is typically included. For instance, when estimating the centroid

of stars, the centroid is calculated by correlating a two dimension gaussian distribution to the intensity of the pixels which are labelled and grouped to the individual stars.

There exist numerous methods to extract suitable features and it is outside the scope of the thesis to list all possible combinations. However, it is important to note the connection between the scene and the objects characteristics to define which signals and features to extract. The methods that do apply to the study cases will be presented appropriately in the respective chapters.

2.1.3 Correspondence Problem

Matching the features that are detected in the image with those expected from the scene or the object can be quite a substantial task. It is extremely important that the right correlation is established in order to conduct the final measure. For example, a star tracker needs to identify the observed stars to those listed in a star catalog in order to measure the attitude of the sensor. The effort needed to be allocated to match the features increases with the number of objects in the scene, how distinct the objects features are and the operational envelope of the application. By the use of triangulation the matching can be somewhat simplified. A system using stereo vision or structured light will constrain the number of possible matches using epipolar geometry. The case studies in the later chapters will have largely varying task of matching the features thus the effort to overcome the task will be presented appropriately.

2.1.4 Relative Navigation Parameters

Once the correspondence between the modelled features and extracted features is made, the actual navigational parameters can be estimated. The parameters relevant to the three study cases are listed in the following. The computation needed to estimate the various parameters varies significantly. With high requirements of accuracy and sparse computational power, the methods used to estimate the parameters often need special attention. Such considerations will be addressed accordingly in the study cases.

Centroid Target's apparent center coordinates in the focal plane.

Line of Sight (LOS) A sighting vector towards the target, seen from the sensor. The LOS is resolved by the centroid coordinates and the focal length of the

optical sensor. The LOS is the referenced parameter when addressing a 2DOF solution.

Range The range is the Euclidean distance from the origo of the sensor's frame to the target. The range and LOS are the referenced parameters when addressing a 3DOF solution.

Translation This is the three dimensional linear translation from the origo of the sensor's frame to the origin of the local frame of the target. Although the translation can be formulated by combing the LOS and range, these will not be merged to a single parameter as the accuracy of the two parameters varies substantially. The translation will be output once a complete 6 DOF solution is obtained.

Lateral translation The lateral translation is defined as the translation of the target along the sensor's focal plane axes X_{CHU} and Y_{CHU} that are orthogonal to the sensor's boresight axis Z_{CHU}.

Attitude The attitude of the target is defined as the spacial orientation of the local target frame relative to the sensor's frame. Typically the attitude is described by a quaternion, but for the ease of interpretation, three sequential Euler rotations are used. The rotation from the sensor's frame to the local target frame is a defined as a $\phi - \theta - \psi$ (2-1-3), sequence [3], a yaw-pitch-roll sequence seen in the frame of the CHU. When addressing a 6DOF solution, it is both the translation and attitude parameters being referenced.

2.2 Requirements of Accuracy, Robustness and Timeliness

Instruments developed for space operations have severe requirements due to the harsh environment and the sheer cost of the research, development, equipment and operational hours put into the instrument. The image processing is no exception. Three key principles to be kept in mind for any implementation:

Robustness It is extremely important that the instrument and corresponding software is robust to the environment and is able to deliver a robust measurement. It holds no value to a spacecraft navigation and control algorithm if a sensors output is not trustworthy. There can be catastrophic consequences if erroneous measurements are output

Accuracy For most applications accuracy is a primary driver. Accuracy is essential for navigational algorithms to perform accurate maneuvers, with the end goal of producing highly valued science and pushing the technology limit set by predecessors.

Timeliness The computational load of the software implementations need to be tightly constrained as on-board computation power is very limited. Ordinary desktop implementations are of a whole different approach where image processes do not need the same level of optimisation as computational power is abundant.

These key principles will be driving the design and implementation for all subjects addressed in the thesis. It is important to note that optimizing to one principle typically comes at a cost of another principle. For instance, high accuracy often comes at the cost of higher complexity and more substantial calculations, ultimately affecting the timeliness. The solutions for any of the study cases will be a balance of the requirements relating to these three principles.

2.3 Tracking Modes

For complex applications it can be a challenge to accommodate all three principles of accuracy, robustness and timeliness at the same time. To overcome this challenge two modes are used:

Acquisition The *Target Acquisition* is the initial mode with the objective to acquire a lock on target with no a priori solution, e.g. no information of a previous solution of line of sight, position or orientation is available. This mode is optimized to acquire a sound and robust solution, resolve any ambiguous solutions and perform sanity checks detecting false positives. The time allocated to achieve a lock on the target is typically longer than for the tracking mode. This is because an initial robust solution is of an high priority. As this only applies to the initial acquisition, requirements on the timeliness are relaxed.

Tracking The objective of the *Target Tracking* mode is to deliver accurate and timely solutions utilizing a priori information from earlier measurements. Using the priori information of size, position, and orientation of the target, the

search for features in the next consecutive image can be highly optimized. By only searching in a restricted Region of Interest (ROI) the computation load is substantially reduced. This allows for a solution update at a higher frequency but also to optimize the solution for accuracy. Although the objective of this mode is not to directly deal with acquiring a lock on the target, sanity checks must also be considered to verify that the previous solution is valid. For instance, if the time since the last solution is several seconds, or even minutes, the forwarded information is not likely to hold. Or if the chasing spacecraft performs an adjustment maneuver. In such a case the mode will fall back to the *Target Acquisition* mode.

2.4 Micro Advanced Stellar Compass

The hardware, central to the work, is the micro Advanced Stellar Compass (microASC). The microASC is a state of the art star tracker providing a highly accurate pointing attitude of the sensor based on pattern recognition of the starry sky. The sensors's attitude is used in a spacecraft's Guidance Navigation and Control (GNC), and/or to map the frame of individual payload instruments to an inertial reference frame. The star tracker was originally developed for the Ørsted satellite, launched in 1999. The mission objective was to map Earths magnetic field and investigate time variation of the field [4]. The camera head of the star tracker is specifically designed not to leave any magnetic signature in order to be placed in close vicinity of a magnetic field sensor. Since then, the star tracker has seen further developing and has matured to a miniature system capable of advanced image processing. The microASC has proven to be a robust and accurate instrument with a substantial amount of flight heritage from various missions like Gravity Recovery and Climate Experiment (GRACE) [5, 6], Swarm [7], Magnetospheric Multiscale (MMS) [8], and Juno [9].

The microASC consists a Digital Processing Unit (DPU) and a separate Camera Head Unit (CHU). Currently, the system is capable of operating four CHUs simultaneously controlled by a single DPU. The CHUs are mounted on a thermally stable structure which interfaces to the payload instrument or system in need of the inertial referenced attitude. Typically two or three CHUs are used in combination as to cover a larger operational area without disturbing objects in the field of view (FOV) of the sensor, and to increase the accuracy of the attitude. The accuracy of a star tracker is given by the Noise Equivalent Angle (NEA), also known

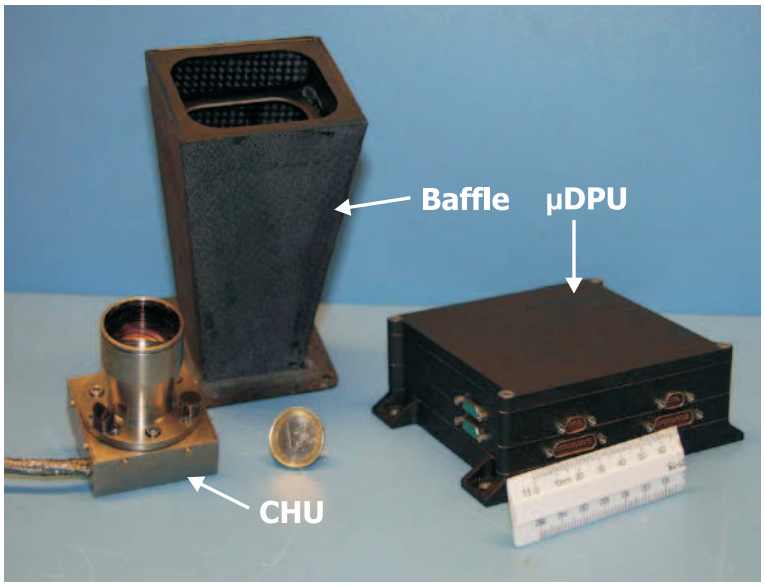

Figure 2.1 *The micro Advanced Stellar Compass, consisting of a Camera Head Unit and Digital Processing Unit together with a baffle for the optical sensor. Credit: MIS*

as Relative Measurement Error (RME) defining it's ability to reproduce the same attitude estimates based on static observations. A single CHU typically achieves a cross-boresight (yaw and pitch) accuracy below $2''$ and a boresight roll accuracy of $15'' - 20''$ [10]. Aligning a second CHU's boresight perpendicular to the first, will improve the roll accuracy seen from a common frame of reference. Inter-calibrating a system with two or more CHUs, effectively improves the overall accuracy of the star tracker system.

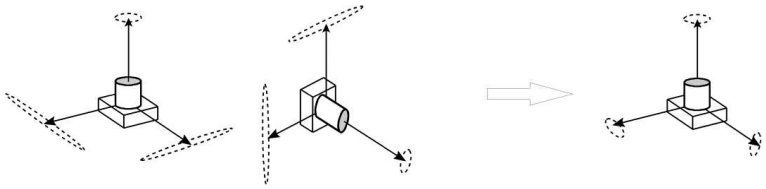

Figure 2.2 *Optimizing the attitude by combining attitude information from two or more Camera Head Units. Credit: P. S. Jørgensen, DTU-MIS*

The light sensitive chip is a Charged Coupled Device (CCD) with a resolution of 752 x 580 pixels, each pixel with a dimension of 8.6 x 8.3 μm. The sensor has a Full Well (FW) capacity of 160.000 photoelectrons per pixel with high anti-blooming characteristics and low dark current. The interlaced analog output of the sensor is fed to an 8 bit Analog to Digital Converter (ADC) with a high gain of 17 e^-/DN as the sensor is targeting very faint objects. The standard optics of the CHU has an effective focal length of $20mm$. The system is configurable to provide an attitude

solution with an update rate of 1, 2, 4, or 8 Hz and is equipped with an automatic electronic shutter.

2.4.1 Visual Based Sensor

During recent years development the microASC has been augmented to a system capable of a large variety of operations widening the scope of the general functionality. The augmented system, called Visual Based Sensor (VBS), was specifically designed as a rendezvous and docking sensor measuring the relative attitude and translation between two spacecrafts [11]. The first in-flight experience with the VBS was with the satellite pair, Mango and Tango, launched in 2010 as part of the Prototype Research Instruments and Space Mission technology Advancement (PRISMA) mission [12]. PRISMA was a technology demonstrator for formation flight and rendezvous technology with Tango designated as the passive target satellite and Mango the active chaser, performing the approaching maneuvers.

Future use of VBS

The VBS functionality holds many opportunities for current and future missions. It is currently operating on-board the Juno spacecraft, as part of the Magnetic Field Experiment (MAG) [13], tracking non-stellar objects as Juno passes through the asteroid belt. When in orbit it is opportune to detect rocky satellites orbiting Jupiter. The VBS will also play a large role in European Space agencie's (ESA) PROBA3 mission [14]. Here the experience from PRISMA will be utilized to form a coronagraph by two spacecrafts flying in closed loop formation. For the close range formation flight a cooperative scenario is used to achieve the accuracy needed for relative navigation. After the primary mission objectives are accomplished, a non-cooperative experiment is planned to take place.

3 Tracking using Structured Light

This chapter presents the first of three case studies. The goal of the study is to design and analyse the performance of a structured light system measuring distances towards a Martian surface. An introduction is given to the scientific objective of the Mars2020 rover leading to the objective of the structured light system. Paper number 1 is included in this chapter describing the demonstration system and corresponding test results to assess the performance of the system.

Today, the exploration to our closest planetary neighbour, Mars, is mainly lead by NASA through the Mars Exploration Program [15]. The program started with the orbiter Mars Global Surveyor (MGS), launching in 1996. The scientific strategy was to "follow the water" as most places where water has been present on Earth also contain the presence of microbial life. The progressive evidence of water, either in the ancient past of Mars or preserved in the subsurface, have led to the present strategy of the exploration,"seek signs of life". The Mars Science Laboratory (MSL), launched in 2011, is the first mission set to study the habitability on the surface of Mars. By analysing the soil and rock composition and local geologic settings enable the assessment of the past Martian atmosphere as well as detection of chemical building blocks of life, i.e. forms of carbon.

The Mars 2020 rover is a cornerstone in the future plans for robotic exploration of Mars. The Mars 2020 mission is based on the configuration of the MSL rover, Curiosity. Although the main objectives of the mission are currently under consideration, the Mars 2020 Science Definition Team has proposed four scientific goals and objectives for Mars 2020 [16]:

Science goals:

- Determine if Mars ever supported life.
- Understand the processes and history of climate on Mars.
- Understand the origin and evolution of Mars as a geologic system.
- Prepare for human exploration.

Primary objectives:

A *Habitability:* Explore astrobiologically relevant ancient environment to assess it's geological processes, history, and past habitability.

B *Biosignatures:* Assess preservation potentials of biosignatures within selected geological environment, and search for biosignatures.

C *Sample Caching:* Demonstrate significant technical progress towards the future return of scientifically selected, well-documented samples to Earth.

D *Prepare for Humans:* Provide an opportunity for contributed Human Exploration and Operations Mission Directorate (HEOMD) or Space Technology Program (STP) participation, compatible with the science payload and within the mission's payload capacity.

The site targeted for investigation, will be chosen based on evidence of ancient aqueous processes and relevant ancient astrobiological environment. To meet the objectives the rover will carry seven scientific instruments and a sample acquisition, processing and caching system. The instruments as a whole, enable the rover to search for signs of potential ancient life: biosignatures. Biosignatures are signs of organic microorganisms or bacteria fossilized in the sediment layers. Once strong evidence of biosignatures is found in an environment, likely to have supported organic life, samples will be cached and stored for future missions to return to Earth.

3.1 Planetary Instrument for X-Ray Lithochemistry

One of the seven scientific instruments chosen for the Mars 2020 rover is the Planetary Instrument for X-ray Lithochemistry (PIXL). PIXL is an X-ray fluorescence spectrometer that will also contain a high resolution imager to determine the fine scale elemental composition of Martian surface materials [17]. This instrument will examine the chemical elements in sub-millimeter scale of rocks and soils. To understand the origin and significance of the measured chemical composition the measurements are correlated with the fine scale texture and micro-structure using the imager. The instrument is best suited for detecting chemical biosignature which are features that may originate from microbial metabolism.

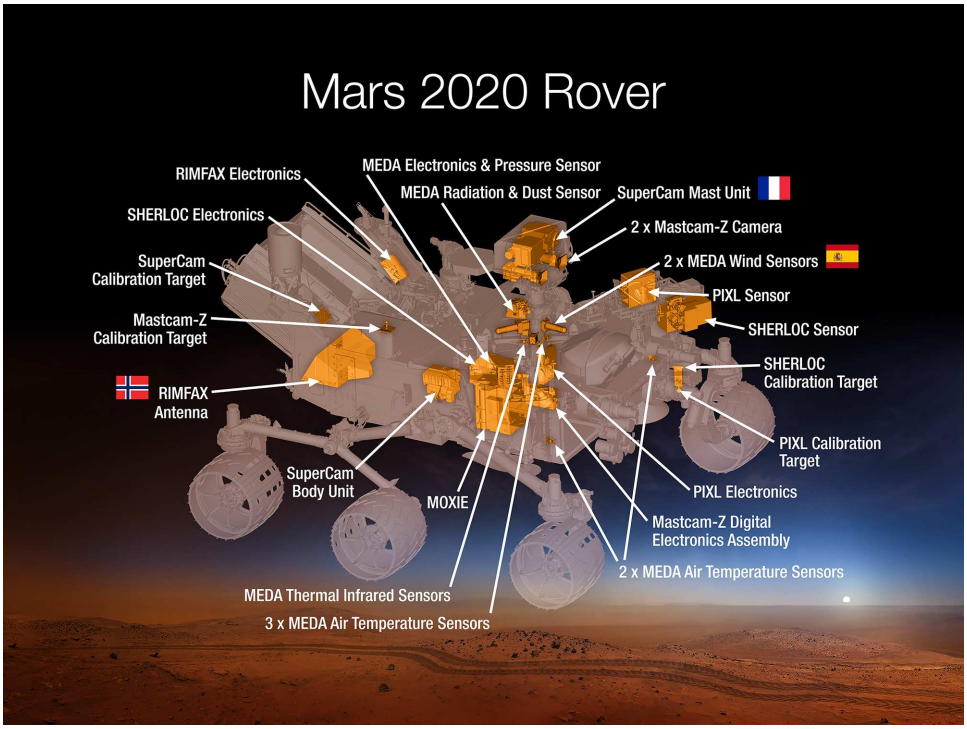

Figure 3.1 *Overview of the scientific instrument payload of Mars 2020 rover. Credit: NASA*

3.1.1 Optical Fiducial System

Investigating the fine scale of the materials the PIXL instrument needs to be positioned close to the surface sample under investigation. Therefore, the instrument is mounted on the turret, which is located at the end of the rover's robotic arm. For the PIXL instrument to make high resolution measurements the X-ray beam needs to be accurately focused to the distance where the beam intercepts the sample surface. The instrument thus needs to measure the stand-off distance towards the surface. To achieve this, the imager will be coupled with two lasers which in combination make up a structured light system, the Optical Fiducial System (OFS). The OFS will project fiducial markers onto the Martian surface in the form of a two dimensional grid of laser spots. The markers will be detected by the imager enabling a measure of the stand-off distance of the X-ray optics relative to the Martian surface for optimal focusing. Furthermore, the OFS is to detect hazards as the targeted surface is approached. The various shapes of the rocks can be a hazard as the nominal distance of the PIXL instrument is 30 mm. If there are any unforeseen objects coming to contact with the instrument irreversible damage can be done. Although, the robotic arm has accurate control feedback, a moderate response to unforeseen motion resistance can be damaging to the equipment for a short period of time, as

the robotic arm is capable of substantial amount of power output. In addition to the high resolution imager and two lasers, the instrument is to be equipped with a bank of Light Emitting Diodes (LED). The LED bank mainly serves two objectives: enable night-time operations for analysing the contents with the imager and minimize shadowing effects during daylight operations.

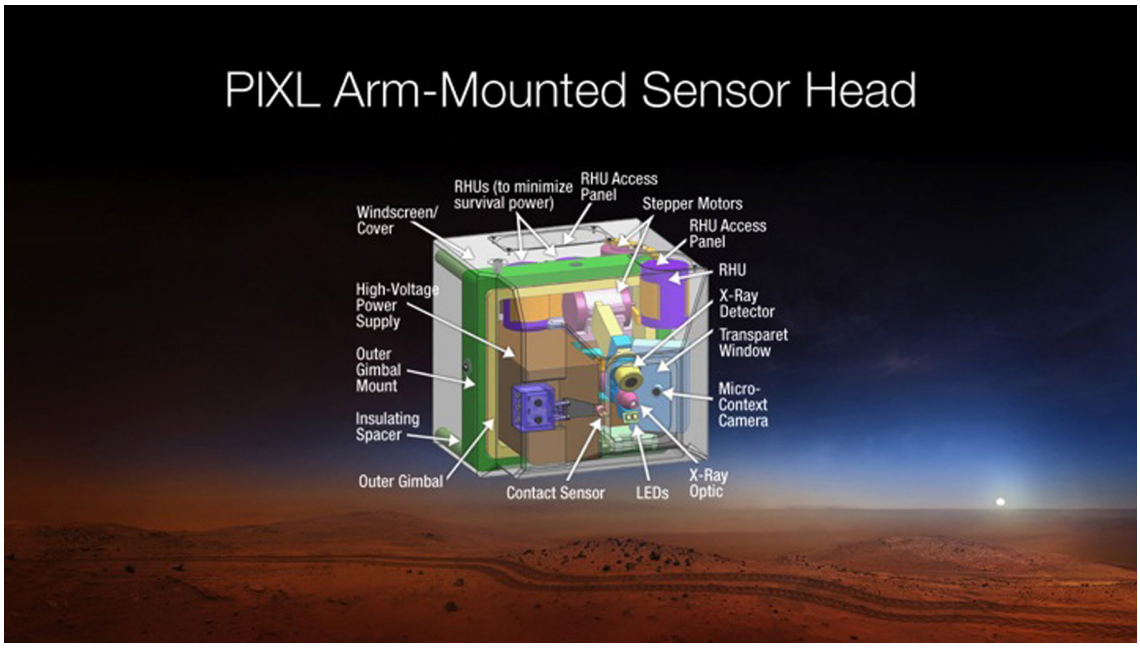

Figure 3.2 *Early design of the Planetary Instrument for X-ray Lithochemistry. Current design has replaced the two LEDs with two laser sources which in combination with the imager constitute the Optical Fiducial System. A bank of LEDs is currently being designed to be placed around the optics for an even distribution of the radiated power. Credit: NASA/JPL*

To encompass both objectives of distance measurements and hazard detection, the OFS is equipped with two lasers. One laser projects a grid of narrow angled beams resulting in a high resolution grid close to the X-ray interception of the surface. This grid will be aligned so it covers the same area of the surface as the intercepting X-ray does within the operational range of the instrument. The second laser projects a grid of wide angled beams with a low resolution but a wide coverage. This grid will be aligned so as to cover the full Field of View (FOV) of the imager when the instrument is at a distance. This grid is to detect any hazards during the approach.

The two lasers will be custom manufactured at NASA/JPL. The light source is a laser diode emitting at 830 nm. The lasers internal optics collimates the light to a 0.5 mm wide elliptical Gaussian profile. At the end of the optical train the two

lasers have a diffraction grating. The one with a narrow angled grid of 3x7 beams, with an angular spacing of 4 degrees between each beam, and the second with a wide grid of 7x7 beams, with an angular spacing of 10 degrees between each beam.

The imager is based on the substantial heritage of the microASC from DTU [18]. The standard lens is replaced with a modified lens optics specifically designed to apply to PIXL. Due to the lasers limited power output a bandpass filter is added to the camera optics, centered at the lasers wavelength $830 \pm 10nm$ in order to reduce the signal from the surrounding environment. Outside the pass band the filter transmits 10% of the signal still allowing for context images being captured using a higher integration time. The housing of the CHU is modified to fit within the mechanical interface of the PIXL instrument. The electronics of both the DPU and CHU are fully compliant to the standard heritage of the microASC. The gain of the system is set to match that of bright daylight at the surface of Mars. Normally the microASC operates under very low light conditions with the need of a high gain of the signal, typically around 19 photoelectrons/DN, thus saturating the 8 bit Analog to Digital Converter (ADC) at 4335 photoelectrons. However, in the case of PIXL, it is not faint stars that are being tracked but laser spots as bright as the surrounding sunlight. The gain of the sensor system is therefore reduced, targeting a saturation at 50.000 to 100.000 photoelectrons

3.1.2 OFS Requirements

The OFS has a number of requirements to fulfil in order to comply with the performance expected from the complete instrument. The requirements of OFS,listed below, are flow down from the system PIXL system requirements.

Operational Requirements

- The nominal distance of operation is 30 mm. The nominal distance is defined as the distance from the front end of the X-ray optics to the Martian surface along the boresight of the X-ray optics.
- The instrument shall be able to operate at distances from 10 mm to 100 mm.
- The instrument shall operate during nighttime with no natural illumination and during daylight under diffuse and direct sunlight.

Measurement Requirements

- At a stand-off distance of 25-35 mm the lateral position of the X-ray beam intersecting the targeted surface shall be determined within 0.5 mm at 3σ. At

a stand-off distance of 20-25 mm and 35-40 mm the lateral position shall be determined within 1.0 mm at 3σ. - Assuming a smooth and flat surface with a maximum deviation of ± 0.5 mm and uniform albedo ≤ 0.15.

- At a stand-off distance of 20-40 mm the stand-off distance shall be determined within 0.5 mm at 3σ. At a stand-off distance of 10-20 and 40-100 mm the stand-off distance shall be determined within 2 mm at 3σ.

3.1.3 Study of System Performance

The following paper describes a demonstration system built to assess the accuracy of the OFS. The paper does not take into account the mechanical flexibility of the instrument structure, which will be put to the test when operating in temperatures ranging from $-150°C$ to $40°C$. The paper discusses the detection and centroiding of the laser spots and how to uniquely identify the each spot. Also, the paper discusses the performance of the system under realistic circumstances, i.e. how the varying albedo of the surface, affects the centroid measurement and thus the distance measure.

The hardware used for the study is a standard microASC DPU and CHU with the lens swapped for a Navitar MLV12WA with a focal length of 12 mm, and a custom manufactured spectral band pass filter, mounted at the front end of the lens. An overview of the setup is listed in table 3.1.

Part	*Specification*	*Value*
Detector	ADC resolution	8 bit
	Gain	17.12 e^-/DN
	Full Well	4366 e^-
	Read Noise	19 e^-
	Dark Current @ 10^oC	2 e^-/s
Navitar MLV12WA	Focal length	12.2 mm
Spectral filter	Center Wavelength	830 nm
	Bandpass Width	$\pm$10 nm
	Transmission within bandpass	100 %
	Transmission outside bandpass	8-12 %
Laser	single spot output power	0.4 mW
	Collimated Beam width	0.5 mm

Table 3.1 *Hardware used to evaluate the performance of structured light system.*

The test hardware has not been adjusted to the saturation level of the flight hardware which has an impact on the accuracy of the centroiding. To represent the expected signal to noise ratio of the flight hardware, the images are stacked.

Table 3.2 compares the signal/noise ratio for the expected flight hardware and to the hardware used for this performance study. The table shows that stacking 22 images, captured with the test hardware, the S/N ratio is representative to that of the expected flight hardware. The dark current noise is not included as it is considered negligible. The read noise, photon noise and quantization noise for the stacked image are estimated based on the error propagation formula, $e_{stack} = \sqrt{n} \cdot e$. Where n denotes the number of images being stacked and e the error in question.

	Unit	*Flight unit*	*EM unit*	*EM unit, 22 stacks*
Full Well	$[e^-]$	100.000	4.365	96030
Read Noise	$[e^-]$	19	19	89
Quantization Noise	$[e^-]$	113	5	23
Photon Noise	$[e^-]$	316	66	310
RSS Noise	$[e^-]$	336	39	323
S/N	$[-]$	297	63	297

Table 3.2 *Comparison between the signal to noise ratio using the flight hardware and the test hardware. By stacking 22 images the signal to noise ratio of the test is representable to that of the expected flight hardware.*

Structured Light System for Positioning Mars Rover Robotic Arm

David Arge Klevang Pedersen*, Carl Christian Liebe**, John Leif Jørgensen*

*The Technical University of Denmark, DTU Space, Elektrovej 327, 2800 Kgs. Lyngby, Denmark

**Jet Propulsion Laboratory, California Institute of Technology, 4800 Oak Grove Dr., Pasadena, CA 91109, USA

***Abstract*- A structured light system is used to position a scientific instrument mounted on a Mars rover robotic arm relative to a Mars surface sample. 50 laser spots are projected on the Mars surface sample. The identification of individual laser spots, the centroiding algorithm and the calibration are discussed. Results show that the system measures the distance to the Mars surface sample more accurately than 50 microns at a nominal operating distance of 30 mm.**

***Index Terms* – CCD, laser, Mars2020, Structured light, Triangulation**

I. INTRODUCTION

The Planetary Instrument for X-ray Lithochemistry (PIXL) is a Micro-focus X-Ray Fluorescence (Micro-XRF) instrument for measuring fine scale chemical variations in rocks and soils on the Martian surface. It has been selected for the Mars 2020 rover science payload [1]. PIXL can measure elemental chemistry of tiny features observed in rocks, such as individual sand grains, veinlets, cements, concretions and crystals [2, 3].

The instrument is mounted on the rover robotic arm and must be located 30 mm +/- 0.5 mm from a surface sample to be examined for the 100 micron diameter X-ray spot to be focused. The sample would typically be abraded prior to investigation by PIXL. The abraded area would be relatively flat with an unknown topography of the surrounding area. The existing Mars 2020 rover robotic arm design does not have sensor instrumentation to position the PIXL instrument accurately relative to the Mars surface sample. Therefore, the structured light subsystem has been added to the PIXL instrument. The objective of the structured light is twofold, 1) Perform a distance measurement of the instrument relative to the Mars surface sample for the X-ray measurement and 2) Perform hazard detection while the robotic arm is approaching and positioning the instrument relative to the Mars surface sample. An artist's conception of the Mars Rover performing measurements with a turret mounted instrument guided by the robotic arm is shown in Figure 1.

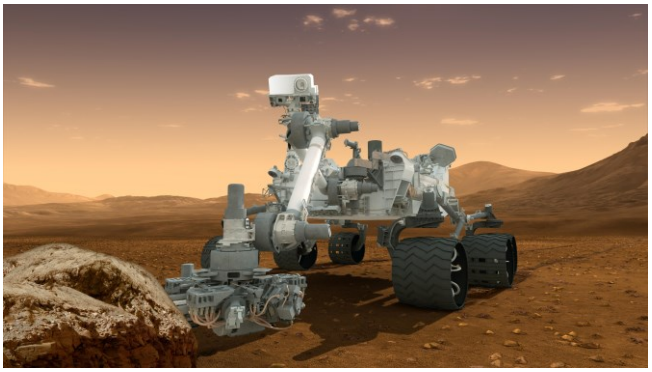

Figure 1: Artist conception of the rover taking a measurement with a turret mounted instrument on the Mars Rover Robotic Arm. (Credit NASA/JPL)

A demonstration model has been constructed to understand the performance of the structural light system. A diagram of the structural light system is shown in Figure 2. The illumination consists of 2 high powered ($200mW$) NIR diode lasers. Each laser is split up in 15 or 35 laser beams in a diffraction grading. This way it is possible to measure the distance to 50 points on the mock Mars surface sample. A modified star tracker, the microASC [4], with abundance of heritage from missions like Juno, GFO, MMS and Swarm is used to detect the laser spots. The microASC consists of a Digital Processing Unit (DPU) and a Camera Head Unit (CHU) with a monochrome CCD chip. For this demonstration system the standard lens of the CHU is replaced by a miniature lens with a low aperture to ensure focus over a large operational range. For this demonstration system a Navitar MLV12WA lens is used. Also a spectral filter is added to the optical chain. The filter primarily transmits light at the laser wavelength, but it also transmits light at other wavelengths so it is possible to acquire an image of the Mars surface sample as context for interpreting the scientific X-ray measurements. A bank of LEDs is also

used to illuminate the Mars sample for night time operation. However, the LEDs are not used for the structural light application. The required accuracy for the structured light system is given in Table 1.

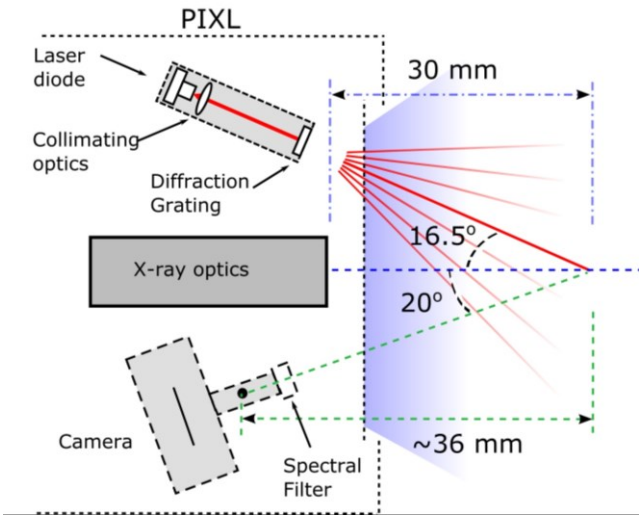

Figure 2: Diagram of the structured light system together with the X-ray optics of the PIXL instrument. The system consists of two collimated laser sources split into 15 and 35 beams, a CCD based camera with a spectral pass band filter and a bank of 40 LEDs. For simplicity only a one laser source is illustrated.

Measurement	3σ accuracy [mm]	Standoff distance [mm]
Standoff distance	0.5	20 - 40
	2.0	10 - 20 & 40 - 100
Lateral position	0.5	25 - 35
	1.0	20 - 25 & 35 – 40

Table 1: Accuracy requirements for the Structured light system.

Sensors used for distance measurements have a wide range of applications where the technology of use depends on the required accuracy and range of operation. The sensor technology is based on the principles of time of flight, phase delay or triangulation. A thorough review of the general technology development is presented by Blais [5] and an overview of the state-of-art applications for three dimensional imaging sensors is given by Sansoni [6]. The projected pattern can consist of a dot, line or a coded pattern. Furthermore the pattern can have grayscales or colors embedded to establish the correspondence between the detected features and the projected features [7, 8]. Early technology developments using structured light for space applications are described by Liebe [9, 10, 11], where the structured light is applied to autonomous hazard avoidance for a spacecraft vehicle. The described system will be infused into an actual Mars rover instrument as a distance meter also enabling hazard avoidance. The challenges for this specific structured light system is the operation over a wide temperature span (-150^oC to 10^oC) on the Martian surface in a space environment with uncontrolled lighting conditions and varying surface properties. The operational standoff distance for this system is 10 to 100 mm with a nominal distance of 30 mm.

Section II of this paper discusses the radiometry of the structured light system. Section III will discuss the centroiding algorithm used in the structured light system. Section IV discusses the algorithm for identifying the individual laser beam corresponding to the 50 laser spots in the image. In section V, the algorithm for converting the centroid measurements into distances are discussed. Section VI will discuss the calibration of the structured light system. Finally, section VII will discuss test results from field testing with the demonstration system.

II. SAMPLE ILLUMINATION RADIOMETRY

The instrument is designed for operation under all illumination conditions, i.e. night time operation and fully sun illuminated conditions. For night time operations, a bank of LEDs is used to illuminate the Mars surface sample to generate context images for the scientific interpretation of the X-ray measurements.

The total radiant exitance of a black body is described by Stefan-Boltzmann Law:

$$M = \varepsilon\, \sigma\, T^4 \quad \left[\frac{W}{m^2}\right], \tag{1}$$

where T is the temperature of the black body, ε is the emissivity (unity for black bodies) and σ the constant of proportionality, given as:

$$\sigma = \frac{2\,\pi^5\,k^4}{15\,c^2\,h^3} \quad \left[\frac{W}{m^2 K^4}\right], \tag{2}$$

Where c is the speed of light in vacuum, k is the Boltzmann's constant and h is Planck's constant. The total solar irradiance at Mars is thus given by:

$$E_{sun} = M\,\frac{R_{sun}^2}{D_{mars}^2} \quad \left[\frac{W}{m^2}\right] \tag{3}$$

Where R_{sun} is the radius of the Sun and D_{mars} is the distance from the Sun to Mars. With the relatively high elliptical orbit of Mars the distance to the Sun varies considerably. The maximum irradiance at perihelion is $717\,W/m^2$ and minimum at aphelion $493\,W/m^2$. Averaging the distance over the mean anomaly gives an irradiance of $583\,W/m^2$.

The Martian atmosphere is approximated to be transparent to radiation in the visual spectrum [12].

The laser beam has an elliptical Gaussian profile of $0.5mm$ (3σ). The laser is derated to $50mW$ and assuming a refractive grating transmission of 0.3, optics transmission of 0.5 and splitting the two laser beams into 35 and 15 collimated beams, results in an irradiance on the target surface of $E_{laser} = 546W/m^2$ and $E_{laser} = 1273W/m^2$.

The intensity of the split laser beams varies up to 30% relative to the brightest beam. For this analysis it is assumed that the laser spots have equal brightness.

A demonstration LED bank consists of 40 white LEDs each with $1.8mW/sr$ radiant intensity. At a distance of $20mm$ to the target surface and a view angle of 120^o the irradiance from a single LED is $4.4W/m\text{^}2$. With 40 LEDs the total irradiance from the LED bank approximates to $E_{LED} = 211W/m\text{^}2$.

At the nominal standoff distance of $58mm$ (from the camera pinhole, not the structured light system, where the nominal distance is 30 mm) the total spectral irradiance upon the Martian target surface is shown in Figure 3.

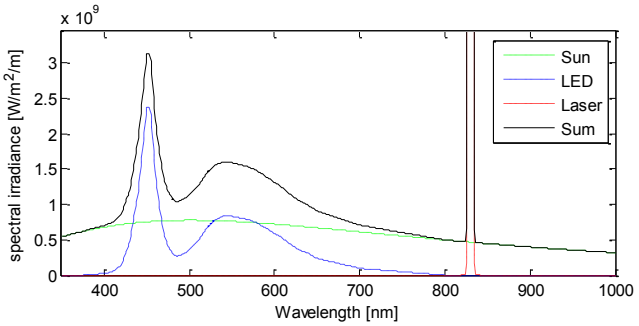

Figure 3: Spectral composition of the three light sources incident on the Martian target surface. The peak of the light from the laser source is not visible as it is several orders of magnitude larger than the other light sources.

Assuming Lambertian reflectance properties the radiant intensity of the radiation reflected of the surface is given by

$$I(\lambda) = \frac{E(\lambda)\,\alpha(\lambda)\,A}{\pi}\ \left[\frac{W}{sr}\right], \tag{4}$$

where A is the surface area covered by the sensors Field of View, $\alpha(\lambda)$ is the albedo of the surface. In this analysis an average albedo of 0.25 [13] is adopted as the spectral albedo will vary depending on the actual surface material. Given the solid angle Ω covered by the lens aperture towards the surface, the total power reaching the aperture is

$$P_a(\lambda) = \frac{E(\lambda)\,\alpha\,A_s\,\Omega}{\pi}\ \ [W]. \tag{5}$$

With the solid angle given by the aperture area and the distance to the surface $\Omega = A_a/D_s^2$, and the surface area A_s given by the CCD pixel size, focal length and distance to the surface $A_s = \frac{pix^2}{f^2}D_s^2$, equation (5) reduces to

$$P_a(\lambda) = \frac{E(\lambda)\,\alpha(\lambda)\,pix^2\,A_a}{\pi\,f^2}. \tag{6}$$

A narrow pass band filter designed to transmit in a $\pm 10\ nm$ pass band around 832 nm and attenuate other frequencies to 10% of the original signal is mounted in front of the camera optics. This increases the signal to background ratio of the laser signal. The number of photoelectrons detected by the sensor is given by

$$N_{e^-} = \frac{QE(\lambda)\cdot B_{BP}(\lambda)\cdot B_L(\lambda)\cdot P_a(\lambda)}{E_{photon}(\lambda)}, \tag{7}$$

Where QE is the quantum efficiency of the CCD, B_{BP} and B_{lens} are the transmission of the band-pass filter and camera optics and E_{photon} is the photon energy, given by

$$E_{photon} = \frac{h\cdot c}{\lambda}. \tag{8}$$

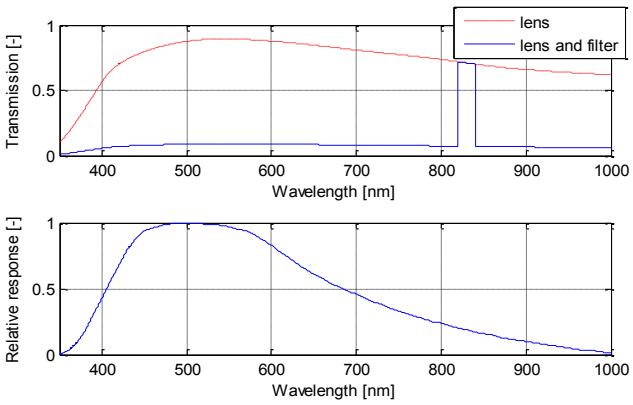

Figure 4: Top: Transmission of the Navitar MVL12WA lens optics together with the band pass filter. Bottom: Relative spectral sensitivity of the CCD.

Figure 4 shows the optical transmission of the lens and the filter together with the spectral sensitivity characteristics of the CCD which has a QE of 65% at the peak around 500 nm. Integrating over the wavelength, λ, gives the total number of photoelectrons. With the optical transmission of the lens + filter, QE of the CCD and camera parameters given in Table 2, the total number of photoelectrons for each of the three light sources is calculated and listed in Table 3.

Focal length	12	mm
F-number	16	No unit
Pixel size	8.6 x 8.3	µm
CCD resolution	752 x 580	Pixels

Table 2: Parameters for the camera system. It is observed that the f/# of the lens is 16. The reason for this is that the system must acquire focused images over a wide range of focal distances.

Sun	6.17 *e*5	e^-/s
Laser	8.09 *e*6	e^-/s
LED bank	3.90 *e*5	e^-/s

Table 3: Total number of photoelectrons detected by a single pixel of the CCD at the nominal distance of 53 mm.

Noise contributions for the measured image intensities are: dark current, read noise, quantization error and shot noise. The dominant error depends on the lighting conditions. The described system will have a full well capacity on the order of 100.000e^-, dark current of 2 e^-/s at 10^oC, read noise of 19e^- and an 8 bit AD converter, resulting in a quantization

error of $\frac{100.000}{2^8\sqrt{12}} = 113e^-$ [14]. The shot noise will a reach a maximum of $\sqrt{100.000} = 316e^-$ which is the limiting factor of the camera system achieving a combined S/N of $\frac{100.000}{\sqrt{19^2+113^2+316^2+2^2}} = 297$.

In conclusion, it is possible to activate sufficient laser illumination with the described system with $\frac{100.000e^-}{6.17e5e^-/s + 8.09e5e^-/s} = 11.5\ ms$ exposure time at a nominal distance under sunlit conditions. An example of an abraded Saddleback Basalt target illuminated by the Sun and single laser spot is shown in Figure 5.

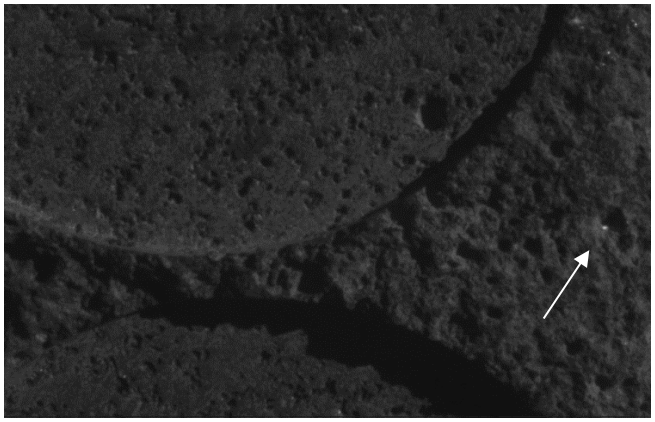

Figure 5: Image of abraded Saddleback basalt surface illuminated by the Sun, corresponding the expected power on the Martian surface, and a single laser spot. The image is acquired with an exposure time corresponding to 40ms at a standoff distance of 107mm.

III. LASER SPOT CENTROIDING

The output of the laser source is a collimated elliptic Gaussian profile. One method of centroiding would be to correlate or fit to a two dimensional Gaussian profile. However, due to the varying albedo and shape of the Martian surface sample the intensity profile will be distorted and deviate substantially from the original profile. Therefore an intensity weighted centroid is used to estimate the center of the laser spot. With the moment given by:

$$M_{pq} = \sum_x \sum_y x^p y^q W(x,y), \tag{9}$$

where p and q define the moment order and W the weighting. The weighting can be unity (binary images) or as in this case correspond to the intensity of a grayscale image. The centroid is given by the zeroth and first moments [15]

$$[x_c, y_c] = \left[\frac{M_{10}}{M_{00}}, \frac{M_{01}}{M_{00}}\right]. \tag{10}$$

To detect the laser spots two images are captured one with the laser on and one with the laser off. Subtracting the two images leaves only information from the laser spot. To assess the accuracy of the centroid algorithm an experiment was conducted. More specifically, a plane surface with varying albedo (representing abraded Saddleback basalt material) was measured with the structured light system positioned at decreasing distances with a step size of 50 microns. The exposure time was set so the laser spot was not overexposed during the test. This is representative of using an autonomous exposure feature optimizing for the brightest of the 50 spots, leaving other spots underexposed.

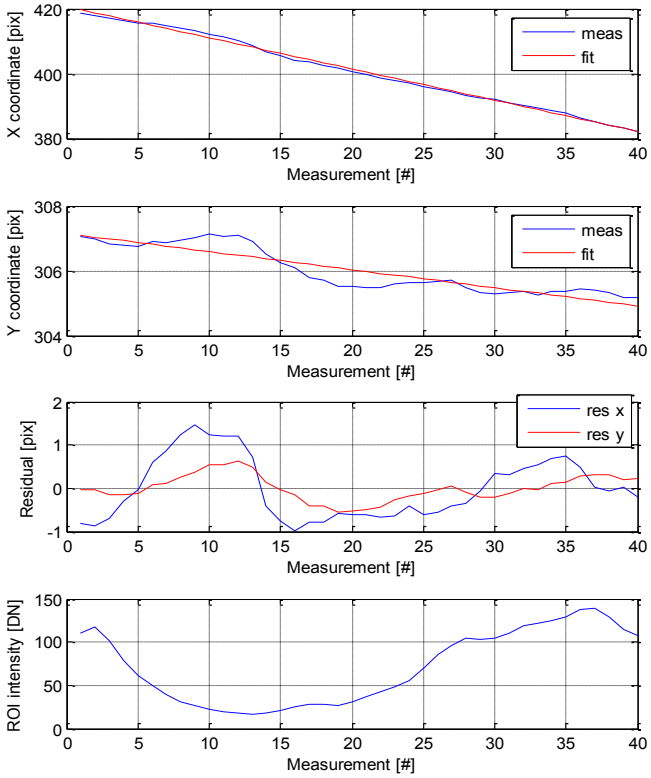

Figure 6: The two top plots show coordinates of centroid measurements of a single laser spot together with a linear fit (red). Plot 3 shows the residual of the centroids for both axes. Bottom plot shows the average intensity of the laser spot region of interest.

The measured centroids are shown in Figure 6 together with a linear fit. The figure illustrates that the measurements are subject to largely varying biases. Observe that the centroid moves in the negative x and y direction, almost aligned with the x axis. Figure 6 also shows the average intensity of the laser spot. It is observed that the intensity decreases to 17 DN at measurement 14. As the laser spot travels from a "bright" to "dark" area a positive bias is seen in the residual in both the x and y axis. The bias is noticeably larger in the x axis which relates to the direction towards the boundary of the dark feature relative to the travelling direction. The standard deviation of the residuals are 0.712 and 0.303 pixels for the x and y axis. This includes both the noise and bias of the centroid measurements. The noise can be estimated using the increment of the centroids $\delta_{cen} = [x_{i+1} - x_i\ , y_{i+1} - y_i\ ]$, shown in Figure 7. δ_{cen} contains noise contributions from two individual samples, so assuming the samples are uncorrelated the noise is estimated by $\sigma(\delta_{cen})/\sqrt{2}$. The noise in the x axis and y axis is

estimated to 0.215 and 0.086 pixels. Note that the noise and bias in the x axis is considerable larger than in the x axis. This is due to the laser spot travelling almost entirely in the direction of the x axis, and close to perpendicular to the darker feature of the sample. The RSS noise of the centroid is thus estimated to a standard deviation of 0.232 pixels.

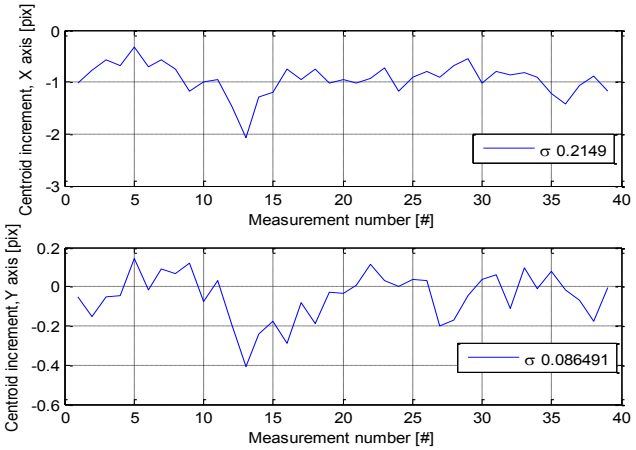

Figure 7: The increment of the consecutive centroid measurements.

IV. LASER SPOT IDENTIFICATION ALGORITHM

One problem, that all multiple beam structured light systems faces, is the following: In an image of multiple laser spots being projected onto a surface of unknown topography, which laser spot is which? This section will describe the algorithm used to establish the identity of the laser dots.

The structured light system consists of 2 individual illuminators. They are not turned on at the same time. The primary reason for this is to simplify the laser spot identification. The 2 structured light illuminators represents 1) a dense grid to establish distance to the Mars sample, close to where the X-ray beam is intercepting and 2) a sparse laser grid, used for hazard detection during approach and positing of the PIXL instrument by the robotic arm. A picture of the two spot patterns at nominal distance is shown in Figure 8 and Figure 9.

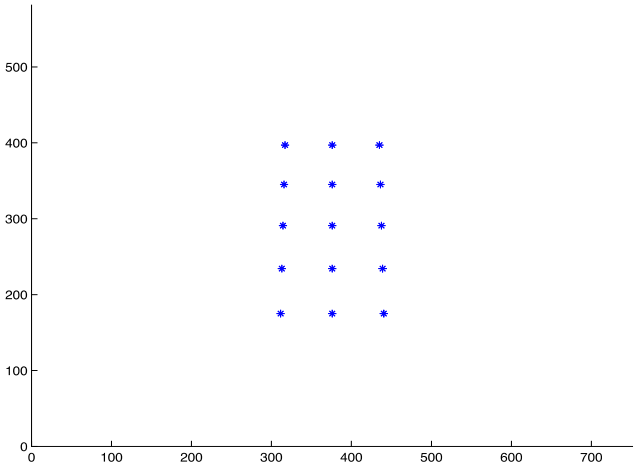

Figure 8: The dense laser spots at nominal (30 mm) distance.

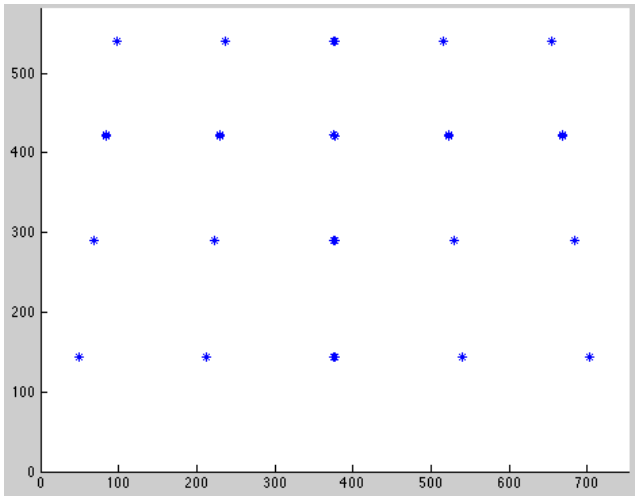

Figure 9: The sparse laser spots at nominal (30 mm) distance.

When the distance to the laser sample is changed, the position of the laser dots are also changed due to the baseline difference between the laser and the camera. As an example, when the Mars sample is imaged continuously between the distances from 20 to 40 mm, the motions of the different laser spots are as shown in Figure 10. This is the range of motion where this dense structured light system has to operate. The coordinates formed from the spots lie on a straight line, referred to as epipolar lines. In Figure 11 is shown the laser spot positions of the sparse array when the distances change from 20 mm to 100 mm.

During calibration, 50 different images are generated (one of each laser spot). The individual images represent all possible positions in the image that this specific laser spot can be located at. Because, there are errors and uncertainties associated with a measurement, the image for each laser spot is dilated 2 pixels. This accounts for the errors. As an example, the image for laser spot 6 (lower right corner in Figure 9) from the dense array is shown in Figure 12.

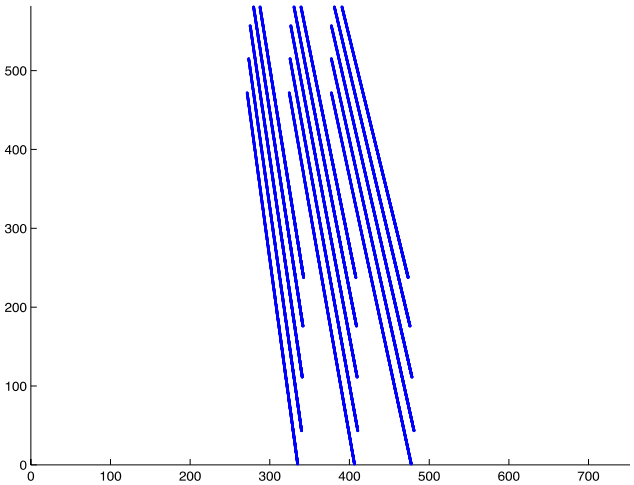

Figure 10: The epipolar lines describe the motion of the 15 laser spots from the dense array as distance is changed from 20 to 40 mm.

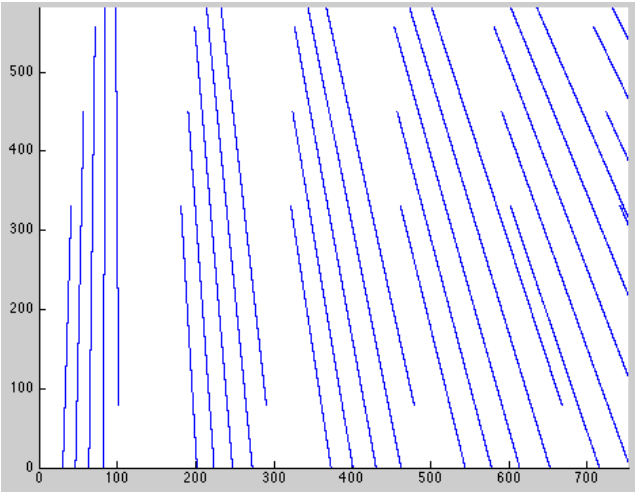

Figure 11: The motion of the 35 laser spots from the sparse structured light system when the distance is changed from 20 mm to 100 mm. The coordinates of the spots lie along the epipolar lines of each laser beam.

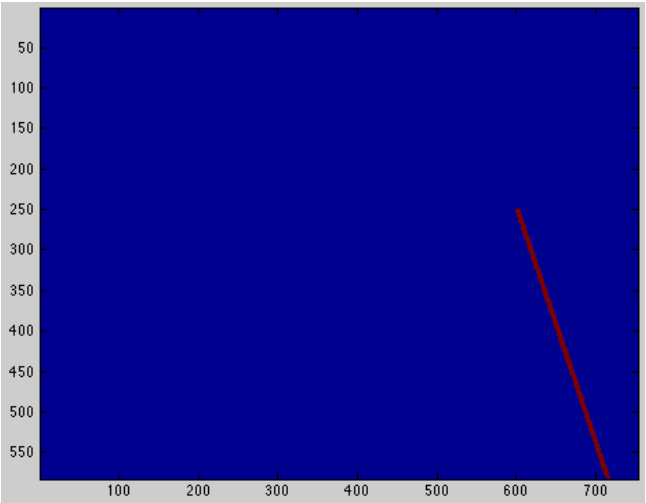

Figure 12: The location map where laser spot 6 can be located.

When the 50 individual laser maps have been generated, the structured light system is ready to do spot identification. An example of an image that the structured light system could encounter is shown in Figure 13.

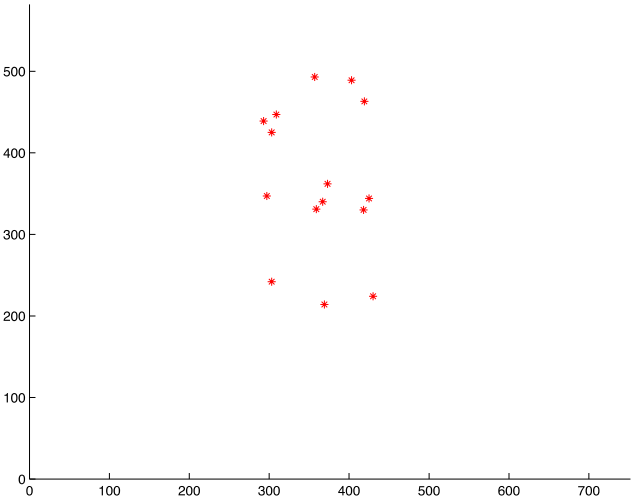

Figure 13: An example of an image that the structured light system could encounter. The system must be able to identify which dot belongs to which laser dot.

The algorithm operates by comparing the individual spots to the 50 individual spot maps. The spot is identified as the image where it has been marked. This is illustrated in Figure 14. It is advantageous to design the system so there is no overlap between the individual spots (the described structured light system does not have overlap). In case there is an overlap, it will sometimes not be possible to uniquely identify the laser spot.

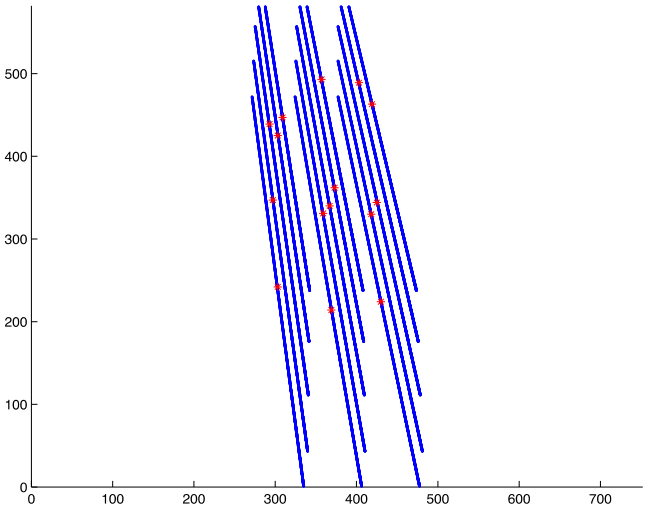

Figure 14: Image with the 15 individual laser maps (for the dense system) overlaid with the picture of the laser dots. It is observed it is easy to identify the individual spots.

V. DISTANCE MEASUREMENT

The centroids of each laser spot allows for a distance measurement. These can be combined to estimate the plane of the abraded area or used separately for topography information or simply using the single spot closest to the X-ray beam. Here a single centroid will be used to estimate the distance. A sketch of the structured light system is shown in Figure 15. The camera system that is located at the equivalent pinhole of the camera lens is utilized. This is the reference for the standoff distance along the camera boresight.

Given the baseline B_x and the angle β_x between the laser and camera boresight a tangential relation is formulated:

$$\tan \beta_x = \frac{Z_x}{X - B_x}. \tag{11}$$

where Z_x is the distance toward the sample along the camera boresight and X is the lateral coordinate. Using the pinhole camera model the coordinates are related to image plane coordinates:

$$X = \frac{x - x_0}{f} \cdot Z_x, \tag{12}$$

Where x_0 is the principal point in the x axis and f is the focal length. Combining equation 11 and 12 the nominal

distance Z_x is described by the centroid coordinate in the image plane:

$$Z_x = \frac{B_x}{\frac{x - x_o}{f} - \frac{1}{\tan \beta_x}} \tag{13}$$

The relation in equation 13 is also valid for the y axis. The calculated distance Z_x and Z_y from both centroid coordinates must be fused, utilizing the baseline angle. The standoff distance d is given as the average of the two, weighed by the cotangent of the baseline angle:

$$d = \frac{Z_x \cot \beta_x + Z_y \cot \beta_y}{\cot \beta_x + \cot \beta_y} \tag{14}$$

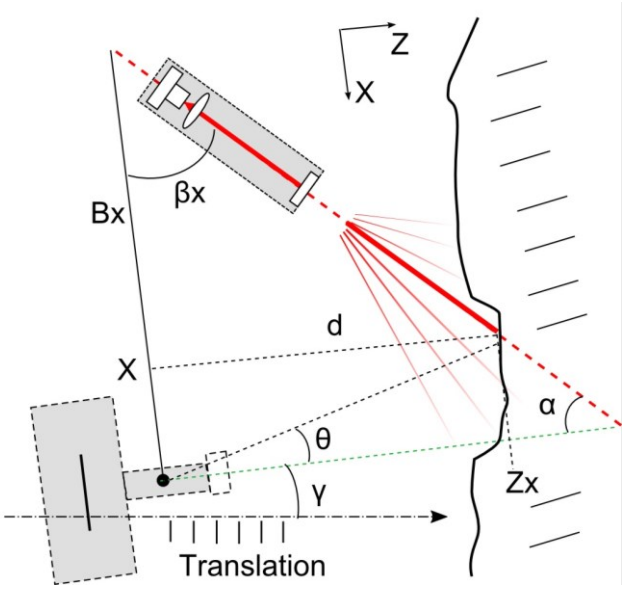

Figure 15: Sketch of the structured light system together with the translation stage and sample target. B denotes the baseline and β the angle between the two boresights.

VI. CALIBRATION

The calibration is performed by translating the structured light system, relative to a plane calibration target with uniform albedo. The structure is translated at a fixed translation step, δ_{step} = 0.5mm using a translation stage with an on-axis accuracy of 5 µm. At each position a centroid measurement is logged and corrected for lens distortion.

A least square cost function is formulated based on the centroid measurements q_i and the modelled centroids p_i

$$r = \sum_{i=1}^{n} r_i^2, \tag{15}$$

where

$$r_i = \sqrt{\left(p_{x_i} - q_{x_i}\right)^2 + \left(p_{y_i} - q_{y_i}\right)^2}. \tag{16}$$

The modeled centroids are given by a pinhole projection

$$p_i = \left[f\frac{X_i}{Z_i}, f\frac{Y_i}{Z_i}\right]. \tag{17}$$

The world coordinates X_i, Y_i, Z_i of the modelled centroids are formulated by the baseline B and the angle β

$$\begin{aligned} X_i &= B_x - \frac{Z_i}{\tan(\beta_x)}, \\ Y_i &= B_y - \frac{Z_i}{\tan(\beta_y)}, \\ Z_i &= Z_0 + dZ_i, \end{aligned} \tag{18}$$

where $dZ_i = i \cdot \delta_{step}$. With the camera's optical axis roughly aligned with the translation, the actual increment along boresight is given by $\delta_Z = \delta_{step}/\cos(\gamma)$. Where γ is the angle between the camera boresight and the direction of the translation stage. Given an initial guess on the variables $B_x, B_y, \beta_x, \beta_y, Z_0$ and γ a minimum for the cost function is estimated using a six dimensional Nelder-Mead optimization [16]. Figure 16 shows the increment of the centroid coordinates for the calibration measurements together with the least square fitted model. The centroid residual for the calibration is 0.167 pixels (1σ). The resulting baseline and angle are listed in Table 4 and an image of the calibrated test setup is shown in Figure 17.

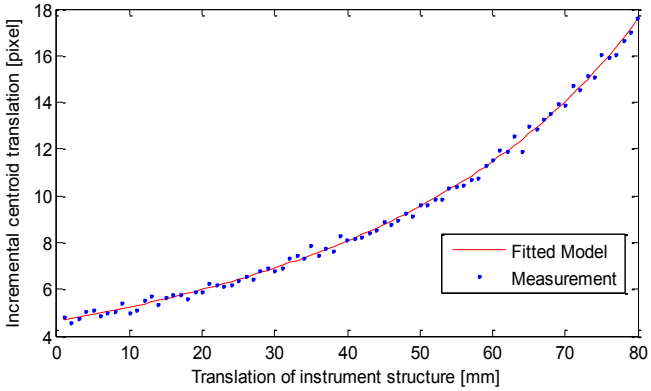

Figure 16: The increment of the consecutive centroid measurements as function of the translation of the structured light system.

B_x	-43.83 mm
B_y	-1.94 mm
β_x	52.35°
β_y	87.90°

Table 4: Calibrated parameters describing the baseline and angle of the structured light system.

Figure 17: The structured light system consisting of the CCD sensor, laser source and LED bank are mounted on a high accuracy translation stage. Here the system is imaged targeting abraded Saddleback basalt.

VII. DISTANCE ACCURACY

To measure the performance of the demonstration system, distance measurements have been performed over the full measurement range. The target surface was a plane photograph of an abraded Saddleback basalt sample. Figure 18 shows the residual of the distance measurements acquired as the translation stage approaches the target. The residual is centered around zero with a standard deviation of $44.7\mu m$ at 1σ. This corresponds to 27 % of the required accuracy for the OFS operating at the nominal standoff distance listed in Table 2. The residual in the lateral direction has a standard deviation of $17.3\mu m$ at 1σ which corresponds to 10 % of the required accuracy at nominal distance operation.

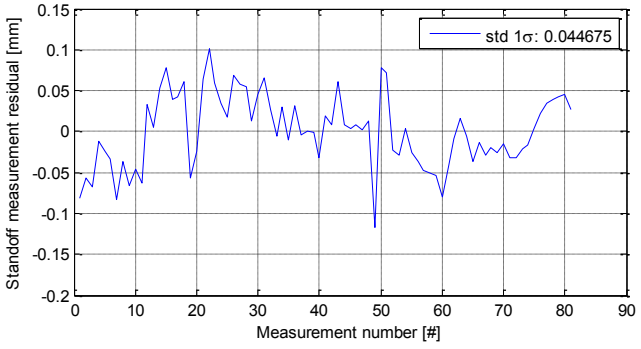

Figure 18: Residual of the measured standoff distance on a planar surface with albedo variations similar to that of an abraded Mars Saddleback basalt surface sample.

Performing the same sequence of measurements on an actual abraded stone will reveal the profile of the surface. Figure 20 shows the measured profile of the sample shown in Figure 19. The linear measurements along the x axis are the flat abraded area. The jump in the middle represents the small dimple in the sample. The jump of $2\,mm$ on the left side is where the laser spot moves outside the abraded area.

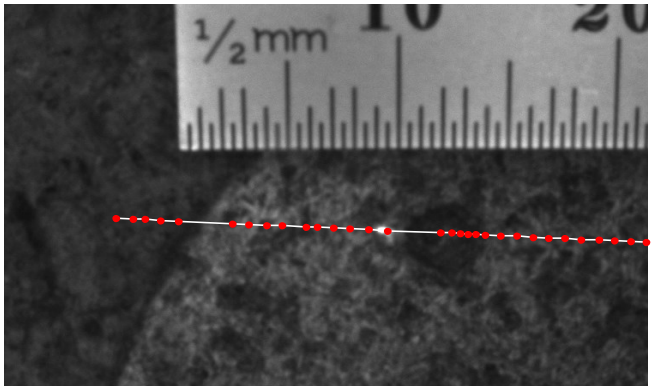

Figure 19: Sample of abraded Saddleback basalt surface sample used for profile measurements. The edge of abraded area seen on the left side and a dimple in the abraded area is located to the right along the scanning line.

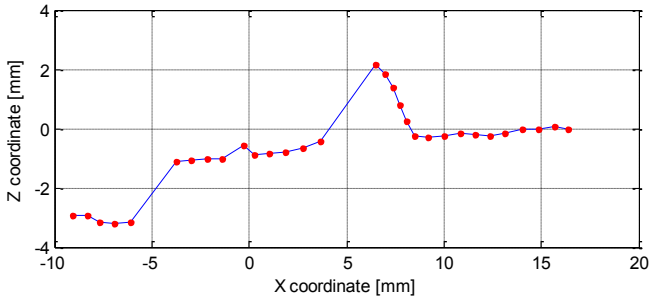

Figure 20: The measured profile of an abraded Saddleback Basalt surface sample. The profile shows a flat surface along the X axis. In the center a dimple in the surface sample is detected, with a depth of ~2.4 mm. On the far left the laser spot has moved outside the abraded area.

VIII. SUMMARY

A structured light system to guide the positioning of a scientific instrument for robotic planetary exploration is presented. The accuracy of the centroiding of the individual laser spots as well as identification of the laser spots is discussed. The centroid accuracy is ~0.7 pixels 1 sigma at the nominal distance of $30\,mm$. The distance accuracy is better than 50 microns 1σ over the full range of operation. It should be emphasized that only a demonstration system has been tested. The real structured light system will be operating more than 150^oC colder than where it is calibrated. It is expected that thermal excursions will drive the error budget of a structured light system operating on Mars.

IX. ACKNOWLEDGEMENT

The research described in this paper was carried out at the Technical University of Denmark and the Jet Propulsion Laboratory, California Institute of Technology and was sponsored by the Technical University of Denmark and the National Aeronautics and Space Administration.

X. REFERENCES

[1] Jet Propulsion Laboratory, California Institute of Technology, »Mars 2020,« [Online]. Available: http://mars.nasa.gov/mars2020/. [Senest hentet eller vist den 7 September 2015].

[2] A. Allwood, B. Clarke, T. Elam, D. Flannery, M. Foote, J. Hurowitz, E. Knowles and L. Wade, ». Texture-specific elemental analysis of rocks and soils with PIXL: The Planetary Instrument for X-ray Lithochemistry on Mars 2020,« i *Proceedings of the IEEE Aerospace Conference*, Big Sky MT, 2015.

[3] A. C. Allwood, L. Wade, J. Hurowitz, R. Hodyss, D. Flannery, »Seeking Ancient Microbial Biosignatures with PIXL on Mars 2020,« American Geophysical Fall Meeting 2014, 2014.

[4] Peter S. Jørgensen, John L. Jørgensen, Troelz Denver, »MicroASC a Miniature Star Tracker,« *Proceedings of the 4S Symposium: Small Satellites, Systems and Services,* 2004.

[5] F. Blais, »A review of 20 years of range sensors development,« *J. Electronic Imaging ,* pp. 13, 231-240, 2004.

[6] Giovanna Sansoni, Marco Trebeschi, Franco Docchio, »State-of-The-Art And Applications of 3D Imaging Sensors in Industry, Cultural Heritage, Medicine, and Criminal Investigations,« *Sensors,* pp. 568-601, 2009.

[7] Joaquim Salvi, Jodi Pagès, Joan Batlle, »Pattern codification strategies in structured light systems,« *Pattern Recognition,* nr. 37, pp. 827-849, 2004.

[8] Jason Geng, »Structured-light 3D surface imaging: a tutorial,« *Advances in Optics and Photonics,* årg. 3, nr. 2, pp. 128-160, 2011.

[9] Carl Christian Liebe, Curtis Padgett, Johnny Chang, »Three Dimensional Imaging Utilizing Structured Light,« i *Aerospace Conference Proceedings, IEEE*, Big Sky, MT, 2004.

[10] Carl Christian Liebe, Keith Coste, »Distance Measurement Utilizing Image-Based Triangulation,« *Sensors Journal, IEEE,* årg. 13, nr. 1, January 2013.

[11] Carl Christian Liebe, Curtis Padgett, Jakob Chapsky, Daniel Wilson, Kenneth Brown, Segei Jarabets, Hannah Goldberg, Jeffrey Schroeder, »Spacecraft Hazard Avoidance Utilizing Structured Light,« i *Aerospace Conference, IEEE*, Big Sky, MT, 2006.

[12] Haberle, R. M., McKay, C. P., Pollack, J. B., Gwynne, O. E., Atkinson, D. H., Appelbaum, J., Landis, G. A., Zurek, R. W., Flood, D. J., "Atmospheric Effects On The Utility Of Solar Power On Mars," in *Resources of Near-Earth Space*, vol. 117 (256 pp), Tuscon, University of Arizona Press, 1993, pp. 845-885.

[13] N. G. Barlow, Mars: An Introduction to its Interior, Surface and Atmosphere, New York: Cambridge University Press, 2008.

[14] W. R. Bennet, »Spectra of Quantized Signals,« *Bell System Technical Journal Vol. 27,* pp. 446-471, 1948.

[15] B. K. P. Horn, Robot Vision, Cambridge: The MIT Press, 1986.

[16] J. W. S. J. Nocedal, Numerical Optimization, Second Edition, New York: Springer Science+Bussiness Media, LLC, 2006.

XI. BIOGRAPHIES

David Arge Klevang Pedersen received the M.S.E.E. degree in 2011 from the Department of Electrical Engineering, Technical University of Denmark. Since 2012, he has been enrolled as a Ph.D. student at the Department of Measurement and Instrumentation at DTU Space, Technical University of Denmark. His research is focused on visual tracking of non-cooperative space borne targets.

Carl Christian Liebe received the M.S.E.E. degree in 1991 and the Ph.D. degree in 1994 from the Department of Electro-physics, Technical University of Denmark. Since 1997, he has been an employee at the Jet Propulsion Laboratory, California Institute of Technology. He is the supervisor of the GN&C Hardware and Testbed Development Group. He has led the development of several metrology systems for space flight

John Leif Jørgensen is professor and head of Measurement and Instrumentation division at the National Space Institute, Technical University of Denmark. Professor Jørgensen is an expert in advanced measurement systems and his research focus is on development of optical guidance and navigation systems.

3.3 Outlook

The results of the performance study show that the presented structured light system is able to meet the OFS requirements and thus support the requirements of PIXL and ultimately the scientific goals of the mission. The study demonstrates the utility of a structured light system performing in-situ distance measurements on real-world targets.

The development phase of the instrument is still at an early stage where the focus has been to verify the fulfillment of the main requirements. Approaching the next phase, the focus will shift to manufacturing of the instrument hardware and to further exploit the possibilities of the structured light and imager available within PIXL. The scientific yield of the mission is naturally constrained by the operational turn-around of the rover. The typical scenario of operating the rover is to perform a planned sequence of trekking and imagery during the daytime, transmit the results to scientists and operators at Earth for evaluation, and plan for the next sequence of operations. In the case interesting rock formations are located, the rover is commanded to back up and perform further investigations. The operation of positioning the instrument, mounted on the robotic arm, relative to the sample of interest holds a large overhead of communication and verification between the rover and ground segment on Earth. Every approach towards a rock sample holds a risk of unforeseen collision. Combining distance measurements from the OFS and stand-alone image processes within the DPU holds opportunities for a fully autonomous and safe navigation of the arm mounted instrument. Besides using the grid of distance measurements for hazard detection, the grid can also be used to estimate the angle of the plane surface of the abraded area. The DPU will be able to detect the circumference of the abraded area and estimate a relative position of the instrument. Combining such measures enables to shorten the turn-around time of positioning the instrument and ultimately increasing the time spent on the end goal science measurements.

4 Tracking of Satellites and Planetary Bodies

This chapter presents the study of tracking a large scale natural satellite, or planetary body. The work herein is described by papers 2, 3, and 4, each contributing to the development, testing and verification of an optical navigation module capable in supporting the process of orbit determination of a spacecraft by measuring the line of sight and range of a planetary target.

The ability to estimate a spacecraft's position and velocity has been an important area of research, ever since the pioneering vehicles of Luna, Gemini and Apollo were destined to orbit and land on the lunar surface. The technology has, naturally, evolved significantly over many decades. From simplistic optical instruments measuring angular differences between celestial references, to large infrastructures like the Deep Space Network (DSN), that determines a spacecraft's trajectory very accurately using radiometric measurements. Although optical observations can not match the capabilities of DSN, they do offer significant value to certain missions where in-flight optical observations of a planet or other body can improve the body's ephemerides or determine the spacecraft's inertial position.

Typically, modern optical observations are performed with the target overexposed in order to detect the stars in the background. The microASC however, has the capability of operating multiple CHUs with a single DPU. Dedicating a single CHU for planetary observations and the remaining CHUs for attitude measurements, the intercalibrated CHUs allow the microASC to measure the attitude of the dedicated CHU, while at the same time observing the correctly exposed target. This enables the microASC to resolve a measure of the target's LOS and range in an inertial reference frame.

The following three papers will each describe the work related to the development, testing and verification of an optical navigation module that is based on the

microASC platform:

Capturing of In-flight observations Paper 2 describes how the microASC system is used as an inertially controlled imager on board the Juno spacecraft. As Juno approached the Earth-Moon system, preparing for the gravity assist maneuver, a single CHU was dedicated to acquire images of the Earth and Moon during the 4 day approach, while maintaining nominal star tracking operations on the remaining three CHUs. The combination of attitude measurements and the optical observations holds the opportunity to perform autonomous observations for in-flight orbit determination. In addition, the combination enables an post-processing of the observations, which can adjust for the slight variations of the image capture triggering that shifted the position of the targets in the focal plane. Therefore, post-processing of the images, effectively countering the rotational motion of the spacecraft using the attitude measurements is also presented. The result of the post-processing was the release of the Juno Earth-Moon time-lapse movie [19].

Processing of in-flight optical observations Paper 3 accounts for the process of tracking both single and multiple targets resolving their individual LOS and range estimate, with the goal of resolving a position of the spacecraft in an inertial reference frame. The images captured during Juno's Earth flyby constitute excellent material for the testing and verification the image-processing for optical navigation. The results from processing the in-flight data are presented.

Characterization of system performance Paper 4 presents a characterization of the optical navigation module's performance over the full operational envelope. This is obtained by simulating the system's performance taking into account the sensor's performance and the target's topography. The simulated results are compared and verified with the results from both in-flight and ground observations.

Acta Astronautica 118 (2016) 308–315

Contents lists available at ScienceDirect

Acta Astronautica

journal homepage: www.elsevier.com/locate/actaastro

MicroASC instrument onboard Juno spacecraft utilizing inertially controlled imaging

David Arge Klevang Pedersen *, Andreas Härstedt Jørgensen, Mathias Benn, Troelz Denver, Peter Siegbjørn Jørgensen, Jonas Bækby Bjarnø, Alessandro Massaro, John Leif Jørgensen

Technical University of Denmark DTU Space, Division of Measurements and Instrumentation Systems, Elektrovej 327, 2800 Kgs. Lyngby, Denmark

ARTICLE INFO

Article history:
Received 4 March 2015
Received in revised form
19 September 2015
Accepted 1 November 2015
Available online 10 November 2015

Keywords:
Juno
Earth fly-by
Star tracker
Attitude
Image processing

ABSTRACT

This contribution describes the post-processing of the raw image data acquired by the microASC instrument during the Earth-fly-by of the Juno spacecraft. The images show a unique view of the Earth and Moon system as seen from afar. The procedure utilizes attitude measurements and inter-calibration of the Camera Head Units of the microASC system to trigger the image capturing. The triggering is synchronized with the inertial attitude and rotational phase of the sensor acquiring the images. This is essentially works as inertially controlled imaging facilitating image acquisition from unexplored perspectives of moons, asteroids, icy rocks and planetary rings.

1. Introduction

The Juno spacecraft, one of NASA's New Frontiers missions, was launched on August 5th 2011 and set its course towards Jupiter, planned for arrival on July 2016. On the 9th of October 2013, en route to Jupiter, JUNO successfully executed the Earth fly-by (EFB) maneuver and gained velocity in order to reach Jupiter. When preparing for the Earth approach it was discovered that a unique opportunity to record images of the Earth and Moon system from afar presented itself. The Earth and Moon would enter the Field of View (FOV) of the micro Advanced Stellar Compass (microASC) Camera Head Units (CHU).

The effort to capture and process the raw image data from the microASC system during the EFB is presented in detail leading to a perspective of future possibilities for the microASC system.

2. The microASC instrument onboard JUNO facilitating inertial controlled imaging

The microASC system onboard Juno consists of four CHUs (denoted CHU A-D) and a double Digital Processing Unit (DPU). A detailed description of the system is found in [1]. The microASC system is a part of the magnetic field investigation package (MAG) onboard Juno [2] and is designed to autonomously deliver high accuracy attitude measurements of the magnetometers on the basis of stellar sky images, see Fig. 1. An overview of the Juno mission is given in [3]. For the purpose of performance analysis, the microASC instrument is capable of capturing and downloading images from any of the four CHUs for analysis on ground.

The Juno spacecraft is spin stabilized, rotating at approximately 2 rpm, so CHU D will only have Earth and Moon in the FOV during a small phase of the rotational sequence. Commanding CHU D to a very low exposure time meeting the expected brightness of Earth and Moon

* Corresponding author. Tel.: +45 45253609; fax: +45 45887133.
E-mail address: dakp@space.dtu.dk (D.A.K. Pedersen).

http://dx.doi.org/10.1016/j.actaastro.2015.11.001
0094-5765/

prevents CHU D from delivering attitude solutions as no stars are detectable at this level of exposure.

There is a need to inertially control the triggering of image acquisition exactly when the Earth and Moon are in the FOV as well as knowing both the timestamp and attitude of the sensor at the time of capture. Utilizing the inter-calibration of the independent CHUs, CHU C is commanded to trigger the microASC system to acquire an image from CHU D at the correct phase of the rotation, once every 5 rotations. This setup ensures that the acquisition of the images occurs at the correct phase of the rotation as well as providing an accurate attitude estimate of CHU D when acquiring the image. The image acquisition with CHU D is based on the real-time attitude measurements from CHU C, operating as a fully autonomous inertially controlled imager. Onboard JUNO, the microASC system operates at 4 Hz. With the optical sensor being an analog interlaced video signal the time between the First Field (FF) and Second Field (SF) is 125 ms. Due to the spinning of the spacecraft the objects in the FF and SF will be offset corresponding to the angular motion of the CHU.

2.1. Integration time adjustment

The microASC system is specifically designed for star tracking with a very light sensitive sensor. Under normal operations the sensor will over bloom with Earth and Moon in the FOV. The microASC system however allows for adjusting the exposure time settings as a means of overcoming blooming effects. Commands to change the microASC exposure were sent to Juno during the approach. The time of execution are marked on Fig. 2 together with the trajectories of Earth, Moon and Juno during the EFB which are extracted from NAIF kernels [4]. From radiometric considerations and tests from a representative test environment appropriate exposure times could be estimated. Initially the integration time was set to 8 μs. As Juno approached Earth the area of the Earth and Moon in the sensor plane increases, thus increasing image artifacts correspondingly. To compensate for this, the exposure time of the sensor was reduced to 6 μs, and later to 4 μs. This level of exposure time was presumed the lowest feasible as the exposure time was affected by jitter in the synchronization pulse from the spacecraft to the microASC instrument, thus affecting the observed intensity of the objects. The fourth command adjusted the floor and ceiling parameters of the microASC's internal Automatic Gain Controller (AGC) effectively expanding the working range of the controller.

3. Image post-processing

The raw image data is influenced by the settings of the instrument being close to the absolute limitations of the sensor, leaving imaging artifacts in the data. These artifacts are described and corrected for in the post processing of the downloaded image data captured during the Earth fly by. The post processing is divided into five successive procedures:

- Cleaning of blooming and smear residuals.
- Matching of object intensity and sharpening of image, compensating for lens blurring.
- Warping of frames.
- Merging of frames.
- Conversion from grayscale to color.

The image artifacts and these five processes are described in detail in the following sections.

3.1. Image artifacts

Fig. 3 shows a typical case of a raw image from the fly-by data series. The figure shows smear residuals as distinct lines through the objects from top to bottom of the image. These lines become more prevalent as the area of objects increase. The smear residuals are divided into vertical lines and tilted lines. The vertical lines are caused by the blooming of a line segment of the sensor chip. The tilted lines are caused by photons tunneling through the light-shielded area of the sensor, constituting the vertical transfer register, as the bright objects move across the FOV during the readout of the image sensor. Furthermore objects in the FOV induce a ghost shifted upwards and slightly to the right from the position of the object itself. The presence of the ghost is due to the method used to synchronize the microASC to the spacecraft master clock, where the instrument's internal timing is halted, thus also halting the readout process. During the halted period photons from the very bright object leak through the light-shielded area to the vertical transfer register.

These image artifacts are not present under normal working conditions of the microASC. It is only present due to the very bright object in the FOV and the setting of a very low exposure time.

The process of cleaning the image for artifacts is initialized by subtracting the background level of the image. The level of the background is determined as the 50% fractile of the image histogram. Next the cleaning process is divided into three subroutines removing the tilted lines, vertical lines and the ghost.

3.1.1. Smear lines

The time delay of 0.125 ms between FF and SF results in a rotation of $\theta = 1.5^\circ$ around the spacecrafts axis of rotation ω as illustrated in Fig. 4. The offset of the objects between FF and SF depends on the position of the objects along the vertical axis (y axis) of the image, e.g. an object at the top of the image has a small offset from FF to SF as the object is close to the axis of rotation of the spacecraft.

The angle of the tilted smear line directly depends on the position of the object along the vertical axis of the image. The tilting of the line is thus smaller for objects at the top of the image than at the bottom. Each tilted smear line must therefore be treated independently. The line is removed by subtracting a 50% fractile profile of tilted columns from the region where the tilted line is present. The vertical smear lines are removed by the same method as the tilted blooming lines. Only the 50% fractile profile of columns is not tilted and is processed on the whole image frame without considering the position of the objects.

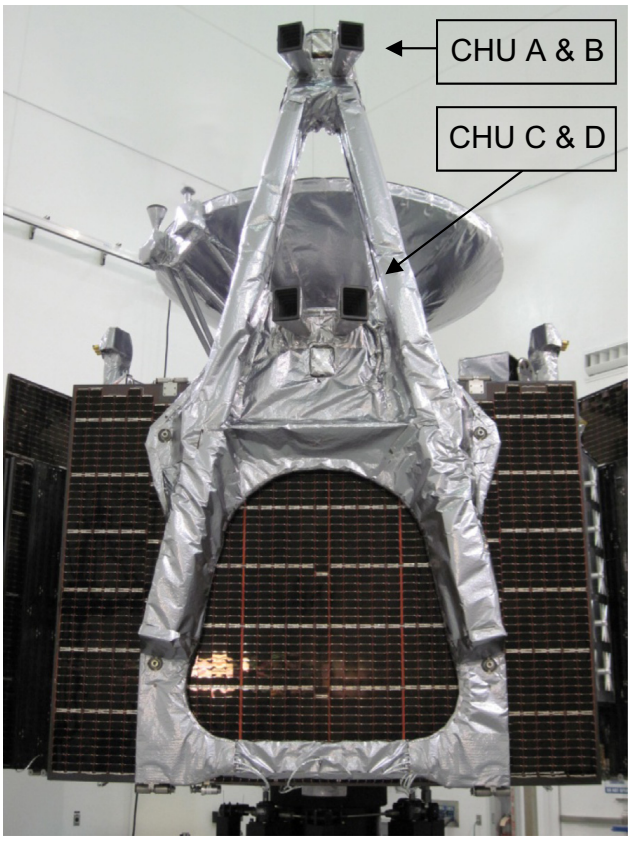

Fig. 1. The four Camera Head Units of the microASC system together with the baffles mounted on the magnetometer boom of the Juno spacecraft prior to launch. Credit: NASA/JPL/Caltech.

3.1.2. Ghost

A ghost is present for bright objects in FOV, the position of which will be offset from the original object. The vertical offset will be constant and the horizontal offset depends on the objects position along the vertical axis, as with the tilt of the tilted smear line. For the simple case where the object is small, the ghost and object will not overlap, so the region containing the ghost is simply set to the background level. For the case where the object and ghost overlap a Region of Interest (ROI) is defined in order to only remove the ghost and not the object. The result of removing the artifacts is shown in Fig. 5. Here the tilted lines from both the Earth and Moon, vertical lines and ghosts from both objects are removed from the image data. Note that the FF and SF are processed independently and only the data from FF is shown in the figure.

3.2. Matching of intensity and sharpening

Due to the proximity of the sensors exposure time to the lower limit of the microASC system, the exposure time is affected by jitter in the synchronization pulse and thus the intensity of the objects can vary considerably. An example is shown in Fig. 6 where the Earth and Moon in FF are barely visible but are clearly visible in SF. Note, however that the ghost of the Earth is still visible in both frames as the internal synchronization is not affected by the jitter. Therefore the intensities of the objects in each frame are matched by a scale defined to equalize the average intensity of the Earth.

Subsequently the image data is run through a sharpening filter to cancel out the lens blurring effect from the optical system.

3.3. Warping of frames

As a consequence of the interlaced technology, the rotational motion of the sensor causes an angular offset between the half frames. The information from the two frames can be combined by warping one frame onto the other or both frames to a predefined view direction.

3.3.1. Attitude measurements

As CHU D is commanded for image capturing it is not possible to obtain attitude measurements from this sensor. However, the CHUs onboard Juno are inter-calibrated and thus the attitude of CHU D is estimated based upon attitude measurements from CHU A. The attitude measurements from CHU A are used to formulate a spin model of the rotational motion of the spacecraft. The spin model consists of an angular velocity vector where each vector element and length of vector is fitted to a first order regression. Using the spin model the attitude of CHU D is estimated based on the timestamp of the captured image. This method of spin modeling is only possible during a maneuver free period, which was the case of JUNOs earth fly-by. Also, nutation and precession are assumed not to be of any significance at this point in time of the mission. Otherwise it must be taken into account in the spin model.

The warping of each image frame is inherently dependent on the accuracy of the attitude measurement of CHU A. Only small disturbances corrupt the warping of the image frames by not placing the Earth and Moon at the exact same position in the image plane. The two half frames FF and SF where not so much affected compared to images captured with minutes between them. The disturbances typically cause the objects to “jump” forward or backwards in the rotational phase. This appears for instance when the Moon enters the FOV of CHU A and thereby adding noise to the attitude measurement from that CHU in particular. The spin model is therefore only based on attitude measurements where no Big Bright Object (BBO) is detected. CHU A had a minimal phase period with the Moon in its FOV and has thus most reliable measurements.

The three axis attitude of the CHUs reference frame is given with respect to the J2000 inertial reference frame. The attitudes are given as spherical coordinates: Right Ascension (RA) and Declination (DEC) with the added rotation (ROT) around the bore sight of the CHU. Given an image with the corresponding timestamps and attitudes for both FF and SF and a defined view direction, three Direction Cosine Matrices (DCM) are used for the warping procedure. The DCMs describe the rotation from the J2000 frame to the CHU frame.

- $\boldsymbol{R}_{FF}$-Rotation from J2000 to CHU D at the time of capturing of FF.

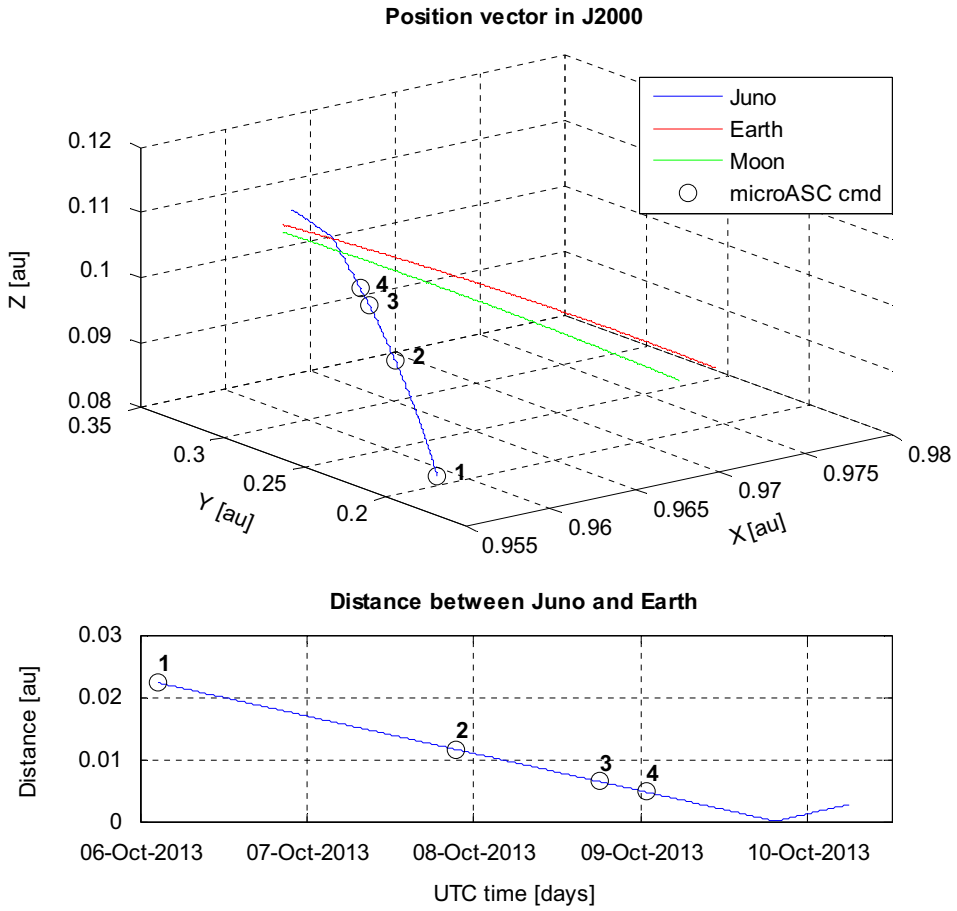

Fig. 2. Top: Trajectory of Earth, Moon and Juno in Geocentric J2000 coordinates during the approach of JUNO towards Earth. Bottom: Distance between Juno and Earth as function of time. The numbered markers indicate the microASC commanding. 1–3: Commanded to 8, 6 and 4 μs integration time. 4: Commanded to fully expand floor and ceiling of the automatic gain controller. (For interpretation of the references to color in this figure legend,the reader is referred to the web version of this article)

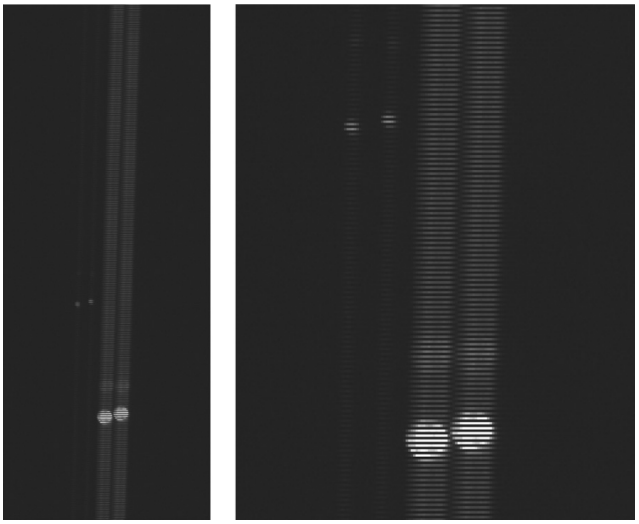

Fig. 3. Left: An example of a cropped raw image with the Earth and Moon in FOV inducing image artifacts. Right: the same image as on the left only zoomed in on the objects. The Earth is identified as the largest object inducing a tilted smear line. The tilted line from the Moon is slightly apparent. For this example Earth induces a strong ghost. Also vertical smear lines are induced by Earth. Note the Earth, Moon and corresponding artifacts are doubled due to the rotational motion of the S/C and the interlacing technology of the sensor.

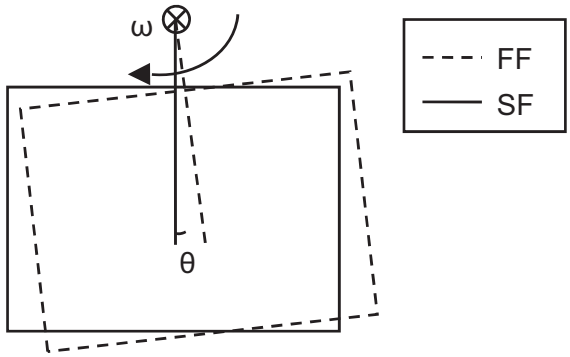

Fig. 4. The angular motion of the Camera Head Unit illustrated by the axis of rotation ω and the attitudes of FF (dashed) and SF with an angular deviation of θ.

- $\boldsymbol{R}_{SF}$-Rotation from J2000 to CHU D at the time of capturing SF.
- $\boldsymbol{R}_{DST}$-Rotation from J2000 to the defined direction of view of the CHU.

The DCMs are defined by three sequential Euler Angle rotations. The first rotation is about the Z axis, aligned with the celestial North Pole. The angular rotation about Z is

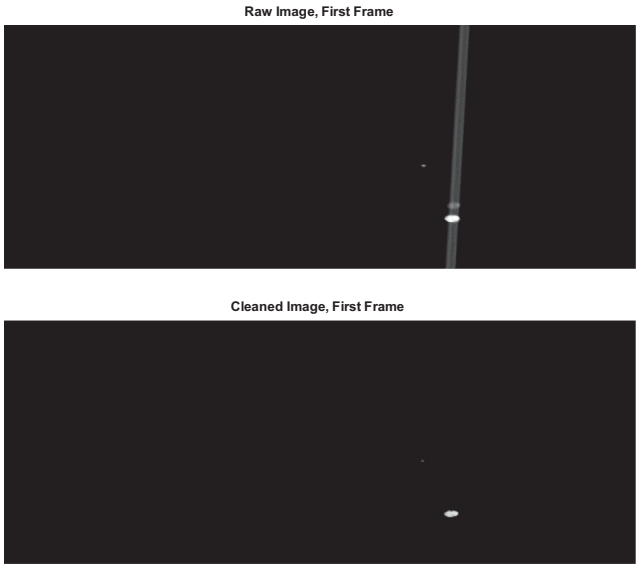

Fig. 5. Top: the raw image data, showing the First Frame of a full image. Bottom: the result from the cleaning process.

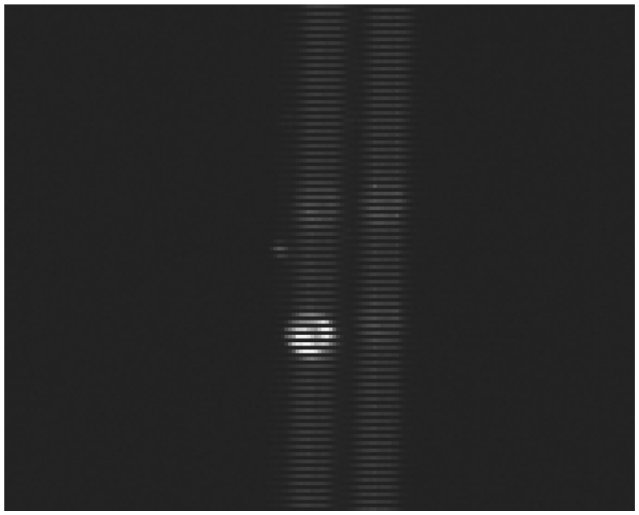

Fig. 6. Intensity of Earth and Moon in the First Frame is so low that the objects are barely visible, however the objects are clearly visible in Second Frame.

Table 1
The attitude of the predefined direction of view, i. e. the destination of the warping procedure.

Right ascension	29.1757	Deg
Declination	15.7393	Deg
Rotation	−75.000	Deg

$\phi = RA$. The second rotation is about the Y axis with the angle $\theta = 90^\circ - DEC$. θ is set so the Z axis is aligned with the equatorial plane prior to rotating according to the declination. This is due to the bore sight of the optical sensor being defined as aligned with the Z axis of the CHU frame. The third rotation is about the Z axis with the angle $\psi = ROT$. The DCMs are thus constructed by 3–2–3 sequential Euler Angle rotations. The direction of view is listed in Table 1.

3.3.2. Mapping of coordinates

The mapping process starts by constructing a set of image coordinates for the output image. The set of coordinates are generated with a scaling factor of 2 so the resolution of the output image is 1504×1160 pixels. The image coordinates are projected onto a sphere resulting in a three dimensional vector $\boldsymbol{q}$ for each pixel coordinate, see Fig. 7. $\boldsymbol{q}$ is defined as

$$\boldsymbol{q} = \left[q_x, q_y, q_z\right]^T \tag{1}$$

$$q_x = (x - x_0) \bullet x_{dim}, \tag{2}$$

$$q_y = (y - y_0) \bullet y_{dim}, \tag{3}$$

$$q_z = efl. \tag{4}$$

where

- x and y are the pixel coordinates.
- x_0 and y_0 are the calibrated coordinates of the lens bore sight.
- efl is the calibrated effective focal length of CHU D.
- x_{dim} and y_{dim} are the dimensions of the pixels of the sensor.

The vector $\boldsymbol{q}$ is normalized so $|\boldsymbol{q}| = 1$ to achieve a sphere of unit radius.

The set of sphere coordinates $\boldsymbol{q}$ of the output image is firstly rotated to the frame of reference, namely J2000, next the coordinates are rotated to the attitudes of FF and SF. According to the rotational matrices, defined earlier, the $\boldsymbol{q}$ vectors rotated to the attitude of FF and SF are defined as

$$\boldsymbol{q}_{FF} = \boldsymbol{R}_{FF} \bullet \boldsymbol{R}_{DST}^T \bullet \boldsymbol{q}, \tag{5}$$

$$\boldsymbol{q}_{SF} = \boldsymbol{R}_{SF} \bullet \boldsymbol{R}_{DST}^T \bullet \boldsymbol{q}. \tag{6}$$

The rotated frames of FF and SF are plotted against the target image frame in Fig. 8. The target attitude is chosen so the x axis of the image roughly aligns with the Earth–Moon orbital plane given in Table 1.

The vectors $\boldsymbol{q}_{FF}$ and $\boldsymbol{q}_{SF}$ are re-projected back to the image plane by the relations below and thus the full mapping from the viewing direction to both frames of the image is completed.

$$x_{FF} = \frac{q_{FFx}}{q_{FFz}} \bullet \frac{efl}{x_{dim}}, y_{FF} = \frac{q_{FFy}}{q_{FFz}} \bullet \frac{efl}{y_{dim}}, \tag{7}$$

$$x_{SF} = \frac{q_{SFx}}{q_{SFz}} \bullet \frac{efl}{x_{dim}}, y_{SF} = \frac{q_{SFx}}{q_{SFz}} \bullet \frac{efl}{y_{dim}}. \tag{8}$$

3.4. Merging of frames

With the pixel coordinates of both FF and SF rotated to the pre-defined attitude, the coordinates do not align with the pixel grid of the defined view direction. This is illustrated in Fig. 9 showing the pixel coordinates of FF mapped onto the pixel grid (axes x and y) corresponding to the view direction. The pixel coordinates with their associated pixel intensity of the rotated frames, are

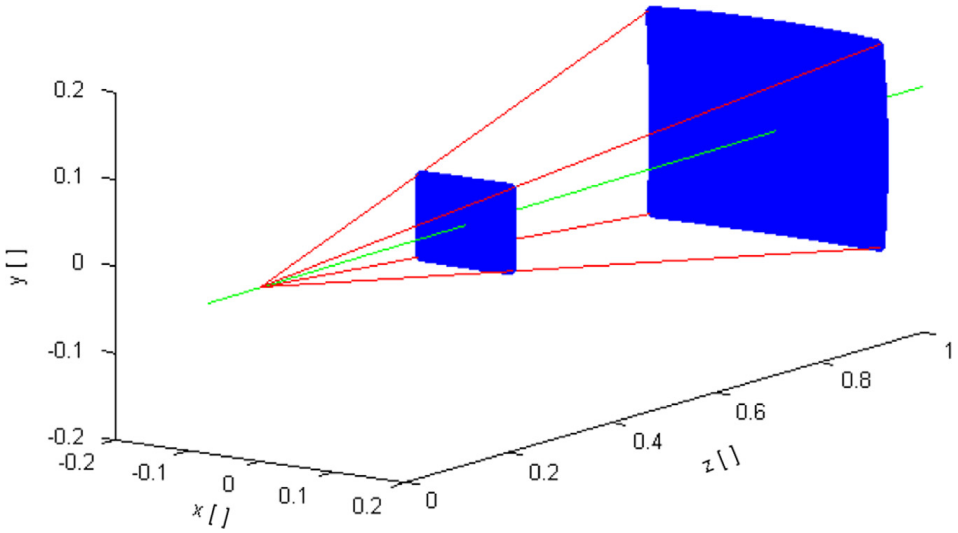

Fig. 7. Projecting pixel coordinates to a sphere of unit radius. Blue dots indicate pixel coordinates on both the image plane and on the unit radius sphere. Note that the focal length is scaled for visual purposes. Red lines indicate the corner pixel coordinates and green is the bore sight.

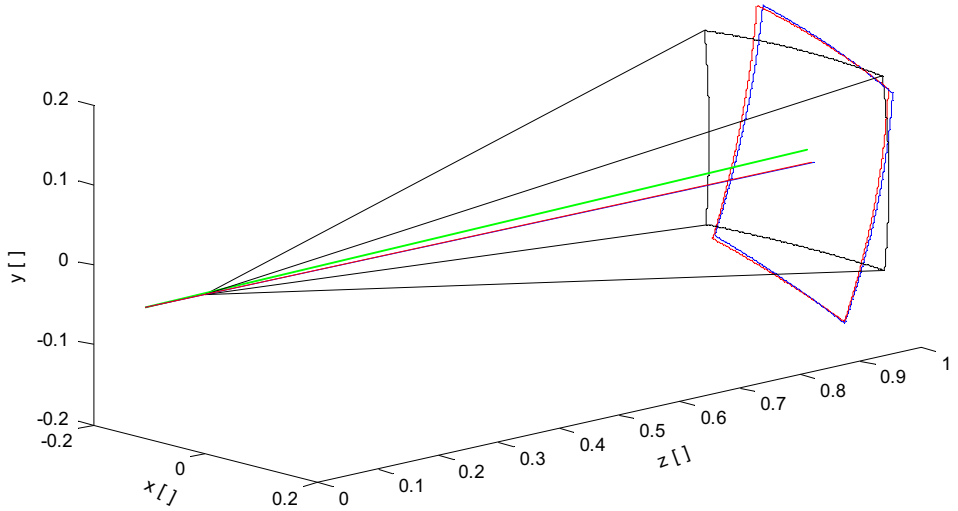

Fig. 8. Illustrates sphere coordinates of the First Frame and Second Frame rotated to the target attitude RA=29.30, DEC=15.55 and ROT=−75.00. The black frame defines the boundary of the destination image with corresponding bore sight (green line). Blue and Red lines define the boundary of First Frame Second Frame, respectively.

interpolated to the target pixel grid coordinates using bilinear interpolation.

Each of the two half frames are interpolated separately resulting in two output frames which are lastly combined to a single frame by averaging the pixel intensity values from the two interpolated frames. Another approach would be to directly construct a single frame from both the mapped FF and SF data. This alternative however reveals minor intensity differences of the objects when merged. Using the average of two independent frames cancels out the intensity differences. The result of warping and merging the half frames is shown in Fig. 10.

3.5. Coloring

As a finalizing step the gray scale representation is converted to color images using a Color Look Up Table (CLUT). The CLUT is only applied on the Earth object, while the gray scale representation of the Moon is retained. This last step is mainly in the interest for public outreach. A sample of the resulting images are shown in Fig. 11 as a sequence covering nearly 50 h of flight during JUNOs approach towards Earth. The 19 images are captured with a time period around 165 min.

4. Outlook

The procedure carried out for the Earth fly-by is currently being considered for Juno's arrival to Jupiter. The microASC system is designed to operate for the whole Juno mission and will be able to perform this kind of procedures in addition to delivering the real-time attitude measurements. These attitude measurements are the most critical part of the process as the warping in the post-

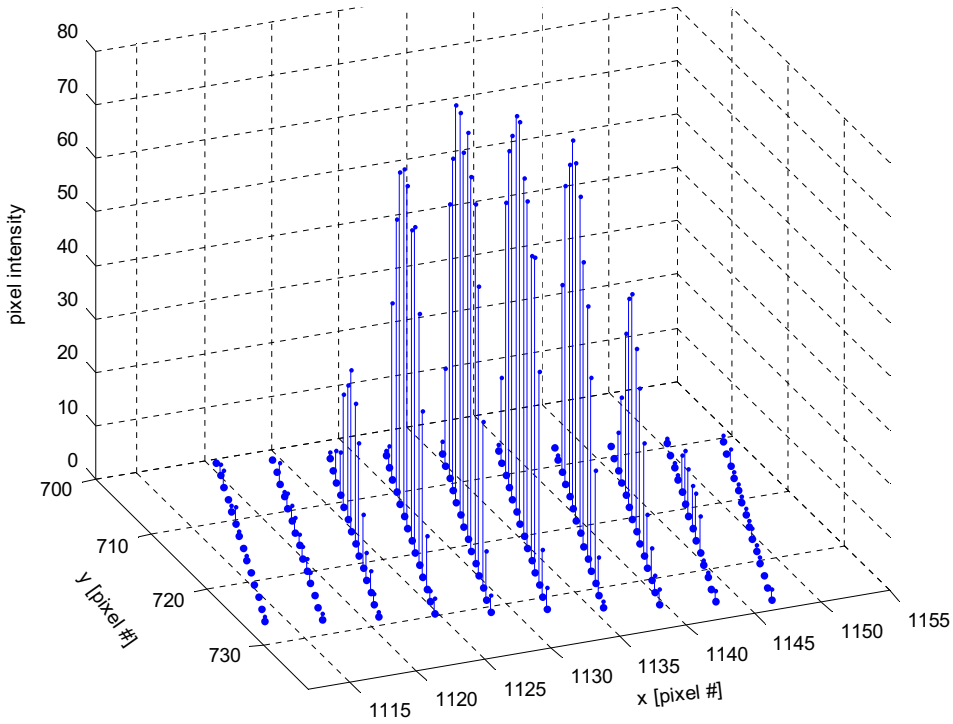

Fig. 9. Illustrating the mapping of a part of the First Frame containing the Moon. The pixel coordinates of FF are mapped to the pixel coordinate grid of the defined view direction, defined by axes *x* and *y*. The pixel intensity is plotted on the third axis.

Fig. 10. A resulting image of the warping and merging of the first and second frame. Earth is the larger object on the left side and the Moon is on the right side.

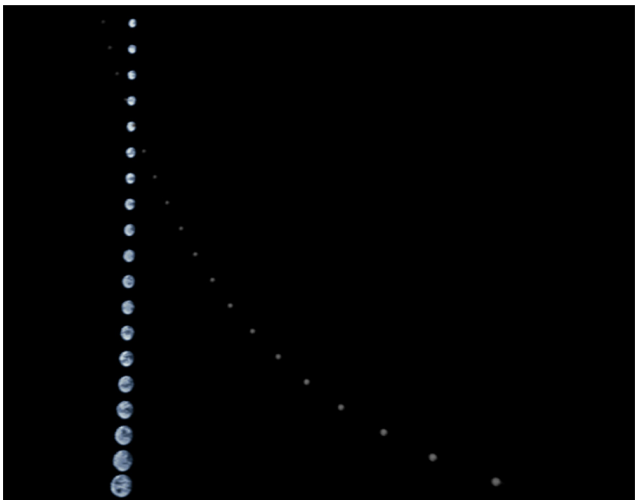

Fig. 11. A sequence of images captured by the microASC onboard JUNO spacecraft showing the Moon passing in front of the Earth as JUNO approaches Earth. The time period is around 165 min, covering nearly 50 h in total. (For interpretation of the references to color in this figure legend,the reader is referred to the web version of this article)

processing is not possible without. Only small errors in the attitude measurements will affect the modeled angular velocity and corrupt the warping and merging of the data. It was found that the attitude measurements where a BBO was detected needed filtering out before estimating the angular velocity. Furthermore, fitting the spin model to a linear regression is dependent of a maneuver free period of the spacecraft.

It is worth noting that due to the very low integration time the acquired images from the Earth fly-by can with good approximation be considered still images. When targeting fainter objects the exposure time will be increased and thus introduce motion blur to the objects. This artifact can be dealt with by adding a deconvolution step to the post-processing chain which is planned for future improvements.

The combined procedure for capturing and post processing possesses unique possibilities for scientific measurements and imaging from unexplored perspectives. General targets like planets, moons asteroids, icy rocks and planetary dust rings are evident. When orbiting Jupiter, plume studies of the Jovian moons and tomographic mapping of the Jovian rings are opportune. Naturally this is also ideal for public outreach.

Acknowledgments

The images were collected to a time-lapse movie which was released by Jet Propulsion Laboratory [5] in collaboration Southwest Research Institute, Goddard Space Flight Center and composer Vangelis. We thank all entities for their valuable and essential contribution.

References

[1] Jørgensen, J. L., Denver, T., Betto, M., Jørgensen, P.S., MicroASC a miniature star tracker, small satellites for earth observations, in: Proceedings of the Fourth International Symposium of the IAA, Berlin, 2003.
[2] Connerney, J., Acuna, M.H., The Juno magnetic field investigation (MAG): Exploration of the Polar Magnetosphere, American Geophysical Union, Fall Meeting 2008, abstract SM41B-1679.
[3] Bolton, S. J., Juno Science Team, The Juno Mission, Proceedings of the IAU Symposium No. 269. 2010, International Astronomical Union.
[4] C.H. Acton, Ancillary Data Services of NASA['s Navigation and Ancillary Information Facility, Planet. Space Sci. 44 (1) (1996) 65–70. (Reference Key ID: ACTON1996).
[5] JUNO microASC Earth Fly By, December 10th 2013, ⟨http://www.nasa.gov/jpl/juno/juno-earth-flyby-20131210.html⟩.

Semi-Autonomous Optical observations for Deep Space Navigation

A. H. Jørgensen, D. A. K. Pedersen, P. Brauer, J. L. Jørgensen

DTU Space, Division of Measurements and Instrumentation Systems,
Technical University of Denmark, Elektrovej 327, 2800 Kgs. Lyngby, Denmark

Abstract

A Module for Optical Observation and Navigation is presented, capable of extracting optical navigation measurements utilizing raw images taken by the DTU advanced stellar compass. The module estimates a line of sight vector and a range to planetary objects seen in the cameras field of view. The performance is characterized through images taken by the Juno spacecraft during the Earth flyby Oct. 9, 2013 and features a centroiding with a standard deviation better than 20 arcseconds.

1 Introduction

Radiometric deep space navigation, supported by optical observation during planetary approach, have been a constant for decades and have proven to be both accurate and reliable. Enhancements in modelling of perturbing forces, radiometric measurements and orbit determination techniques have provided considerable improvement in accuracy during the last decades.

During the cruise phase, the perturbing force models are well known and the orbit determination enables high precision temporal extrapolation. However, when approaching a planetary object, the orbit extrapolation deteriorates as a consequence of uncertainties in the planetary ephemerides and in the modeled forces. At this point, the time delay prevents the navigation decisions to be utilizing the best and latest information. The consequence constitutes fuel inefficiency due to a delayed non optimal response, and a degradation of scientific data caused by miss orientation of the scientific instruments. These drawbacks have led to an increased request for autonomy for spacecraft navigation. A fully autonomous onboard navigation system would eliminate the propagation delay, circumvent operational related delays, and reduce system cost.

Several attempts have been made to design autonomous or semi-autonomous optical systems. Most notably are the asteroid/comet approach missions, where the high uncertainties in the ephemerides have constituted a need for real-time optical navigation [1], [2], [3]. For Rosetta the comet Churyumov-Gerasimenko was known with an accuracy of 10000km [4].

The NASA New Millennium Program Deep Space 1, launched in 1998, demonstrated the first autonomous optical navigation system to be used in deep space. The navigation system was designed to interact with the imaging, attitude control and propulsion, to accomplish fully autonomous navigation. The system was able to determine the spacecraft heliocentric position better than 200km and 2m/s during a 28-day period and 0.5km for the close flyby [5]. The overall success of Deep space 1, and the asteroid/comet missions have proven the feasibility of autonomous optical navigation.

This work is dedicated to the design and verification of a Module for Optical Observation and Navigation (MOON), capable of extracting optical measurements of nearby planets seen by the DTU stellar compass cameras [6]. The work does not seek to solve the orbit determination, but to provide the optical observations necessary to the orbit determination process. The observations are designed to support either an autonomous onboard orbit determination or a radiometric orbit determination. The module has been characterized and verified through the Juno Earth flyby images.

The work is restricted to only encompass planetary bodies that can be approximated by ellipsoids. By conducting a preliminary comparison study of the shapes of planetary bodies provided by [7], it is concluded that the accuracy of an ellipsoid approximation is better than 0.5% of the radius, for planetary bodies with a radius larger than 200km.

2 The µASC platform

The micro Advanced Stellar Compass (µASC) is a flight proven, high accuracy star tracker, featuring reliable and fully autonomous functionality [6]. With more than 50 instruments presently in operation on international satellite missions, the µASC has successfully demonstrated significant space flight heritage. The µASC consists of a data processing unit (DPU) that drives up to four camera heads (CHU). The CHU enables up to 22 attitude solutions per second, however as the CHU is photon limited; full accuracy can only be achieved by running the CHU at maximum 8Hz. Consequently the µASC has considerable amount of computing power available for other applications that can be triggered or implemented depending upon the mission profile. These 'add on' modules run separately on the DPU, and will not impact the performance of the µASC as an attitude sensor.

Deep space missions generally carry multiple star trackers to ensure optimal performance, negate sun blinding and to provide redundancy. This platform provides the optimal conditions for an autonomous navigation system by featuring high attitude accuracy and multiple camera sky coverage.

During standard operation, the µASC system automatically detects objects moving with respect to the celestial

background. For unresolved objects, the light emanating from planetary objects is convolved by a point spread function of the camera optics. The centroiding is performed similarly to the star detection, by cross correlating a Gaussian shape. This function is a highly sophisticated core function of the star tracker with a Line Of Sight (LOS) accuracy below 0.1pixel, while compensating for spacecraft rotation below 4RPM.

For resolved objects, the star tracking accuracy is typically reduced due to the increased radiance, and the solution for the given CHU is typically ignored. At this point, the automatic gain/exposure control optimizes light condition for the planetary detection. The orientation of the camera is estimated by the intercalibration of the remaining active star trackers. If the CHU's are located on a thermal elastic bench this calibration is typically accurate down to 20" for an extended time period. This setup enables the optimal exposure for the star tracking CHUs and a low exposure for the planetary detecting CHU, allowing for operation during high rotation rate of the spacecraft.

The µASC supports inertial controlled imaging, enabling the images of planetary bodies to be acquired once the optimal focal plane orientation is reached. The inertial reference vector can be uploaded to the DPU, through the heritage telemetry. The inertial controlled imaging thus ensures a precise location of the planetary body in the image frame, thereby improving the image quality.

The work described herein, demonstrate a highly cost efficient solution, that produces both attitude data from the star trackers, and the navigation observations. Alternatively the µASC supports a dedicated navigation camera with increased focal length, for enhanced performance.

3 Centroiding Procedure

The Module for Optical Observation and Navigation (MOON) is a semi-autonomous module incorporated into the µASC, capable of extracting optical observations. The software is designed to support either a radiometric orbit determination, or a fully autonomous orbit determination onboard. The software is semi-autonomous, as it requires the time and a rough estimate of the spacecraft position to recognize the planetary bodies.

Once the solar system body is recognized, information, if available, concerning the position, bidirectional reflection distribution function (BRDF), shape and orientation will be recovered from memory and significantly improve the centroiding. The shape and rotational information is generally available for solar system bodies from the IAU working group on cartographic coordinates and rotational elements [7]. The Solar System Dynamics Group at Jet Propulsion Laboratory [8] provides to date the highest precision ephemerides for solar system bodies, including planets, moons, comets, asteroids and meteor streams. The data is readily available for all, with downloadable files and browser software to retrieve and analyze the ephemerides.

The MOON centroiding procedure relies on determining the apparent "edge" of the object and fitting a limb profile to the edge. The operational range is generally restricted by surface features becoming dominant. The procedure is illustrated in Figure 1, and is discussed in the following.

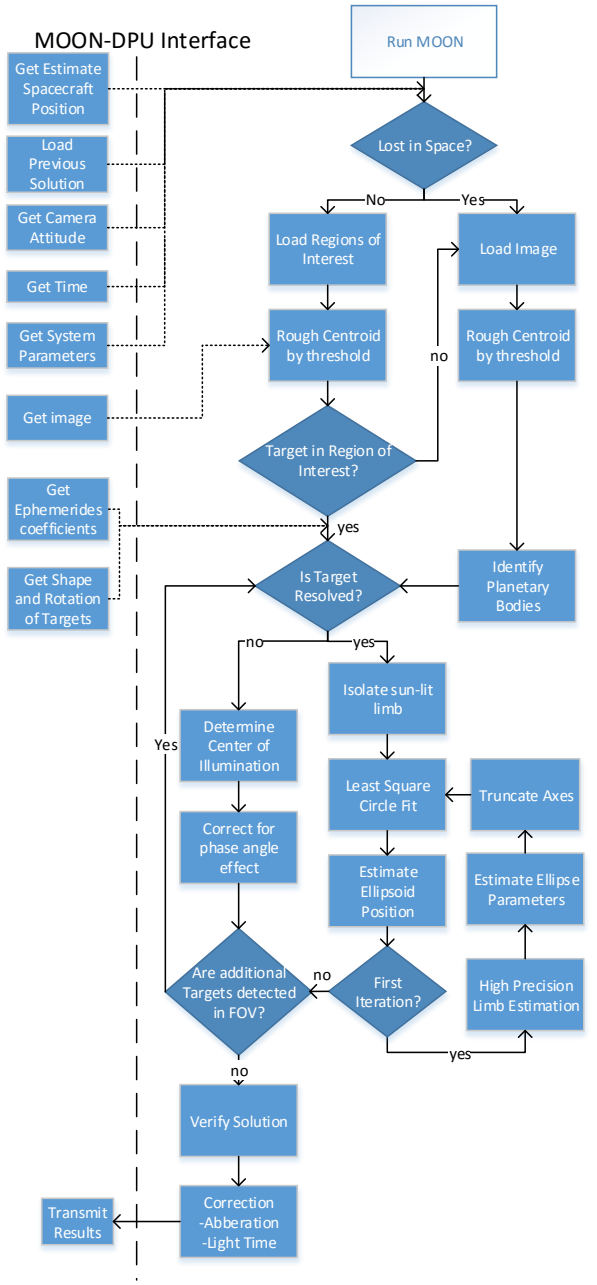

Figure 1, System Flowchart of the MOON algorithm.

3.1 Lost in Space

The software has been designed to operate real time at 4Hz, in order to maximize the number of optical observations, and thereby the knowledge of the spacecraft position. To obtain this objective without deteriorating the µASC star tracking capabilities, a strong focus has been put into minimizing the computational load.

The MOON initializes in a Lost in Space mode, where the entire image is searched for planetary bodies, and the objects are recognized through the identification procedure, described below. The objects are isolated by a simple

dynamic threshold search. Once a solution has been found, the software leaves the Lost in Space mode and tracks the planetary bodies within the field of view. The tracking is obtained by predicting the location of the target, from the apparent change in attitude between the frames. Once tracking is lost, the software reenters the Lost in Space mode.

3.2 Identification Procedure

The planetary identification is based upon a rough estimate of the centroid and radius. To assist the identification process, a sphere is defined around each planet that encompasses all the moons of the planet. These spheres are denoted "systems", and restrict the preliminary search. The procedure is written as:

a) Load the "System" ephemerides and radius
b) Identify which "systems" are within Field of View, plus a small margin.
c) Load the ephemerides and shape of all planetary bodies in the identified systems.
d) Exclude planetary bodies that are outside the Field of View, plus a small margin.
e) Exclude planetary bodies deviating more than 50% of the apparent radius.
f) Identify the planetary body by the least angular deviation. If two planetary bodies overlap: Identify the object as the planetary body with the largest apparent radius and flag the event.

3.3 Image Projection

The ellipsoid assumption enables an analytical solution to the image projection. The analytical solution presents an opportunity to estimate the ellipsoid position from a known image profile, and the image profile from a known ellipsoid.

The image projection of the ellipsoid can be simplified by rotating the coordinate system into the body coordinates of the ellipsoid and normalizing the ellipsoid axis. The linear transform thus convert the ellipsoid to a sphere, and tilts the focal plane, as illustrated in *Figure 2*. Due to symmetry, the limb of the sphere, seen from the focal point, forms a circle. A cone can thus be formed from the focal point towards the circle. The focal plane, and thereby the image projection, can be seen to form a conic section. The conic section retrain its properties during the inverse linear transform back into camera coordinates.

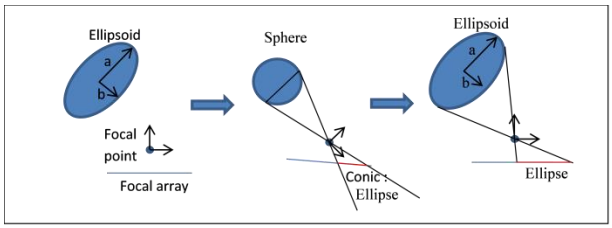

Figure 2, illustrate the image projection of an ellipsoid. By normalizing the ellipsoid axis, the ellipsoid is converted into a sphere. Due to symmetry the image projected of the sphere forms a cone at the focal point, where the focal plane creates a conic section.

The conic section will form an ellipse if the entire circle is located in-front of the focal point, in the optical axis direction, and a hyperbola, if any point of the circle is located behind the focal point. The hyperbola thus becomes applicable when the spacecraft is located close to the surface of the target. At this point, the surface features predominate the errors, and the hyperbola can therefore be approximated an ellipse without loss of accuracy.

The mathematical transform from an ellipse to an ellipsoid and the reverse transform of acquiring the ellipse parameters from a known ellipsoid are derived in [9].

3.4 Least Square

Acquiring the ellipsoid position thus becomes a problem of determining the ellipse parameters. However, ellipse least square fitting techniques have demonstrated an ambiguity for small arcs <90˚ [10]. In addition, the ellipse techniques seek to minimize the least square error of the noisy limb detections, and do not take the physical image projection into account. The ellipse fitting therefore presents a possibility to find solutions, which are not physically possible.

An alternative approach is proposed for this work. By acquiring a preliminary estimate of the ellipsoid position, the theoretical major and minor axes can be estimated. Then by truncating the limb, in the direction of the major axis, the ellipse is converted into a circle. The method ensures the laws of physics, to the degree of precision provided by the initial guess, and enables the usage of the simpler, faster, and more accurate, circle least square techniques.

The hyper accurate algebraic fit presented by [10], was chosen for the implementation as it demonstrates superior performance on small arcs, without the need for iterative methods.

3.5 High Precision Limb Estimation

The limb detection based upon a dynamical threshold, provide a reasonable rough estimate, but is ultimately a function of system gain, exposure time and lens distortion. The limb estimates, are improved by correlating the limb profile with a theoretical model, based upon the targets bidirectional reflectance distribution function (BRDF). If a BRDF cannot be acquired, a simple Lambertian reflection is assumed. The correlation is performed at an angle -90˚ to 90˚ of the image projected sunvector, where the pixel resolution and angular resolution is user definable.

3.6 Unresolved Targets

If the spatial extend of the target does not exceed 9pixels, the target is considered unresolved and only a center of illumination can be acquired. The center of illumination will be biased in the sunward direction due to the phase angle, and must therefore be corrected.

The phase angle is acquired from the target ephemeris in solar system coordinates, and the spacecraft position. The module supports post correction, and when enabled by a single command, the relevant information is conveyed to aid a post orbit determination correction.

3.7 Strategy for verification:

The verification procedure runs concurrently with the main algorithm, with the objective to rule out any possible

solution, if they deviate more than expected from the solution. The software allows for a small residual in the sunlit limb from the expected circle, controlled by a user defined threshold.

The day-night terminator provides the most recognizable feature for verification. Once a solution is acquired, the expected day-night terminator can be derived from the phase angle and an image projection. The day-night terminator can similar to the ellipsoid, be shown to form an ellipse in the image plane. By acquiring the ellipse parameters of the day-night terminator projection, the axis can be truncated and fitted by a circle least square. The residual is calculated as the difference between the image detected day-night terminator and the theoretical ellipse parameters. A secondary user defined threshold is provided, that defines the maximum allowed residual.

3.8 Corrections:

The MOON software has the capabilities to correct for relativistic aberration and light time. The corrections will be based upon the spacecraft-target standoff distance, and a relative estimate of the spacecraft velocity derived from the input spacecraft positions. Alternatively the software supports a post orbit determination correction, by conveying the relevant information.

4 Precision Analysis

The system output includes the target ephemeris **E** and the optical observations; a high accuracy sighting vector **L** and a range estimate ρ. The instantaneous absolute position of the spacecraft **r** is given by:

$$\boldsymbol{r} = \rho \cdot \boldsymbol{L} + \boldsymbol{E} \tag{1}$$

In the event that two or more objects can be detected within a small timeframe, the spacecraft position can be estimated as the point of least distance between the LOS vectors. Given the two targets position $\boldsymbol{P_1}, \boldsymbol{P_2}$ observed by the sighting vectors $\boldsymbol{L_1}, \boldsymbol{L_2}$, the position is found by solving the equations:

$$\boldsymbol{P_2} - \boldsymbol{P_1} = \boldsymbol{L_1} \cdot \lambda_1 + (\boldsymbol{L_1} x \boldsymbol{L_2}) \cdot 2 \cdot \lambda_3 - \boldsymbol{L_2} \cdot \lambda_2 \tag{2}$$

For λ_{1-3}. The spacecraft position is given as:

$$\boldsymbol{P_s} = \boldsymbol{P_1} + \boldsymbol{L_1} \cdot \lambda_1 + (\boldsymbol{L_1} x \boldsymbol{L_2}) \cdot \lambda_3 \tag{3}$$

And the range by $\rho = \sqrt{\lambda_1^2 + \lambda_3^2}$.

The uncertainty of sighting vector θ_s and angular extension θ_e is controlled by the image centroiding procedure. In applications where precise information of the target (rotation, shape, reflection) and lightning conditions (sun direction, attitude information) are obtained a priory, the centroiding is typical limited by a fraction of a pixel. Approximating the target as a sphere of radius R_m, at a distance d, located on the optical axis, the range precision is given as:

$$\Delta d \approx d - \frac{R_m}{\tan\left(\operatorname{atan}\left(\frac{R_m}{d}\right) + \theta_e\right)} = \frac{(d^2 + R_m^2)\, tan\theta_e}{R_m + d\, tan\theta_e} \tag{4}$$

For multiple targets the uncertainty in range is given by the uncertainty in the sighting vectors θ_{s1}, θ_{s2}, the angle between the objects θ, and the distance to each d_1,d_2. The situation is illustrated in Figure 3. The worst case error is at point A, at this point the error is given by:

$$r = \sqrt{a^2 + r_2^2} = \sqrt{\frac{(r_2 + \frac{r_1}{\cos\varphi})^2}{tan\varphi^2} + r_2^2} = \sqrt{\frac{(d_2 sin\theta_{s2} + \frac{d_1 sin\theta_{s1}}{\cos(\theta - \theta_{s1} - \theta_{s2})})^2}{\tan(\theta - \theta_{s1} - \theta_{s2})^2} + (d_2 sin\theta_{s2})^2} \tag{5}$$

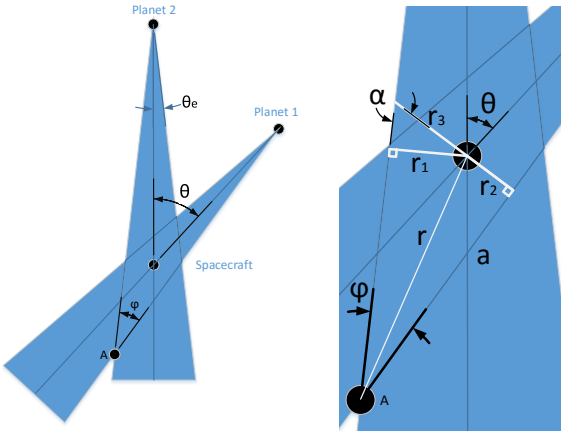

Figure 3, Precision of range estimation from two targets. The range estimation method, is chosen based upon a precision analysis of single and multiple target tracking.

The algorithm switches between tracking single and multiple targets for range estimation, based upon the precision analysis. Typically single planet navigation is recommended for close approach, while multi-planet navigation remains advantageous for larger distances.

5 Juno Earth Flyby

The Juno spacecraft was launched from Cape Canaveral Aug. 5. 2011, with the primary scientific goal of investigating Jupiter's formation, evolution and structure. On Oct. 9, 2013, the Juno spacecraft flew past Earth, performing a sling shot maneuver setting it on course for Jupiter. The Earth approach was identified as a unique opportunity to record images of the Earth and Moon system seen from afar. The effort to capture and process the raw image data was performed in cooperation between the Technical University of Denmark (DTU SPACE) and the US National Aeronautics & Space Administration (NASA).

The ellipsoid axis and rotation of Earth and Moon is provided by [11]. The bidirectional reflection distribution function for the Moon was provided by [12]. The BRDF of Earth is governed by cloud cover and large scale surface features. While the cloud height offset is negligible for the distances featured in the Earth flyby, the continuously varying BRDF is difficult to replicate. Consequently the BRDF of Earth is approximated by a Lambertian.

5.1 Juno Imaging System

The Earth Flyby (EFB) images were captured and processed by the micro Advanced Stellar Compass (µASC). The µASC system onboard Juno consists of four Camera Head Units (CHU) denoted CHU A-D and a double Digital Processing Unit (DPU). A detailed description of the system in found in [13]. The µASC is part of the magnetic field investigation onboard Juno [14] with the goal of monitoring the orientation of the magnetometer sensors. For the purpose of performance analysis, the µASC is capable of capturing and downloading images from any of the four CHUs for analysis on ground.

Juno spacecraft is spin stabilized, with a spin rate varied during the mission. During the EFB the spin rate was held at approximately 2 rotations per minute (RPM). The orientation of the spacecraft rotational axis during approach only provided CHU D to view Earth and the Moon during a small phase of the rotational sequence. The µASC optical sensor provides interlaced video signals, with 125ms between the first and second field. Due to the spinning of the spacecraft the first and second frame is offset by the angular motion and was analyzed separately.

The µASC system is designed for tracking faint stars, with a very light sensitive sensor. In addition the Juno CHU's was designed with a high gain preamplifier to accommodate the low light operation at Jupiter. In order to view the Earth and Moon system, the exposure time was set to 8-4us close to the limit of the star tracker and the inherent 4us jitter on the Juno onboard clock. This lead to an over blooming of Earth later in the imaging series.

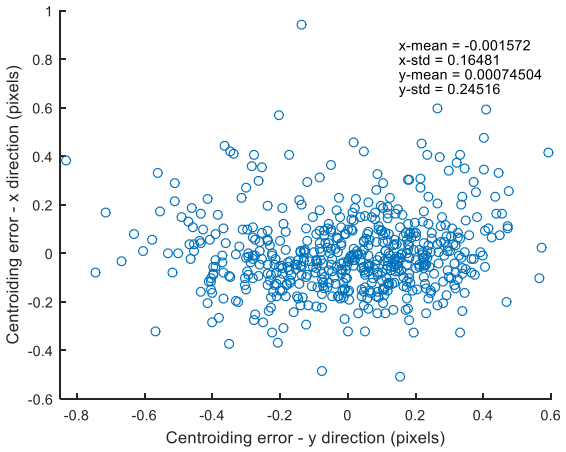

Figure 4, Moon Centroiding residual from the Juno Earth Flyby images. No significant bias is observed.

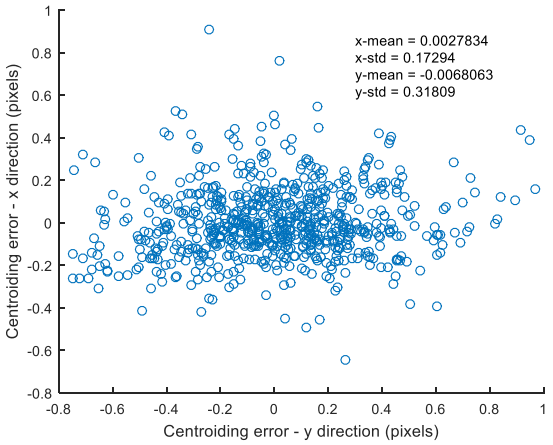

Figure 5, Earth Centroiding residual from the Juno Earth Flyby images. No significant bias is observed.

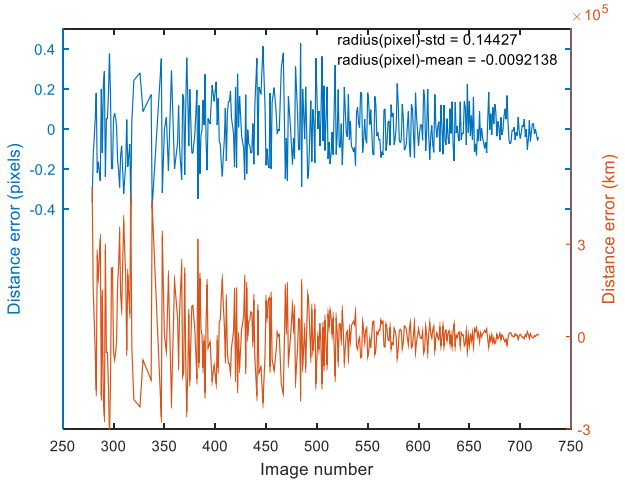

Figure 6, Range residual, single target tracking of the Moon from the Juno Earth flyby images. The pixel noise reduces for larger image numbers as the signal to noise ratio of the limb estimation improves

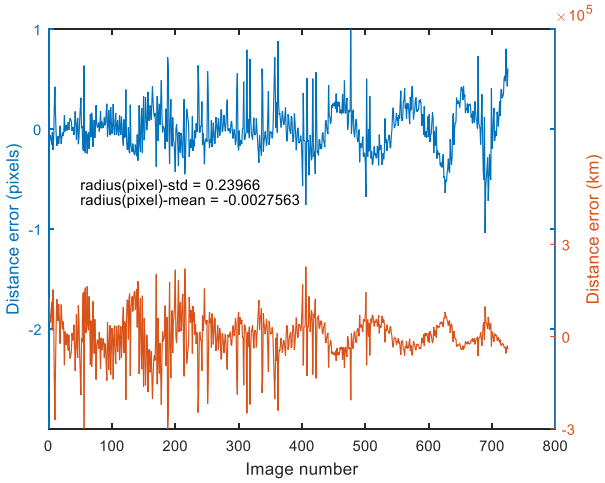

Figure 7, Range residual, single target tracking of the Earth from the Juno Earth flyby images. The residuals are significantly larger compared to the Moon range residuals, and display non Gaussian noise. These results can be explained by the Lambertian BRDF mod

6 Results

The EFB event spanned from Oct. 6 2013 at a Juno-Earth distance of 3.4 million kilometer to the Earth-flyby Oct. 9, 2013 providing 1036 images of the Earth and Moon. The considerable variation in apparent radius, in combination with the two planetary bodies in the field of view, provided a unique case study for the MOON software. An overview of the image series is shown in Figure 8. The reference position of Juno was estimated from the radiometric orbit determination, and was provided as an input for the MOON software. The planetary identification procedure was performed for each image, and the correct target was identified for all images.

The Earth and Moon were tracked as both single targets and as multiple targets when available. For all images the centroiding residuals were calculated as:

$$Centroid\ Residual = Centroid\ - Computed \qquad (6)$$

Where the 'Computed' was estimated from the radiometric orbit determination **P** and the target ephemeris **R**. The 'Centroid' is the image centroid rotated into ICRS and corrected for stellar aberration and light time. The range residual was calculated as:

$$Range\ Residual = Range\ - |\boldsymbol{RP}| \qquad (7)$$

Where Range, is the MOON range estimate, from either single or dual tracking.

The centroiding residual is shown in Figure 4 and Figure 5, for the Moon and Earth respectively. The precision is as expected superior for the Moon as a consequence of the accurate BRDF model. The noticeable divergence in x and y accuracy is a consequence of the µASC acquiring interlaced half frames. The biases are relatively small and assumed random; no significant sunward bias is observed.

Figure 6 and Figure 7 show the range residual, given in kilometers and pixels. The Moon range estimate is comprised of Gaussian noise with a standard deviation of less than 0.15 pixels. The pixel residual can be seen to improve as the Moon becomes more detailed. The range residual of Earth exhibit a substantial temporal evolution, which can be explained by cloud movement and the rotation of Earth. Despite the evident distinction from a Lambertian surface, the range residual remains less that a pixel at all time with a low standard deviation.

The dual tracking range residual is shown in Figure 9. The maximal theoretical error from equation (5), assuming a 0.2 pixel uncertainty, is included for comparison. The discontinuity in the data points, is when the Moon passes in front of the Earth. The effect of the angle between Earth and Moon approaching zero is apparent in both the theoretical and actual error. The residual is as expected significantly reduced for duel target tracking.

The Position Estimate of the Juno spacecraft for single and dual tracking is shown in Figure 10 and Figure 11 respectively.

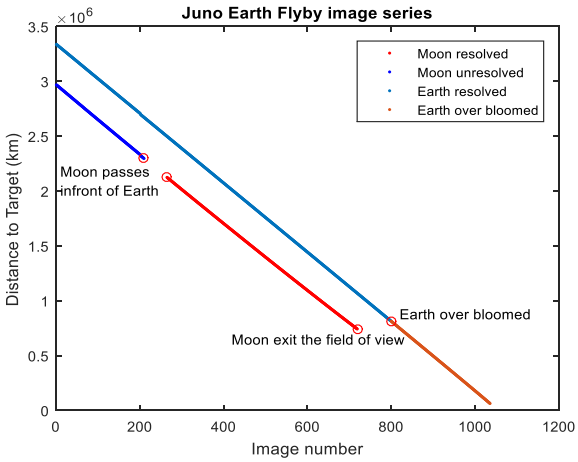

Figure 8, The Earth is visible throughout the serie, spanning from a radius of 4.6pixels to 100 at close proximity. After image 800 Earth becomes over bloomed. The Moon is visible but unresolved in the first 210 images, at image 210 the moon passes in front of Earth and once cleared, the moon is resolved and remains in the field of view till image 719.

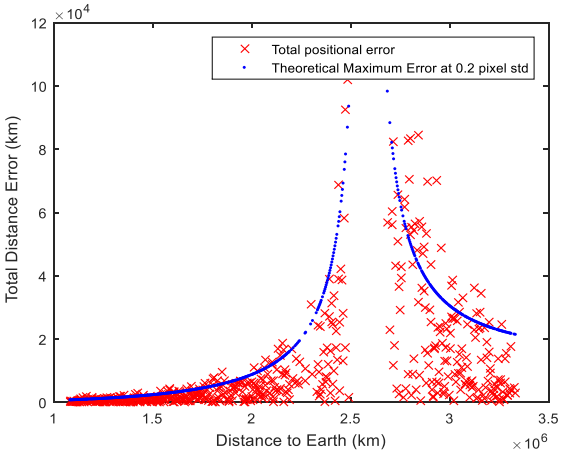

Figure 9, Total positional residual vs. distance to Earth from tracking Earth and Moon as dual targets. The rapid increase in residual corresponds to the angle between the objects approaching zero.

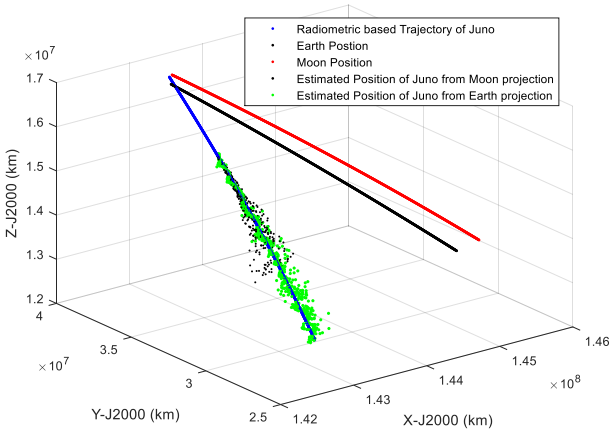

Figure 10, Position Estimation of Juno-spacecraft from single target tracking of Earth and Moon.

7 Outlook

In this work a Module for Optical Observations and Navigation has been presented, utilizing the DTU µASC star tracker platform. The navigation system measures relative position of planetary bodies, enabling improved orbit determination and orientation of scientific instruments. The work was validated through the Juno Earth flyby images. The instantaneous centroiding and range observations of the Moon, was performed with a <0.25pixel accuracy for all images, enabling an orientation of a scientific instrument towards any point on the surface with better than 40" accuracy.

The MOON software provides a cost effective solution to the optical navigation problem, featuring practically no additional system costs. The light sensitive µASC CHU's enables low exposure time and thereby operation on high rotation spacecraft's. The MOON software is designed to be independent of the image platform and the µASC system can be expanded by a dedicated navigation camera to obtain higher accuracy measurements.

Optical navigation has great potential and will undoubtedly play an increasing role for the future interplanetary endeavors. Despite the progress of optical navigation, the technology is still considered a high risk operation. It must be the ambition of future work within the field of autonomous optical navigation, to demonstrate the performance and reliability that can be provided by optical observations.

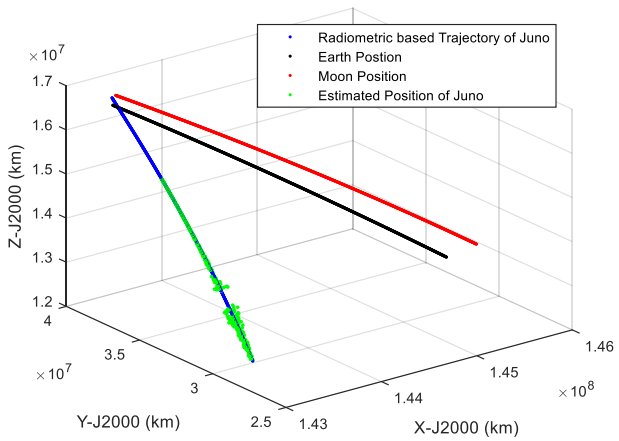

Figure 11, Position Estimation of Juno-spacecraft from dual target tracking of Earth and Moon.

7.1 Acknowledgements

The images where collected to a time-lapse movie, which was released by Jet Propulsion Laboratory [15] in collaboration with Southwest Research Institute, Goddard Space Flight Center and composer Vangelis. We thank all entities for their valuable and essential contribution.

8 Bibliography

[1] N. Mastrodemos, D. G. Kunitschek and S. P. Synnott, "Autonomous Navigation for the Deep Impact Mission Encounter with Comer Tempel 1," *Springer,* 2005.

[2] P. N. Desai, D. T. Lyons, J. Tooley and J. Kangas, "Entry, Descent, and Landing Operations Analysis for the Stardust Entry Capsule," *American Institute of Aeronautics and Astronautics,* 2008.

[3] M. Uo et. al., "Hayabusa Touching-Down to Itokawa - Autonomous Guidance and Navigation -," *The Journal of Space Technology and Science Vol. 22,* 2006.

[4] A. Accomazzoa et. al., "Rosetta operations at the comet," *Acta Astronautica Vol 115,* 2015.

[5] J. E. Riedel et. al., "Using Autonomous Navigation for Interplanetary Missions: The Validation," in *IAA Paper L-0807, Fourth IAA International Conference on Low-Cost Planetary Missions*, 2000.

[6] J. L. Jørgensen, T. Denver, M. Betto and P. S. Jørgensen, "MicroASC a Miniature Star Tracker," in *Small Satellites for Earth Observation, 4th International Symposium of the International,* 2003.

[7] B.A.Archinal_et.al, "Report of the IAU Working Group Coordinates and Rotational Elements," *Springer Science + Business Media B.V.,* 2009.

[8] JPL_Ephemerides, "ssd.jpl.nasa.gov/?ephemerides," [Online].

[9] A. H. Jørgensen and D. A. K. Pedersen, "High precision visual centroiding techniques of icy moons," *Submitted to IEEE Transactions on Aerospace and Electronic Systems,* 2015.

[10] A. Al-Sharadqah and N. Chernov, "Error analysis for circle fitting algorithms," *Electronic Journal of Statistics Vol 3,* 2009.

[11] B. A. Archinal et. al., "Report of the IAU Working Group Coordinates and Rotational Elements," *Springer Science + Business Media B.V.,* 2009.

[12] A. J. Verbiscer, R. French and C. A. McGhee, "The opposition surge of Enceladus: HST observations 338-1022nm," *Icarus 173,* pp. 66-83, 2004, June 19.

[13] J. L. Jørgensen, "MicroASC a miniature Star Tracker, Small Satellites for Earth Observations," *Fourth International Symposium of the IAA, Berlin,* 2003.

[14] J. Connerney and M. Acuna, "The Juno Magnetic Field Investigation (MAG): Exploration of the Polar Magnetosphere," *American Geophysical Union, Fall Meeting 2008, abstract #SM41B-1679.*

[15] "JUNO microASC Earth Flyby," 10 12 2013. [Online]. Available: http://www.nasa.gov/jpl/juno/juno-earth-flyby-20131210.html.

[16] D. Pedersen, A. Jørgensen, M. Benn, T. Denver, A. Massaro, P. Jørgensen, J. Bjarnø and J. Jørgensen, "MicroASC instrument onboard Juno Spacecraft enabling inertially controlled imaging," *Acta Astronautica,* 2015.

[17] W. Gander, G. H. Golub and R. Strebel, "Least-Squares Fitting of Circles and Elipses," *BIT Numerical Mathematics Vol 34,* 1994.

Characterization of Optical Observations for Deep Space Navigation

David Arge Klevang Pedersen*, Andreas Härstedt Jørgensen. John Leif Jørgensen

The Technical University of Denmark, DTU Space, Elektrovej 327, 2800 Kgs. Lyngby, Denmark

Email: dakp@space.dtu.dk; Tel: +45 45253609; Fax: +45 45887133

Abstract

The performance of an optical sensor used to measure the centroid and distance of a planetary body is characterized by Monte Carlo simulations. It is investigated how a centroid algorithm applied on the extracted rim of the body, is influenced by the topography of the surface. The performance over the operational envelope is characterized and the boundaries, at which the performance is limited by the apparent surface features and the sensor's geometry, are identified.

1 Introduction

Since the early days of spaceflight, cislunar- and interplanetary navigation have been an important area of research. During the Luna, Gemini and Apollo era the technologies advanced significantly. Both autonomous and man-operated methods were developed for redundancy in case of up-link failures. For future space vehicles such as NASA's Orion, a fully autonomous and redundant navigational system is preferred, where the vehicle is capable of navigating, solely relying on the onboard system [1, 2]. In addition, the interest in landing automatic small vehicles on the Moon is steadily increasing with private organizations making an effort to develop low cost technology [3].

Christian and Lightsey [1] present a comprehensive overview of the options for autonomous cislunar navigation that enable absolute references to be updated onboard. The preferred method of determining the orbit of a translunar or interplanetary spacecraft is by the principles of the Doppler shift and Time of Flight. These measurements are conducted using traditional ground based tracking, primarily via the Deep Space Network [4]. These facilities enable an accurate measure of an inertially referenced position and velocity. Onboard accelerometers and gyros are effective in propagating the state of the spacecraft. However, they are prone to accumulating errors and drift from the true state. The external inertial reference is essential for updating the propagated state of the spacecraft and the process can be cumbersome and expensive.
Onboard Apollo, astronauts were equipped with an optical instrument similar to a naval sextant [5]. The principle of an angular measurement relative to a known celestial object is exploited to constrain the position of the vehicle along the propagated trajectory. An optical sensor provides a line of sight measure towards the center of the target. In addition, the range to the target can be estimated based on the apparent size of the object. A method, similar to the sextant, can be automated by using a star tracker in combination with an additional optical sensor that can measure the range and centroid of a planetary body. For translunar journeys, the Sun, Earth and Moon are apparent objects. For missions targeting the Jovian or Saturnian systems the planet and its' natural satellites are opportune.

Recent research has augmented the capabilities of the micro Advanced Stellar Compass (microASC) [6] to estimate the centroid and range of a planetary body to support a spacecraft in autonomously updating the state from an inertial reference. The aim of this study is therefore to characterize the performance of such a system within the operational envelope and gain an overview of significant error sources. For this work, the target is the Moon because an accurate topographic model of the lunar surface exists, - and comparison and verification of actual measurements are easy to obtain from on-ground observations.

2 Monte Carlo simulation

The accuracy of the centroid and range is assessed by numerical Crude Monte Carlo simulations [7]. This approach serves as a substitute for parts of a complete image process. The flow diagram of such an image processing approach is shown in Figure 1, together with the flow diagram of the Monto Carlo simulation. The simulation substitutes the image capturing, object detection, contour search, and limb extraction with the following steps:

- For each position and orientation, the horizon of the planetary body's surface is sampled corresponding to the resolution of a camera model.
- The horizon data is projected to the focal plane of the modelled sensor.

Common to both the simulation and the complete image process are the following steps:

- The focal plane data are corrected for elliptic geometry resulting from the perspective projection.
- The center and radius of a circle is estimated, from which the distance to the target is directly extracted.

Note that the simulation extracts the actual horizon of the planetary body, rather than rendering actual images. This will have an impact on the performance as no pixelation will be modelled.

In the following paragraphs a detailed description of the five steps of the simulation are described.

2.1 Height and Position Grid

In order to obtain a representative result it is necessary to perform calculations from different positions and orientations relative to the lunar surface. A grid of 500 random latitude and longitude coordinates is constructed. Figure 2 shows an example of a coordinate grid together with a topographic plot of the lunar surface. For each position the simulation is run at heights ranging from 20e3 km to 2e6 km, relative to the surface. The lower limit is chosen below a low lunar orbit and the higher limit farther than a weak stability boundary trajectory to the Moon. At each grid point the sensor's boresight is oriented towards the horizon as illustrated in Figure 3.

2.2 Sampling of sphere horizon

When centroiding a planetary body the phase of the shadow has to be taken into account. A straight forward way is to only consider the Sun illuminated limb, and discard the contour along the day/night terminator. Therefore only half of the spherical surface is sampled. Note that the arc will diminish at close proximity when the horizon is limited by the sensor's Field of View (FOV). Two principles of sampling are tested where the horizon is either sampled according to the camera's pixel resolution, as illustrated in Figure 4 or at a fixed angular interval resulting in 100 samples along the 180 degree arc.

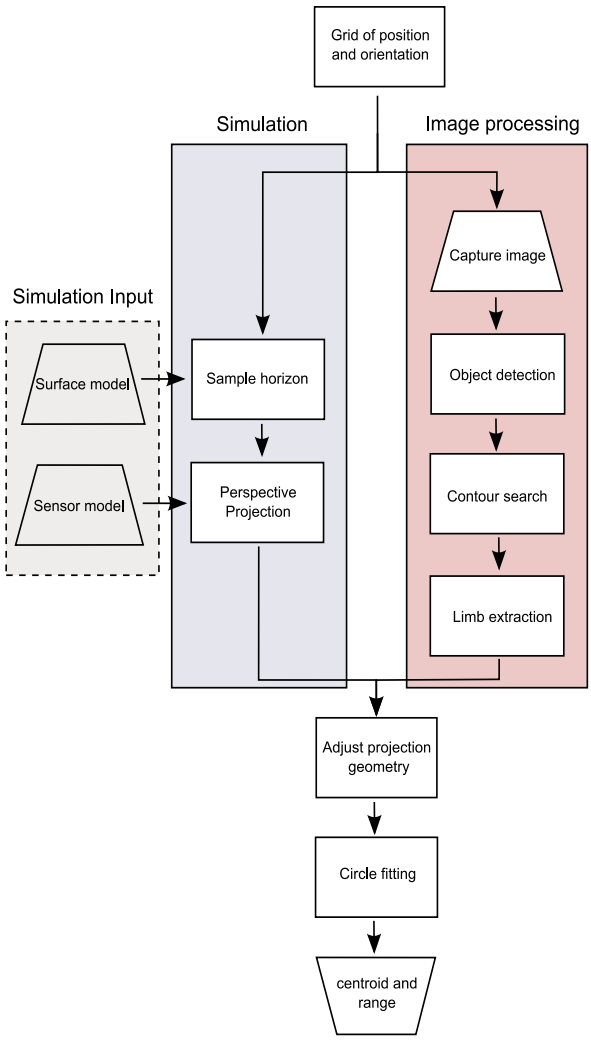

Figure 1: Flow diagram of the Monte Carlo simulation compared with the flow of processing an image.

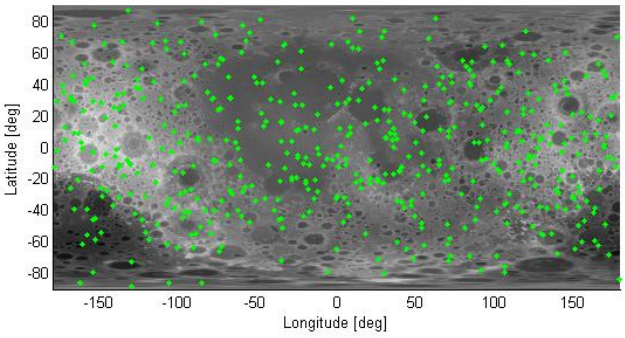

Figure 2: A Plate Carrée projection of the Lunar surface height from the LOLA data set [8]. The green marks are random distributed positions on the sphere, at which the Monto Carlo simultion is run.

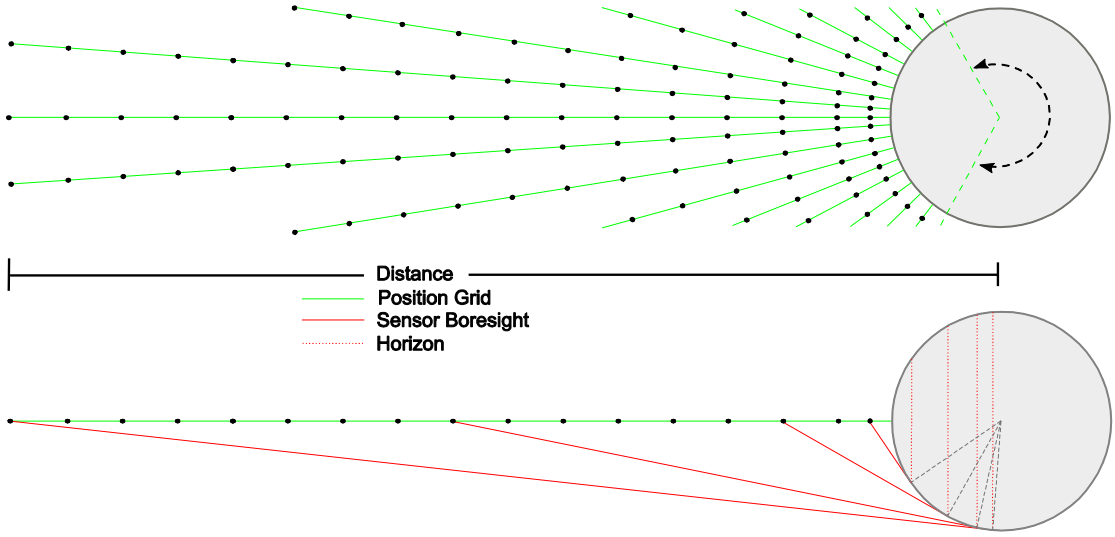

Figure 3: Top illustration shows the grid of positions around and above the lunar surface. Bottom illustration shows the orientation of the sensor's boresight oriented towards the lunar horizon

2.3 Adjust horizon to surface topography

The samples described in section 2.2 are only valid considering a perfect sphere. The observations by the Lunar Orbiter Laser Altimeter (LOLA) instrument onboard the Lunar Reconnaissance Orbiter (LRO) is used to model the surface of the Moon [8]. The global elevation model has a grid resolution of 15×15 arcmin. Introducing a topographic model of the lunar surface the horizon samples need to represent the "highest" point of the surface along a projected line of sight. A section of the topography is illustrated as a blue line and the line of sight as a red line dot in Figure 4 and Figure 6. In order to encompass the highest mountain, Mons Huygens (5500m), a section of the topography is interpolated along the line of sight. The topographic section interpolated with the angular interval $\gamma = \pm \operatorname{acos}\left(\frac{R_M}{R_M+5500m}\right) = \pm 5.9^o$. The sample with the largest angle composed from the center of Moon and the horizon is chosen as the horizontal data point for the specific pixel sample. The coordinates of the horizon are projected to the focal plane and thus constitute the detected horizon in the image.

2.4 Compensate projection geometry

The planetary objects relevant for this study are close to perfect ellipsoids. The flattening of Earth and Moon are 3.4e-3 and 1.2e-3 [9], respectively. For the purpose of this work the planetary body can with close approximation be considered a spherical geometry. Assuming a pinhole camera model, projecting a sphere onto the focus plane will result in a conic section, as illustrated in Figure 5: With the center of the Moon aligned to the camera´s boresight the projection is a circle; Deviating from the alignment results in an elliptic geometry where the circle is elongated in the radial direction relative to the principal axis; With the projected horizon aligned with the focal plane the projection is a parabola; and when the planetary body is behind the pinhole the projection is hyperbolic. The transition from elliptic to hyperbolic section occurs at the distance $\sqrt{1737^2 + 1737^2} = 2457km$. In most practical cases the projection will be elliptic.

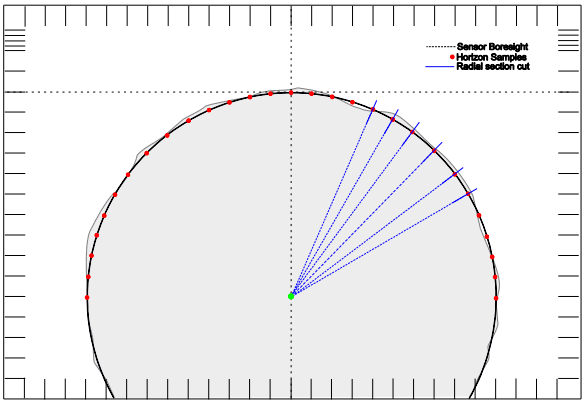

Figure 4: The sensor's boresight is aligned with the lunar horizon and sampled along a 180 degree arc according to the pixel resolution of the camera model (red dots). The horizon samples are constructed based on a perfect sphere, thus the samples are corrected topography using sections of the lunar surface model (blue lines).

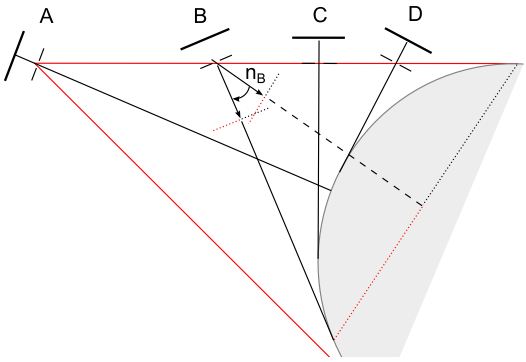

Figure 5: Perspective projection of a sphere results in a conic section; case A is a circle, case B is an ellipse, case C is a parabola, and case D is an hyperbolic. The solid black lines indicate the camera's boresight.

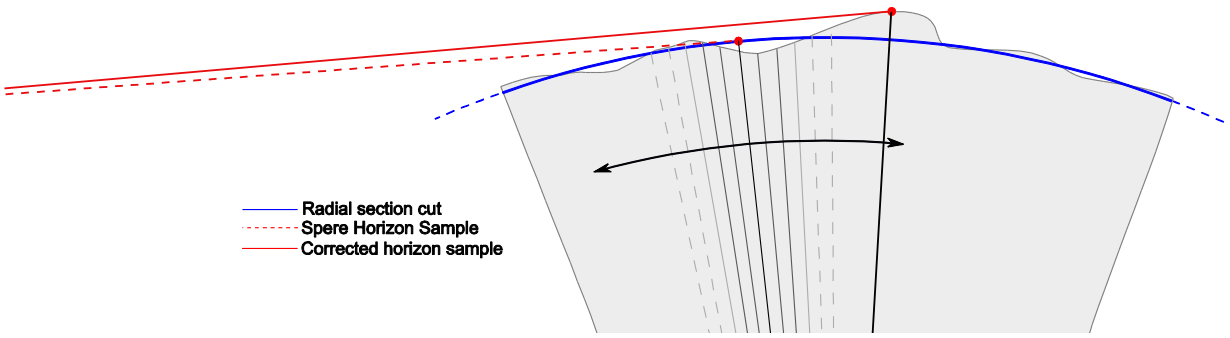

Figure 6:The sample of the sphere horizon is corrected according to the topography of the modeled surface. The blue curve shows the section of the topography to estimate the correct "height" of the horizon sample.

As illustrated in Figure 5 the horizon of the object in the three dimensional plot all lie on a plane. This is utilized by back projecting the image plane coordinates to a unit sphere. In these 3D coordinates the plane is still represented. The plane normal is estimated by a least square fit [10]. The residuals from the LSQ fit will to a large extent only be present in the z axis (along boresight), due to the topographic samples along the line of sight. With the equation of the plane

$$q_{z_i} = Aq_{x_i} + Bq_{y_i} + C, \tag{1}$$

The residual is described by

$$r_i = \left(Aq_{x_i} + Bq_{y_i} + C\right) - q_{z_i}. \tag{2}$$

The LSQ minimization problem is given by

$$\begin{aligned} E(A,B,C) &= \sum_{i=1}^{n} (r_i)^2 \\ &= \sum_{i=1}^{n} \left(Aq_{x_i} + Bq_{y_i} + C - q_{z_i}\right)^2. \end{aligned} \tag{3}$$

This function a hyperparabolid, where the gradient at the vertex equals zero, $\nabla E = (0,0,0)$. Thus leading to the equation

$$\nabla E = 2\sum_{i=1}^{n} \left(Aq_{x_i} + Bq_{y_i} + C - q_{z_i}\right)\left(q_{x_i}, q_{y_i}, 1\right), \tag{4}$$

which describes a system with three linear equations. Solving the linear system provides the LSQ solution to the plane parameters, A, B and C, which together describe the plane normal $n = [-A, -B, 1]$.

The plane normal is used to construct a rotation matrix, describing the rotation from the plane normal and the boresight. By rotating the unit vectors from the horizon in the image, with this rotation effectively compensates for the elliptic shape of the projection. The unit vectors are projected back into the image plane and a fit to a circular shape is performed.

Solving the linear system on a desktop computer system is an easy and straight forward task. For an implemented solution on a Digital Procession Unit (DPU) with limited resources, solving a linear system might not be a viable solution. One approach could be to pre-estimate the center of the projected ellipse and thereafter correct for the elliptical shape.

2.5 Circle fitting

Fitting data to a circular shape one has the choice of a geometrical fit or an algebraic fit. Generally, algebraic fits are fast to compute but do not obtain as good a fit as the geometrical fit. However the problem of geometrical fit is non-linear and requires iterative calculations that do not always converge to the minimum solution [11]. Considering an implementation in a DPU for inflight calculations it is essential that the solution is extremely robust against divergence and erroneous results. The computation load is also critical as an onboard DPU has limited resources. Furthermore it is important for the fitting algorithm to perform well against surface features becoming apparent, when in close proximity, and be robust against large biases when operating on small arcs. In addition, operating at far distances results in a sparse number of samples of the horizon. These considerations are the reason not to directly estimate an ellipse as opposed to the two step procedure of plane normal estimation (or pre-circle fit) followed by a circle fit.

Al-Sharadqah [12] performed a comprehensive statistical error analysis of the most popular algebraic methods; Taubin [13], Kåsa [14], Pratt [15] and the geometrical fit [11]. Al- Sharadqah derived explicit expressions for the variance and essential bias for the methods and showed that all methods have the same variance. The difference is traced to the essential bias by which the performance of the methods can be ranked. As expected the geometrical method showed the smallest essential bias and thus the best performance. Taubin's and Pratt's methods showed similar performance just short of the geometrical fit and the Kaså method is prone to poor performance for small arcs. In addition, Al-Sharadqah also presented a new algebraic

method, called Hyperfit, which has no essential bias and thus superior performance. The Hyperfit is a non-iterative method, meaning fast computation, no divergence or local minimum solutions. For this application the Hyperfit is the favorable choice.

2.6 Sensor model

The sensor model is an optical detector with a focal length of 20 mm and a resolution of 752 x 580 pixels with a pixel dimension of 8.6 µm x 8.3 µm. The sensor optics is modelled as a simple pinhole camera. To reassemble the performance of a limb detection method used on the data set from the microASC star tracker data onboard Juno spacecraft, the performance is simplified by adding noise to the projected horizon data. The noise is added in the radial direction of the planetary body. Processing the data captured by the microASC instrument from JUNOs earth fly by [16, 17], showed an orthogonal error between an estimated circle and the detected limb of the Moon in the order of 0.2 pixels at one standard deviation. This simple measure will be used to model the sensor system in combination with a limb detection method.

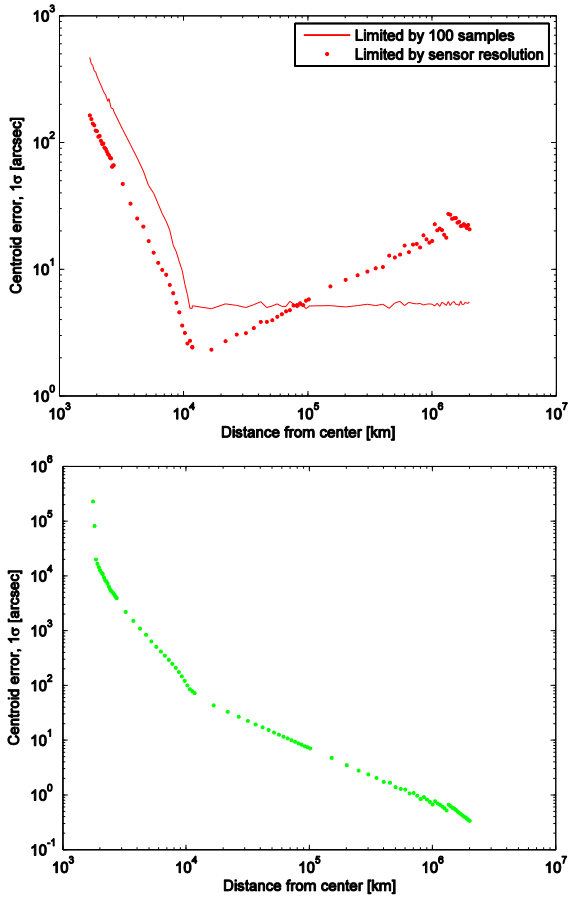

Figure 7: The standard deviation of the centroid estimate as a function of the range to the Moon. Top: The solid line describes the centroid with a constant number of horizon samples and the dots described the centroid when sampling the horizon according to the pixel resolution. Bottom: Here the lunar surface is modelled with the LOLA topography data and no noise in input to the system.

3 Simulation results

A number of simulations are conducted in order to fully describe the performance and limiting factors over the range of operation. The expected contributing factors are listed below:

- *Arc*: When estimating a circle fit the angular size of the arc has an impact on the accuracy of the centroid and radius estimate. The smaller the arc, the larger the bias. The estimate is also sensitive to the number samples along the arc.
- *Topography*: The surface topography of the planetary body will introduce a bias to the centroid and range estimations.
- *Sensor*: The geometry of the sensor has a limited FOV and resolution which will couple to the size of the arc at close proximity and the number of arc samples with the planetary body at a distance.

3.1 Performance limited by sensor

The sensor will limit the performance at some point due to the natural limitations of FOV, resolution and noise. The effect of these parameters is sought clarified. The initial simulations are thus considering the planetary body as a perfect sphere with no surface variations.

Figure 7 shows the result when using a sensor noise of 0.2 pixels in the radial direction and a FOV corresponding to the sensors internal dimensions. The solid line is the result where the horizon is sampled with 100 samples. Firstly, the figure reveals how the performance is limited by the FOV at ranges below $10^4 km$. Secondly, the performance remains at a constant level at ranges above the FOV limitation. This is to be expected as the sensor is modelled with an infinitely large resolution. The dotted curve however, is the result where the arc is sampled according to the pixel resolution, although with a minimum limit of 4 samples is applied. Comparing the two curves it is clear that below $\sim 8e4 km$ the sampling according to the pixel resolution outperforms the initial simulation. This is due to a larger number of samples of the arc. In addition, the transition from elliptic to hyperbolic projection does not impose a noticeable bias. As the distance increases the standard deviation increases by $\sqrt{n}$, where n is number of samples, which essentially translates to $\sqrt{R}$, where R is the range to the planetary body. It is worth noting the stepping behavior at large distances which is caused by the incremental decrease of the number of arc samples resulting in large bias shifts. The bias will be prone to move along the projected sun-vector. In between the steps the performance actually improves due to the increased distance and the resulting smaller projection. This behavior is a direct consequence of not rendering images with pixilation effects but projecting the horizon directly.

3.2 Performance limited by topography

Replacing the spherical model with the LOLA lunar surface model and the removing the sensor's noise will reveal how the lunar surface affects the centroid measure. The result is shown in Figure 7 where the limitation by the FOV and sample step behavior from the first simulation is present. Beyond the range of $10^4 km$ the performance improves as a function of R. Note the increasing degradation of the performance as very close proximity. This is the effect of local surface features that impose a large bias in the result by distorting the arc.

3.3 Overall performance

To assess the overall performance both the noise and surface topography are included in the simulation. The result in Figure 8, shows the estimated centroid and distance error, respectively. It is clear that the transition from one dominating element to the other occurs around $10^5 km$. The overall performance can be divided into 4 zones defined by the element that is limiting the performance, see Table 1. This gives a good overview of which elements affect the performance as a function of the distance to the planetary body.

In the bottom plot of Figure 8 the accuracy of the estimated distance is plotted as a function of the actual distance that results a minimum ratio of 10e-3 in zone 4. At closer proximity in zone 1 and 2 the ratio increases rapidly and reaches 5e-2 at an orbit height of 100 km.

Figure 9 shows the average of the estimated distance and the ratio of the average estimated distance as a function of the actual distance. The figure shows a fluctuating mean at distances above 1e6 km which corresponds to the very sparse number of samples, although the mean fluctuation is relatively small compared to the scale of the standard deviation. It also shows a tendency to underestimate the distance at close proximity to the surface. It is fair to conclude that the bias is centered at zero for the remaining operational window.

Zone	Range	Description
1	Below $2e^3 km$	Limited by local topography of the planetary body.
2	$2e^3 km$ to $1e^4 km$	Limited by the sensor's Field of View.
3	$1e^4 km$ to $1e^5 km$	Limited by global topography of the planetary body.
4	Above $1e^5 km$	Limited by sensor noise and resolution.

Table 1: The four zones defining the ranges of which the different elements dominate the performance of a centroid and range estimate.

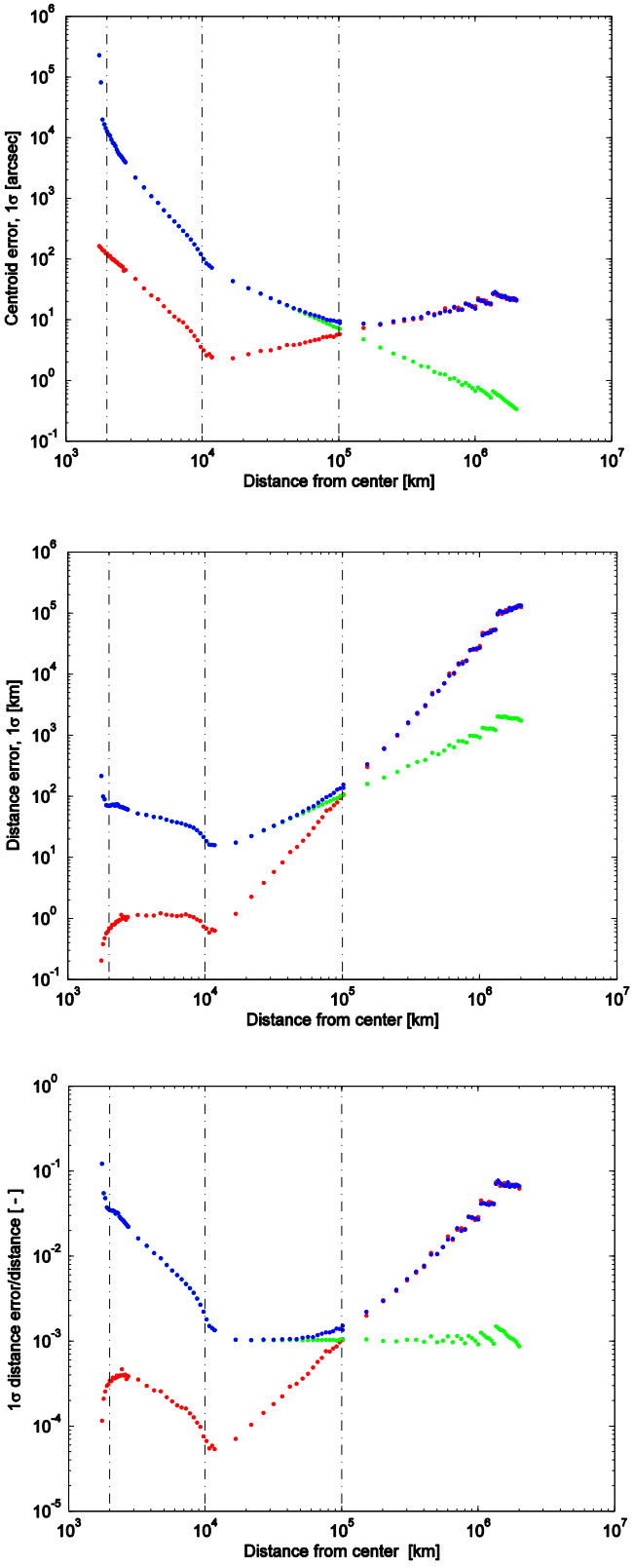

Figure 8: Top: The standard deviation of the centroid. Middle: The standard deviation of the distance. Bottom: The ratio of the distance standard deviation over the actual distance. . Red curve shows the result with sensor noise and without topography. Green curve shows the result with the Moon's surface topography but without sensor noise. Blue curve shows the result with both the surface and sensor noise included. The dashed lines indicate the zone transitions.

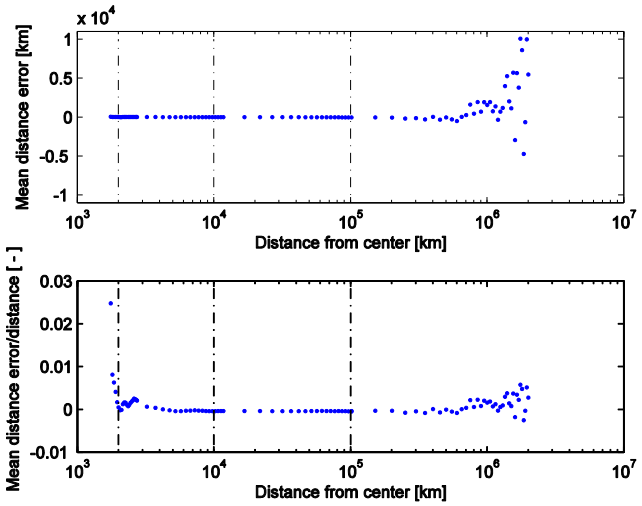

Figure 9: Top plot: The mean of the estimated distance. Bottom plot: The ratio of the mean distance over the actual distance. The dashed lines indicate the zone transitions.

3.4 Comparison with measurement data

To verify the simulation results, measurements from ground and in-flight observations, are compared with the simulation. The in-flight measurements are the Juno Earth Fly By data set [16] and the ground based observations are from test campaigns at Mauna Kea observatories in Hawaii and Calar Alto observatories in Spain. Figure 10 shows the standard deviation of the distance from the simulation together with the distance errors from the test data, where the blue dots indicate the simulation measurements, green dots the in-flight measurements, and green crosses the Earth based measurements with a red fractile indication at 25% and 75% as well a red cross at 50%.

The in-flight data is obtained at a continuously decreasing distance, resolving an error decreasing accordingly. The gradient of the decay is in full agreement with the simulation. The two ground observations registered at a distance of $2.8e^4 km$ and $7.0e^4 km$ are accomplished by substituting the standard microASC lens by a 100mm and 250mm lens and thereby emulating that the observations are carried out at a shorter distance. The results from these measurements are on very good agreement with the simulation. In the remaining ground observations registered around $3.8e^4 km$ a standard lens is used. These measurements have a slightly larger error than the simulated result. It is noticed that the radial error from the circular fit is 0.3 pixels instead of the 0.2 pixels, as observed from the in-flight data. This is traced to be caused by atmospheric effects and a varying shutter time in the ground measurements. Note that the shift is not observed in the data using the longer lenses which is due to the global features dominating the performance.

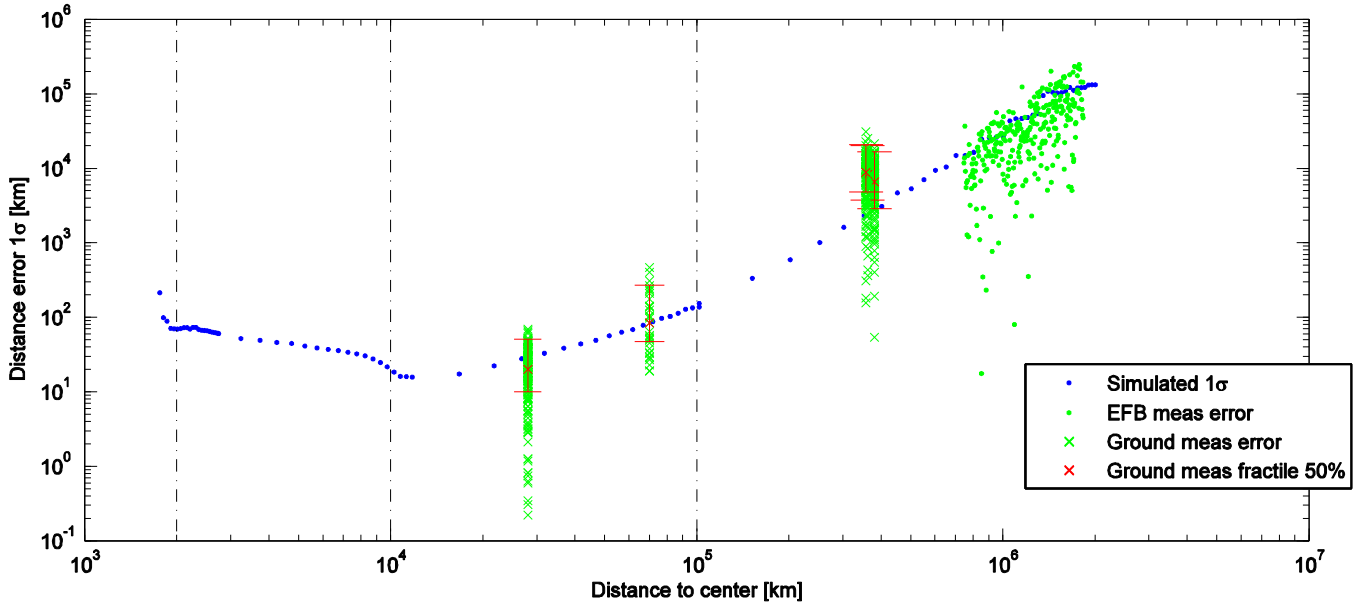

Figure 10: Comparison between the simulated error and error measured in ground and in-flight observations. The in-flight observations are from the Juno Earth Fly By [16, 17] and the ground observations are from test campaigns at Mauna Kea in Hawaii and Calar Alto in Spain. Two ground observations are conducted with an increased focal length which effectively emulates that the observations are made at a closer distance. The interval marked in red defines the 25% and 75% fractile of each corresponding measurement series test.

4 Conclusion

The performance of an optical sensor used to measure the centroid and range towards a planetary body is characterized over the range where the target is resolvable. The characterization is based on Monte Carlo simulations with the lunar topography used as a model for the planetary body. The results from the simulation reveal four operational zones that are defined by which effect is limiting the obtainable accuracy. At greater distances, the performance is limited by the sensor's noise level and resolution. At medium range global surface variations appear and become the limiting factor. At close proximity the sensors FOV limits the arc size and local surface features become apparent. The simulated results show good correspondence with in-flight and ground observations.

For future implementations, the described approach does not consider any shadowing or optical properties of the lunar surface as the horizon is directly projected to the focal plane. To include shadowing and surface properties an artificial image should be rendered. Such an approach will also include pixelation effects. In addition, rendering an image will also facilitate tests of a limb detection method and can thus test the whole image processing procedure. Furthermore, the approach is restricted to objects that are close to a spherical shape. If targeting objects with ellipsoid shapes, biases will be inherent and will need to be compensated for.

5 Bibliography

[1] John A. Christian, E. Glenn Lightsey, "Review of Options for Autonomous Cislunar Navigation," *Journal of Spacecraft And Rockets*, vol. 46, no. 5, pp. 1023-1035, 2009.

[2] C. D'Souza, T. Crain, F. C. Clark, "Orion Cislunar Guidance and Navigation," *American Institute of Aeruonautics and Astronautics*, 2008.

[3] XPRIZE, Google Lunar, "lunar.xprize.org," 14 June 2015. [Online]. Available: http://lunar.xprize.org/.

[4] N. Jet Propulsion Laboratory, "Deep Space Network," 15 June 2015. [Online]. Available: http://deepspace.jpl.nasa.gov/.

[5] D. Woods, How Apollo Flew To the Moon, Springer Praxis Books, 2008.

[6] John L. Jørgensen, Troelz Denver, Betto Maurizio, Peter S. Jørgensen, "MicroASC a Miniature Star Tracker," *Small Satellites for Earth Observation, 4th International Symposium of the International Academy of Astronautics*, pp. 157-162, 2003.

[7] D.P. Kroese, T. Taimre, Z.I. Botev, Handbook of Monte Carlo Methods, New York: Wiley Series in Probability and Statistics, John Wiley and Sons, 2011.

[8] NASA, "PDS Geosciences Node Data and Services: LRO LOLA," [Online]. Available: http://pds-geosciences.wustl.edu/missions/lro/lola.htm. [Accessed 14 June 2015].

[9] N. Goddard Space Flight Center, "NASA Space Science Data Coordinated Archive," [Online]. Available: http://nssdc.gsfc.nasa.gov/. [Accessed 14 June 2015].

[10] P. C. Hansen, V. Pereya, G. Scherer, Least Squares Data Fitting With Applications, Baltimore: John Hopkins University Press, 2013.

[11] N. Chernov, "Circular and Linear Regression: Fitting Circles and Lines by Least Squares," *Chapman & Hall/CRC Monographs on Statistics & Applied Probability*, vol. 117 (256 pp), 2010.

[12] Al. Sharadqah, N. Chernov, "Error Analysis for Circle Fitting Algorithms," *Electronic Journal of Statistics*, vol. 3, no. 886-991, 2009.

[13] G. Taubin, "Estimation of Planar Curves, Surfaces and Nonplanar Space Curves Defined By Implicit Equations, with Applications to Edge and Range Image Segmentation," *IEEE Trans. Pattern Analysis Machine Intelligence*, vol. 13, no. 1115-1138, 1991.

[14] I. Kåsa, "A Curve Fitting Procedure and its Error Analysis," *IEEE Trans. Inst. Meas.*, vol. 25, no. 8-14, 1976.

[15] V. Pratt, "Direct Least-Squares Fitting of Algebraic Surfaces," *Computer Graphics*, vol. 21, no. 145-152, 1987.

[16] A. H. Jørgensen, D. A. K. Pedersen, M. Benn, A. Massaro, P. S. Jørgensen, J. B. Bjarnø, J. L. Jørgensen, "Semi-Autonomous Optical Observations for Deep Space Navigation".*Submitted to IEEE Transactions on Aerospace and Electronic Systems.*

[17] D. A. K. Pedersen, A. H. Jørgensen, M. Benn, T. Denver, P. S. Jørgensen, J. B. Bjarnø, A. Massaro, J. L. Jørgensen, "MicroASC instrument onboard Juno Spacecraft enabling inertially controlled imaging," *Acta Astronautica*, vol. 118, pp. 308-315, 2016.

4.4 Outlook

The three papers describe how the microASC platform is augmented to be used as an instrument that supports onboard orbit determination of a spacecraft. A full characterization of the system is presented together with in-flight and ground observations.

The current development of the system is envisaged to be applicable in a variety of mission cases. First of all, as the microASC is a miniature system designed for a high level of autonomy and robustness, the system is very suitable for future vehicles that rely on an onboar d autonomous and redundant navigation system. Supplying the microASC with a timestamp and an initial position or trajectory the module will be able to perform onboard orbital determination, which can be of interest to organizations seeking to develop low cost autonomous vehicles.

Secondly, the system can play a supporting role to the established ground infrastructure by delivering continuous in-flight observations of either the spacecraft's or the target's inertial position. Using an initial reference from the DSN, the system can perform continuous in-flight observations for days, only logging the LOS, range and inertial position. This data will consume a small volume of the data storage, which can be transmitted to Ground Segment once the observations are done. If tracking a body who's trajectory is not well determined, such observations can be used to improve the ephemerides of the target. And vice versa, if the spacecraft is exposed to orbital disturbances that are difficult to model, observations of a target, who's trajectory is well established, can improve the orbital determination of the spacecraft.

At last the system is envisaged to perform immediate tracking of a target to aid a spacecraft in maintaining a specific attitude, relative to the target, instead of an inertial reference. This can be of value during a flyby, where other scientific instruments are directed towards a specific point of interest of the target to optimise the scientific yield of the flyby.

5 Tracking of Artificial Satellites

This chapter will address the subject of tracking an artificial satellite by non-cooperative means. An introduction to in-flight relative navigation relating to non-cooperative tracking is presented, together with an overview of the opportunities offered by the PROBA3 mission. An analysis of the scene, target and the operational envelope will be presented which leads to an image processing approach aimed for man made targets. Results from mock-up test facilities will be presented and discussed in details.

The process of Rendezvous and Docking (RVD) is still considered as one of the riskiest elements of space flight, because, it essentially constitutes a controlled collision. and if any instrument reading is out of nominal it can have devastating consequences. However, RVD technology, and formation flight in general, is considered one of the key technologies that can overcome the limitations of mass and volume budgets constraining today's missions [20, 21]. In Low Earth Orbit (LEO) such operations are normally performed with the ground segment and astronauts in the loop. This puts natural constraints to a missions profile. Therefore, frontiers of this technology are seeking to validate fully autonomous and robust technologies that enable missions related to robotic servicing and Mars sample and return (MRS). In addition, highly accurate formation flight will allow very large structures, as satellite pairs are flying in formation, to constitute one scientific instrument.

5.1 Mission Profiles

Within the area of RVD and formation flight, non-cooperative tracking of satellites applies to a subset of mission profiles:

Sample and Return Returning soil samples of other solar system bodies safely to Earth is highly valued as it enables thorough studies of the soils content. Instruments based on Earth are naturally more capable than in-situ instruments thus the scientific outcome can be increased. Future missions are set

on returning samples from comets and Mars. The Mars 2020 rover is planned to collect and store promising samples waiting to be picked up by future mission. The general approach to return the samples is to launch both a lander and an orbiter. The lander will collect the samples, store them in a canister and return it into orbit around Mars. The ascending canister will rendezvous with an orbiter which will have enough propellant for a Mars-Earth transfer orbit. Studies show that performing rendezvous in an elliptical orbit has some advantages compared to rendezvous in a circular orbit. The amount of ΔV needed to compensate for orbital drift at apoapsis during a V-bar approach is about half of that needed in a circular orbit, if performed in the vicinity of apogee. Furthermore the disturbing forces from gravity gradient is substantially reduced at apogee [22, 23, 24]. The budgets for such an ascent vehicle also impose strict requirements on the RVD technology. Such a mission must completely rely on autonomous RVD technologies due to the communication latency to Earth ground segment and can not rely on absolute positional measurements, like GPS. In addition to a limited budget of volume and mass, the technology must tolerate two launches, two landings and the environmental conditions on the surface of Mars. Although it is evident to mount beacons or markers on the exterior of the ascending vehicle a backup instrument would be appropriate to ensure robustness in case off any malfunctions. A visual instrument capable of tracking the ascending vehicle without any cooperation is therefore of high value to the mission.

Servicing Robotic servicing of Earth orbiting satellites has had a steady increase of interest during the recent decades. Servicing applications relevant to non-cooperative tracking are instances where targets are malfunctioning, de-commissioned or simply considered debris. Although the space surrounding Earth is vast, the useful and most populated orbits in LEO ranging from 500 km to 1200km and GEO at 36.000 km are slowly being filled up with debris and outdated equipment, which comprises an increasing risk of collision, thereby scattering more debris to the valuable orbits and imposing an even greater hazard. In these instances the servicing objective is to reduce the probability of collision by capturing and eliminating the debris. For a LEO orbit the obvious action is to either de-orbit the equipment or reduce the natural decay to a few years time. Whereas for a GEO a de-orbiting maneuver requires a substantial amount of ΔV and therefore the equipment is transferred to a so called

graveyard orbit a few hundred kilometers above the GEO orbit [25]. If still functioning these targets are not necessarily equipped with any technology for docking or capturing, however, robust mechanical interfaces to the launcher or the apogee kick motor can be used for grappling [26]. Neither are the target spacecrafts equipped with relative navigation capabilities. If malfunctioning, cooperative navigation is ruled out. Thus, an instrument capable of measuring the relative position and attitude by non-cooperative means, is essential for a successful mission.

5.1.1 Operational Phases of Rendezvous

The relative position of the two spacecrafts can be viewed in the Local Horizontal Local Vertical (LHLV) frame of the target, where the V-bar is the axis pointing in the direction of the orbital velocity vector, but not necessarily aligned, and R-bar is the direction of the radius vector toward the center of the object being orbited, see figure 5.1. Typically there are four phases of a RVD procedure [27]:

Phasing Assuming both vehicles are in orbit with nearly co-aligned orbital planes, the objective of the *Phasing* stage is to reduce the phase angle between the two vehicles. This is simply achieved by the chaser having a higher or lower orbital height resulting in different orbital velocity allowing the chaser to catch up with the target. The typical position accuracy during the this stage is a few hundred metres in the orbital height and a few kilometers in the orbital direction.

Homing With the phase angle at a suitable level the *Homing* stage is initiated, where objective is to cancel out the orbital height differences bringing the relative velocity of the vehicles to an appropriate rendezvous velocity. Also mission timelines are synchronized with regards to illumination and communication windows. The end position of this maneuver constitutes at safe holding point, *p1*, to where the chaser can recede in case of any off nominal performances. This is typically at a distance of a few km from the target. During this stage relative navigation is typically initiated measuring LOS and range. The position accuracy decreases from around 100m to 10m at the end of the stage.

Closing The next procedure is the *Closing* where two burns are initiated to reduce the distance. The end point of this procedure also constitutes a safe holding

point, *p2*, typically a few hundred meters from the target. From here either a fly-around maneuver to the R-bar can be performed or a linear translation along the V-bar can be performed. The position accuracy shall be within 1% of the range.

Final Approach The last phase is the Final Approach where the chaser approaches the target either by small incremental burns followed by a force feed motion or solely relying on force feed control. The objective is to bring the vehicles in position and alignment for either docking or capture. During this stage the relative 6DOF measure is to be resolved and used for navigation. The accuracy of the relative position shall, to a large extent be within 1% of the range, lateral position within a few cm and the attitude within 1°.

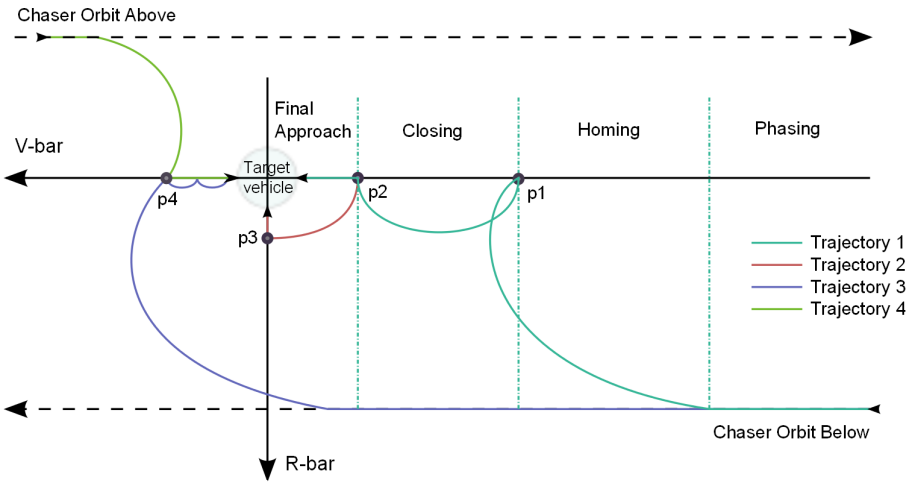

Figure 5.1 *Example of rendezvous phases and various approaches towards the target spacecraft, seen in the Local Horizontal Local Vertical frame of target. Note: the figure is not to scale.*

The trajectories shown in figure 5.1 present three examples of initial phases and ending in three different approach directions, +V-bar, -V-bar, and R-bar. The illustrated trajectories with the hold points are mostly apply to circular or near-circular orbits. For highly elliptical orbits hold points do not exist in the LVLH frame, although the different phases apply to both orbits. Regarding Serving of geostationary satellites and MSR in high elliptic orbits, the chaser is envisaged to perform the final approach along the V-bar [22, 28, 24].

5.1.2 Instrumental Suite for non-Cooperative Tracking

Generally, space missions seek a form of redundancy in order to tolerate unforseen failures. Typically by installing multiple units of critical hardware and backups of software. Considering the mission profile of Servicing and MSR they both rely on a high level of autonomy and redundancy. The relative navigation is no exception where a suite of instruments are envisaged, each relying on different measurement principles and hardware, in order to achieve a seamless and fault tolerant performance. A short overview of optical instruments supporting non-cooperative tracking is given in the following.

Lidar: A lidar is an active sensor where light, typically a laser beam, is emitted towards the target, reflected of the surface and registered by a detector on the sensor. The range estimate is typically obtained by the principle of Time of Flight (TOF), measuring the time from emitting and receiving the signal, or the principle of phase shift, measuring the phase difference between the emitted and received signal. Generally, the TOF principle has a wider operational range while the phase shift is more accurate but range limited by the ambiguity of the phase shift. There are mainly two types of lidars used for relative spacecraft navigation: A *scanning lidar* or *flash lidar*. The flash lidar flashes a laser beam with a wide FOV and detects the returned signal by an array of detectors. The scanning lidar emits a narrow laser beam and has only a single detector, where a spacial array of distances is obtained by scanning a larger FOV using rotating mirrors. The lidar is capable of measuring the LOS and range to the target and is generally independent of the lighting conditions [29].

Camera: As a stand-alone unit a camera is a passive sensor with a very wide range of useful measures. Capable of measuring 6DOF solution at close range and LOS at far ranges. A range can also be estimated at intermediate range solely based on the apparent size of target. A camera is dependant on the surrounding lighting conditions where both the intensity and the angle of illumination can affect the performance. An infrared sensitive camera or floodlight can compensate for this drawback, enabling navigation during eclipse, for instance. At close range operations the accuracy of the 6DOF pose can be improved by using two camera heads which enables the use of stereo vision.

Structured Light: Augmenting a detector with a laser source enables highly accurate range measurements by the principle of triangulation. A structured light system can be a stand-alone instrument. But if integrated with camera, as

described in chapter 3, the measurements can be combined resulting in a single system with the large operational range from the camera together with the highly accurate range measurements at close range, ultimately, also improving the 6DOF pose estimation. Another possibility is to pair structured light with a lidar instrument, that is also capable of LOS, range and 6DOF pose measurements [30]. Laboratory tests show a relative attitude and position accuracy of 1° RMS and 10mm RMS at a distance of 11m.

5.2 Objectives of non-Cooperative Tracking

Based on the mission objectives of a MSR and Servicing mission, the objectives of tracking a non-cooperative spacecraft are the following:

A *The accuracy of the LOS, range, and 6DOF pose shall comply with the required accuracy of RVD related relative navigation.*

B *Obtain a 6DOF pose independent of target's orientation.* In the case of a Servicing mission the target might be in an uncontrollable state, i.e. tumbling, imposing that a solution shall be obtained from any direction. This objective is also relevant to a MRS mission where the non-cooperative tracking mode mainly works as a redundant and fault-tolerant backup. In case of any failure, this objective will ensure a high level of robustness.

C *Support GNC update rate.* An update rate of 1 Hz is assumed to support most GNC requirements. Note, that this does not apply to the initial acquisition of the pose, but rather the consecutive tracking where a priori solution of the state is available. In the acquisition mode a solution should be obtained within 10 s.

D *Seek a generic approach* The approach in designing the tracking software shall support a wide range of shapes and optical properties and not rely on specific features of the target. The reason for this is twofold: During mission design and development the target might change geometric shape and surface properties which makes it difficult to rely on specific features. In addition, if relying on a specific features the approach might not support other future missions, and thus the in-flight validation is without value. Note, that this does not exclude a subsequent process which is optimized to the specific target at hand, either in terms of robustness or accuracy. This objective is to ensure an overall generic approach that can support a large variety of targets.

5.3 Prior In-flight Experience

In-flight experience with relative navigation between a chaser and a non-cooperative target has mainly been through demonstration missions seeking to mature sensors, actuators, and Guidance Navigation and Control (GNC) algorithms [31, 32, 33]. These missions have shown promising results navigating with a vision sensor capable of measuring LOS, range and 6DOF pose at close proximity. However, it is reported that the 6DOF pose is obtained by the use of active markers mounted on the target. This means that pose is measured by cooperative means. Some in-flight results of non-cooperative tracking using a combined lidar and structured light are reported with promising results [34].

5.3.1 VBS Onboard PRISMA

As mentioned in chapter 2, the VBS was one of the sensor systems designed for relative navigation. The system consists of two optical sensors: One optimized for far range and one for short range navigation. The far range optics is a standard microASC CHU detecting the very small and faint target amongst the starry background. The short range optics was optimized to focus at short range and equipped with a spectral bandpass filter excluding wavelengths below Near Infrared (NIR). Furthermore, the target spacecraft, Tango, is equipped with NIR LEDs scattered on the surface of the spacecraft.

The system has three modes of operation: far range, intermediate, and short range. At far range the target is a small and faint dot amongst the stars in the background. Non-stellar objects are detected and the target is recognized through a filtering process resulting in a Line of Sight (LOS) measure. At intermediate range the target outshines the stars in the background and can thus be easily detected. At far and intermediate range operations the system only makes use of a non-cooperative principle as no information is actively transmitted from Tango. At short range the LEDs on the target become apparent and resolvable in the image, and by pattern recognition and pose estimation a 6DOF pose is resolved, thus operating by cooperative principles at short range.

5.3.1.1 Post Processing In-Flight Data

To prepare for further development of the VBS capabilities, in-flight images of Tango were captured during a fly-around maneuver by the short range sensor. Figure 5.2

shows a few sample images of Tango at various orientations and at close proximity. The operational envelope of the two spacecrafts is sub-optimal for non-cooperative tracking, due to the solar panels of the two spacecrafts are required to always be Sun pointing. The formation allowed is illustrated in figure 5.3, resulting in an operational envelope of $\pm 45^\circ$ yaw rotation, leaving only a small window optimal for non-cooperative tracking. However, when the sunlit face is observable and well defined, the information in the image is sufficient for pose estimation. An effort, to post-process the in-flight data shows promising results in determining the pose of the target [35], where the estimated pose of Tango is compared with positional data from GPS measurements and attitude data from sun- and magnetic-sensors. The error are in the order of 10 degrees and $10cm$ at a range of $10m$, giving an error/range ratio of 1%. Although the errors seem large, they do lie within the error budget for formation flight at this operational range. The results reported in [35] are very valuable because the in-flight test data is highly representative of the actual scenery, as opposed to data captured in test facilities. However, the method was only tested on a single image, and does not represent the performance from various orientations, distances or incident angle of the Sun.

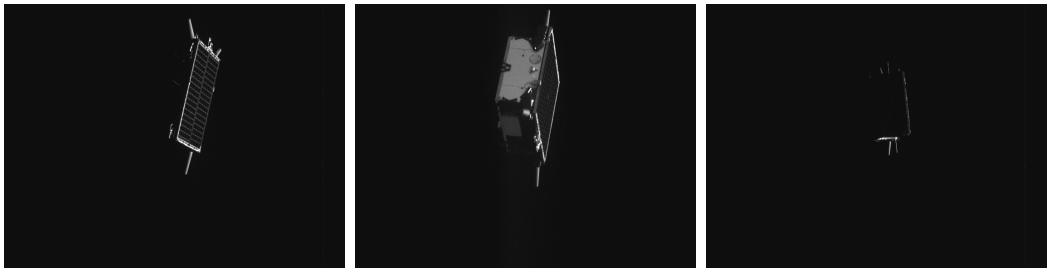

Figure 5.2 *In-flight images of PRISMA Tango spacecraft, captured by the VBS instrument. Credit: MIS, DTU Space*

5.4 Opportunities With PROBA3

PROBA3 is the fourth technology demonstration mission in ESAs low-cost Project for On-Board Autonomy (PROBA) series, where the objective of the series is to validate new technology while carrying a scientific payload. This mission's objective is to demonstrate key technologies for in-flight formation flight increasing technology readiness level of various sensors and navigation and control algorithms [14]. The mission will consist of a small satellite pair flying in closed loop formation in an highly elliptical orbit. Compared to a circular orbit a high elliptic orbit is advantageous for accurate formation flight due to minor disturbance forces at apogee

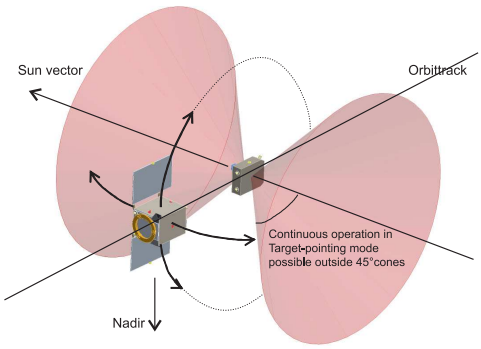

Figure 5.3 *The formation of the PRISMA satellite pair is limited to ±45° between sun-angle and the normal of the satellites sun panels. Credit: Swedish Space Corporation (SSC) and M. Benn [11]*

from gravity gradients, radiation pressure and drag [36]. An overview of the mission objectives is given below, listed according to the priority:

Mission objectives:

A Validate formation flying control algorithms, demonstrate the autonomy and robustness of formation flight, and increase technology readiness level of sensors and instruments

B Return valuable science enabled by high precision formation flight

C Conduct Rendezvous Experiments (RVX): covering high elliptical orbits, 6 DOF control only using thrusters as actuators, and perform realistic collision avoidance maneuvers

The scientific payload of the mission is a solar coronagraph were one spacecrafts constitutes the occulting disc, Occulter Spacecraft (OSC), and the other carries the detector, Coronagraph Spacecraft (CSC). Together the two spacecraft form a coronagraph with a nominal range of 150 m, allowing for a unprecedented investigation of the close corona. The corona is expected to be observed at 1.08 solar radii. The spacecraft will act as a virtual rigid structure commanded to re-orient and point the instrument and also re-size the focal length.

The Rendezvous Experiment (RVX) is aimed to validate simplistic relative GNC solely based on relative measurements obtained by the VBS, as opposed to absolute positions from GPS or relative positions from laser technology. The rationale is to prepare for rendezvous between an orbiter and a sample canister in an elliptical orbit around Mars with the focus on simplicity, autonomy and robustness [37]. During these planned experiments the VBS will run in cooperative mode.

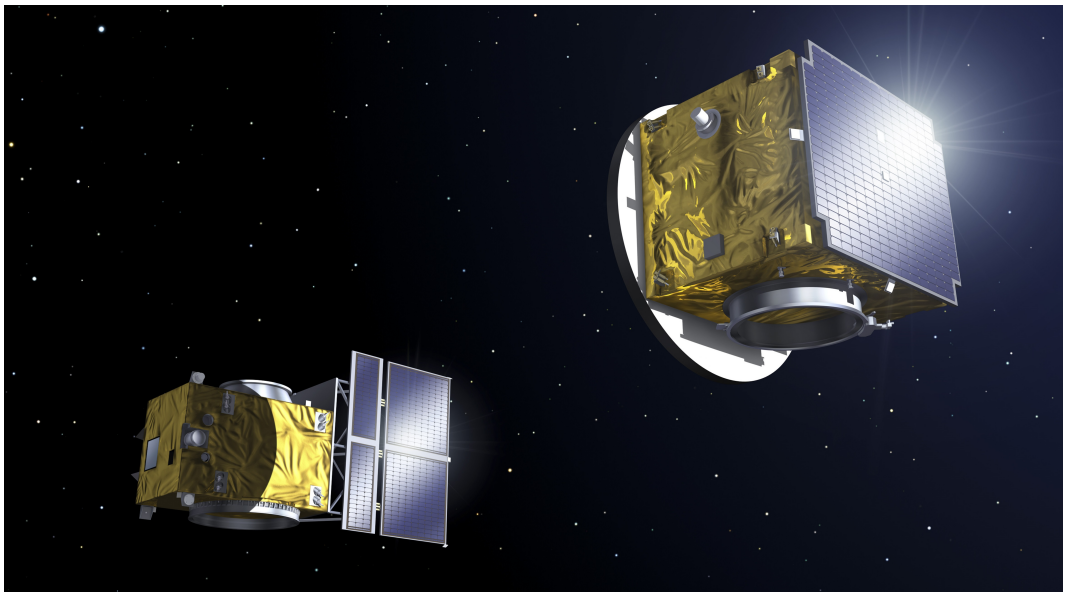

Figure 5.4 *An artists drawing of the PROBA3 satellite pair flying in formation with the Coronagraph Spacecraft (CSC) on the left and Occulter Spacecraft (OSC) on the right. Credit: ESA*

One experiment with high potential is to perform non-cooperative tracking in-flight with the objective to validate the image processing methods and also GNC software which has to rely on a less accurate solution, when compared to cooperative mode. The potentials with such an experiment is to accede the interests of non-cooperative tracking in relation to servicing and sample return missions. For these experiments the OSC is considered the chaser and the CSC the target, which will be adopted throughout the chapter.

5.4.1 Instrument Payload for Relative Navigation

A number of instruments are to be used for the relative navigation between the satellite pair. These include a mixture of Relative GPS, lidars and vision based sensors.

Relative GPS At apogee GPS signals can not be utilized, so Relative GPS (RGPS) solutions that are obtained during the perigee passage, are propagated to apogee. By modelling the differential solar radiation pressure acting on the satellite pair, the positional error is expected to be within 10 m. If not compensated for an positional error of 50 m is expected [38, 14].

Coarse Lateral Sensor By emitting a defocused laser beam towards the target, the beam is retro-reflected towards the chaser by a corner-cube and received by

a detector estimating a pointing vector towards the corner cube. The Coarse Lateral Sensor (CLS) is expected to resolve a lateral position error of $1mm$ at the nominal operating range of $150m$ [14].

Fine Lateral and Longitudinal Sensor The Fine Lateral and Longitudinal Sensor (FLLS) works much by the same principle of the CLS, only with a narrower beam and a the capability of measuring the distance, by comparing the output signal with the received signal. At the nominal distance the lateral position is expected to by accurate to $21\mu m$ and the range accurate to $30\mu m$ [14].

Vision Based Sensor The VBS will have two CHUs mounted on the positive X axis of OSC (see figure 5.6, each optimized to operate at far and nominal range ($150m$). The far range CHU is expected to have a $20mm$ focal length and will resolve a LOS towards the CSC. The CHU designed nominal range has a $100mm$ focal length and will resolve a 6DOF pose of the CSC relative to the OSC by recognizing a specifically designed active LED pattern that is mounted on the negative X face of CSC. Note, that the VBS has the capability of operating in both, cooperative mode at nominal range, and non-cooperative mode at both far and close range.

5.4.2 Operational Envelope

Being a part of the PROBA series, a large emphasis is put into the autonomy of the mission. The satellite pair is planned to acquire, lose and re-acquire formation on a daily basis without intervention by the ground segment. The phases of the formation during an orbit is illustrated in figure 5.5 together with the orbit parameters for OSC in table 5.1. In the proximity of perigee the satellites are in free flight and sun-pointing. During this period GPS signals are within reach. Exiting the perigee the GPS signals will be lost by which the RGPS solutions from perigee are propagated to apogee. Approaching the apogee the formation will be acquired, using the relative navigation sensors, from where a window of approximately $6h$ allows for scientific operations and experiments. The coarse navigation instruments acquire the lateral position of CSC.When exiting this operational window the formation will be broken and perigee entrance will be prepared.

Both spacecraft are required to always be sun-pointing because of power requirements from the solar arrays. The face normal of the spacecraft with the solar panels must not deviate more than 30° from the sun-pointing vector. This restricts the relative orientation to an operational cone described by the angle Sun-CSC-OSC

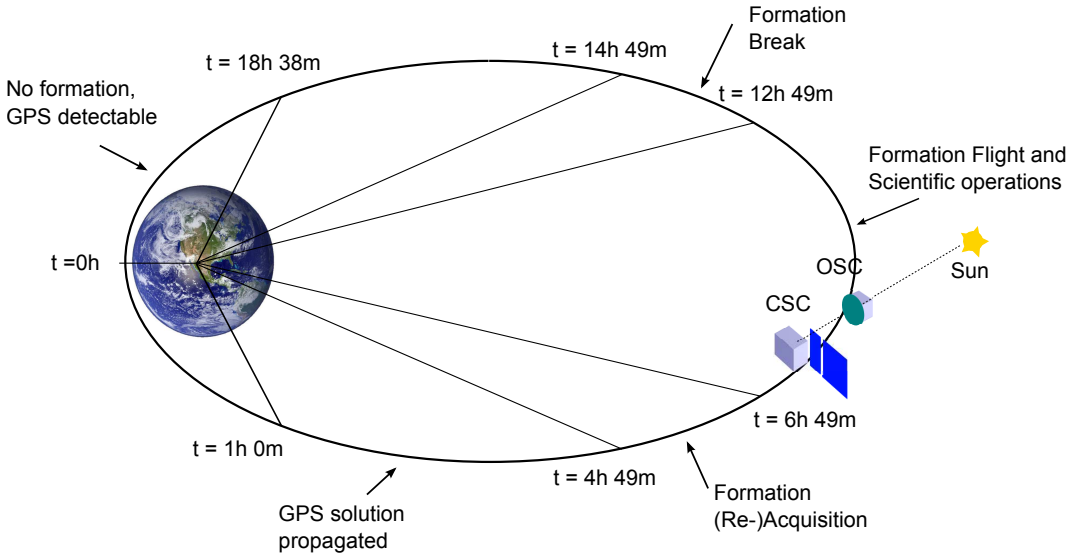

Figure 5.5 *Orbital routine for PROBA-3 where formation is acquired prior to entering apogee leading to fine formation flight performed around apogee. Credit: Adapted from [39]*

Parameter	Value
Perigee height	600 km
Apogee height	60530 km
Semi-major axis	36943 km
Eccentricity	0.8111
Inclination	59°
Right Ascension of the Ascending Note	84°
Argument of Perigee	188°
Orbital Period	19h38m
Launch Date	4th quarter 2018

Table 5.1 *Orbital parameters of the Occulter Spacecraft (OSC). Credit [39]. Note: Launch date updated October 2015.*

being less than 30° as illustrated in figure 5.6. The relative navigation is expected to be performed at a maximum distance of 5 km down to around 25 m, where the most critical performance is at distances below $200m$, were a 6DOF solution should be available.

With the VBS operating in cooperative mode the $-X$ face of CSC, with the LEDs mounted, is required to be oriented towards the OSC, with an off-axis angle below 20°. This is due to the excited radiation of the LEDs is designed to subtend a maximum half cone angle of approximately 20°.

At current time there is no strict requirement on the orientation of the CSC with the VBS operating in non-cooperative mode. Only the angle between the axes

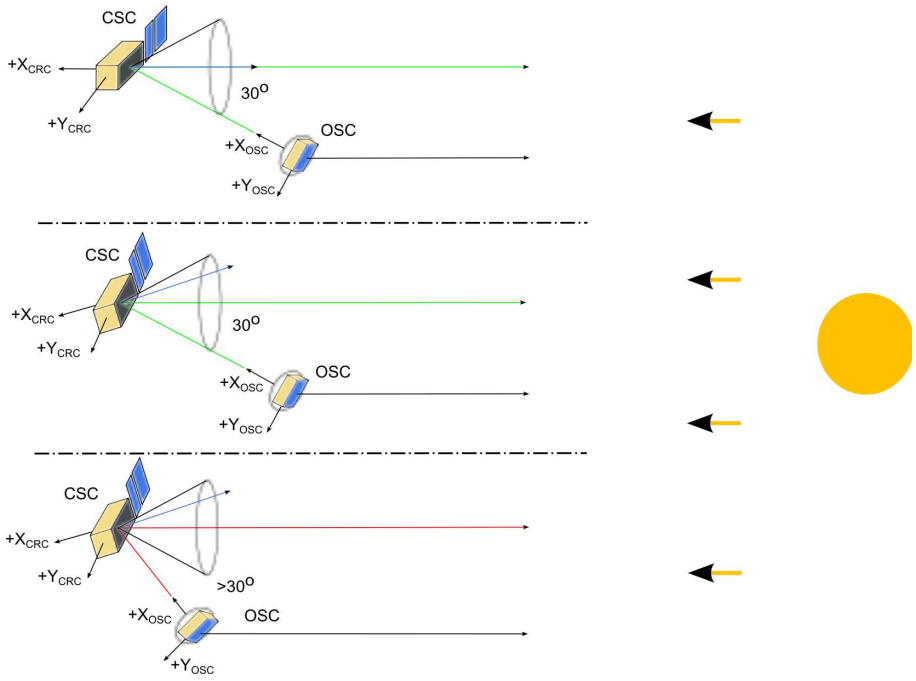

Figure 5.6 *The operational envelope is described by a* 30° *half angle cone defined by the Sun-OSC-CSC angle where the top two illustrations are within the operational envelope and the bottom outside the envelope.*

$-X_{OSC}$ and $-X_{CSC}$ is restricted to be within 60°. In terms of a RVD scenario , this is a rather large deviation from the nominal state where both axes are aligned. When planning an RVD scenario, the approach is always synchronized for optimal lighting conditions, i.e. with the Sun-CSC-OSC angle close to a few degrees.

With the requirements of Sun-pointing, as stated above, a scenario where Earth might enter FOV of the VBS-CHU can occur. Considering a circular orbit, this will only be the case when approaching the target from -R-bar. However, with a highly elliptic orbit, such a scenario will depend on the time of year for when conducting the RVX and non-cooperative tracking at close quarters. In order to scope this thesis, it is assumed that by careful planning and timing of critical mission phases facilitate optimal lighting conditions where Earth in the background is considered an off-nominal case. Thus, for the remainder of the thesis, it is assumed that only the single non-cooperative S/C target is within the sensors FOV.

5.4.3 Properties of Target Spacecraft, CSC

The target spacecraft consists of a rectangular body and a solar array with approximate dimensions of $1.5x1.2x1.0m$ and $1.5x1.6m$, respectively. An overview of the spacecraft structure is illustrated in figure 5.7 where additional views are

shown in appendix A. The front optics of the scientific payload is approximately at $[-0.5, 0.7, 0.6]m$ where an optical bench goes through the spacecraft body and attaches to the triple CHU star trackers on the X_{CSC} side. As a result this part of the spacecraft will be in the shadow of the Sun during the scientific measurements. In addition four thruster pairs are mounted on the $-X_{CSC}$ face of the body. The mechanical interface to the fairing the OSC is seen on the $-ZCSC$ and $+Z_{CSC}$. Note that the normal of the solar array is slightly angled from the $-X_{CSC}$ axis so that optical sensors observing from the OSC are not blinded by the reflected sunlight.

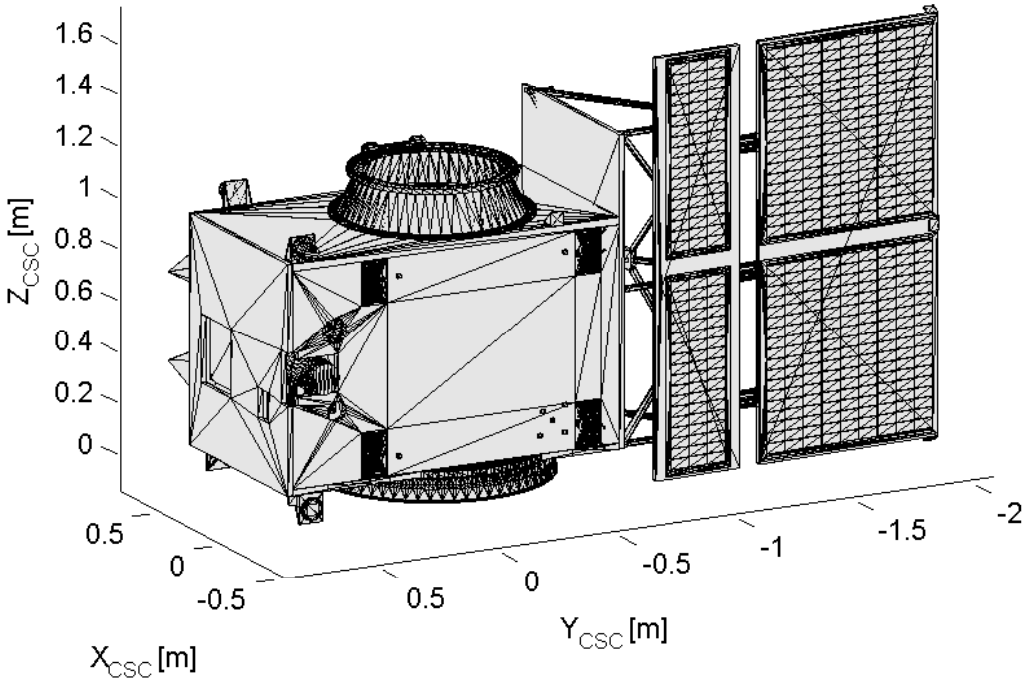

Figure 5.7 *A 3 dimensional triangulation mesh extracted from a CAD model of the Coronagraph Spacecraft (CSC). This frame considered the body reference frame of the CSC.*

In the process of designing and building a spacecraft structural elements and instruments can be expected to be moved around. This is a natural consequence of a continuous process that narrows down the design to fit all components and still comply with requirements and budgets. This fact presents a challenge in designing tracking software as the shape, materials and optical properties of the target are not necessarily frozen at the time of designing the software. However, the overall shape of the spacecraft is to a large extent maintained throughout the process. The overall structure thus constitutes the most reliable descriptor of the target.

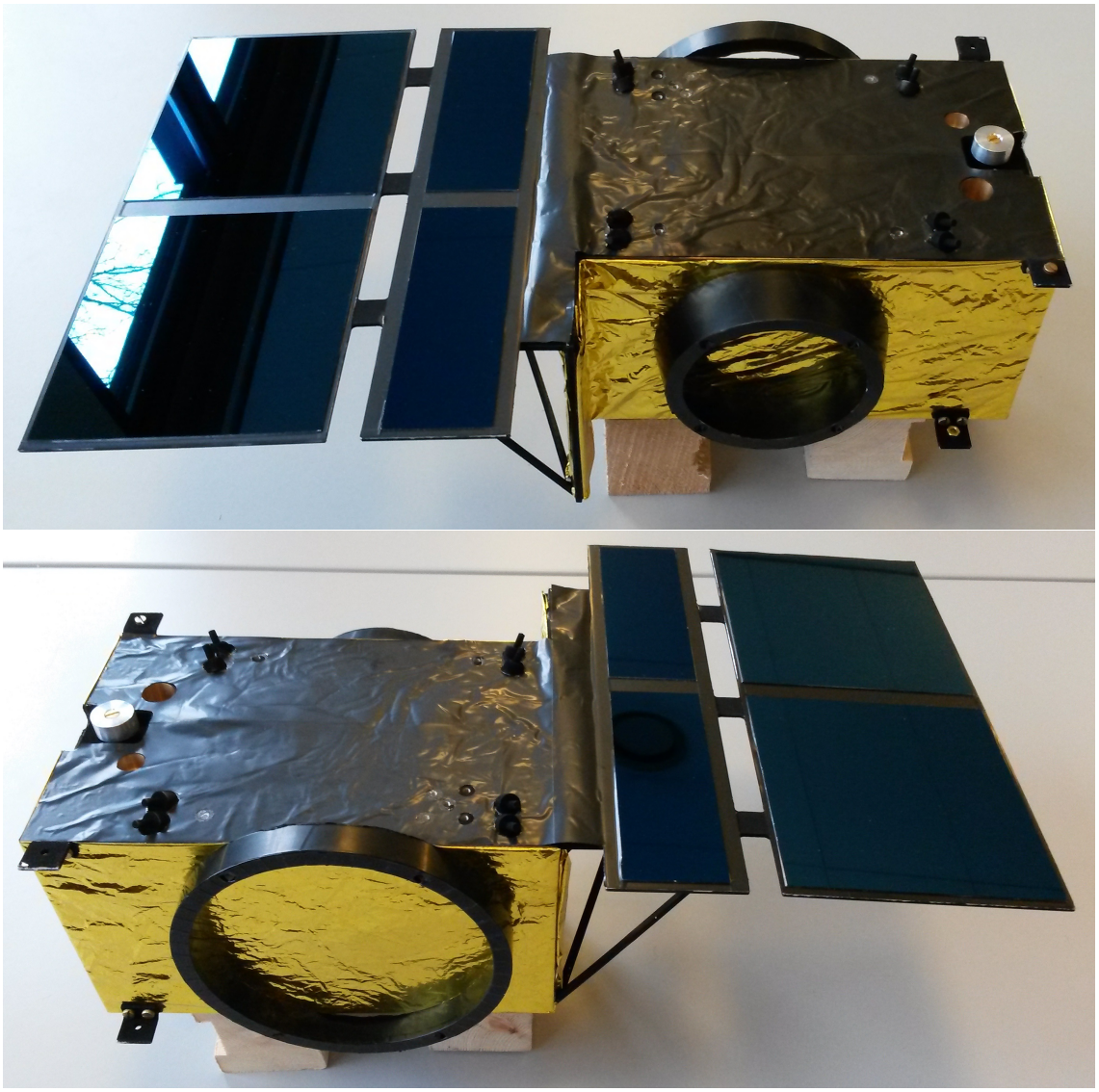

Figure 5.8 *A 1:7.15 scaled mockup model of the Coronagraph spacecraft.*

A 1:7.15 scaled mock-up model of the CSC was build in late 2013 in connection with a preliminary study of a non-cooperative tracking of the CSC. The manufacturing of the model was based on expected surface materials and available CAD model at present time, as shown in figure 5.8. The body of the CSC is covered in Multi Layer Insulation (MLI), with exception of optical apertures and antennas. The Sun facing side is covered by black MLI and the remaining body is covered in shiny MLI. The structure supporting the solar panels is black together with the mechanical interfaces to the GPS antennas, fairing and OSC.
Observing the mockup model, the optical properties of MLI is specular in nature and the texture has an undulating character. The reflected light varies substantially depending on the angle of illumination and the angle of observation. The mechani-

cal interface and structure of the solar panel appears to have a diffuse reflection and make up a firm and even texture, resulting in a fairly robust signal to track.

5.5 Method of Approach

The approach of the target tracking is based on the general principles described in chapter 2, where it is sought to meet the stated objectives of non-cooperative tracking. In the following an overview of the tracking approach is given together with a flow diagram of the overall process in figure 5.9.

The two modes of *Target Acquisition* and *Target Tracking* are implemented, where each mode seeks to accommodate the objectives of robustness, timeliness and accuracy. The initial mode of *Target Acquisition* deals with establishing a sound and robust solution of the relative pose. The process of establishing the initial lock is cumbersome and is not likely to comply with the requirement of 1Hz update rate. However, as this is only the initial mode, this requirement is relaxed. Once the lock is acquired, the process will continue in the *Target Tracking* mode. In the *Target Tracking* mode the prior relative state of the target is utilized so a thorough correspondence search to obtain the correct match is not needed. Thus, the *Target Tracking* will comply with the update rate requirement. In addition, the *Target Tracking* is optimized for an accurate solution of the relative pose.

The tracking is initiated by searching for objects using a simple binary threshold, whereafter the features are extracted in a region around each object. Depending on the size of the object the tracking mode will proceed in either *Far Range, Intermediate Range or Close Range* mode. The threshold for entering *Intermediate Range* is set to a projected object area of 50 pixels. This set to ensure that the point spread function of the optics does not impose an unwanted bias on the crude range estimate. When in this mode the LOS is measured based on the apparent center of mass and the crude range estimate is based on the apparent area of the target in the focal plane. Assuming the target's solar panels are Sun-pointing and facing the chaser, the projected area of the target is assumed the area of target's $-X_{CSC}$ face. The crude range measure will be imposed by a relatively large bias due to unknown orientation and unresolved features that can result in a smaller projected area. Assuming a median off-nominal orientation of 30°, the ratio between the range error and the true range will be 0.15, as a result of the diminished projected surface area of the target. Another alternative is to base the range estimate on an expected

average of the projected area of the target, which is appropriate when approaching a tumbling target. The threshold for entering the *Close Range* is an objects area of 2000 pixels, roughly 45 pixels across. At this distance the features are beginning to be defined well enough to resolve a 6DOF pose.

As a consequence of the body being covered in MLI it is challenging to extract any meaningful and robust signal within the body itself. With the most reliable descriptor being identified as the large scale geometry of the target, it is sought to extract large scale linear features, describing the geometry only. Thus, the features will to a large extent lie along the contour. The background will be pitch black when approaching the target from the V-bar and +R-bar which facilitates a strong contrast to the sunlit target. With the Sun positioned behind the optical sensor, the faces of the target that are visible to the sensor, will, to a large extent, be sunlit and not in the shade, as opposed to the case of the PRISMA mission, see figure 5.2.

The most challenging part of the tracking procedure is to resolve the 6DOF relative state of the target when no priori knowledge of the state is available. Which is also the focus in this research. The overall approach of acquiring the initial lock works by a consecutive matching and filtering process of assorting high residual matches from a list of possible viewing directions. Viewpoints that are evenly distributed on a sphere constitute a so called *solution space*. For each filtering process the viewpoint solutions with the highest residuals are discarded and by the end of the process only a few solutions remain. The remaining solutions are stored and propagated as the baseline of possible solutions for the next image. Within three consecutive image frames the list of possible solutions is reduced to a single solution with the lowest residual. Initially, one would be inclined to settle with the lowest residual solution after processing only a single frame. This however, will be an issue when observing the target from a perspective with ambiguous solutions. A way to overcome this is to utilize the incremental change in the pose between two frames to assort the erroneous solution from the correct one. The filtering process consists of five processes that each match the linear features, or corresponding vertexes, with a model of the target. Two models are used: contour lines extracted from a complex CAD model of the CSC body, and a manually generated list of vertexes that define the overall geometry of the target. Each filter reduces the solutions space to the half by discarding the solutions with a residual larger than the median residual. Thus, with 200 initial solutions, corresponding to 12° between the viewpoints, only 6 solutions remain at the end of processing the first frame.

The first and second filter match the lines extracted from the image with a contour database for each of the 200 viewpoints. In order to confine the computational load, an inverse relationship between the amount of information vs. the number of possible viewpoints is implemented. The first filtering process only uses the 3 most significant lines from the image to evaluate the residual, whereafter the solution space is halved, and the second filtering process evaluates the residua,l using all lines from the image. In the third process the residual is calculated based on the vertexes, whereafter the solution space is reduced again. In the last two processes the pose for each solution is refined with a Nelder-Mead optimization, based on the matched vertexes. The principle of inverse relationship, is adopted to the accuracy of the pose optimization and the number of solutions. Where the former optimization is a crude refinement, whereafter solutions space is reduced, and the latter optimization is an accurate refinement performed on fewer solutions.

The methodology of using a finite number of possible viewpoints is very agile as the viewpoints can be adjusted to only incorporate certain attitudes of the target. For instance, if assuming a mission profile where the target will only be viewed from the face with solar panels, the possible viewpoints can be reduced to a hemisphere, thus reducing the computational load and avoiding some ambiguous solutions.

In the following paragraphs each step of the tracking process is described in detail.

5.5.1 Model of Target

As for any tracking approach, a suitable model of the target is made, to which the extracted features need to be matched with. Following the approach of only relying on the geometry of the target a typical approach is to construct a simple line model as reported in [40, 35, 41]. Such a model is easy to construct and serves as a good representative for large scale linear features. This simplistic model is usually manually constructed on the basis of a subjective interpretation of the target. For instance a line model of the CSC can be simplified to a solid rectangle with two planar rectangles attached. The shortcoming of such a model is the lack of details. The circular shape of the fairing interface and details of antennas and instruments, poking out of the body, are not included. Thus, these elements will break the linear contour of the simplified model. An effort has been made to generate a model that encompasses the actual linear features of the contour, regardless of the origin, and without compromising the computational load.

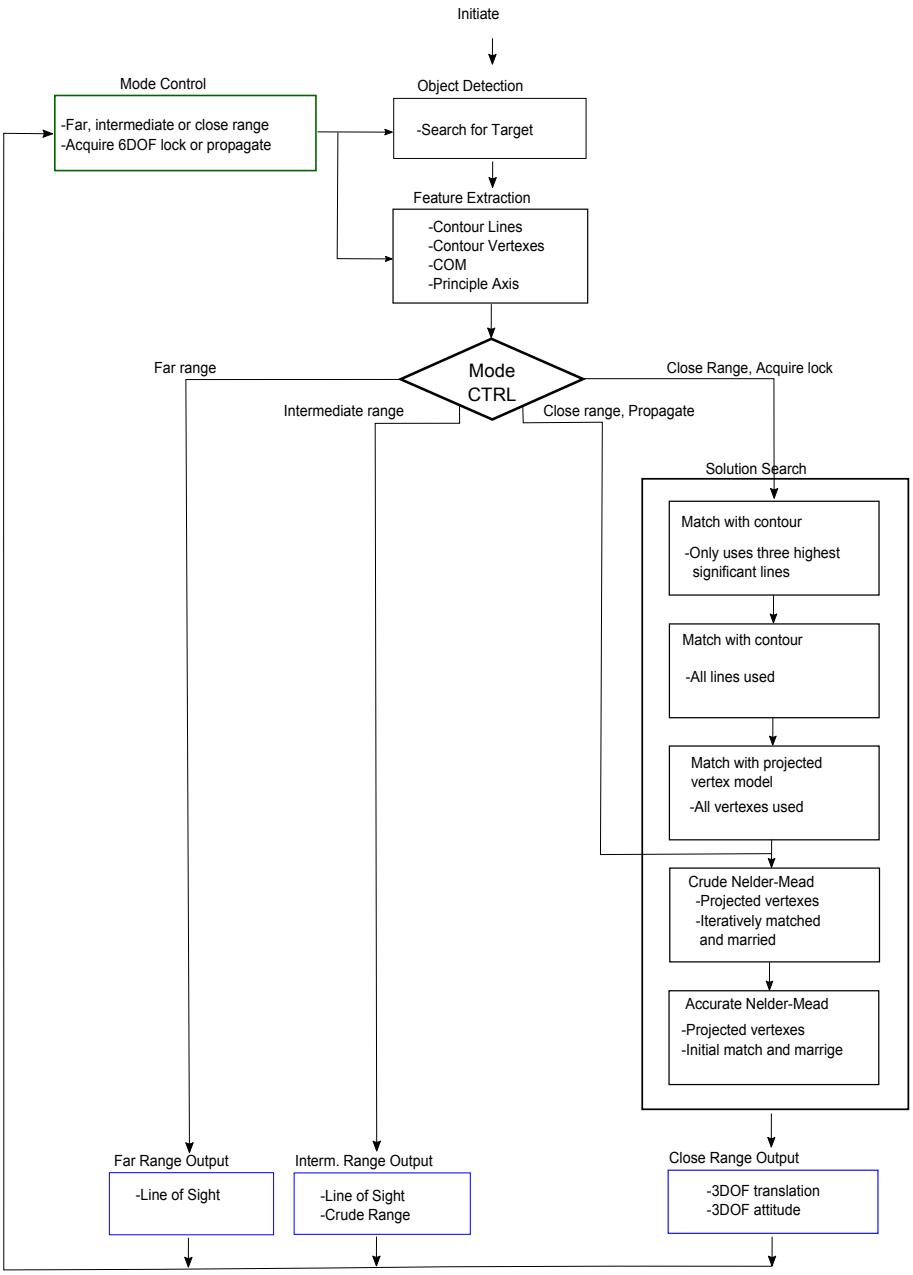

Figure 5.9 *Flow chart of the overall tracking principle.*

The most reliable model of the geometry is a complete mechanical CAD model of the target spacecraft, where all mechanical parts are accurately represented. Representing the CAD model by a triangulation mesh, will resulting in no less than 500,000 vertexes. This is excessively detailed and so a reduced mesh of less than 10,000 is used where the geometry of the model is retained and only small scale elements are distorted. For each sample of an evenly distributed set of orientations, the pathes of the mesh model are orthographically projected and merged to construct the contour of the model. The lines of the projected contour of each orientation are

stored, ready to be loaded when needed for the initial matching. Storing the set of contour lines for each orientation removes a large portion of the computational load, as the rotation and translation of a complex 3D model does not need to be manipulated on the fly. The stored contour data is normalized according to the apparent center of mass. An example of 200 evenly distributed samples of viewpoints, with about 12° apart, is shown in figure 5.10 together with an example of the contour from the projected CAD model. As shown in the figure, the true contour is a mix of linear and curved trends. The 20 longest lines of the true contour are stored, - the rest are discarded. This has the objective of discarding small and curved features, and restrain the computational load for the process of matching the model and the extracted features. The contour data-set is normalized to the apparent center of mass for scale independency.

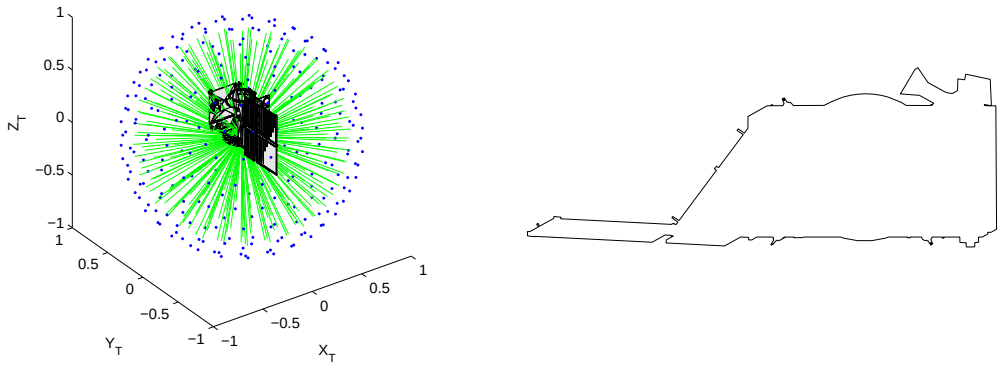

Figure 5.10 *The left plot shows the orientation of the boresight in the frame of the target. The example shows 200 evenly distributed orientations along a unit sphere. The right plot shows an example of the contour generated from the orthogonally projected CAD model.*

In addition to the contour-line data-bank, a general list of vertexes are manually chosen according to a simplistic solid- and planar rectangle. With the pose being iteratively refined, the vertex model serves the purpose of further reducing the computational load, once an initial pose is established.

5.5.2 Features

The large scale shape of the CSC mostly consists of a variation of polygons. Some circular shapes are represented by the mechanical interface to the launcher and the nozzle of an apogee kick motor. When projecting these to the focal plane these shapes are represented by lines, vertexes or arcs. The vertexes constitute

the simplest feature being defined by two coordinates only. A line needs two or four parameters, depending on the line being represented in polar form or with endpoints. The arc is represented by a minimum of three or four parameters when formulated as a circle or ellipse, respectively. It is critical that the formulation of the features are as simplistic as possible in order to minimize the computational effort. Both when formulating the features, but also in the subsequent processes of matching and pose refinement. Examining a sample image of the mockup in figure 5.11 the information in the contour is dominated by linear features and it's vertices which are the ones sought extracted.

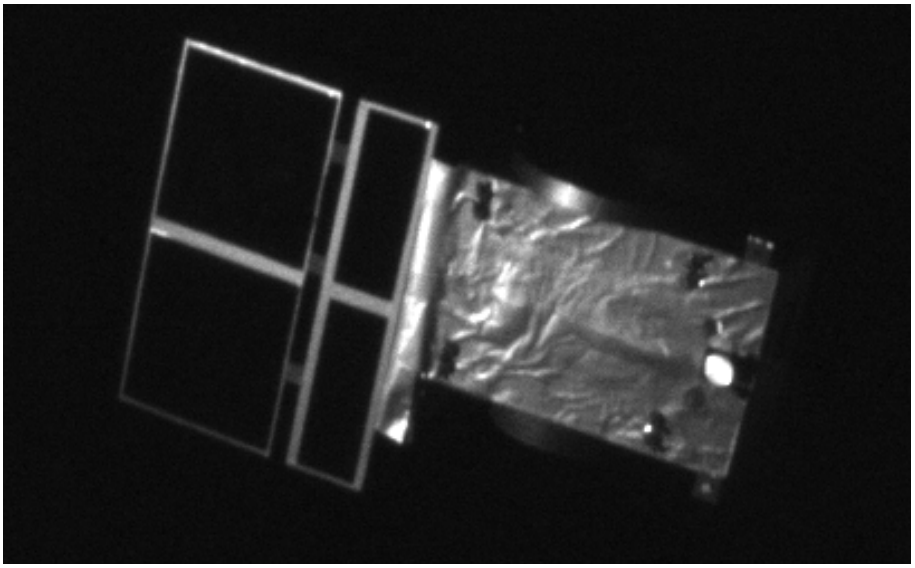

Figure 5.11 *The mockup model imaged in the Calibration and Validation facilities at DTU Space by a microASC CHU with a 12 mm focal length.*

Contour To extract the signal of the features the most simple approach is to register pixels who's DN is above a threshold that is defined by the background level. This seems a valid approach with a pitch black background. However, the intensity of the target is not at a constant level. This will especially affect the registering of the solar panel's edge. In figure 5.12 different binary thresholds are used. It clearly shows that the edge of the solar panel vanishes at a threshold level that is useless to detect the body itself. Locally adaptive, or dynamic, thresholds can be considered for a better registration of the target body. But this method still lacks the capability of detecting very low intensity features of the solar panel as seen in the lower left edge in figure 5.11 and right edge of the target in figure 5.12. More advanced dynamic thresholds is not a viable approach as the computational effort will be extensive already at this stage of the processing.

The magnitude of the gradient, shown in figure 5.13, reveals that there simply is very little information in the image to detect the complete edge of the solar panel. Setting a very low threshold for the gradient magnitude typically results in an increase of false edge detections. Assuming that the true weak gradients are in extension of strong edges, the false edges can be assorted from the true ones. This is essentially what the Canny edge detection method does, where two thresholds are used to detect strong and weak edges, followed by a hysteresis detection of the true weak edges [42]. The resulting edge detection is shown in figure 5.13 where the left most edge of the solar panel is detected. The Canny edge detection clearly proves a strong method for the edge detection, but it is not without cost due to evaluation of the gradient. Naturally it is not necessary to process the full image with the Canny method, only a Region of Interest (ROI) is processed. The ROI is defined by the binary detection of the object. In addition it the area within the object detected by a high binary threshold is naturally excluded for edge detection. Superimposing the data from Canny's method into a binary image data essentially gives a well defined contour of the target, see left plot of figure 5.13. Based on the superimposed Canny and binary data the contour of the target is extracted by a simple 8-connectivity search along the rim of the binary object. An example of the contour is shown in figure 5.13.

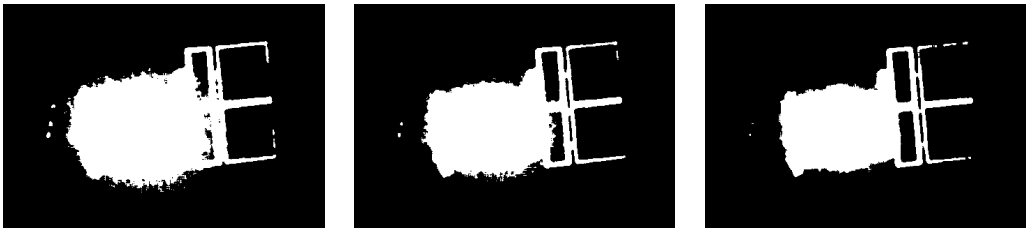

Figure 5.12 *Binary threshold defined by a multiple of the standard deviation of the intensity in the image. From left to right the factor increases from 3-5.*

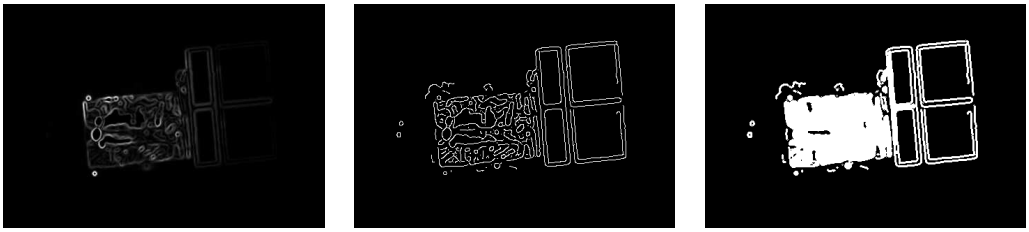

Figure 5.13 *Left: The gradient magnitude. Middle: The image processed by the Canny edge detection. Right: Binary threshold and Canny edge detection are superimposed to detect the silhouette of the target.*

Line Extraction A cluster of data points do not by them selves tell much which is why the contour data needs to be grouped into lines. The Hough transform is a powerful approach but can be sensitive to the resolution of ρ and *theta* making up the Hough space. Instead, a more deterministic approach is chosen where linkage between the data points in the contour is exploited [41]. The contour is recursively subdivided into segments where the division is defined by the data point deviating the most from the linear trend of the segment data. The linear trend of each segment is defined by the segments' endpoints. The division repeats until there are minimum 4 data points in each segment where each segment is given a significance described by $s = \frac{l}{d}$, where l is the length of the segment and d is the maximum deviation from the linear trend. Then, unwinding the recursion a decision is made whether to replace the lower level segments with the single higher level segment. If any of the subsegments have a higher significance than the higher level segment, the subsegments are returned. If not, the single higher level segment is returned. With the segment process done, only the segments with a significance above 4 are preserved, the rest are discarded.

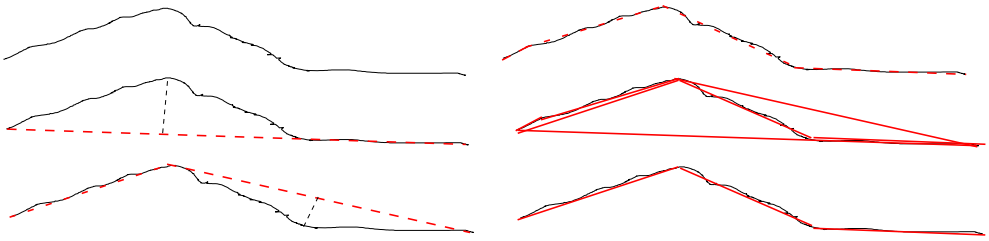

Figure 5.14 *An example of the recursive line segmentation. The order of the process is column wise, starting from the top-left. Dashed lines represent the recursively divided line segments. The final solid lines represent the resulting line segments. Credit: Illustration adopted from [41]*

Accurate Edge Extraction The discrete data points that constitute the line segments are at this point defined by the size of a pixel. This is not very accurate and thus the coordinates of the data points are adjusted according to the curve of the local gradient. The peak of the gradient is found by estimating the peak of a quadratic curve based on three gradient magnitude samples extracted along the direction of the gradient. The coordinate for the peak replaces the coordinate of the data point at hand. This process is stable for well defined edges. But as the edges of the target's body are irregular, due to the MLI, only a delta value of 2 pixels is accepted. Otherwise the original coordinate is preserved. With the accurate edge identified, the data is finally corrected for lens distortion.

Accurate line estimate So far the linear trend of the line segments have been defined by the end-points of the segment's data set. With the data points defined at sub-pixel accuracy the trend is formulated by a linear least square fit.

Line Merging As the recursive segmentation exploits that the contour data points are linked, large scale linear features can be broken by an instrument or antenna. Therefore, lines that can be considered representing the same edge are sought merged together. Starting with the most significant lines, they are merged by a set of criteria that checks for co-linearity, parallelism and end-point proximity:

- The angle between the base line and the compared line shall be less than 10°.
- The distance from the mid-point of the compared line to the base line shall be less than two pixels.
- The distance between the closest endpoint of the compared line shall be less than half the length of the base line.

Following the merging process, the lines are filtered to assort the significant lines from the spurious and random insignificant lines. In order to be invariant to the size target in the image, the filter thresholds are based on the distribution of the significance and number of data points representing the lines. The thresholds are set to half of the median for both measures. This ensures that when the target is small and few lines are extracted the vast majority of the lines, if not all, are preserved, and when the target is large the majority of insignificant lines are discarded. The result of the merging process is shown in figure 5.15 and will constitute the baseline of linear features. Note that the example in figure 5.15 has a "broken" contour due to the weak edges of the solar panel. this is case likely to appear, and thus an implementation must be robust against such artifacts.

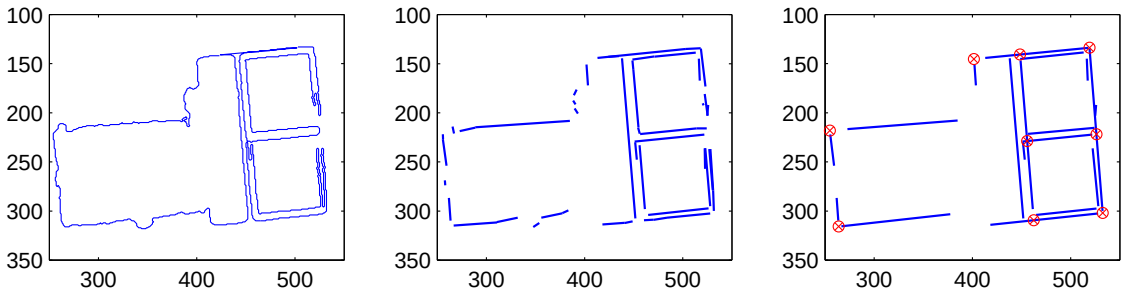

Figure 5.15 *The contour data points are segmented to 149 linear trends in the left plot. After merging the line segments the number is reduced to 25 line segments, plotted on the right.*

Vertexes Based on the baseline linear segments a set of intersections are found that constitute the vertexes between the most significant lines. These vertexes are very valuable when seeking to optimize, or refine, a pose solution candidate. Because of the single coordinate, the matching, and residual is straightforward when compared to matching line segments. Furthermore, the computational load is substantially reduced. Based on the following criteria a set of vertexes are extracted, with the objective of only using meaningful and significant vertexes.

- The angle between the two line segments must be within an interval of $[20° : 160°]$
- The distance between a vertex and the closest end-point of a line segment must not be more than the line segment itself.
- The vertex must not be outside the original ROI of the target.

Extracting vertexes using the above criteria, there is the chance of two vertexes being in close vicinity of each other. Here, $\frac{1}{10}$ of the target's size is considered close vicinity. To choose between the these vertexes the significance of the lines is used. The vertex' significance is formulated as the sum of the lines' significance that constitute the intersection, and thus the vertex that has the highest significance is chosen and the other discarded.

5.5.3 Solution Space Filtering

The process of matching the extracted lines and vertexes to the corresponding part of the model is one of the main challenges of the non-cooperative tracking. As introduced in the section 5.5, when initiated in the acquisition mode the challenge is to identify the correct correspondence among a vast number of false positives which is a cumbersome and computationally intensive process. Having acquired a lock on the correct match and pose, the prior solution is forwarded in the tracking mode, where the vast search of the possible solutions is not necessary, only the process of refining the pose solution is performed.

Being initiated in the *Target Acquisition* mode, the default solution space consists of 200 viewpoints uniformly distributed around a sphere. For each viewpoint a set of contour lines are available in the database. The linear features from the image are matched to the contour. Processing 200 viewpoints will be cumbersome, when considering a contour data-set of 20 lines and a set of 10-30 lines extracted from the image. To constrain the computational load, it is presumed that the most

significant line from the image is present in the contour data-set, and is thus chosen as an anchor-line. The anchor-line, together with the three most significant lines, are consecutively translated and aligned with each of the 20 contour lines. For each alignment, a score is calculated to quantify the quality of the alignment. The alignment with the highest quality is chosen as the match for that viewpoint in particular. This procedure is conducted for all viewpoints, whereafter the half of the solution space with the worst quality is discarded.

The quality of the match between two lines is based on the product of the angle between the lines α, and the distance, d, that is the projected distance from the midpoint of line A to line B, as illustrated in figure 5.16. This product considers how well the lines are aligned, thus the lower the score, the better the alignment. However, this approach does not consider the proximity along the lines themselves. Therefore, if the projected line from the midpoint of A falls outside the end-points of line B, then d is defined as the distance from the midpoint of A to the closest end-point of B, noted as d_1 in figure 5.16.

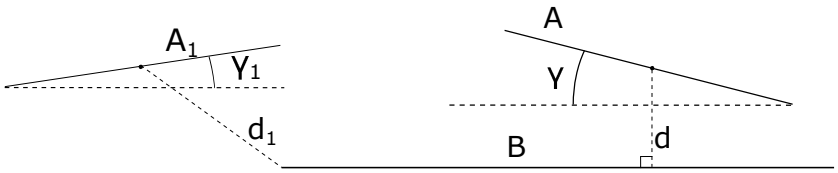

Figure 5.16 *The quality of the match between two lines is based on the product of the angle and the shortest distance from the midpoint of the comparing line A to the reference line B.*

The process of matching the linear features with the contour is conducted once again, only now the quality of the match is based on all lines from the image, whereafter the solutions space is halved once again. Having the solution space reduced to a quarter of the original size using linear features and the contour, the filtering shifts to the use of vertex features and a vertex model projected on the focal plane based on the remaining viewpoints and estimated crude range. Although, the lines constitute good features, the use of vertexes has significantly fewer calculations in the process of calculating a match score, by only calculating a two dimensional euclidian distance. This will especially be advantageous when iteratively refining the pose estimate.

The initial matching between the image and model vertexes follows the scheme known as the marriage problem, where the vertexes are paired so that they mutually are each others best match. The quality of the match is based on the average residual

for each of the matched vertex features. Again, the solution space is halved, leaving an 1/8 of the original solutions to be forwarded for pose refinement. In appendix B, an overview of the solution space and corresponding viewpoints is illustrated for each filtering process.

5.5.4 Pose Refinement

At this stage of the processing none of the solutions are fitting well with the model due to the discrete samples in the solution space. The remaining solutions are refined in two stages using a Nelder-Mead optimization process [43]. The former is a crude refinement, whereafter the half of the solutions are discarded. The latter is an accurate refinement with significantly lower thresholds for exiting the optimization process. During the crude refinement the conditions for matching the image and model vertexes might change. Therefore this matching scheme is based on the Iterative Closest Point algorithm [44], where the vertex matching is performed at every iteration. With regards to the accurate refinement the matching follows the principle of the marriage problem and is only performed once.

The choice of using a Nelder-Mead optimization process is mainly due to the derivative free process that requires fewer evaluations for every iteration. As this procedure will be carried out when in the *Target Tracking* mode it is essential that the pose refinement process is completed within the given time frame. Optimizing for a 6DOF pose, a simplex of 7DOF is constructed, which the Nelder-Mead method is more than capable of handling. The residual from the matched vertexes in the image and the projected model is formulated as a two dimensional euclidian distance in the image plane. The cost function is based on an L^1-norm of the vertex residual, as opposed to an L^2-norm. This is due to the L^1-norm being less sensitive to outliers. In the case of an erroneous extracted vertex feature, or an erroneous match between the image and model vertexes, a L^2-norm will be more influenced by the outliers. In addition, each vertex residual is weighted by the corresponding significance of the vertex. This weighting improves the robustness and accuracy of the procedure substantially as the optimum solution seeks towards the vertexes that are based on the most significant lines, e.g. the lines from the solar panel. The weighting is essential in order to be robust against instable vertexes extracted from the MLI covered body. Figure 5.17 shows an example of the difference between weighting and not weighting the vertex residual, showing an attitude difference of more than 20°. This clearly shows the importance of including the weighting when refining the

pose estimate. It should be noted that further enhancing the weighting factor, by defining the vertex significance by the lines' product, as opposed to the sum, will reduce the influence of the vertexes from the body too much. It was seen in the dynamic test, presented in section 5.8, that when the solar panel does not present much perspective in the image data, but the opposite end of the body does, the vertexes on the body are essential to maintain an accurate pose. If using a product defined significance, the body vertexes are simply too insignificant to maintain the correct pose. Therefore, the significance of the vertexes is defined by the sum of the two lines' significance.

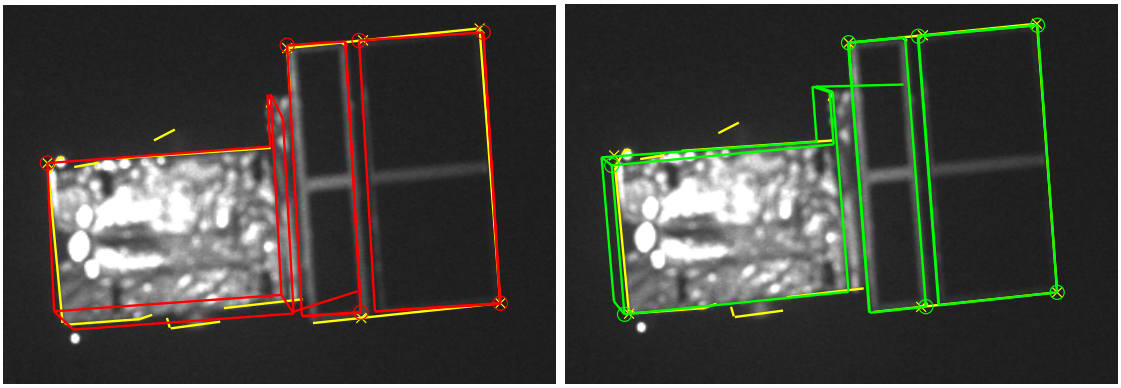

Figure 5.17 *The estimated pose is projected onto the image (green and red). The yellow lines are the features extracted from the contour. The circles indicate the vertexes from the model that are matched with the vertexes from the image, indicated as crosses. The difference in the two estimations is weighting the residual of the matched vertexes with their corresponding significance when refining the pose estimate. Clearly the weighted residual has a better result. The difference of the estimated attitude is more than* $20°$.

5.6 Test Facilities

In order to characterize and verify the functionality and performance of the tracking software, it must be tested with a representative target and scenario. The test scenario is sought to represent the highest fidelity possible within reasonable costs, in terms of physical facilities and associated hardware.

There are mainly two ways to go about testing the tracking software. Either synthetic images of the scene and target are generated by graphical rendering software or a mock-up model is built and staged in a scene with representative lighting.

The former approach is advantageous when limited facility resources are available as the test setup only needs a desktop computer running the rendering software and

tracking software. Furthermore, a well designed rendering software is relatively simple to adjust for testing a large variety of trajectories and mission scenarios. The approach is a viable solution when the rendering is paired with an already developed tracking module to test and verify GNC algorithms [45, 46]. In relation to the Prisma-HARVD (High-integrity, Autonomous, multi-range RVD) study, an optical stimulator (ViSOS) was developed and manufactured with the objective of validating GNC test facilities including the sensor hardware in the loop. The rendering software used within this platform was a package specifically designed to render images in the context of planetary approaches and RVD scenarios [47]. Owing to the inclusion of the sensor hardware within the test platform, a higher level of realism is achieved. Figure 5.18 shows the optical stimulator in use with the DTU's VBS. Experience with the rendered models show that the synthetic images did not represent a sufficient level of fidelity of target's optical properties. The geometry, shadowing and Bi-Directional Reflectance Function (BDRF) of the surface where all acceptable, but the level of detail was insufficient. Furthermore, such as system does not address the de-focussing of the target as a function of the distance. Although, this test platform is not suitable to mature the tracking software for flight performance, it has demonstrated a valuable asset in validating GNC algorithms together with existing hardware and tracking software, that is not too sensitive to the lack of rendered details. For the interested reader, further information and details of the test platform is given appendix C and E.

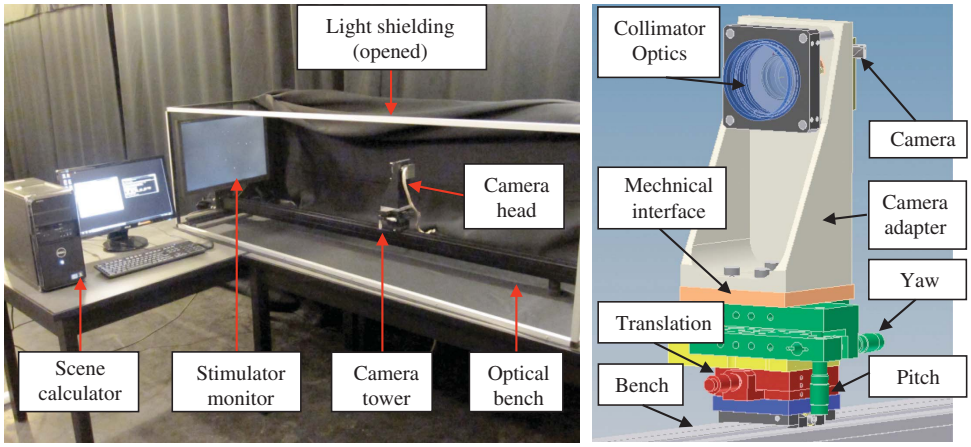

Figure 5.18 *The VBS operating in the optical stimulating test platform, ViSOS.*

The latter approach of building a mock-up model requirers larger facilities and equipment to control the lighting and relative state of the target. But in turn provides a highly realistic scene, as the model is manufactured from the same materials

as the real target and thus, has the same optical properties as the real target. The mock-up model is likely to deviate somewhat from the mechanical drawings when covering the body with MLI. This will also be the case with the spacecraft, although the deviations are relatively smaller compared to that of a scaled model. These deviations are expected to induce a stress on the refined pose estimation and result in a bias. The verification and validation facilities at DTU Space premises constitutes an agile laboratory capable of controlling a CHU in 6DOF and a target mock-up model in 1DOF, operated in close formation [48]. The light sources, used in the CalVal facilities, are of the type Dedolight 400D, that have a close resemblance to the relative spectral composition of Sunlight within the sensitive bandpass of the sensor, see figure 5.19. The facilities feature a scaled 7.15:1 mock-up model of the PROBA-3 CSC vehicle, and a 1:1 mock-up model of the PRISMA tango vehicle.

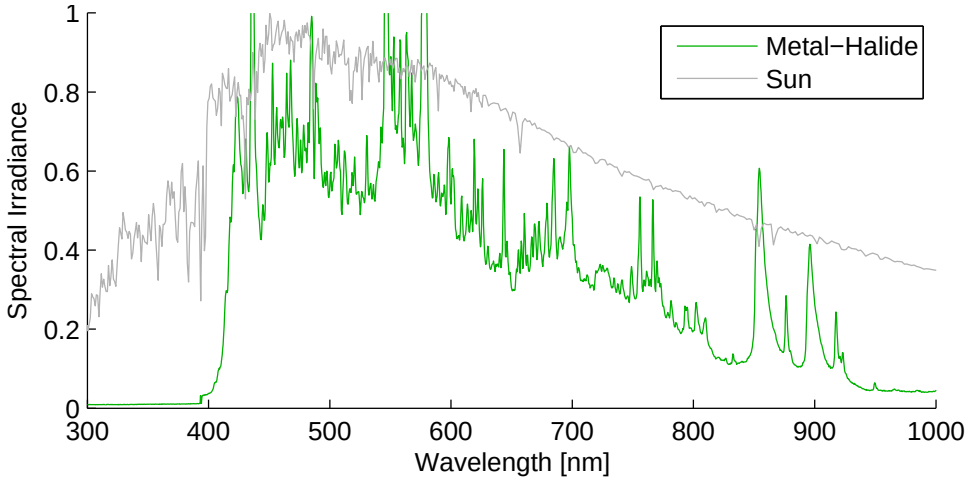

Figure 5.19 *The spectral composition of Sunlight and the Metal-Halide lamp in Dedolight 400D. Credit: A. Massaro, DTU Space.*

The accommodation of the envisaged scene with a pitch black background and the Sun behind the CHU, present a few practical challenges as the light source illuminates the background wall, or blanket, behind the target model. Thus, significantly reducing the contrast between the target and the background. In order to facilitate a representative scene, the light source is slightly angled to $15° - 30°$ from the nominal state, and a simple light-trap is constructed, where the light falling on the background is not visible to the CHU. Now, only the mount, on which the model resides, needs to be invisible to the CHU. For that purpose a custom rotational stand, with the functionality of rotating the scaled model around a $25mm$ steel pole, is manufactured. A PI M-061.PD precision rotation stages is attached to the other end of the pole, for accurate control of a rotation sequence. The rotational

stand is placed so the pole holding the mock-up model is in the shadow that is cast by the model. An overview of the setup is shown in figure 5.20, and an example the scene is shown in figure 5.21.

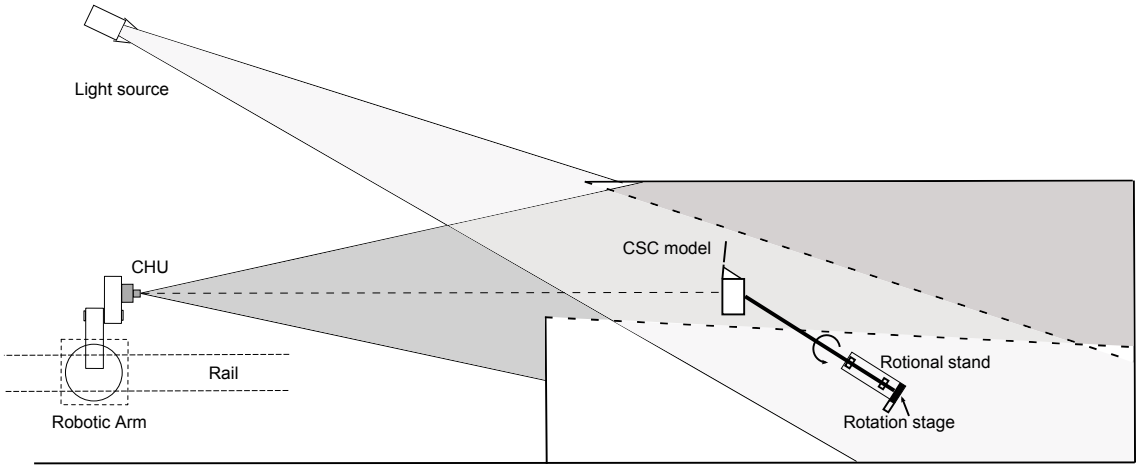

Figure 5.20 *A sketch showing the test setup in the verification and validation facilities at DTU premises. A simplistic light trap is constructed, in order to achieve as large and contrast as possible between the target in the foreground and the background. The CSC model is mounted on a rotational stage that resides in the shadow cast by the model.*

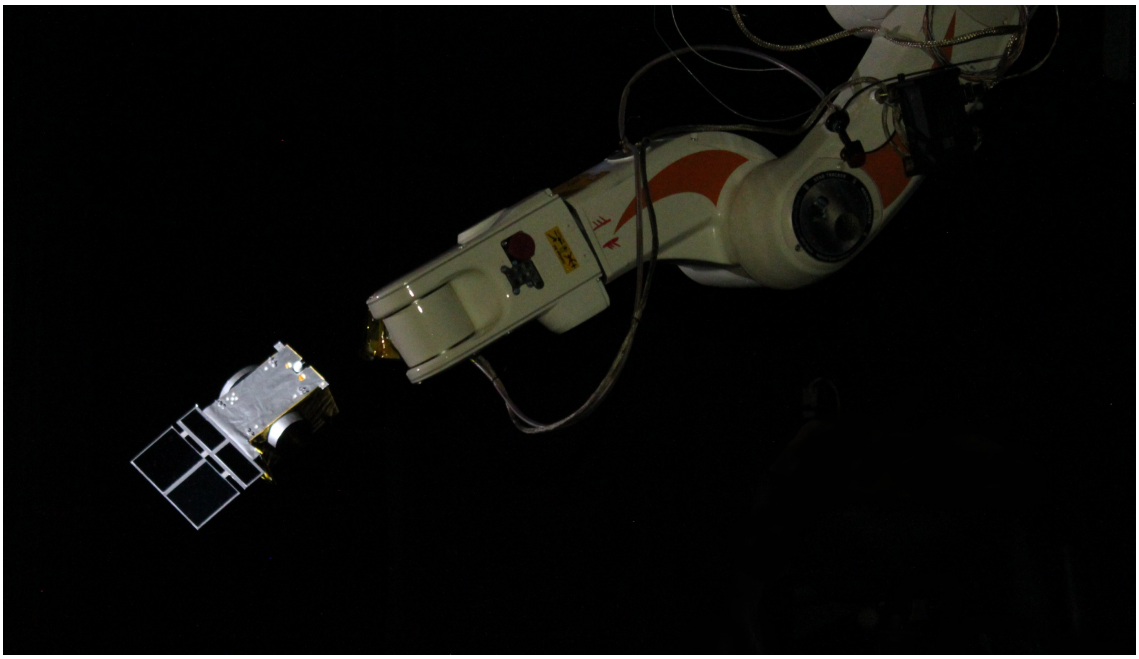

Figure 5.21 *A snapshot of the DTU CalVal facilities in use. The robotic arm with a CHU attached in the foreground and the illuminated CSC model in the background. The illuminated background and the rotational stand are present within the frame, but are not visible.*

5.7 Test Results With Optical Stimulator

The test platform of the optical stimulator is a favourable choice when testing the system at intermediate range, as the need for a large facility is not needed and a trajectory is easily simulated. An elliptical helical trajectory is simulated with the VBS restricted to operate in far range, only delivering the LOS and the target is the PRISMA tango satellite. The result of the LOS measure is shown in figure 5.22. The figure shows a bias taking effect from a distance of around $100m$ and below. At approximately $40m$ distance the LOS is severely influenced by an offset. The offset is a result of the apparent center of the illuminated target body is not aligned with the gravitational center of the target. In the mission profile of PRISMA, the Sun is at an angle of minimum 45° from boresight, which will induce a relatively large offset. In the case of PROBA3, the offset it not considered an issue, both due to the 100mm focal optics and that the 6DOF pose will be resolved before the bias has any significant effect.

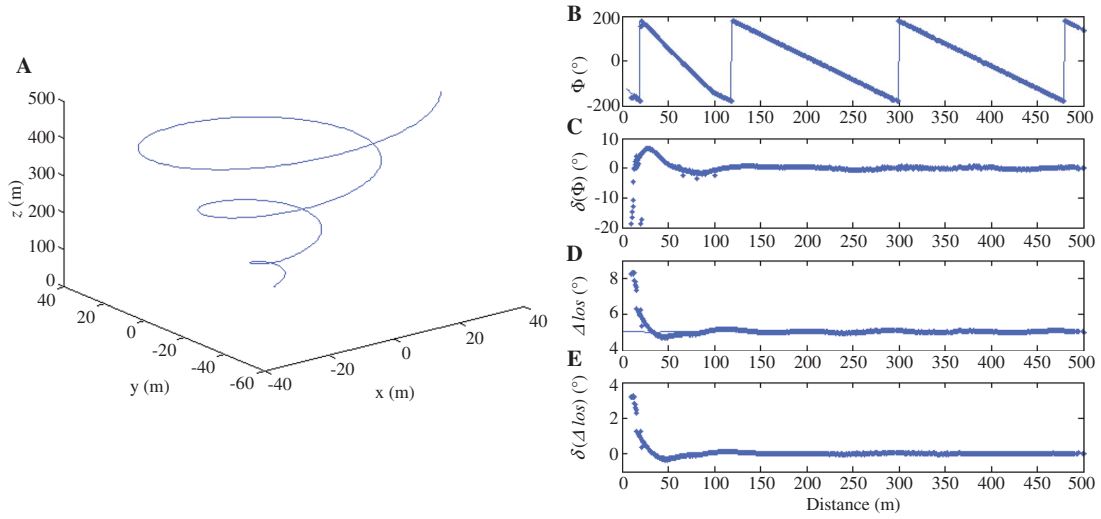

Figure 5.22 *On the left is a simulated trajectory of the chaser approaching the PRISMA Tango spacecraft, seen in the reference frame of the sensor. Angle ϕ is the azimuth on the focal plane of the sensor. ΔLOS is the angle to the boresight. Both angles refer to the center of gravity of the spacecraft. The $\delta()$ values are the angular deviations. Credit: Reprinted from [45]*

5.8 Test Results With Mock-up Model

Using the verification and validation facilities at DTU Space premises a series of static and dynamic tests have been performed to assess the accuracy of the tracking

module. The static tests reveal the accuracy directly while the dynamic test can reveal if any relative bias is present. The test setup is not calibrated to give absolute measurements, but at this stage in the development the relative bias expected from the dynamic test is sufficient to assess the performance.

To describe the pose of the CSC model, relative to the instrument, a set of navigational parameters are defined. The following parameters are all formulated in the frame of the CHU that is assumed a pinhole model relating the 3D frame to the 2D frame of the focal plane. The origin of the CHU frame is the effective pinhole within the lens, where the Z_{CHU} axis is aligned with the CHU's boresight that is defined by the principal point, $[x_0, y_0]$, in the focal plane. The X_{CHU} and Y_{CHU} axes are aligned with the x and y axes of the focal plane, respectively, and complete a right hand Cartesian coordinate system.

All tests are conducted using standard microASC DPU and CHU hardware. In the static tests a 20mm lens is mounted on the CHU and in the dynamic a 12mm lens is used.

5.8.1 Static Scene, Intermediate Range

The accuracy of the pose estimation will strongly depend on the range to the target. In order to assess the accuracy as a function of the range, two test series are conducted where the pose is maintained and the range is decreased at discrete intervals from above $40m$ down to around $2m$. The solar angle, equivalent to the Sun-CSC-OSC angle, is maintained at 29.6° for both series. The tracking is initiated in acquisition mode and will lock on the target within a few frames and thereafter continue forwarding the last known state of the target. The given accuracy is based on measurements where a lock is acquired.

Starting the measurements at at distance of $40m$ a 3DOF solution, i.e. LOS and range, is output from the tracking module. In figure 5.23 the angular variation of the LOS vector as a function of the range is plotted. Generally, at a distance the LOS is well defined and as the range decreases the accuracy of the LOS vector gradually worsens. - As expected due to centroiding a larger apparent area. Note that the accuracy from 35 m and farther starts to deteriorate. This is because of a transitional zone where the edge of the solar panels begin to vanish. Thus, imposing a larger variation. At even farther distances the accuracy of the LOS will improve again as target's projected area diminishes. At no point does the LOS vary more

than 40″ which corresponds to half a pixel.

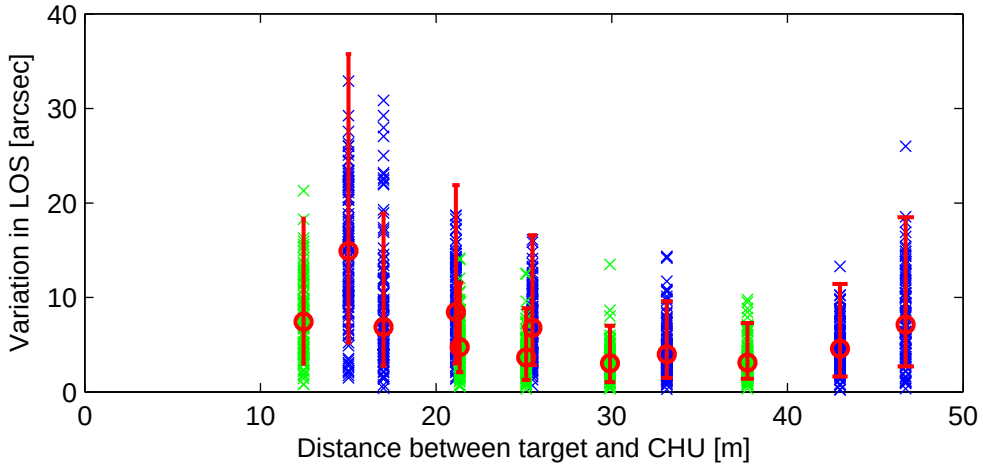

Figure 5.23 *The angular variation of the sighting vector from the CHU towards the target. The colors green and blue indicate two different poses and the red line indicates the* 25%, 50% *and* 75% *fratile of each measurement.*

Figure 5.24 shows the accuracy of the crude range estimate as a function of the actual range, where the accuracy improves as the range decreases. The ratio of the accuracy and the actual range is around 1% over the whole range. This estimate, however, is prone to large biases. To give an indication of this a laser range finder was used to register the actual distance between the target and the CHU. Based on this measure the bias becomes apparent in figure 5.25. As expected the bias depends on the orientation of the target so the crude range estimate will be over- or underestimated. From this test series the worst case ratio is 12% of the true distance. An overview of the accuracy of the LOS and range measurement is given in table 5.2.

5.8.2 Static Scene, Close Range

At close range the target's features are resolved in the image, enabling the tracking module to solve a 6DOF pose. The resulting accuracy of the distance and lateral translation is shown in figure 5.26. The accuracy of the range is within 1% over the entire close range envelope, starting at 0.8% at 12.5m ending at 0.2% at 2.5m. The accuracy of the lateral translation is a few centimeters at the farthest distance and improves to a couple of millimeters at 2.5m.

The variation of the three Euler angles is shown in figure 5.27, from which one can see that the accuracy also improves as the CHU approaches the target. Note

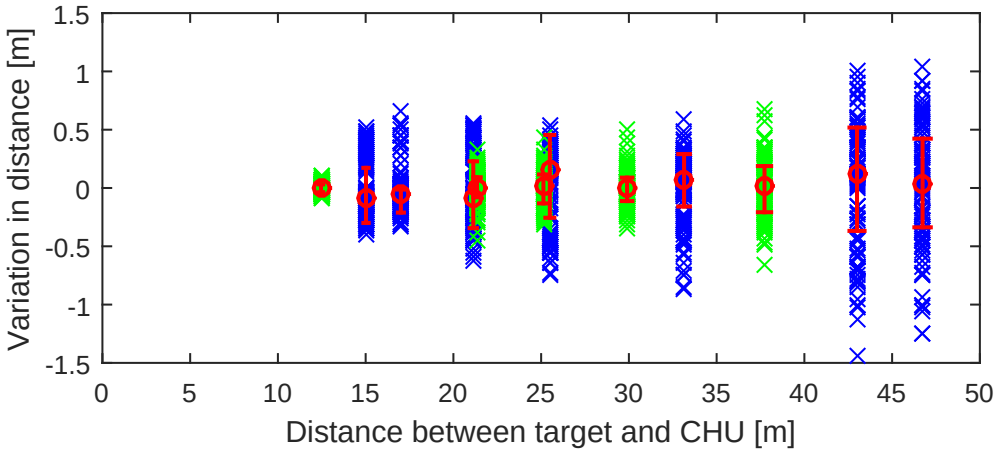

Figure 5.24 *The variation of the crude range estimate. The colors green and blue indicate two different poses and the red line indicates the* 25%*,* 50% *and* 75% *fractile of each measurement.*

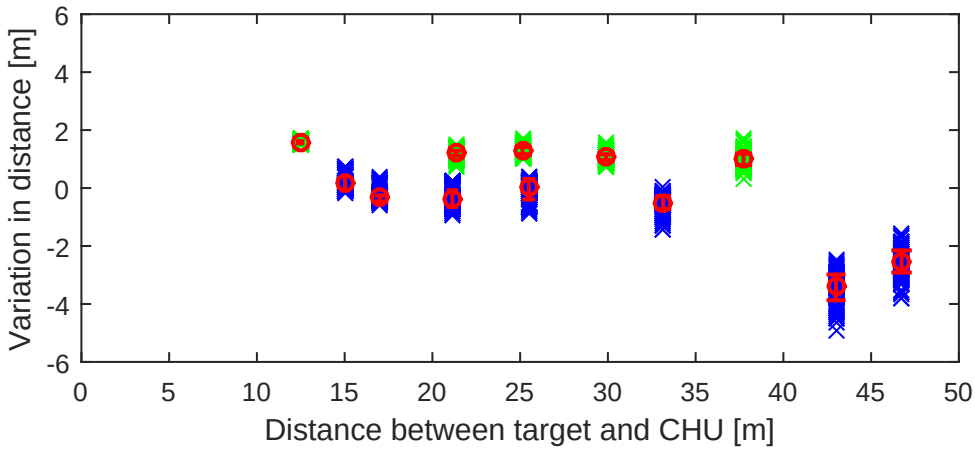

Figure 5.25 *The deviation of the range estimate from the actual range reveals biases. The colors green and blue indicate two different poses and the red line indicates the* 25%*,* 50% *and* 75% *fractile of each measurement.*

that the accuracy of θ is significantly better than the two other rotations. This is a result of target's X axis, see figure 5.7, being closely aligned with the boresight, and thus to a large extent constitutes the instantaneous delta roll angle, which inherently is more accurate than the deltas of pitch and yaw. The reason for this is traced to the distribution of the extracted features, and is further addressed in the following paragraph.

It is noticed that ϕ is slightly more accuracy than ψ, which is counter intuitive as the baseline along target's Y axis is longer than along the Z axis, which should result in the opposite. The reason for this is traced to the properties of target's

Test	True range	Range Error		LOS Error	
	$[m]$	$\mu[m]$	$\sigma[m]$	$\mu[''']$	$\sigma[''']$
A01	46.735	-2.576	0.532	8.032	4.847
A02	43.000	-3.505	0.552	4.997	2.704
A03	33.145	-0.567	0.305	4.601	2.990
A04	25.495	-0.141	0.359	7.136	3.636
A05	21.134	-0.306	0.325	9.123	4.500
A06	17.008	-0.247	0.227	9.234	6.934
A07	15.020	0.228	0.265	14.683	7.036
B12	37.728	1.000	0.255	3.329	2.059
B11	29.898	1.073	0.157	3.243	1.894
B10	25.130	1.302	0.159	3.971	2.251
B09	21.343	1.196	0.135	4.995	2.649
B06	12.458	1.582	0.043	7.942	4.265

Table 5.2 *The accuracy of the LOS and crude range measurement for two static poses at discrete ranges. The error in the range measurements are absolute errors. The LOS is a relative pointing accuracy only, listed with a bias and a standard deviation.*

surface. The baseline along the Y_T axis is defined by the solar panel at one end and the body's MLI at the other. Whereas the baseline of Z_T is defined by the solar panel at both ends. Due to the MLI the edge is poorly defined, thus resulting in a degraded accuracy of ψ, e.i. the rotation about Z_T. The angular variation of target's three axes is shown in figure 5.28. The measurement at 10.6m shows that the solution has a tendency to jump between to solutions. This is because of the lines from the body being poorly defined and therefore the corresponding vertexes either have a very low significance or are simply discarded. This behavior can be addressed using a temporal filter that limits the solutions to a certain envelope defined by the priori solution. But it should be noted that this behavior only appears when close to the boundary for resolving the features of the target. At close range all three axes of the target are defined within 1°. Table 5.3 lists the standard deviation of each element of the 6DOF pose together with the angular accuracy of target's body axes. The table shows that in series A the translation along Y is more accurate than along the X axis, while in series B the opposite is the case. This is due to the target being rotated approximately 90° about the roll axis between the two test series. These numbers reveal that the noise depends on the extended baseline of the target itself. From the target's viewpoint, the position will be more accurate along the Z_{CSC} than along $YSCS$.

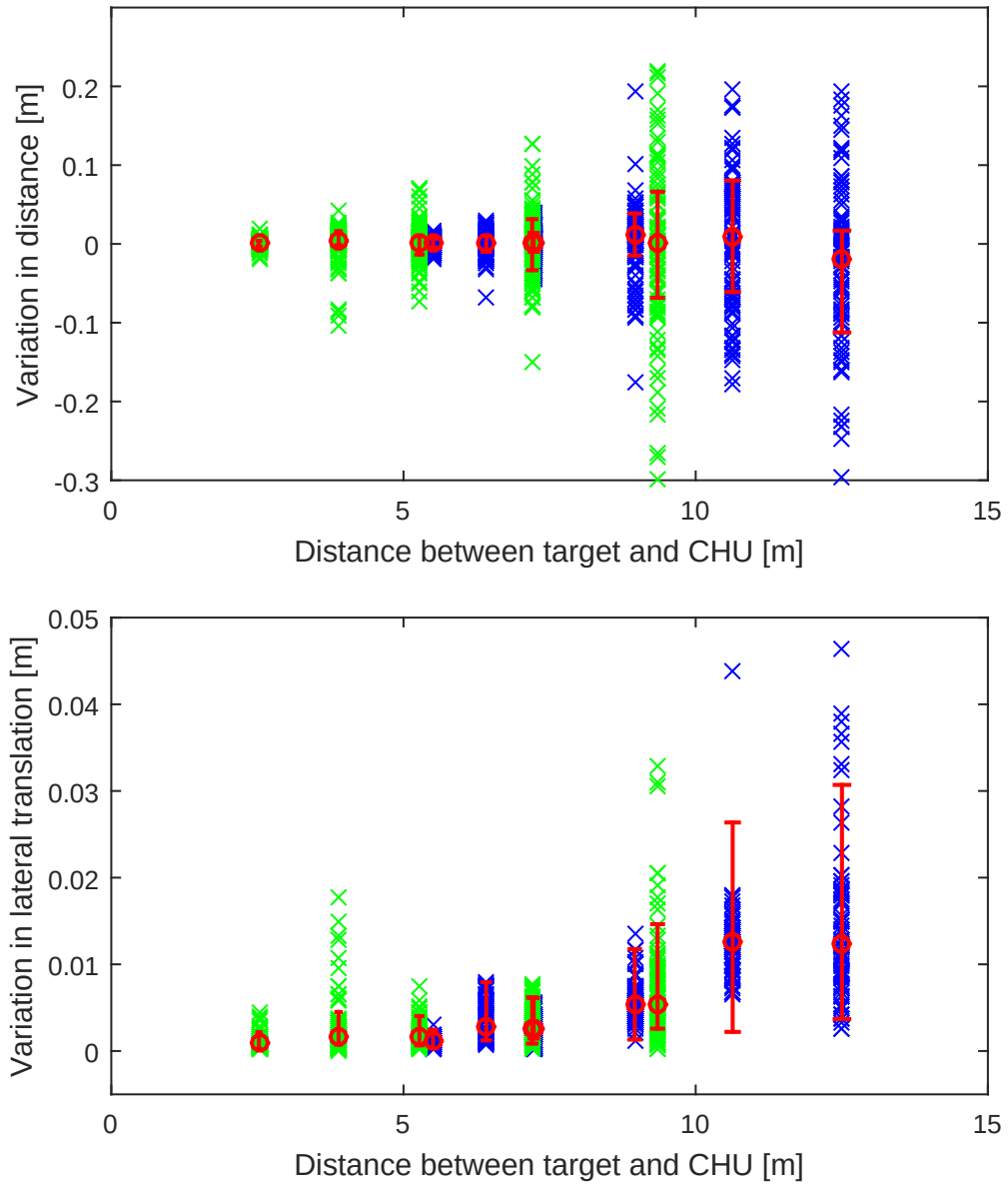

Figure 5.26 *The variation of the distance and lateral translation to the target. The colors green and blue indicate two different poses and the red line indicates the* 25%, 50% *and* 75% *fractile of each measurement.*

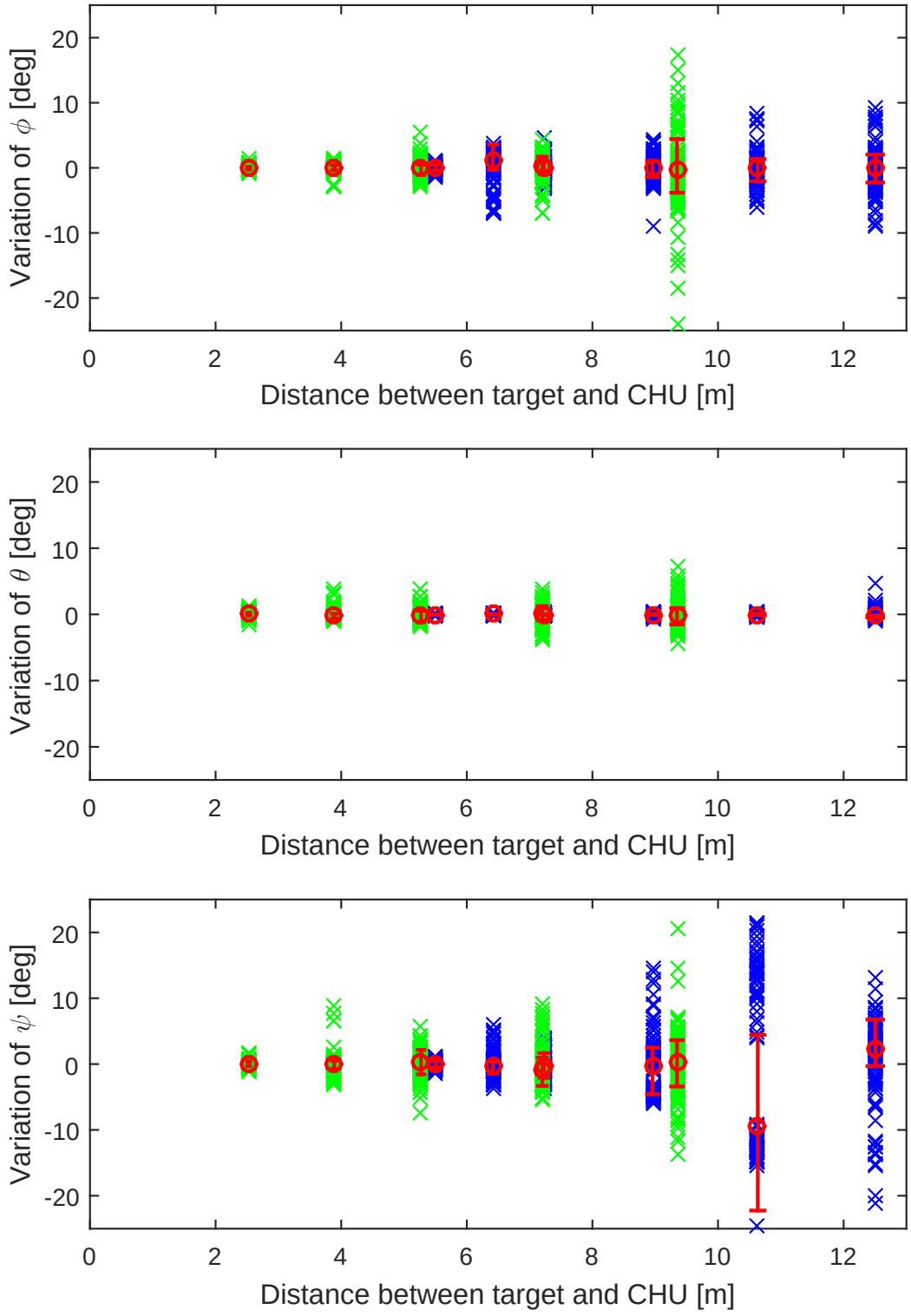

Figure 5.27 *The variation of the three Euler angles describing the attitude of the target relative to the CHU. The attitude is formulated as a $\phi-\theta-\psi$ (2-1-3) rotational sequence. The colors green and blue indicate two different poses and the red line indicates the 25%, 50% and 75% fractile of each measurement.*

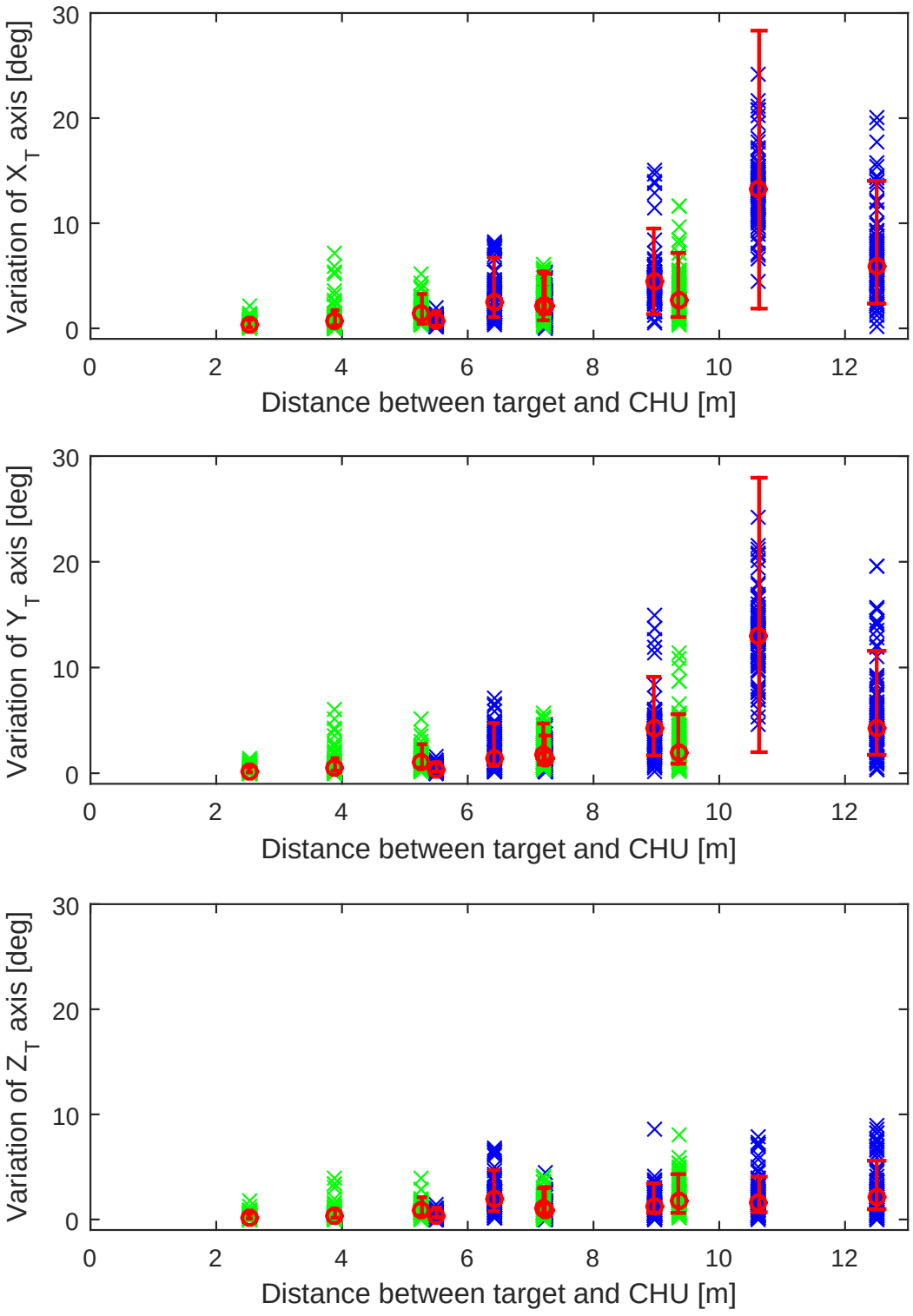

Figure 5.28 *The variation of the axes defining the coordinate frame of the target. The variation of the The colors green and blue indicate two different poses and the red line indicates the 25%, 50% and 75% fractile of each measurement.*

Test		Translation [m]			Euler angles [°]			Axes of CSC [°]			Attitude
		X_{CHU}	Y_{CHU}	Z_{CHU}	ϕ (yaw)	θ ()	ψ	X_{CSC}	Y_{CSC}	Z_{CSC}	[°]
A08	σ	9.06e-3	2.06e-2	2.69e-1	3.70	0.72	7.03	4.22	4.50	2.29	4.30
A08	μ	-3.29e-1	1.49e-1	1.25e+1	89.38	17.94	163.57	6.67	5.60	2.75	6.68
A09	σ	5.15e-3	1.24e-2	8.90e-2	2.88	0.15	13.74	3.51	3.74	1.81	3.45
A09	μ	-1.68e-1	7.09e-2	1.06e+1	90.94	17.81	178.74	13.43	13.09	2.05	13.53
A10	σ	2.69e-3	5.36e-3	4.94e-2	2.03	0.16	5.09	2.78	2.87	1.26	2.70
A10	μ	-2.56e-1	6.65e-2	8.96e-0	91.05	17.86	183.59	4.75	4.29	1.47	4.74
A11	σ	1.55e-3	2.46e-3	1.97e-2	1.71	0.09	2.12	1.34	1.14	1.03	1.41
A11	μ	-1.92e-1	2.68e-2	7.23e-0	93.14	17.85	-182.48	2.11	1.52	1.25	2.32
A12	σ	3.93e-3	1.29e-3	1.54e-2	2.90	0.08	2.04	2.24	1.81	1.61	1.95
A12	μ	-1.38e-1	2.57e-2	6.42e-0	95.84	18.05	-181.01	3.18	2.07	2.23	2.94
A13	σ	8.45e-4	8.07e-4	7.50e-3	0.60	0.05	0.59	0.30	0.31	0.31	0.34
A13	μ	-7.06e-2	1.55e-2	5.50e-0	99.08	18.20	-183.84	0.72	0.45	0.48	0.77
B05	σ	9.09e-3	3.34e-3	1.43e-1	6.86	2.06	5.48	2.34	2.34	1.44	5.49
B05	μ	-2.62e-1	-1.45e-1	9.35e-0	167.16	-77.92	124.39	3.33	2.69	2.03	7.10
B04	σ	2.80e-3	1.99e-3	4.73e-2	2.10	1.53	3.18	1.31	1.31	0.94	2.16
B04	μ	-3.45e-2	-1.67e-1	7.20e-0	166.18	-76.98	121.63	2.45	2.11	1.28	3.45
B03	σ	2.06e-3	1.11e-3	2.53e-2	1.38	1.10	2.35	0.92	0.87	0.63	1.51
B03	μ	-1.85e-2	-1.32e-1	5.27e-0	-195.94	-78.02	124.53	1.53	1.23	0.94	2.51
B02	σ	3.40e-3	1.74e-3	2.14e-2	0.70	0.82	1.71	1.09	0.97	0.63	1.53
B02	μ	8.63e-2	-1.21e-1	3.89e-0	9.98	-75.56	-123.30	0.94	0.79	0.56	1.33
B01	σ	1.07e-3	7.11e-4	5.20e-3	0.32	0.35	0.47	0.29	0.25	0.24	0.36
B01	μ	2.94e-3	-1.50e-1	2.53e-0	6.61	-74.83	-121.29	0.42	0.30	0.27	0.56

Table 5.3 *The relative standard deviation of the translation and attitude of the CSC mockup for two static poses at varying distances. In the Axes columns the relative accuracy of each target body axis is listed where a mean and standard deviation describe the angular deviation from the average orientation of the corresponding axis. The same applies for the Attitude column.*

5.8.3 Dynamic Scene, Close Range

The performance reported from the static scene tests gives a clear indication of the precision of the system. However, the static tests do not reveal any offset in the measurements, as the test setup is not calibrated. As the most critical phase of the RVD is when navigating at close quarters, a dynamic test is conducted in order to assess any bias in the relative state of the 6DOF measurements. With the mock-up model of CSC attached on the 1DOF rotation mount, a rotational sweep is conducted from $-50°$ to $50°$, relative to the nominal orientation of the CSC, with an angular rate of $1°$ pr. sampled image. The CSC-OSC-Sun angle is set to $30°$ for this test.

Figure 5.29 shows the relative state of the target in the CHU frame from the instantaneous measurements. This figure shows a lower noise level in Z_{CHU} as the distance increases. This is counterintuitive as the static test cases clearly show the opposite behavior. The reason for this is traced to the distribution of the extracted features, and is further addressed in the following paragraphs. The position of the target's local frame in the CHU frame is shown in figure 5.31 together with an estimated circular trajectory. The estimated trajectory is based on a least square estimated plane normal followed by a least square circle fit. Figure 5.32 shows the absolute deviation of the estimated trajectory and the measurements. The error in the both lateral directions has a standard deviation of approximately $1mm$ while a standard deviation in the Z_{CHU} is $4.4mm$. The deviations in the lateral translation also show a bias shift at around $40°$ rotation.

Using the initial pose measurement as a baseline, the evolution of the attitude is estimated based on the average axis of rotation. The rotation axis is estimated based on the relative attitude known to be $60°$ apart in order to minimize erroneous rotations. Figure 5.33 shows the absolute deviation between the modelled and measured evolution of the attitude where the standard deviation of the attitude is $0.65°$. From this figure a bias shift is clearly visible around $40°$. The bias shift taking place after 40 degree rotation is due to the distribution of the extracted features on the body of the target. In the beginning of the test, the significant linear features are only found on the âĂIJlower-rightâĂİ side of the target, seen from the image in figure 5.30. After a 40 degree rotation, significant features are also extracted on the opposite side of the target body, âĂIJupper-rightâĂİ side, so that features are extracted on both sides of the target body. This results in a bias shift of the pose and also a more accurate pose estimate. This effect is due to the model of the

target not fitting perfectly to the built mock-up model. It is difficult to overcome this behavior in the image processing, but can be compensated for by calibrating the model to the actually built model.

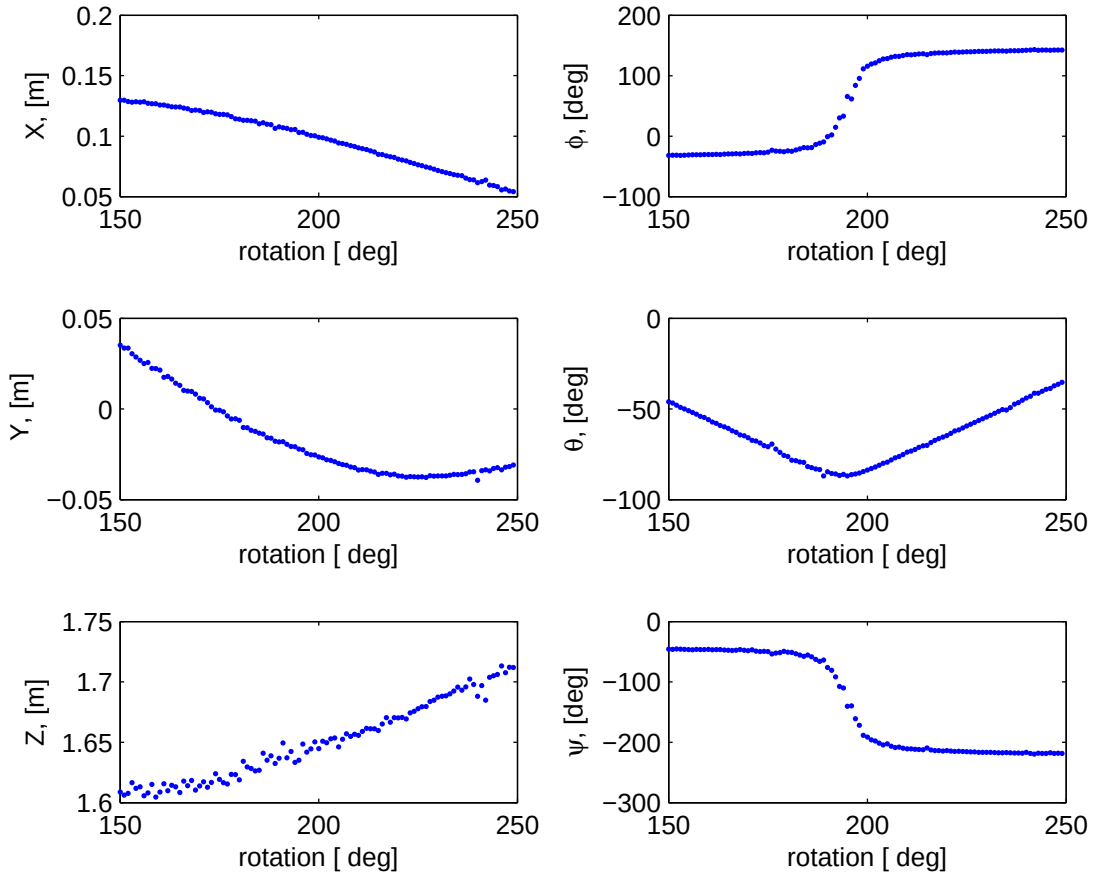

Figure 5.29 *The measured evolution of the CSC mock-up model during a* 100° *rotational sequence, given in the CHU reference frame.*

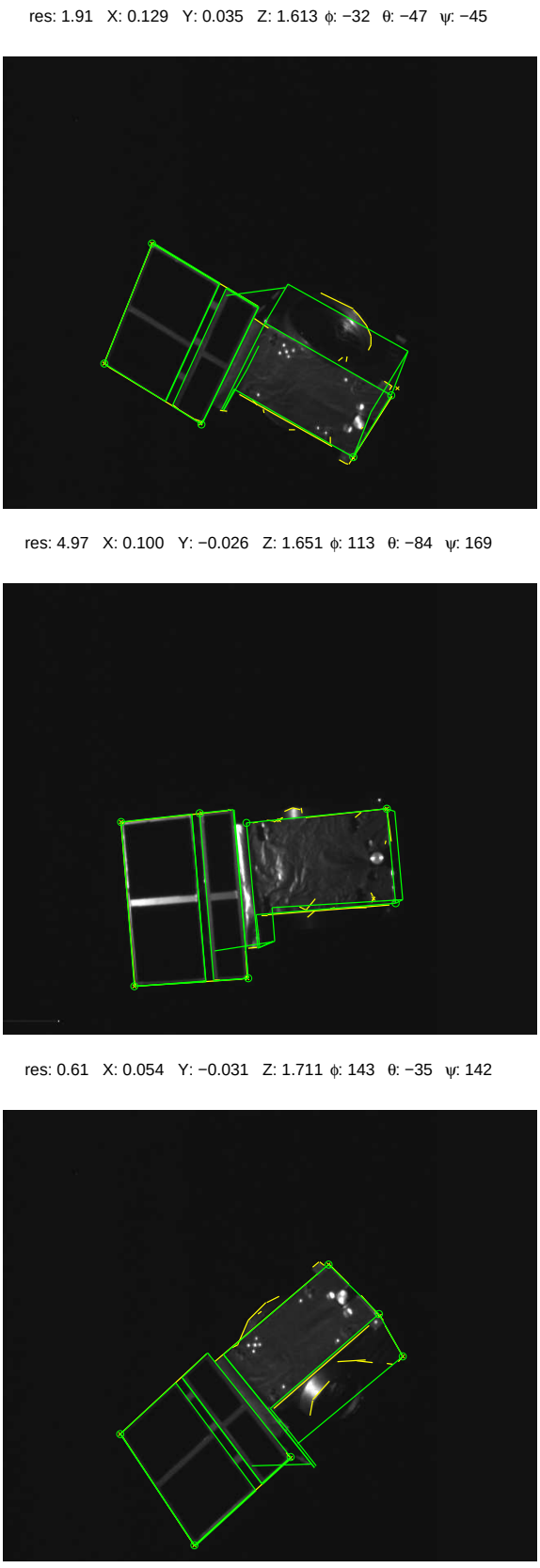

Figure 5.30 *Three instances of the rotational evolution of the CSC model during the dynamic test. The leftmost image is the initial position and the rightmost image is the last position. The yellow lines are the extracted features along the contour and the green lines represent a projected line-model corresponding to the estimated pose.*

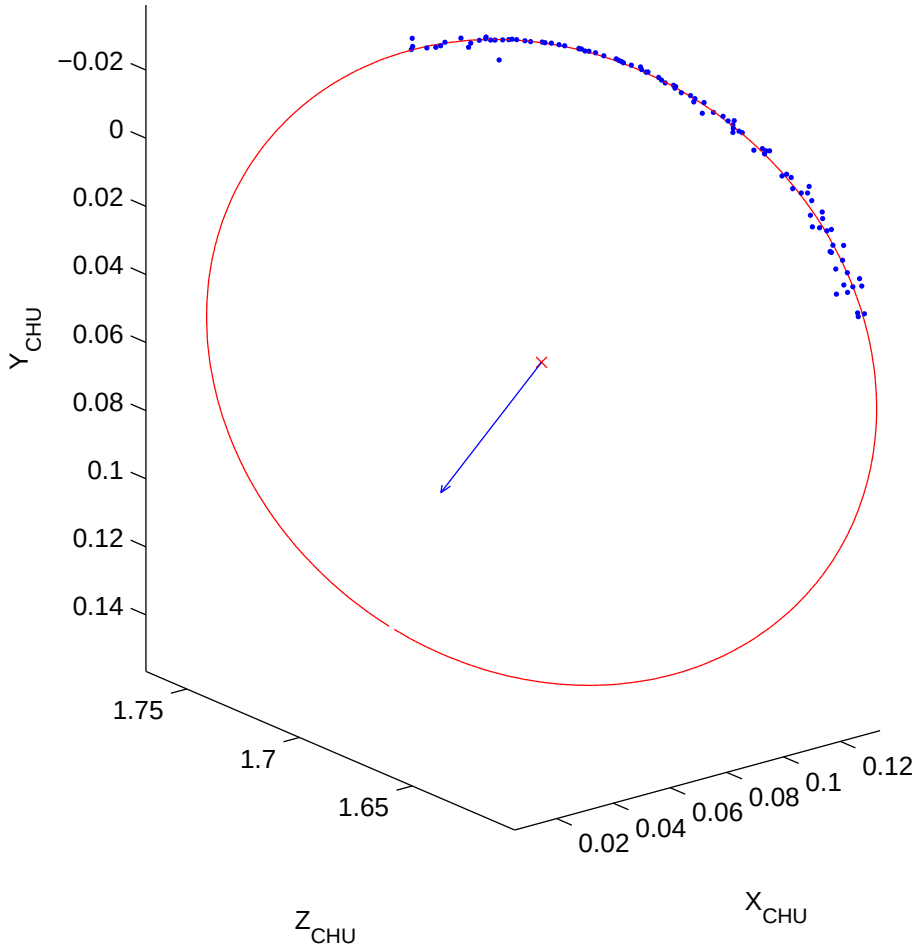

Figure 5.31 *The evolution of the position of CSC mockup given in the CHU frame. A circular motion is fitted to the trajectory together with an estimated rotational axis ω. The circular fit is shown in red and the instantaneous measurements in blue.*

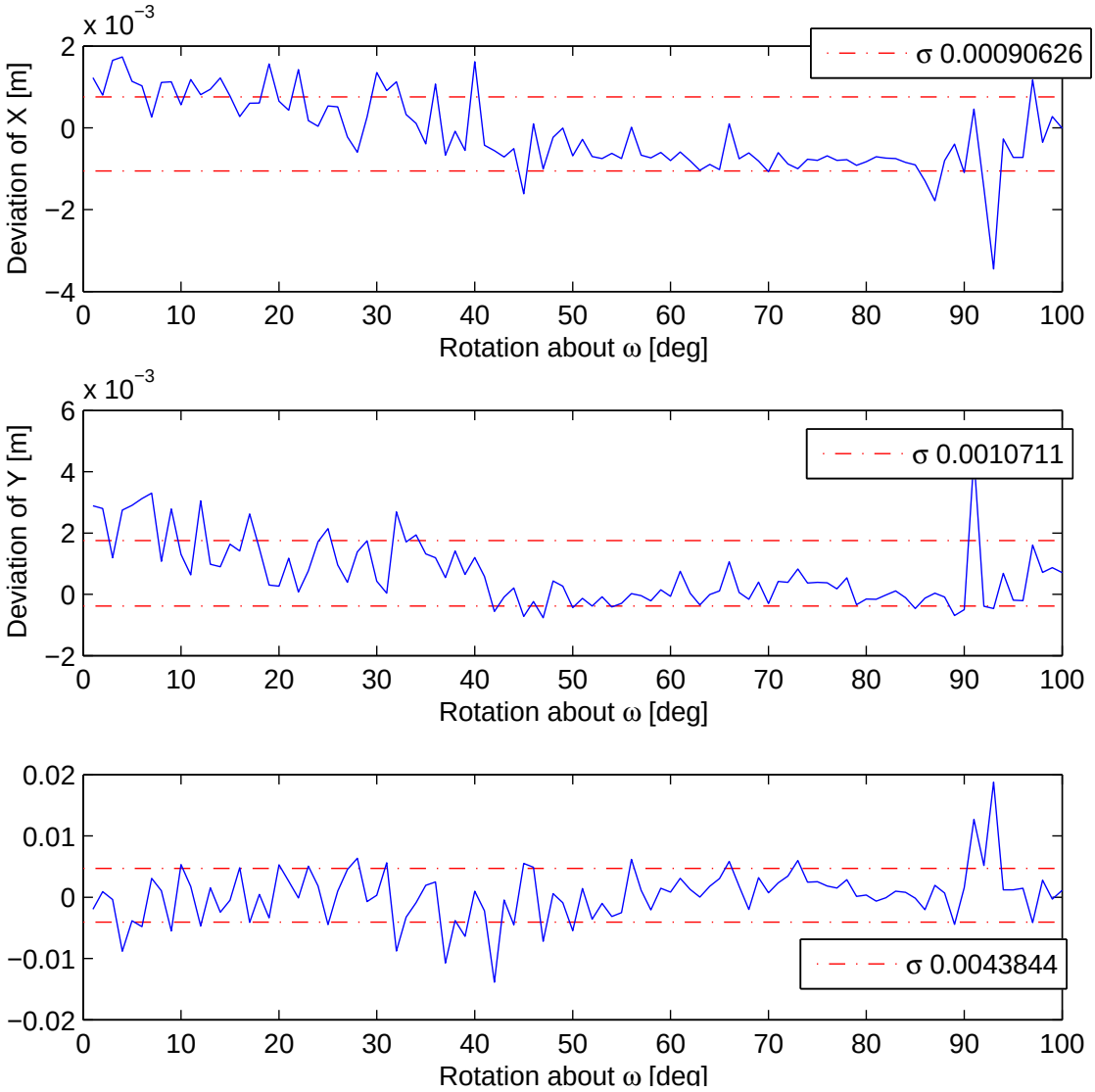

Figure 5.32 *The deviation of the measured and estimated trajectory of the CSC mock-up model.*

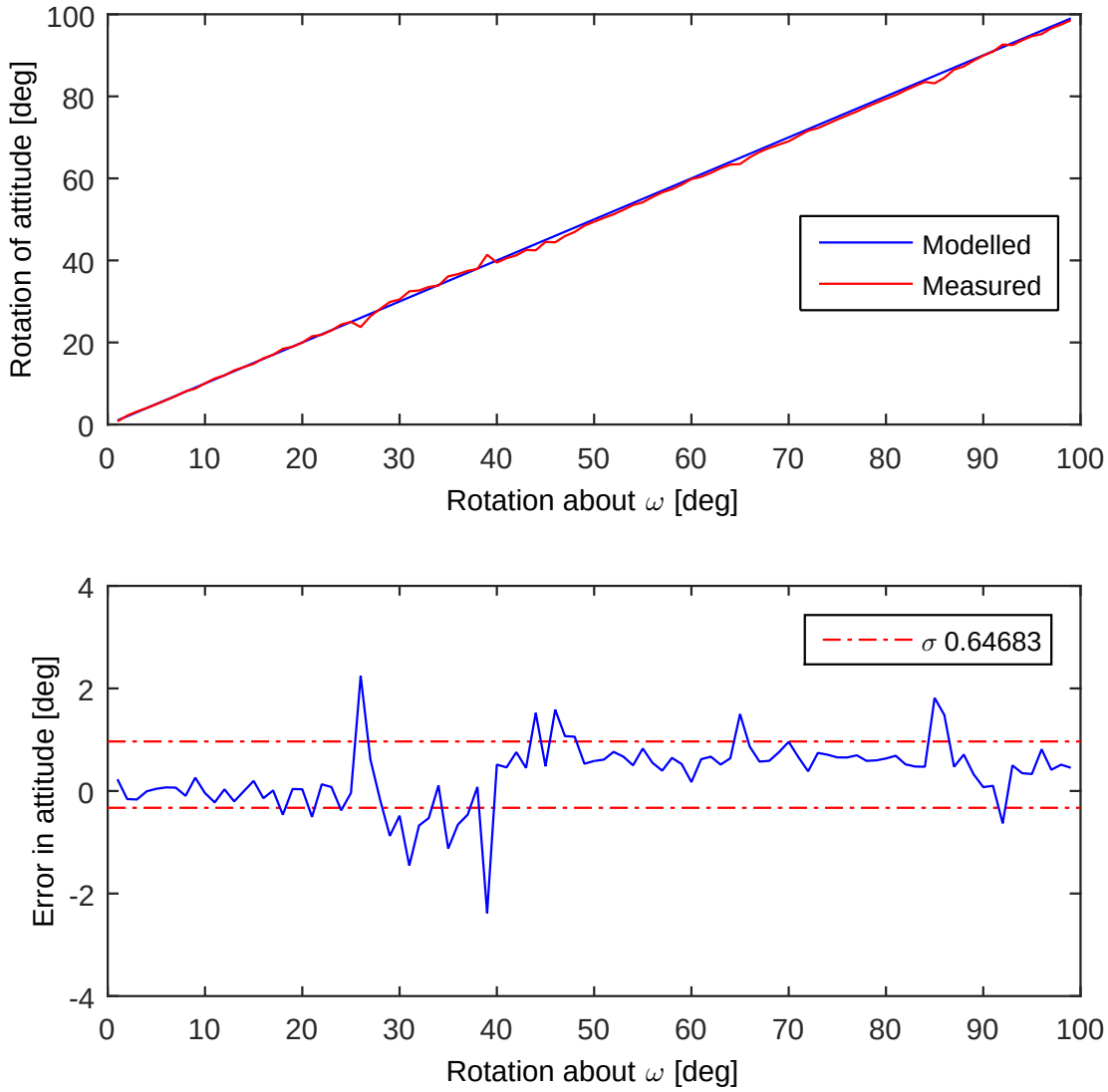

Figure 5.33 *Comparison between the measured and modelled attitude during the rotational sequence. The top plot shows the rotation relative to the initial pose. The bottom plot shows the angular deviation between the modelled and the instantaneous measurements.*

5.9 Performance Summary for PROBA3

Based on the static and dynamic tests with the scale model of CSC, a summary of the expected performance of tracking the actual CSC target using the planned 20mm and 100mm optics is presented. The results from tests are scaled according to the 7.15:1 scale of the model.

In table 5.4 an overview of the output parameters' accuracy is listed. Although, the *Far Range* mode has not been treated in this thesis, as it is described in [11, 49] and has demonstrated excellent in-flight performance on PRISMA mission, the parameter is listed in the table for a complete overview. When in the *Far Range* mode,the target is a dot among the stars and a centroid accuracy of approximately 0.2 pixels ($20''$) is expected. This accuracy has shown to be valid all the way though the *Intermediate Range*. The crude range error will be subject to large biases, depending on the unknown orientation. Here a median angle of 30° from the nominal orientation is used as the baseline.

Mode	Parameter		Wide FOV	Narrow FOV
Far Range	LOS		$20''$	$5''$
Intermediate Range	LOS		$20''$	$5''$
	Crude Range		0.15	0.15
Close Range	Translation	Lateral	5 to 160 mm	5 to 160 mm
		Range	0.002 to 0.02	0.0004 to 0.004
	Attitude	Roll	0.05° to 2°	0.05° to 2°
		Yaw & Pitch	0.4° to 17°	0.4° to 17°
		3DOF	0.6° to 17°	0.6° to 17°

Table 5.4 *An overview accuracy of the measured parameters. The range are listed as percentages of the actual range. The attitude is given as the instantaneous yaw, pitch and roll angles, as seen from the CHU.*

Figure 5.34 gives an overview of the expected operational range for both the narrow and wide angled CHUs. The distances corresponding to an attitude accuracy of 1° and 5° is marked for each CHU. The transition from *Far Range* and *Intermediate Range* is marked where the projected area of the target, including the solar panel subtends an area of 2000 pixels. The dashed lines indicate the transition if only the body of CSC is visible. The figure gives an indication of the interaction between the two CHUs. When the target exceeds the FOV of the narrow CHU, the wide CHU will take over being in the *Close Range* mode. At this translation the attitude accuracy is degraded to around 5° and the range to 0.005. Decreasing the distance

further the performance improves accordingly.

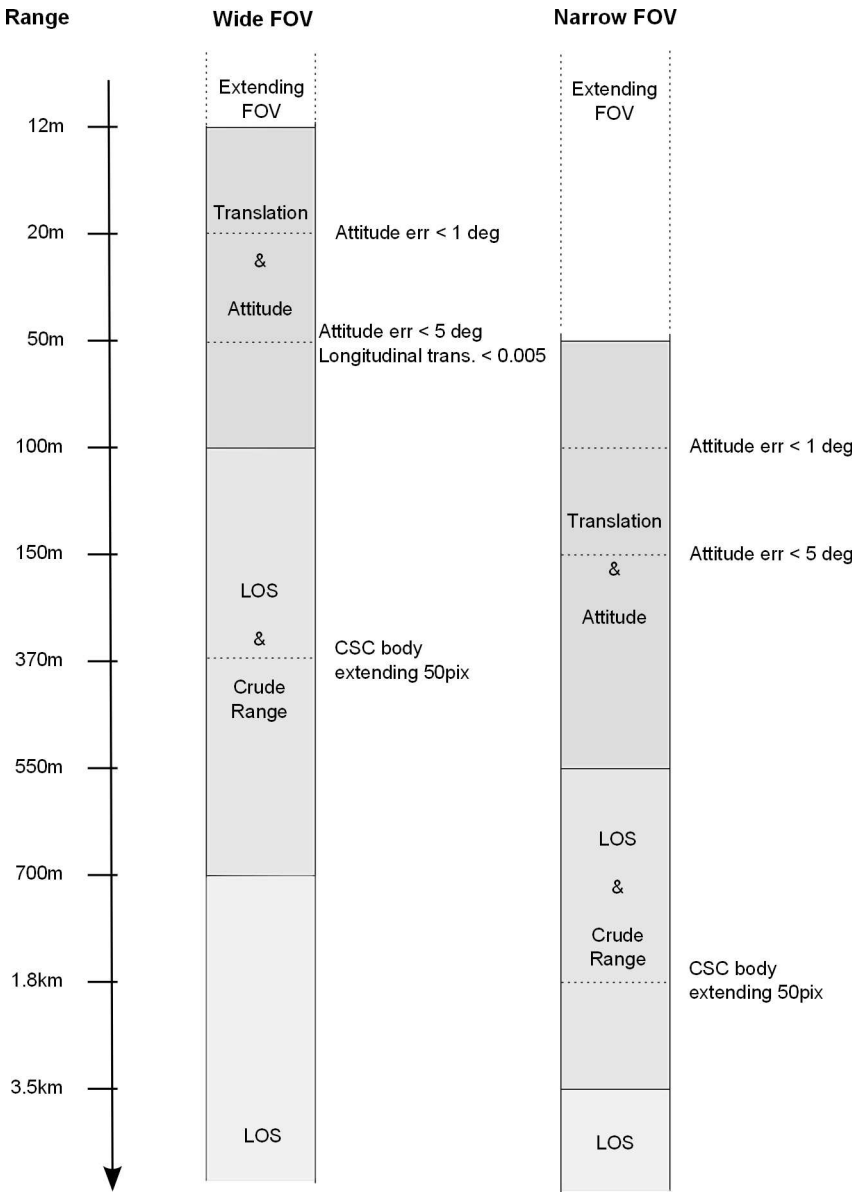

Figure 5.34 *An overview of the measured relative state of the target spacecraft from each of the two optical heads planned for the PROBA3 mission. The range axis does not display as actual scale.*

5.10 Improvements

In the immediate future an implementation of the tracking module to the DPU is envisaged. The method of approach has been designed with the end goal of running on a dedicated DPU. With the preliminary design being functional, an implementation in the DPU is the next step forward.

However, there are some improvements that should to be addressed:

- Sanity checks should be performed to restrain the pose refinement from jumping between two local minimum and verify that the minimum is not an ambiguous or faulty solution. This can be done by algorithms that directly calculate the pose based on a set of matched features, as reported in [11], [50].
- Use a temporal filter bank of the latest measurements to verify that the current solution is within expected values to detect erroneous measurements.
- The approach of extracting features along the contour will not be a viable solution when target extents FOV of the camera. In order to tackle this scenario the tracking should be augmented with the capability of extracting features within the contour that correspond to specific geometries on the target. Such as the apogee kick motor or the mechanical interfaces to the fairing. Depending on the docking or berthing procedure chosen for a specific mission the features need naturally be in FOV from the angle of approach. With this improvement the non-cooperative tracking will have functional capabilities in the complete operational envelope of RVD. Secondly, the VBS instrument can be augmented with active structure light for very accurate range measurements when in the docking or berthing phase of the RVD.

Furthermore, tests of the target acquisition from all orientations should be conducted in order to identify regions where acquisition is challenged due to the geometry of the target. As of now, acquisition tests have only been covering the operational envelope of PROBA3.

5.11 Outlook

The work described in this chapter is in an on-going development and is to be considered the foundation on which a dedicated implementation on the microASC DPU can be based on. The current state of the tracking module has demonstrated that the performance complies with navigation requirements for the phase of *Final Approach*: The range estimate is better than 1% of the actual range, the lateral translation is within a few cm, and the attitude is determined within 1°. Although the required update rate of $1Hz$ is not verified at this point in time, it is expected to comply with this requirement when in *Target Tracking* mode.

The method of approach has been designed to accommodate a large variety of body shapes, without relying on specific features or optical properties of the body

surface. This approach complies with the expected mission profiles of a V-bar and -R-bar approach in relation to both circular and high elliptical orbital trajectories.

6 Concluding Comments

The work described in this dissertation has addressed the subject of image analysis and processing with the objective of tracking non-cooperative targets. Image processing and optimization techniques have been customized to further enhance the technological capabilities of space exploration. Three distinct study cases have been presented, each with a specific application and objective, but common to them all is to facilitate autonomous navigation to further improve the scientific outcome and enable autonomous mission scenarios.

A demonstration model of a structured light system is constructed. As a part of the Mars2020 payload PIXL, the structured light system, OFS, has the objective to support the main payload by measuring the relative distance towards the Martian surface. Both to navigate the robotic arm and to aid the PIXL instrument in optimizing the scientific measurements. The performance of the demonstration model was assessed on real-world samples, reassembling that of Martian surface, verifying that the performance is well within the requirements.

An optical navigation module has been developed, based on the platform of the microASC, with the objective to perform in-flight orbit determination. The system is envisaged to operate onboard far reaching probes and lunar landers, performing continuous observations, either as a support to the ground based radiometric measurements, or support the navigation of a fully autonomous vehicle, or to aid a probe in navigating relative to a planetary body or satellite.

At last, a novel approach of tracking an artificial satellite is presented. Test results show that relative navigation requirements for the final phase of a RVD scenario are fulfilled. The method is envisaged to be tested and validated in-flight in connection with the VBS onboard PROBA3, with the goal of supporting future servicing and sample return missions.

Bibliography

[1] JPL, Jet Propulsion Laboratory, "Deep space network." http://deepspace.jpl.nasa.gov/. Retrieved on 30/10/2015.

[2] R. M. Haralick and L. G. Shapiro, *Computer and Robot Vision*, vol. 1. Addison-Wesley Publishing Company, 1992.

[3] M. J. Sidi, *Spacecraft Dynamics & Control*. Cambridge Aerospace Series, Cambridge University Press, 1997.

[4] T. Neubert, M. Mandea, G. Hulot, R. von Frese, F. Primdahl, J. L. Jørgensen, E. Friis-Christensen, P. Stauning, N. Olsen, and T. Risbo, "Ørsted satellite captures high-precision geomagnetic field data, eos," *EOS Transactions American Geophysical Union*, vol. 82, pp. 81–96, February 2001.

[5] J. L. Jørgensen, P. S. Jørgensen, M. Betto, T. Denver, and L. J. Tuñón, "Enhanced mission performance from autonomous instrument guidance," *Acta Astronautica*, vol. 59, no. 8-11, pp. 981–989, 2006.

[6] B. D. Tapley, S. Bettadpur, M. Watkins, and C. Reigber, "The gravity recovery and climate experiment: Mission overview and early results," *American Geophysical Union*, vol. 31, 2004.

[7] E. Friis-Christensen, H. Lühr, and G. Hulot, "Swarm: A constellation to study the earth's magnetic field," *Earth Planets Science*, vol. 58, pp. 351–358, 2006.

[8] J. L. Burch and J. F. Drake, "Reconnecting magnetic fields," *American Scientist, Sigma Xi, The Scientific Research Society*, vol. 97, 2009.

[9] S. J. Bolton and the Juno Science Team, "The juno mission," in *Proceedings of the International Astronomical Union*, vol. 6, pp. 92–100, 2010.

[10] R. Michelsen, "micro advanced stellar compass - general information, asc-dtu-prp-3000," tech. rep., DTU Space, Space Instrumentation Group, 2006.

[11] M. Benn, *Vision Based Navigation Sensors for Spacecraft Rendezvous and Docking*. PhD thesis, DTU Space, National Space Institute, Technical University of Denmark, 2010.

[12] S. Persson, P. Bödin, E. Gill, J. Harr, and J. L. Jørgensen, "Prisma - an autonomous formation flying mission," in *Small Satellite Systems and Services - The 4S Symposium*, 2006.

[13] Goddard Space Flight Center, National Aeronaurics and Space Administration, "Juno magnetic flield investigation." http://junomag.gsfc.nasa.gov/. Retrieved on 04/10/2015.

[14] L. T. Castellani, J. S. Llorente, J. M. F. Ibarz, M. Ruiz, A. Mestreau-Garreau, A. Cropp, and A. Santovincenzo, "Proba-3 mission," *International Journal Space Science and Engineering*, vol. 1, no. 4, 2013.

[15] NASA, National Aeronautics and Space Administration, "Mars exploration program." http://mars.nasa.gov/. Retrieved on 25/09/2015.

[16] Jet Propulsion Laboratory, California Institute of Technology, "Mars 2020 science objectives." http://mars.jpl.nasa.gov/mars2020/mission/science/objectives/. Retrieved on 25/09/2015.

[17] A. Allwood, B. Clarke, T. Elam, D. Flannery, M. Foote, J. Hurowitz, E. Knowles, and L. Wade, "Texture-specific elemental analysis of rocks and soils with pixl: The planetary instrument for x-ray lithochemistry on mars 2020," in *Proceedings of the IEEE Aerospace Conference*, (Big Sky, MT), 2015.

[18] P. S. Jørgensen, J. L. Jørgensen, and T. Denver, "Microasc a miniature star tracker," in *Proceedings of the 4S Symposium: Small Satellites, Systems and Services*, 2004.

[19] NASA, Jet Propulsion Laboratory, Calfornia Institute of Technology, "Earth and moon seen by passing spacecraft with music by vangelis." http://www.nasa.gov/jpl/juno/juno-earth-flyby-20131210.html. Retreived 24/11/2015.

[20] E. D. of Technical and O. Support, "Technologies for exploration, aurora prprogram proposal: Annex d," tech. rep., 2001.

[21] N. Aeronautics and N. Space Administration, "An assessment of the technology of automated rendezvous and capture in space," tech. rep., Marshall Space Flight Center, July 1998.

[22] N. G. Smith and P. E. Hong, "Elliptical rendezvous at mars," *Advances in the Astronautical Sciences*, vol. 76, no. 2, pp. 1573–1586, 1992. in Proceedings of the AAS/AIAA Astrodynamics Conference.

[23] E. Gogibus, H. Charbonnel, and P. Delpy, "Autonomous and robust rendezvous guidance on elliptical orbit subject to j2 pertubation," *Astrium Space Transportation*, 2009.

[24] E. D. Sotto, J. C. Bastante, and R. Drai, "System and gnc concept for rendezvous into elliptical orbit for mars sample return mission," in *AIAA Guidance, Navigation and Control Conference and Exhibit*, 2007.

[25] N. Aeronautics and N. Space Administration, "On-orbit satellite servicing study," project report, Goddard Space Flight Center, GSFC, 2010.

[26] K. Landzettel, B. Brunner, R. Lampariello, C. Preusche, D. Reintsema, and G. Hirzinger, "System prerequisites and operational modes for on orbit servicing," in *International Symposiym on Space Technology and Science, ISTS*, May - June 2004.

[27] W. Fehse, *Automated Rendezvous and Docking of Spacecraft*. Cambridge University Press, 2003.

[28] B. W. Barbee, J. R. Carpenter, S. Heatwhole, F. L. Markley, M. Moreau, B. J. Naasz, and J. V. Eepoel, "A guidance and navigation strategy for rendezvous and proximity operations with a noncooperative spacecraft in geosynchronous orbit," *Journal of Astronautical Sciences*, vol. 58, pp. 389–408, July-September 2011.

[29] J. A. Christian and S. Cryan, "A survey of lidar technology and its use in spacecraft relative navigation," in *AIAA Guidance, Navigation, and Control (GNC) Conference*, (Honolulu, HI, USA), 2008.

[30] S. Ruel, C. English, M. anctil, J. Daly, C. Smith, and S. Zhu, "Real-time 3d vision solution for on-orbit autonomous rendezvous & docking," in *Spaceborne Sensors |||, Proceedings of SPIE* (R. T. Howard and R. D. Richards, eds.), vol. 6220 622009-1, 2006.

[31] T. Kasai, M. Oda, and T. Suzuki, "Results of the ets-7 mission - rendezvous docking and space robotics experiments," in *Fifth International Symposiym on Artificual Intelligence. Robots and Automation in Space*, 1-3 June 1999.

[32] S. Persson and S. D. J. Harr, "Flight results from prisma formation flying and rendezvous demonstration mission," in *61st International Astronautical Congress, IAF*, (Prague, CZ), 2010.

[33] R. M. Pinson, R. T. Howard, and A. F. Heaton, "Orbital express advanced video guidance sensor: Ground testing, flight results and comparisons," in *AIIA Guidance, Navigation Control Conference and Exhibit*, August 2008.

[34] S. Ruel, T. Luu, and A. Berube, "On-orbit testing of target-less tridar 3d rendezvous and docking sensor," in *10th International Symposium on Artificial Intelligence, Robotics and Automation in Space, i-SAIRAS*, (Sapporo, Japan), August 2010.

[35] S. D'Amico, M. Benn, and J. L. Jørgensen, "Pose estimation of an uncooperative spacecraft from actual space imagery," in *Proceedings of 5th International Conference on Spacecraft Formation Flying Missions and Technologies*, (Munich, Germany), 2013.

[36] G. Skinner, B. Dennis, J. Krizmanic, and E. Kontar, "Science enabled by high precision inertial formation flying," in *Proceedings of 5th International Conference on Spacecraft Formation Flying Missions and Technologies*, (Munich, Germany), 2013.

[37] J. C. Bastante, J. Vasconcelos, M. Hagenfeldt, L. F. Peñín, J. Dinis, and J. Rebordão, "Design and development of proba-3 rendezvous experiment," *Acta Astronautica*, vol. 102, pp. 311–320, 2013.

[38] J.-S. Ardaens, S. D'Amico, and A. Cropp, "Gps-based relative navigation for the proba-3 formation flying mission," *Acta Astronautica*, vol. 91, pp. 341–355, 2013.

[39] J. Peyrard, D. Escorial, A. Agenjo, A. Kron, and A. Cropp, "Design and prototyping of proba-3 formation flying system," in *Proceedings of 5th International Conference on Spacecraft Formation Flying Missions and Technologies*, (Munich, Germany), 2013.

[40] A. Cropp, P. Palmer, and C. Underwood, "Pose estimation of target satellite for proximity operations," in *14th Annual/USU Conference on Small Satellites*, 2002.

[41] D. G. Lowe, "Three-dimensional object recognition from single two-dimensional images," *Artificial Intelligence*, vol. 31, pp. 355–395, March 1987.

[42] J. Canny, "A computational approach to edge detection," *IEEE Transactions on Pattern Analysis and Machine Intelligence*, vol. 6, pp. 679–698, 1986.

[43] J. A. Nelder and R. Mead, "A simplex method for function minimization," *The Computer Journal*, vol. 7, no. 4, pp. 308–313, 1965.

[44] S. Rusinkiewics and M. Levoy, "Efficient variants of the icp algorithm," in *Third International Conference on 3D Digital Imaging and Modeling*, 2001.

[45] D. Rössler, D. A. K. Pedersen, M. Benn, and J. L. Jørgensen, "Optical stimulator for vision-based sensors," *Advanced Optica Technologies*, vol. 3, no. 2, pp. 199–207, 2014.

[46] V. Barrena, P. Colmenarejo, M. Sautoni, D. Rössler, D. A. K. Pedersen, and F. Ankersen, "Use of in-flight data to validate mars sample return autonomous rvd gnc," in *Proceedings of the International Astronautical Congress, IAC*, vol. 10, pp. 8461–8469, 2012.

[47] O. Dubois-Matra, S. Parkes, and M. Dunstam, "Testing and validation of planetary vision-based navigation systems with pangu," in *The proceeding of the 21st International Symposium on Space Flight Dynamics (ISSFD)*, (Toulouse, France), 2009.

[48] A. Massaro, *Synthesis and Validation of Vision Based Spacecraft Navigation*. PhD thesis, DTU Space, 2013.

[49] M. Benn and J. L. Jørgensen, "Autonomous vision based detection of non-stellar objects flying in formation with camera point of view," in *Proceedings of 5th International Conference on Spacecraft Formation Flying Missions and Technologies*, (Munich, Germany), 2013.

[50] M. A. Abidi and T. Chandra, "Pose estimatin for camera calibration and landmark tracking," in *Robotics and Automation, 1990 Proceedings, IEEE International Conference on*, vol. 1, pp. 420–426, 1990.

Appendices

A Structural overview of Coronagraph spacecraft (CSC)

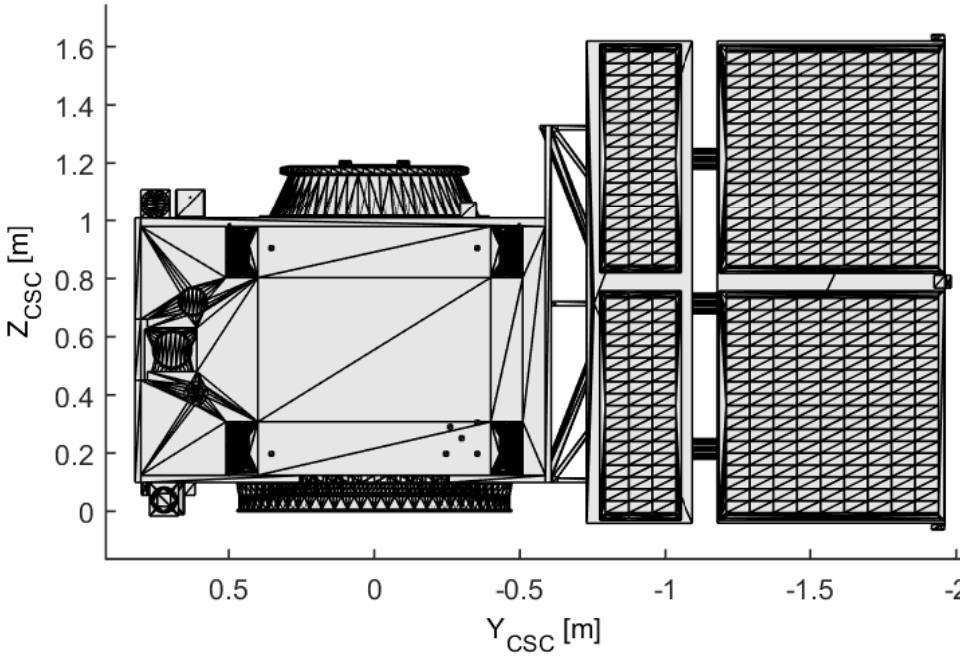

Figure A.1 *The CAD model of Coronagraph Spacecraft (CSC), viewed from* $-X_{CSC}$.

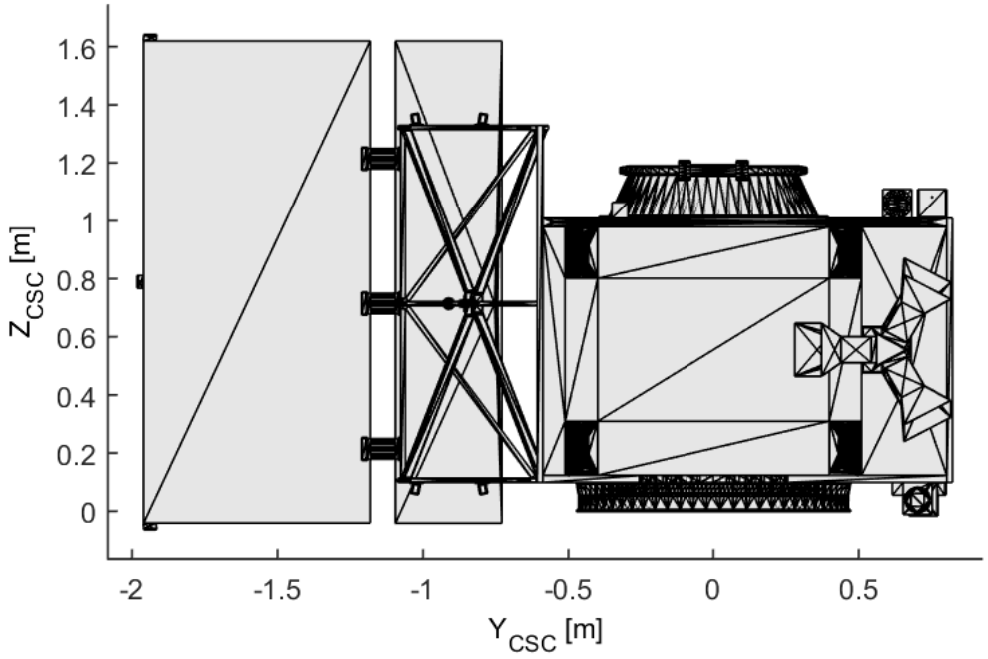

Figure A.2 *The CAD model of Coronagraph Spacecraft (CSC), viewed from* $+X_{CSC}$.

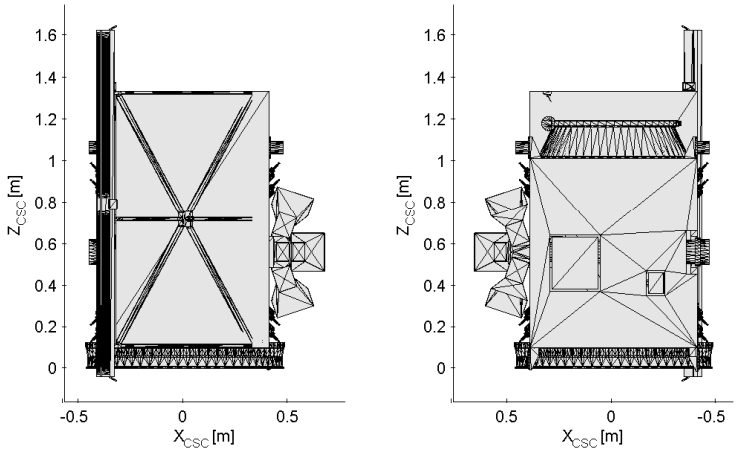

Figure A.3 *The CAD model of Coronagraph Spacecraft (CSC). The left view is from* $-Y_{CSC}$ *and the right is from* $+Y_{CSC}$.

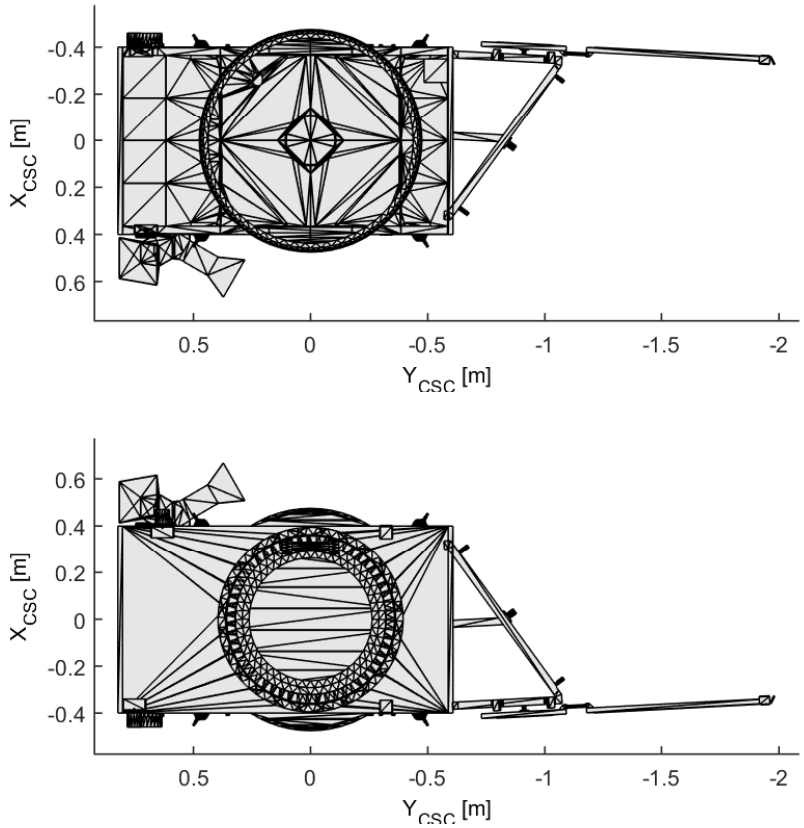

Figure A.4 *The CAD model of Coronagraph Spacecraft (CSC). The left view is from $-Z_{CSC}$ and the right is from $+Z_{CSC}$.*

B Example of filtering the solutions space

An example of the filtering process of the solution space. In this example, the initial solution space consists of 100 viewpoints uniformly distributed over a hemisphere. Figures B.1, B.2,B.3 , B.4, B.5 and B.6 show how the solution space is narrowed down during the filtering process. The floating point number over each solution indicates the score the corresponding viewpoint and the integer number is the viewpoint ID.

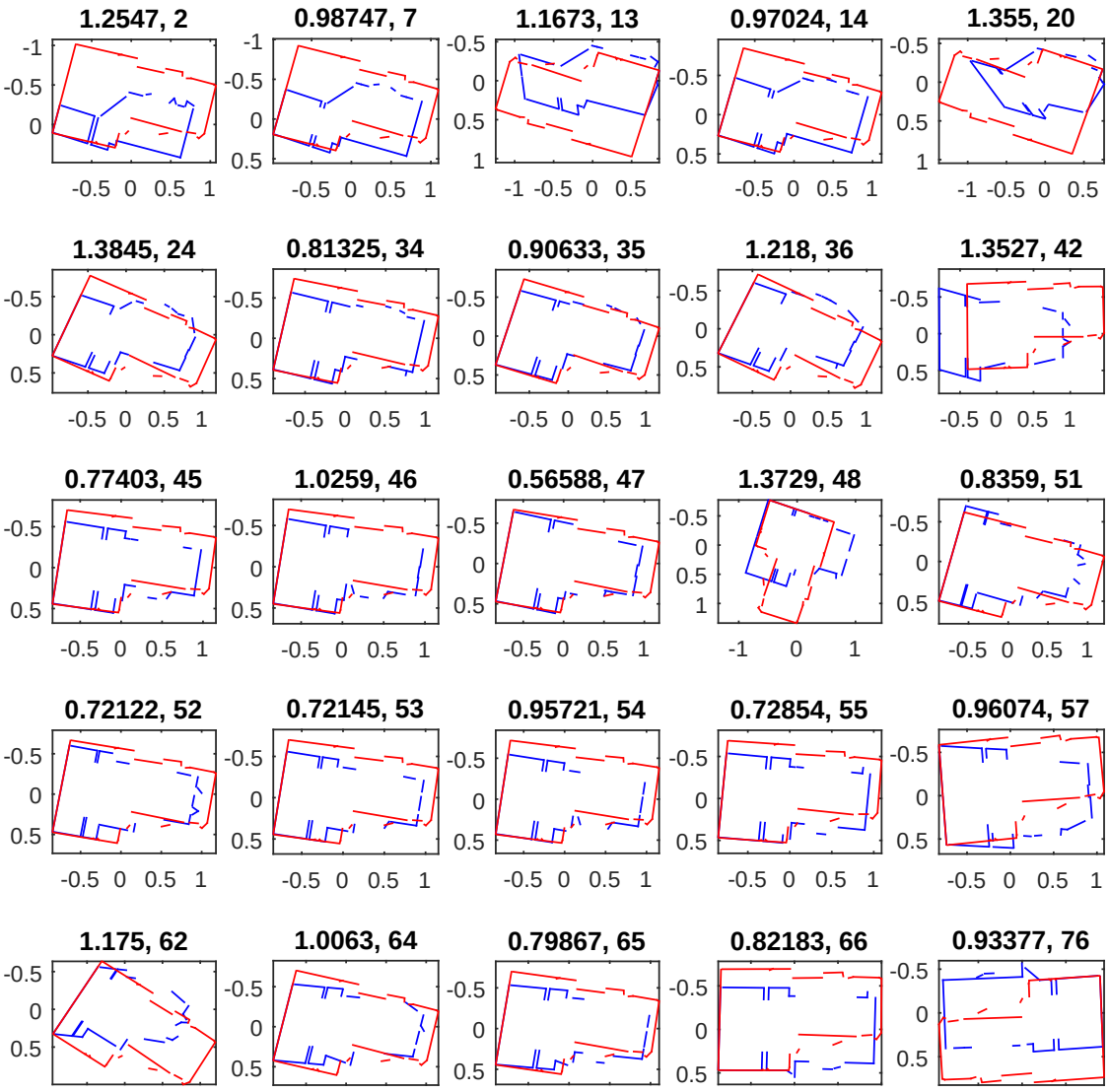

Figure B.1 *The resulting solution space after matching the extracted features (red) with the contour data (blue).*

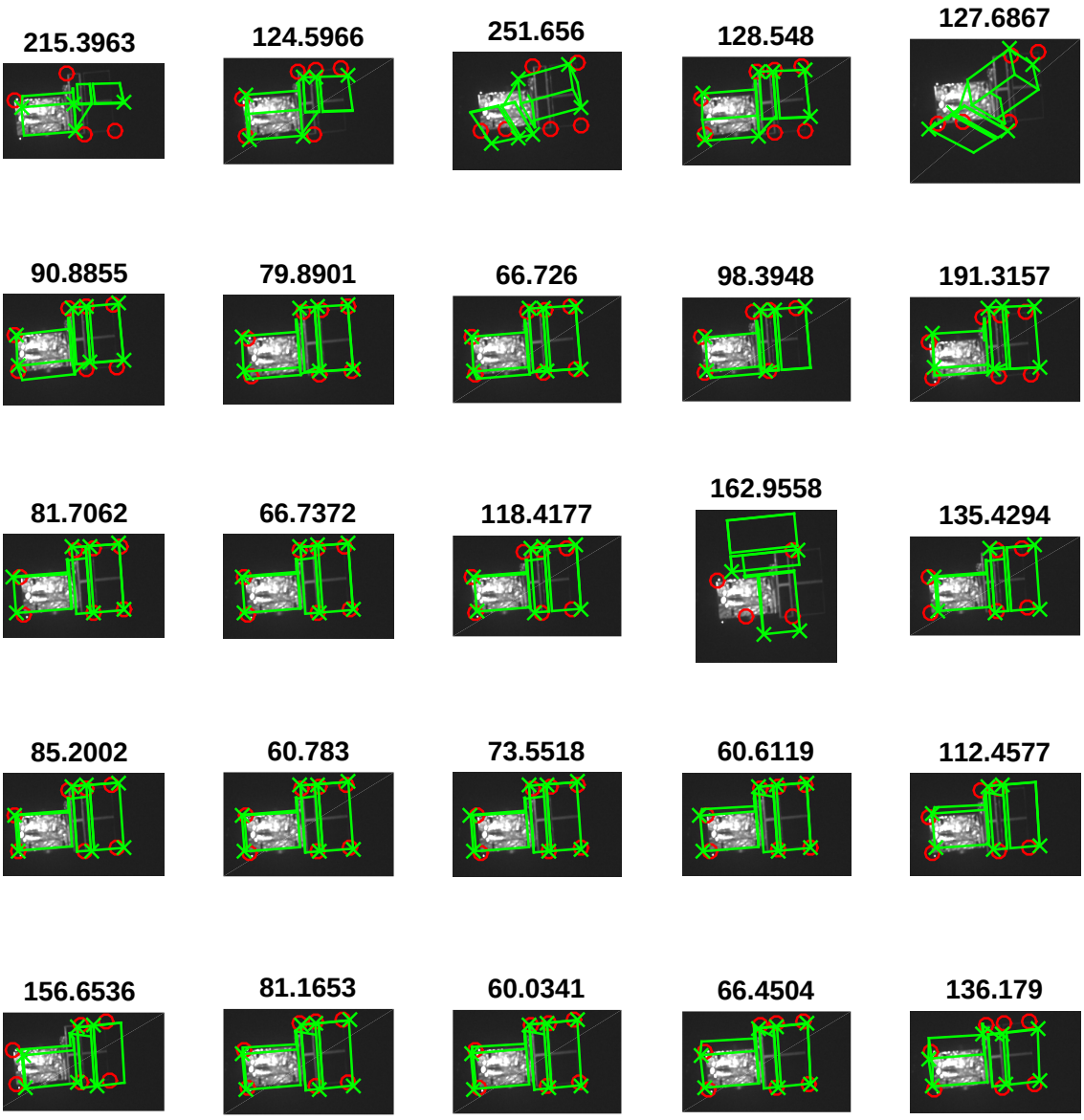

Figure B.2 *The initial score of matching the vertexes. Half of these are discarded.*

Figure B.3 *The score of after performing a crude Nelder-Mead optimization on the 6DOF pose. Half of these solutions are discarded.*

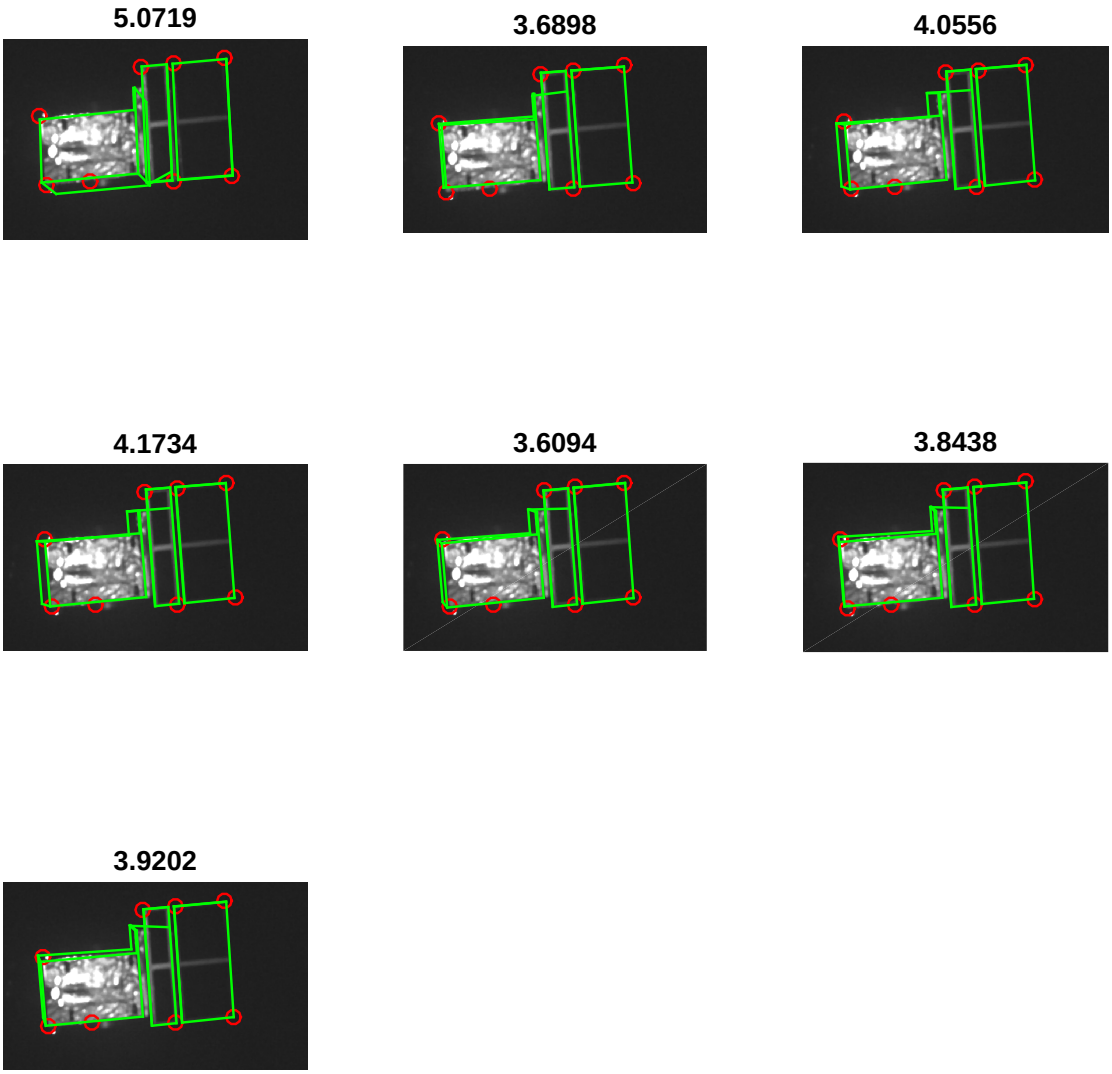

Figure B.4 *The score after an accurate Nelder-Mead optimization. Half of these are forwarded to the next image frame processing, constituting a much reduced solution space.*

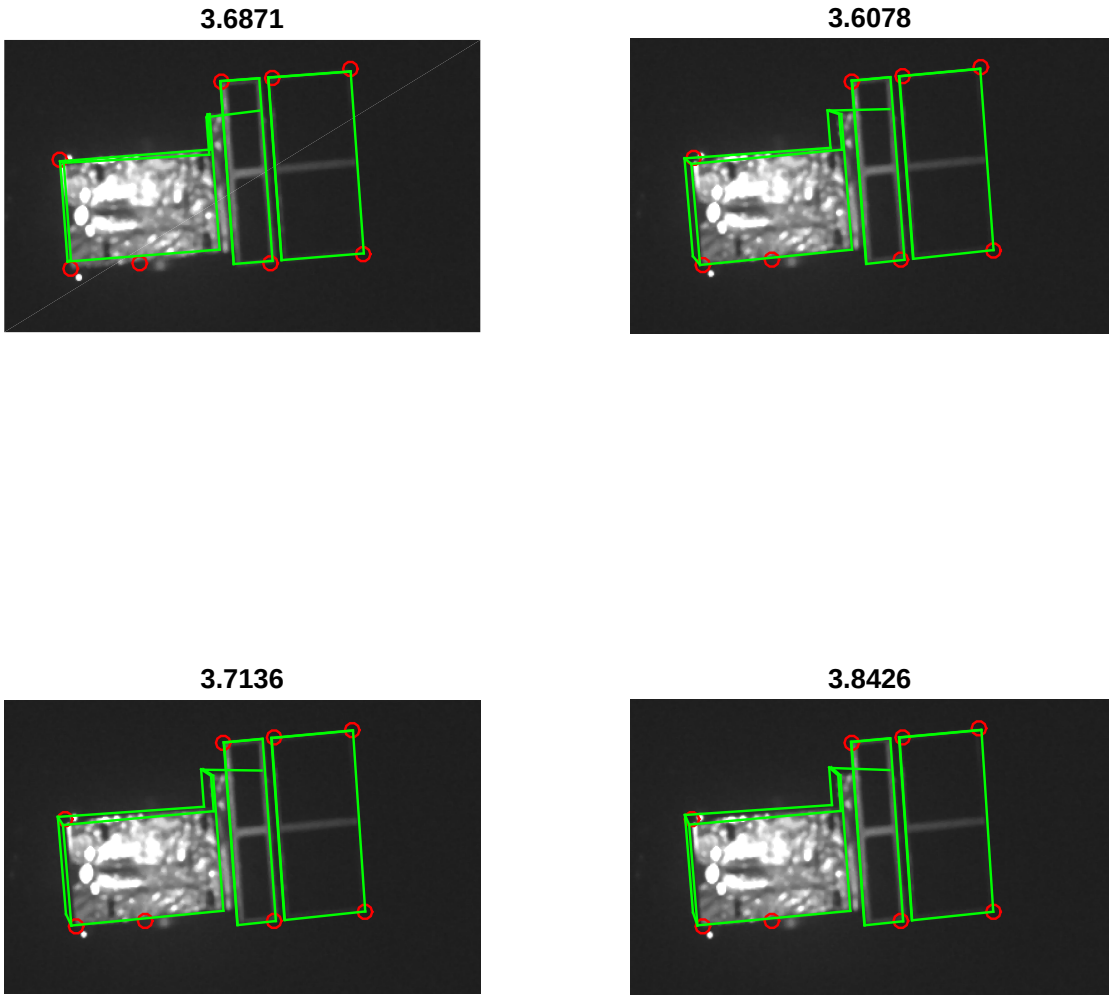

Figure B.5 *Using the same frame as the first one, the solution search will only make use of the crude and accurate Nelder-Mead processes in the filtering sequence. Two of these are forwarded to the processing of the next image frame.*

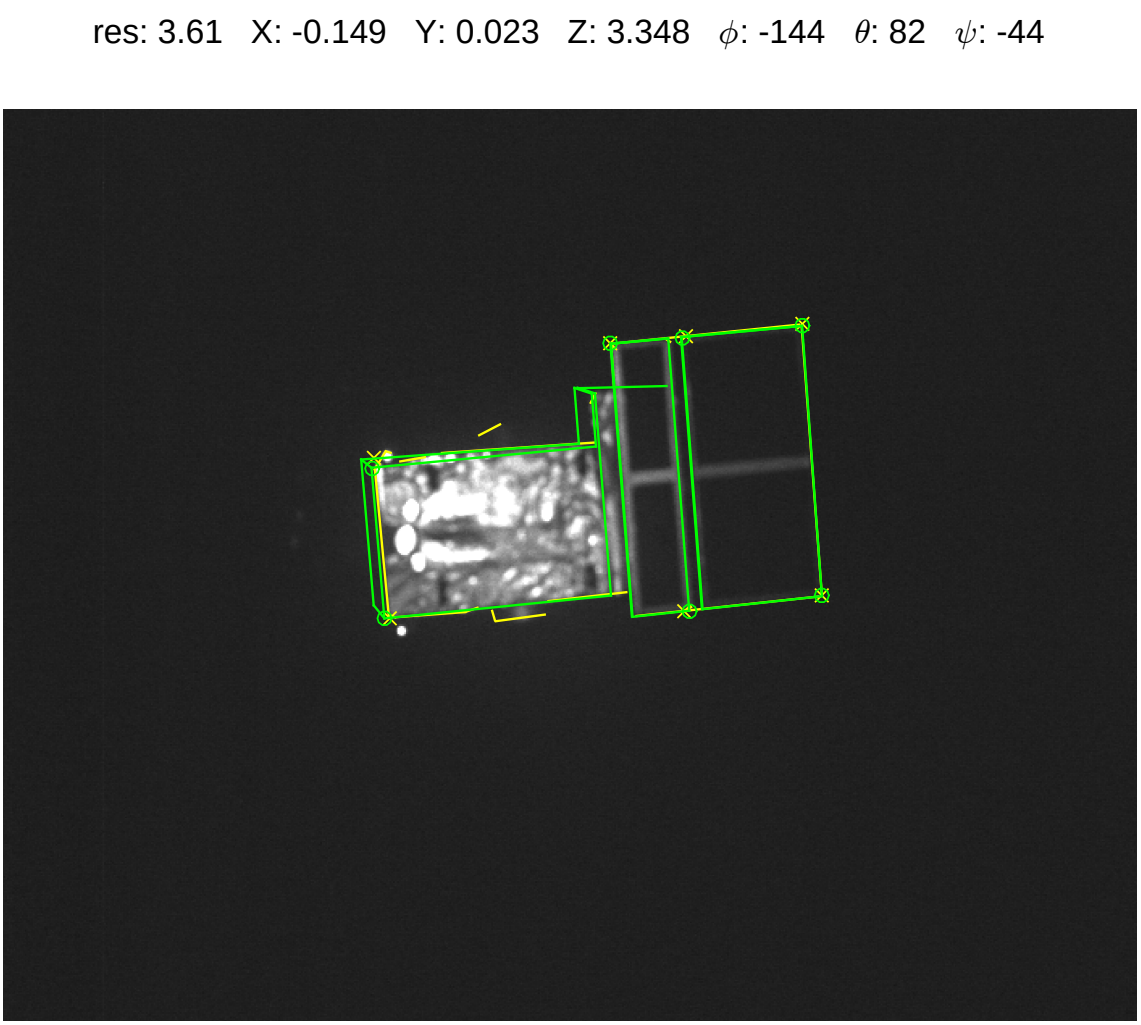

Figure B.6 *Using the same image frame a third time results in only a single viewpoint solution with a residual of 3.61 pixels.*

C Optical stimulator for vision-based sensors

DE GRUYTER DOI 10.1515/aot-2013-0045 — Adv. Opt. Techn. 2014; 3(2): 199–207

Research Article

Dirk Roessler[a,]*, David A.K. Pedersen, Mathias Benn and John L. Jørgensen

Optical stimulator for vision-based sensors

Abstract: We have developed an optical stimulator system for vision-based sensors. The stimulator is an efficient tool for stimulating a camera during on-ground testing with scenes representative of spacecraft flights. Such scenes include starry sky, planetary objects, and other spacecraft. The optical stimulator is used as a test bench to simulate high-precision navigation by different types of camera systems that are used onboard spacecraft, planetary rovers, and for spacecraft rendezvous and proximity maneuvers. Careful hardware design and preoperational calibration of the stimulator result in high precision and long-term stability. The system can be continuously used over several days. By facilitating a full camera including optics in the loop, the stimulator enables the more realistic simulation of flight maneuvers based on navigation cameras than pure computer simulations or camera stimulations without the involvement of the actual optics.

Keywords: flight simulator; optical stimulator; rendezvous and proximity maneuver; spacecraft attitude; star tracker camera; vision-based navigation.

[a]Now at: GFZ German Research Centre for Geosciences, Potsdam, Germany

***Corresponding author: Dirk Roessler,** National Space Institute, Division Measurements and Instrumentation, Technical University of Denmark, Elektrovej 327, room 221, 2800 Kgs. Lyngby, Denmark, e-mail: d-roessler@web.de

David A.K. Pedersen, Mathias Benn and John L. Jørgensen: National Space Institute, Division Measurements and Instrumentation, Technical University of Denmark, Elektrovej 327, room 221, 2800 Kgs. Lyngby, Denmark

1 Introduction

Since the pioneering development of star tracker cameras such as the Advanced Stellar Compass [1], the microAdvanced Stellar Compass [2], and others [3], digital cameras have been successfully used for autonomous attitude determination of spacecraft based on the observation of stars. Accurate relative range and attitude determination as well as fully autonomous rendezvous and proximity operations between spacecraft by means of vision-based navigation have proven feasible since the development of the vision-based sensor (VBS) [4]. Such sensor systems will be of growing importance for future proximity, rendezvous, and docking maneuvers between spacecraft as well as for landing of spacecraft on planets and other celestial bodies.

Spacecraft maneuvers require careful preparation, realistic simulations, and testing. On-ground flight simulations with flight-representative test benches are cost-effective and flexible alternatives to expensive in-flight tests. Owing to the key role of camera systems for spacecraft attitude control and navigation, the involvement of the physical camera during such simulations and testing of maneuvers increases the representativeness of a test bench.

Therefore, different approaches have been followed to develop star tracker stimulators for different real cameras in the loop [5, 6]. The Optical Stimulator for Vision-Based Sensors (OSVBS) has been developed, verified, and tested by the National Space Institute of the Technical University of Denmark. It enables the flexible stimulation of a variety of navigation cameras in open and closed loop and can be embedded within complex test benches [7]. Here, we describe the mechanical and software setup of the OSVBS as well as results from testing.

2 System setup

The main objective of the OSVBS is the realistic stimulation of navigation cameras with flight scenarios in space. The scenarios include spacecraft navigation based on star observations as well as rendezvous and proximity operations between spacecraft or between a spacecraft and celestial bodies. Typically, scene rendering by software [8, 9] results in perfect images. However, actual camera images are distorted due to the involved optics, electronics, and software. The effects include geometric distortion

and noise. For realistic simulations of optical navigation, a camera including the optics must therefore be stimulated and included in the loop.

OSVBS supports a wide range of real navigation cameras, without the need for major modifications. The cameras are stimulated in the loop by static or dynamic monitor images that are viewed by the camera optics (Figure 1). The images represent scenes in space and are characterized by high fidelity, appropriate geometry, and intensity.

The main criteria of the system's design are

1. Ability to stimulate different camera systems with high fidelity,
2. Modularity such that the main individual components can be replaced,
3. Cost efficiency by using components off the shelf.

2.1 Hardware

The modular hardware design of OSVBS mainly consists of a standard desktop PC as scene calculator and an optical stimulator. The optical stimulator is connected to the PC and hosts the camera optics.

The scene calculator generates the scene images. Taking into account the sensor's dimensions and the focal length of the mounted camera, space-representative color images are computed utilizing PANGU [8], but other simulator software such as Celestia [9] can also be used. In this way, the generic images appear as perfect space images without involving the optics and the electronics of the camera. Scene control is realized based on commands from an external real-world simulator (Figure 2) and an external timing system that enables near real-time commanding. The command interface is defined by the involved software used for the scene generation.

The hardware of the optical stimulator in the loop includes a standard 24″ LED monitor with 1900×1200 px screen resolution. The monitor receives video input from the scene calculator, and it is this that is used for the camera stimulation.

A carefully designed optical bench connects the monitor to the camera tower, which hosts the camera being involved (Figure 1, left). The camera tower hosts the mechanical interface to the camera. Cameras with a wide range of physical dimensions can be considered. Together with the optical bench, the camera tower provides stable and adjustable connection to the stimulator monitor. The camera mount, itself, depends upon the camera. An additional camera adapter may be required between the camera and the mechanical interface (Figure 1, right). The different stages of the camera tower (Figure 1, right) allow a 3 DoF (degree of freedom) adjustment of the camera, namely, translation along the optical bench and rotation approximately about yaw and pitch of the camera. Translations between 0 and 1850 mm are supported. The yaw and pitch adjustment enables the pointing of the camera toward the monitor. Orienting the camera to within 1° to the normal of the monitor can be done rapidly with the remaining geometric distortions compensated for by the software.

An additional optic, being specific to the camera, in front of the camera lens may be required for the correct

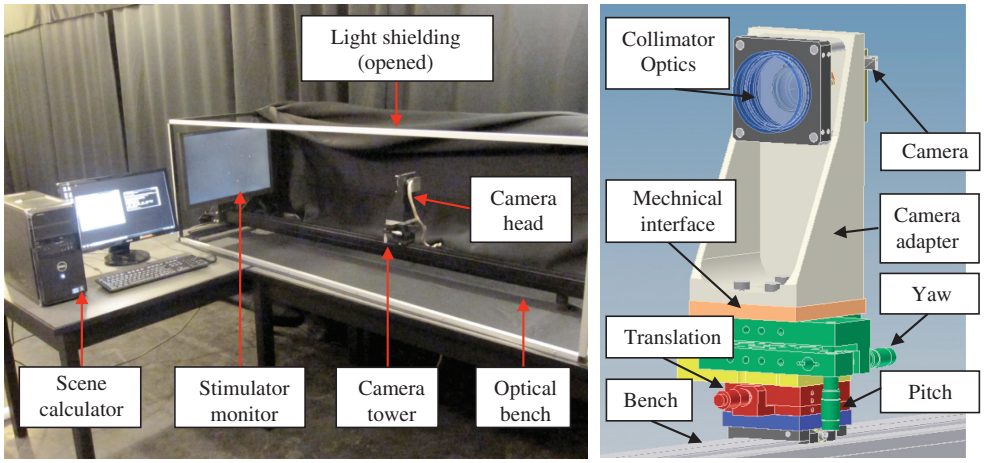

Figure 1 System setup. Left: OSVBS with mounted camera head. The light shielding is opened to allow viewing of the inner part. Right: CAD drawing of the camera tower sitting on the bench with the camera mounted through the camera adapter to the mechanical interface atop the 3 DoF (degree of freedom) stage (2 DoF rotations, 1 DoF translation along the bench).

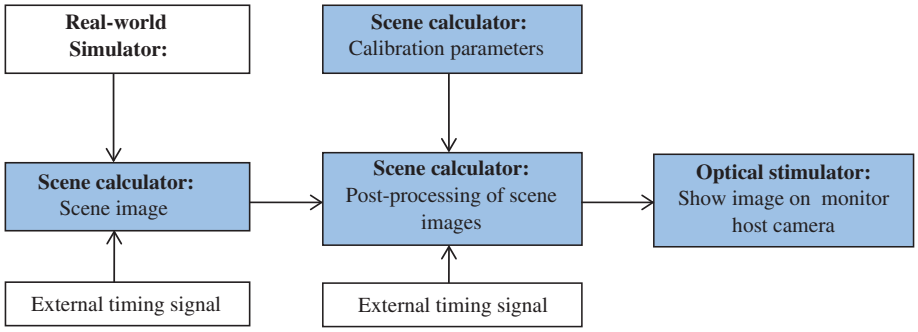

Figure 2 Process flow of signal generation for the camera stimulation commanded by the Real-World Simulator. Blue boxes indicate components of the OSVBS.

focusing of the camera on the monitor, in combination with the translation stage. In the case of DTU's microASC [2], one standard 1000-mm collimator lens is used. The lens surface is coated to suppress reflections of light in the wavelength range of 400–700 nm, e.g., multipathing between the camera lens and the collimator. Mounted on the camera adapter, the lens is placed directly in front of the camera lens.

The optical stimulator is shielded against secondary light (Figure 1, right). The modular system setup allows for the easy replacement of individual hardware items such as the monitor and software components such as the scene generator and the use of different camera models in the loop.

2.2 Software

In order to make use of the high precision of the considered navigation systems (e.g., microASC [2]), it is essential that the geometry of the image projected onto the monitor is extremely accurate. While the accurate mechanical alignment of the camera with respect to the monitor is provided by the camera tower, variations in camera roll are not supported. Furthermore, the fine adjustment of the camera's pointing to better than a few tens of a degree can be extremely time consuming and is not performed. However, the resulting geometric distortions can be easily corrected by software. Likewise, the involvement of additional optics and the camera lenses result in distortion of the field-of-view of the camera, which must also be accounted for after image generation by the PC.

Therefore, software is applied to account for lens distortion and for position and pose of the optical system by image manipulation applied to the generic images. The image manipulation is carried by a combination of preoperational optical calibration and image postprocessing in the loop. Both are carried out using software developed at DTU Space on the basis of OpenCV [10] libraries.

2.2.1 Optical calibration

Let (x_p, y_p, F) be a point on the sensor chip of a perfect pinhole camera and (X, Y, Z) be the coordinates of a viewed object in the same coordinate frame [10]. Then,

$$\begin{bmatrix} x_p \\ y_p \end{bmatrix} = \begin{bmatrix} f_x X/Z + c_x \\ f_y Y/Z + c_y \end{bmatrix}, f_x = F s_x, f_y = F s_y,$$

where (s_x, s_y) and (c_x, c_y) are pixel densities and the coordinate of the principle point along the x- and y-axis of the sensor chip, and F is the effective focal length of the camera. We assume that (s_x, s_y) is known from the camera manufacturer or from the camera's calibration.

Owing to radial and tangential distortion of the image by the camera lens system, points (x_p, y_p) are really in the wrong position (x_d, y_d)

$$\begin{bmatrix} x_p \\ y_p \end{bmatrix} = (1 + k_1 r^2 + k_2 r^4 + k_3 r^6) \begin{bmatrix} x_d \\ y_d \end{bmatrix} + \begin{bmatrix} 2p_1 x_d y_d + p_2 (r^2 + 2x_d^2) \\ p_1 (r^2 + 2y_d^2 + 2p_2 x_d y_d) \end{bmatrix},$$

where k_i and p_i are distortion coefficients describing the radial and tangential lens distortion, respectively, and r is geometric distance of (x_d, y_d) from the principle point in the sensor plane.

The parameters (s_x, s_y), (c_x, c_y), F, p_i, and k_i are the intrinsic parameters. (c_x, c_y), p_i, and k_i are to be determined by calibration. They result from the combination of the camera lens and the additional optics in front of the camera. The distortion $\boldsymbol{d}$ vector is formed such that $\boldsymbol{d} = [k_1\ k_2\ p_1\ p_2\ k_3]^T$.

The extrinsic parameters describe the rotation and translation of a viewed object with respect to the camera. They are given by the homography, a projective mapping

between two planes. We define the viewed object point $\boldsymbol{Q}$ with $\tilde{\boldsymbol{Q}}=[X\,Y\,Z\,1]^T$ and $\tilde{\boldsymbol{q}}=[x_p\,y_p\,1]^T$. The translation $\boldsymbol{T}$ between a point in the plane of the camera sensor and a point on a viewed plane is $\boldsymbol{T}=origin_{viewed}-origin_{camera}$. The 3D rotation between the two planes is described by the rotation matrix $\boldsymbol{R}$. With $\boldsymbol{M}=\begin{bmatrix} f_x & 0 & c_x \\ 0 & f_y & c_y \\ 0 & 0 & 1 \end{bmatrix}$, $\boldsymbol{W}=[\boldsymbol{RT}]$, and $\boldsymbol{R}=[\boldsymbol{r}_1\,\boldsymbol{r}_2\,\boldsymbol{r}_3]$, the transformation between $\tilde{\boldsymbol{q}}$ and $\tilde{\boldsymbol{Q}}$ is given by

$$\tilde{\boldsymbol{q}}=s\boldsymbol{M}\boldsymbol{W}\tilde{\boldsymbol{Q}},$$

where s is an arbitrary scaling factor. Assuming that $\boldsymbol{Q}$ lies on a plane through the origin of the viewed plane, $Z=0$. Then

$$\tilde{\boldsymbol{q}}=\begin{bmatrix} x_p \\ y_p \\ 1 \end{bmatrix}=s\boldsymbol{M}[\boldsymbol{r}_1\,\boldsymbol{r}_2\,\boldsymbol{r}_3\,\boldsymbol{T}]\begin{bmatrix} X \\ Y \\ 0 \\ 1 \end{bmatrix}=s\boldsymbol{M}[\boldsymbol{r}_1\,\boldsymbol{r}_2\,\boldsymbol{T}]\begin{bmatrix} X \\ Y \\ 1 \end{bmatrix} \text{ and } \tilde{\boldsymbol{q}}=s\boldsymbol{H}\widetilde{\boldsymbol{Q}'}.$$

Here, $\boldsymbol{H}$ is the 3×3 homography matrix. The inverse of the homography matrix can be used to project the given points in the plane of the camera to the other plane such as a monitor. Therefore, $\boldsymbol{H}$ contains all the sought extrinsic parameters.

The intrinsic parameters and $\boldsymbol{H}$ are sought during the calibration of the optical system representing the entire optical system including the camera and the additional optics. Application of them enables the correct projection of the image in the field-of-view of the camera as it would be in nature.

For calibration, a well-known chessboard pattern projected onto the monitor is viewed by the camera. The conditions for homography are met as both the camera sensor and the viewed monitor screen form planes. For calibration of intrinsic and extrinsic parameters, OpenCV routines [10] are applied to downloaded camera images. The corner positions of the chessboard are extracted at subpixel accuracy and associated with the corner positions of the generic image. The intrinsic parameters are first determined in an attempt to straighten all lines connecting the points in x and y directions [11, 12]. Corner positions are corrected for lens distortion based on the determined intrinsic parameters. The homography matrix is computed by comparison of the corrected corner positions on the camera sensor and the known values on the monitor. The translation vector as well as pitch, yaw, roll of the camera are derived from the homography matrix [10].

Initially, the extrinsic parameters are considered for the mechanical adjustment of the camera pointing within 1°. The final optical calibration is carried out based on several, up to 10, uncompressed camera images from a single, projected chessboard image. Calibration is required only once prior to the operation of OSVBS. Depending on the download speed of the camera, typical calibrations are time efficient and take no more than 10 min. Thereafter, the system can be used for several days without interruption, given that temperatures are stable. The extrinsic calibration parameters can also be used to assist opto-mechanical adjustment of the camera.

2.2.2 Image manipulation

Based on the determined intrinsic and extrinsic calibration parameters, the image manipulation SW adjusts the images at subpixel accuracy and projects them on the stimulator monitor. The matrices $\boldsymbol{M}$, $\boldsymbol{H}$, and $\boldsymbol{d}$ are employed to compute rectification look-up maps using the OpenCV routine cvInitUndistortRectifyMap() [10]. The look-up maps contain the mapping from the pixels of the monitor to the pixels of the camera. They are used in the OpenCV routine cvRemap() [10] to manipulate the generic images and project them onto the monitor. In this way, the image projection is efficient, and projected images attain an extremely accurate geometry with respect to the viewing camera.

The camera stimulation is synchronized to an external clock by a pulse-per-second (PPS) signal or to the internal clock of the scene calculator.

The optical stimulator is embedded in an on-ground test bench (Figure 3) where it can be operated in open and closed loop modes. When connected to the stimulator, the camera operates independently of the OSVBS. Only for calibration, camera-taken images must be uploaded to the computer. Depending on the camera, the direct sending and receiving of telemetry and telecommand (TM/TC) packages may be possible by the computer.

3 Accuracy

The accuracy of the geometry of the projected images is given by the performance of the optical calibration and image manipulation. OSVBS reaches a high level of scene accuracy, in-flight representativeness, and high long-term stability. The accuracy of the projected images is tested based on projected star images viewed by DTU's micro-ASC [2]. Like in standard operation, the microASC computes the camera attitude based on the stars in the images

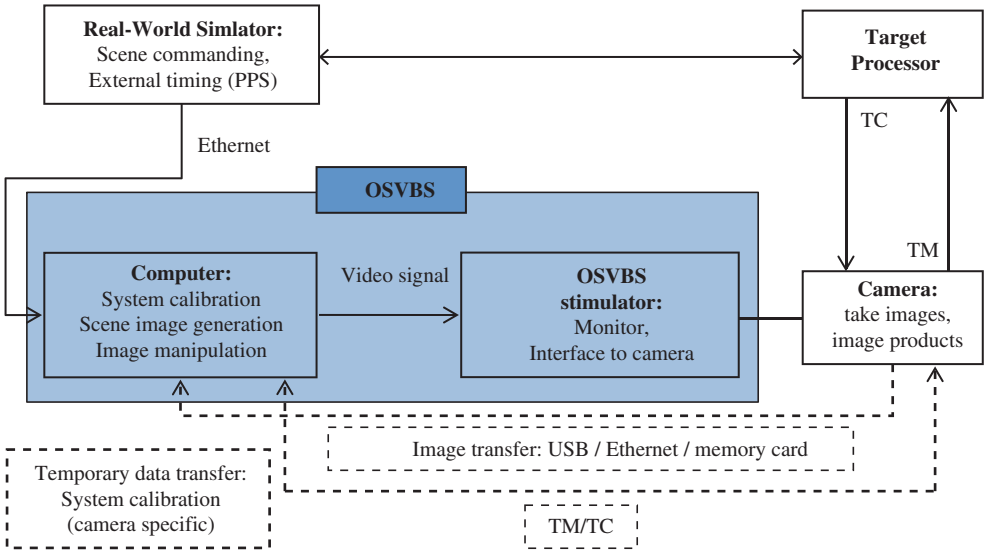

Figure 3 OSVBS embedded in a possible on-ground test bench with the camera, Target Processor, and Real-World Simulator in closed loop. Straight lines show essential connections during close-loop operation. Dashed lines show optional connections during calibration where TM/TC package can also be transmitted using another computer.

shown on the monitor. The camera solutions are compared to values used for image generation.

Owing to system calibration and hyper-accuracy image manipulation, the accuracy of the projected images as given by the attitude solutions of DTU's microASC [2] is always better than 20 arcsec for yaw and pitch and better than 200 arcsec for roll. Typically, these values are significantly below 10 arcsec and 100 arcsec, respectively.

In thermally stable environments, the system has been continuously operated without loss of accuracy for more than 20 h and up to 1 week without re-calibration. Therefore, the stimulator can be used to simulate ambitious space flight maneuvers. The requirement to perform re-calibration can be tested by the stimulation of the camera using static star images or other calibrated images.

4 Test examples

OSVBS has been carefully tested and used along with DTU's microASC [2] and VBS camera [4] (Figure 4). Onboard a spacecraft, the microASC/VBS autonomously determines the attitude of the camera, itself, based on star observations. It also measures the line-of-sight angles of nonstellar objects such as spacecraft in the field-of-view of the camera. The parameters can then be related to other coordinate systems such as that of the spacecraft. The camera has a typical pointing accuracy of about 1 arcsec in right ascension and declination in the J2000.0 coordinate system.

For testing the accuracy of the image geometry and the scene fidelity, the camera is stimulated with scene images projected onto the monitor. Such scenes represent starry sky or other spacecraft. Static and dynamic scenes are considered. As onboard a spacecraft, the camera is used autonomously to determine the attitude parameters and the line-of-sight parameters. The solutions are retrieved by telemetry/telecommands sent between the camera and another external PC connected to the camera. All tests are performed using the calibration parameters obtained from standard system calibration before the tests.

4.1 Static starry-sky scenes

Static images representing starry sky are a simple yet powerful means to assess the image fidelity. In the case of the microASC, small image distortions will result in obscured or even invalid camera solutions. The quality of

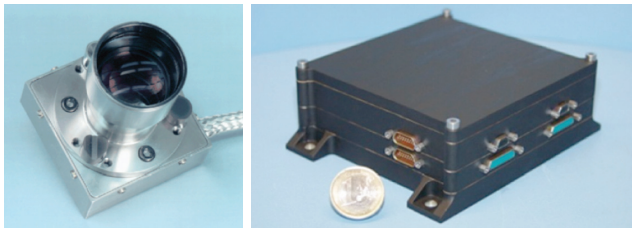

Figure 4 Camera head unit (left) and data processing unit (right) of DTU's microASC [2] and VBS [4].

the viewed images is therefore assessed by comparison of the attitude values assumed for the image generation with the camera solution.

Involving OSVBS for camera stimulation, high-precision camera attitude solutions are obtained (Table 1, Figure 5). The obtained uncertainties in attitude angles are very low (Table 1) and close to the values for camera operations in space. Therefore, the image geometry is highly representative of real scenes.

The obtained results are representative for the operation of OSVBS with still images where the average pointing precisions are typically below 10 arcsec for right ascension and declination and always better than 20 arcsec. Standard deviations are <10 arcsec.

Table 1 Mean and standard deviation σ of the differences Δ between angles from camera attitude solutions and generic values (compare Figure 5).

	Mean (Δ)	σ
Δ(*ra*) (right ascension)	0.2″	2.8″
Δ(*dec*) (declination)	1.2″	3.4″
Δ(*rot*) (rotation)	8.1″	54.5″

The viewed image is static, representing starry sky. Angles: *ra*, right ascension; *dec*, declination; *rot*, rotation in J2000.0 coordinate frame.

4.2 Dynamic starry-sky scenes

Dynamic star scenes represent scenes with transient changes in the attitude of the camera. Such scenarios correspond to a rotation of the camera, e.g., by the rotation of the spacecraft while orbiting Earth.

An analysis of dynamic scenes is used for the evaluation of the representativeness of the scenes together with the timing of OSVBS and the camera. A realistic flight-representative simulation has been carried out by mimicking attitudes measured by one of DTU's star-tracker camera onboard of the PRISMA satellite [4] during one orbit (Figure 6).

Attitudes assumed for image generation and attitudes obtained by the camera viewing the monitor (Figure 6) are very similar and highly correlated. The correlations between the measured and assumed angles of right ascension, declination, and rotation and their rates are 1.0 for zero time lag in all cases.

As in flight conditions, the differences between measured and generic attitudes are rate-dependent. The angular rates of the camera reach almost 2000 arcsec/s but are typically near 200 arcsec/s. The rates correspond to the low orbit height of the satellite. First-order polynomial fitting yields the dependency of the angular differences on the angular rates (Table 2).

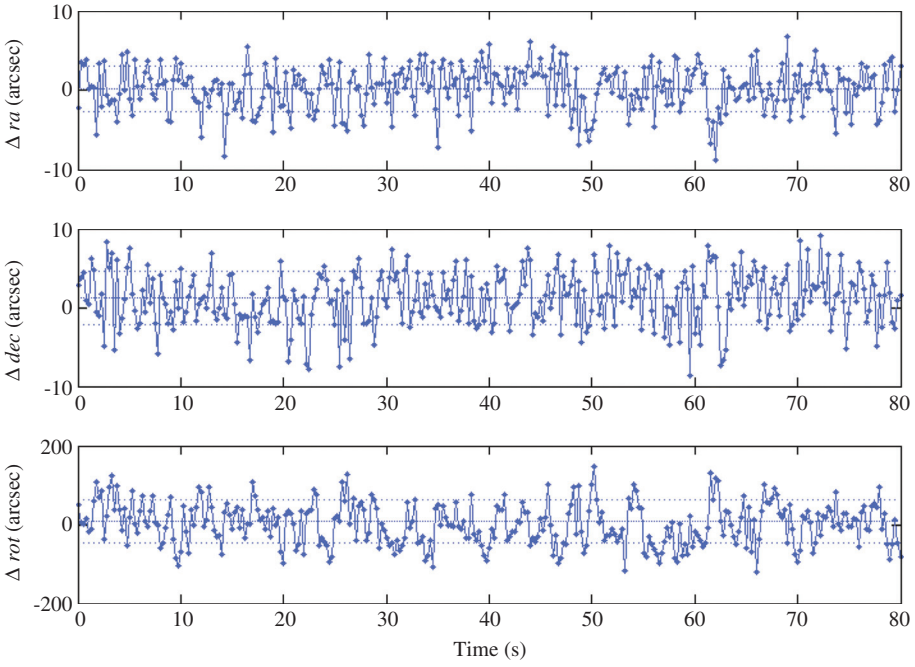

Figure 5 Angular differences between camera attitude solutions and values assumed for image generation. Camera attitudes are calculated by viewing a static starry-sky image. Straight lines: mean difference, dashed line: one standard deviation interval around the mean (compare Table 1).

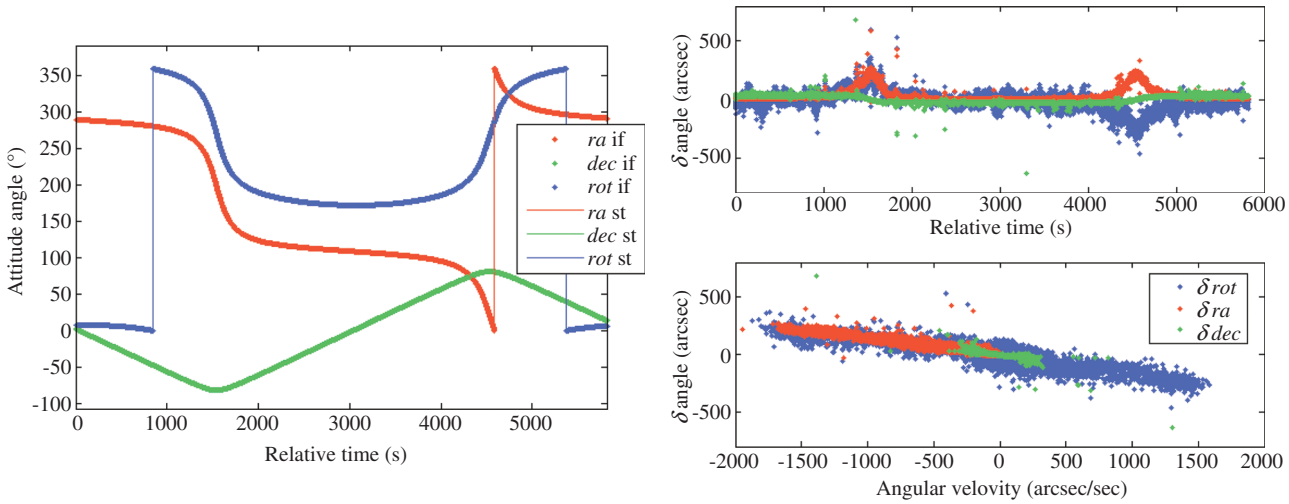

Figure 6 Dynamic scene: (left) Attitudes assumed for the generation of star images (dots) and the solutions of the camera viewing the monitor (thin line). Assumed attitudes are based on the in-flight camera solutions of PRISMA. Jumps in attitude solutions are related to the 360° angular periodicity. The simulated attitudes represent camera solutions of the PRISMA satellite [4] during one true orbit. Note that the dots are so close that they appear as a thick line on top of the thin line. (right) Angular differences (δ) for *ra*, *dec*, *rot* between camera solutions and values assumed for scene generation as function of flight time (top right) and angular velocity (lower right). Compare Table 2. Outliers correspond to missing or invalid solutions of the in-flight camera.

Table 2 Linear dependency of the angular differences Δ on the angular rates for *ra*, right ascension, *dec*, declination, *rot*, rotation.

	$\Delta/(d\Delta/dt)$ ["/("/s)]	Offset ["/("/s)]
Δ(*ra*) (right ascension)	-0.1	1.4
Δ(*dec*) (declination)	-0.1	0.8
Δ(*rot*) (rotation)	-0.1	-13.3

The offset values in rates in Table 2 represent the average differences a rate of zero arcsec/s (i.e., corresponding to still images) for the particular angle. The values confirm the observations from static star images.

The perfect correlation and the similarity between measured and assumed angles demonstrate that the stimulator is also able to represent dynamic scenes

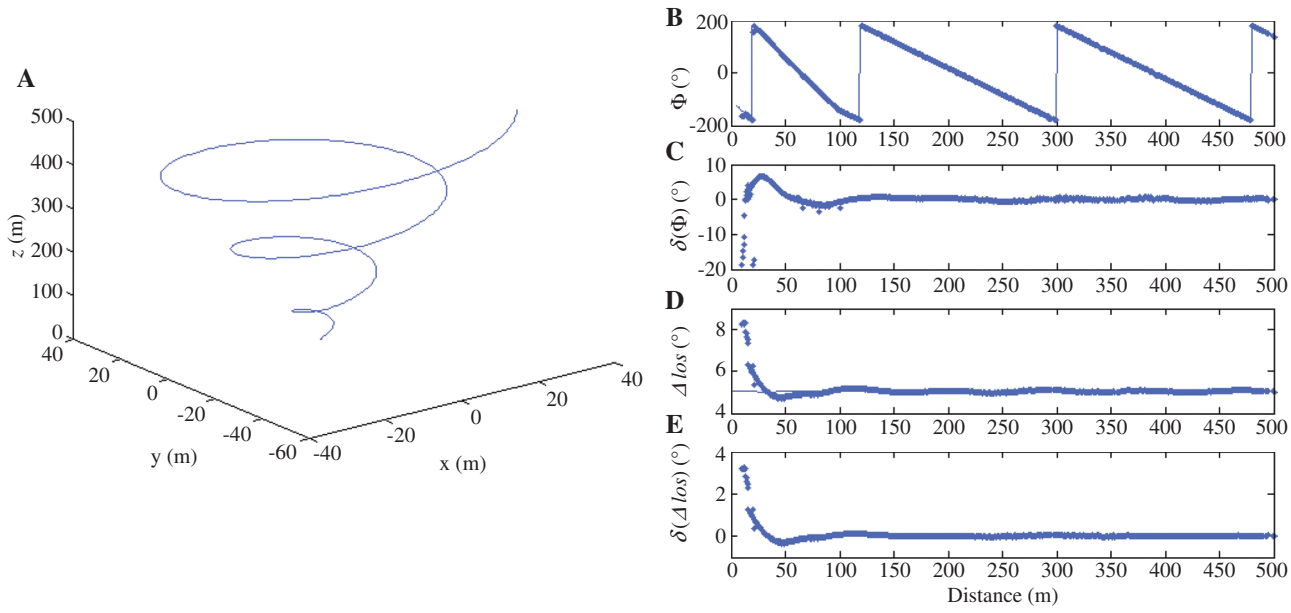

Figure 7 (A) Simulated flight trajectory of the viewing camera in the reference frame of the viewing camera. Angle Φ is the azimuth in the CCD plane of the camera, Δlos is the angle to the boresight. Both angles refer to the center of gravity of the spacecraft. (B, D) Camera observations (dots) and assumed values (line) for Φ and Δlos and their differences $\delta(\Phi)$, $\delta(\Delta los)$ (dots in C, E).

with high fidelity and that the timing of system is appropriate.

4.3 Spacecraft rendezvous

The approach of a spacecraft toward another spacecraft's camera view is simulated along a weakly elliptical helical trajectory at distances between 500 m and close up (Figure 7, left). The viewed spacecraft is a small model representing the PRISMA Tango spacecraft. With a size of about 0.8×0.8×0.4 m (scaling: of 1:1) and complex surface features, it represents a simplification of the real satellite. Owing to the shape of the flight trajectory, the spacecraft is viewed by the camera at different angles and different sides. Spacecraft detection by the camera is automatic.

The viewed spacecraft is detected, and the line-of-sight in the field-of-view of the camera is computed fully autonomously by the camera and retrieved by telemetry/telecommands. Viewing the monitor of the stimulator, the spacecraft is detected and located (Figure 7, right). The line-of-sight angles Φ (azimuth) and Δlos (angle to camera boresight) are successfully retrieved. Owing to the extent of the spacecraft and the complexity of the surface properties, the illumination intensity of the spacecraft is not centered around the center of gravity of the spacecraft. Therefore, distance-dependent deviations in the line-of-sight solutions from assumed values are expected and observed. These deviations are most visible at distances <100 m (Figure 7, right).

5 Conclusion

An optical stimulator for vision-based system (OSVBS) has been successfully developed and tested. The stimulator enables the involvement of a navigation camera in the loop during the simulation of various critical spaceflight scenarios such as attitude determination from star observations and the rendezvous and docking of spacecraft.

The representativeness of the camera stimulation increases with the fidelity of the scene image generation and projection. It further depends on the ability of the system to create images with the correct geometry in the field-of-view. We have employed powerful computer programs for scene rendering and developed software tools that guarantee high accuracy of the image geometry. Currently, available monitors that meet the system criteria use LED technology and retain a certain level of background illumination and provide a limited dynamic range. For low-intensity condition such as starry-sky or extreme high-light conditions, e.g., with the Sun near, within the field-of-view, this may require an adjustment of the camera shutter or integration time. With the availability of OLED monitors, this issue is expected to diminish soon at least for low-light conditions. The modularity of the OSVBS supports this development.

Owing to the involvement of the camera, including the camera head unit, in the image processing chain, OSVBS reaches a higher level of realism than other simulators without a camera in the loop such as pure computer simulation or direct scene injection into the data processing unit of the camera. The high geometrical accuracy of the camera stimulation allows for flight-representative operation of the camera in the loop.

The system is composed of low-cost hardware components that can be easily replaced to adapt to changing requirements. The robustness and relative simplicity in the hardware design is accomplished by software-assisted optical calibration and image manipulation. The careful mechanical setup and the combination of optical calibration and image postprocessing result in camera stimulation with high image accuracy and with long-term stability.

OSVBS can be used during the development and testing of new optical navigation sensors, for design tests of spacecraft maneuvers and for the validation of Attitude Determination and Control Systems (ADCS) in open and closed loop modes.

Acknowledgments: The development of this stimulator has received funding from GMV Aerospace and Defense SA within the framework of a project of the European Space Agency (ESA). Two anonymous reviewers are acknowledged for their helpful comments and Kevin Flemming for editorial suggestions. Both have led to significant improvements of the manuscript. We thank the entire staff at DTU Space, Measurement and Instrumentation, for their enthusiastic support throughout the project.

Received July 30, 2013; accepted March 6, 2014

References

[1] J.L. Jørgensen, A. Eiserman, C. Liebe and G. Jensen, in Proceedings of the 3rd ESA Symposium on Spacecraft Guidance, Navigation and Control Systems, ESTEC, ESA (1997).
[2] P.S. Jørgensen, J.L. Jørgensen, T. Denver and P. van den Breambussche, in Small Satellites for Earth Observation: Selected Proceedings of the 5th International Symposium of the IAA. Walter de Gruyter, 299-303, ISBN: 3-11-018851-1 (2005).
[3] M.M. Birnbaum, Acta Astron. 39, 763–773 (1996).
[4] J.L. Jørgensen and M. Benn, NordicSpace, 16–19 (2010).
[5] G. Rufino, D. Accardo, M. Grassi, G. Fasano, A. Renga and U. Tancredi, Int. J. Aerospace Eng. 2013, 13 pp. (2013).
[6] Astrium, A Minitiarized Star Tracker Optical Simulator. URL: http://www.astrium.eads.net/media/document/stos_2013-01.pdf, last visited: 15/10/2013 (2013).
[7] V. Barrena, P. Colmenarejo, D. Roessler, D.A.K. Pedersen and F. Ankersen, Use of In-Flight Data to Validate Mars Sample Return Autonomous RvD GNC, 63rd International Astronautical Congress, Naples, Paper code: IAC-12,D1,6,3,x16030 (2013).
[8] S. Parkes, I. Martin, M. Dunstan, D. Matthews and A. Milne, in 3rd International Workshop on Astrodynamics Tools and Techniques, ESTEC, ESA (2006).
[9] Celestia, http://www.shatters.net/celestia/, last visited on 15/10/2013.
[10] G. Bradski, A. Kaehler, in 'Learning OpenCV', (O'Reilly Media, Inc., Sebastopol, 2008). ISBN: 978-0-596-51613-0.
[11] D.C. Brown, Photogramm. Eng. 37, 855–866 (1971).
[12] J.G. Fryer and D.C. Brown, Photogramm. Eng. Remote Sens. 52, 51–58 (1986).

Dirk Roessler is responsible for the development of the hardware and the software of the stimulator. He worked at the Measurements and Instrumentation group at the National Space Institute, Technical University of Denmark, from 2011 to 2013. Roessler holds a diploma degree in Geophysics from the University of Leipzig, Germany and a doctoral degree in Geophysics from the University of Potsdam, Germany.

David A.K. Pedersen works with image analysis and develops methods and software related to DTU's microAdvanced Stellar Compass and Vision-Based System. Pedersen joined the Measurement and Instrumentation group at the National Space Institute, Technical University of Denmark 2011. Pedersen holds a MSc E.E. from the Technical University of Denmark.

Mathias Benn develops methods, software, and hardware related to DTU's microAdvanced Stellar compass and vision-based systems for closed-loop formation flying of spacecraft. He joined the Measurements and Instrumentation group at the National Space Institute, Technical University of Denmark, in 2007. Benn holds a MSc E.E. with focus on Space Technology and a PhD in Space Technology from the Technical University of Denmark.

John L. Jørgensen is Professor and Head of Measurement and Instrumentation division at the National Space Institute, Technical University of Denmark. Jørgensen is expert in space technology and systems such as rockets, satellites, and advanced measurement systems. He has developed the world's first fully autonomous star tracker camera. His research focus is on the development of technology for future spacecraft formation flying as a condition for many ambitious space missions such as manned expeditions to Mars, extremely large and precise telescopes, and Earth observation missions.

D Validation of Automatous Mars Sample Return GNC

IAC-12-D1.6.3

USE OF IN-FLIGHT DATA TO VALIDATE MARS SAMPLE RETURN AUTONOMOUS RvD GNC

Valentin Barrena
GMV, Tres Cantos (Madrid), Spain, vbarrena@gmv.com

Pablo Colmenarejo, Matteo Suatoni
GMV, Tres Cantos (Madrid), Spain, pcolmenarejo@gmv.com, msuatoni@gmv.com

Dirk Rößler, David A.K. Pedersen
DTU Space, Copenhagen, Denmark, dros@space.dtu.dk, dakp@space.dtu.dk

Finn Ankersen
ESA-ESTEC, Noordwijk, The Netherlands, Finn.Ankersen@esa.int

During the last years, the number of studies having as objective rendezvous and docking/capture missions around Mars or other planets/asteroids has significantly increased.

Following this tendency, a team led by GMV has developed HARvD (High Integrity Autonomous Rendezvous Docking Control System), an ESA-funded activity implementing a high integrity autonomous multi-range rendezvous and capture control system demonstrator for future exploration missions around Mars, Earth or potentially other planets, with a wide set of scenarios and particularizing on the MSR (Mars Sample Return) mission. HARvD is based on RF, camera and LIDAR measurements. It includes design, prototyping and verification at three different levels: algorithms design and verification in a Functional Engineering Simulator, SW demonstrator verified in Real Time Avionics Test Benching and Dynamic Test Benching.

Moreover, the technology readiness of the SW demonstrator will enable to envisage as a next step the in-flight demonstration of an autonomous docking and capture GNC system. In this respect, PRISMA mission was identified as a suitable platform for validation of the HARvD-GNC system, and the development, calibration and testing of a vision based optical stimulator (ViSOS by DTU) to enhance the on-ground validation capabilities. After checking different alternatives for the proposed HARvD-GNC experiment with PRISMA resources, an efficient but cost-effective approach was chosen. The approach is based on designing MSR-like dedicated manoeuvres sequencing using the already existing on-board PRISMA GNC/AOCS system (based on relative GPS measurements for the closed-loop execution of the manoeuvres sequencing and acquiring RF and camera images as part of the HARvD-GNC experiment data). This option allows downloading the sensor measurements and telemetry data from PRISMA to validate off-line essential functions of the HARvD-GNC, as well as calibrating and testing ViSOS system with real flight images. While the HARvD control system validation is limited by the nature of the off-line approach, it shall be highlighted that in this approach the on-board SW does not require modification. Such modifications are costly and complex. Therefore the results of the HARvD system validation can be maximized with respect to the involved effort.

This paper presents the experiment definition and development of the HARvD-PRISMA experiment and the use of the in-flight data as an economic way to achieve the testing and validation up to TRL6 of essential functions of the HARvD-GNC in the off-line approach. The approach itself is suitable to be applied to other systems and using other experiment hosting platforms.

I. INTRODUCTION

The HARvD (High Integrity Autonomous RVD Control System) activity included design, prototyping and testing at three different levels (Functional Engineering Simulator, Real Time Test Benching and Dynamic Test Benching) of a complete autonomous GNC system for a generic rendezvous and docking/capture scenario.

This system was developed and validated (for details see [3] and [4]) as shown in Fig. 1:

- The FES phase is based on simulations using Matlab/Simulink models and simulates the full system in no-Real Time.
- The next step is the RT test bench (RVD-RT). Here, the Simulink models are converted into C code with the dSPACE tools and compiled. While the real world is simulated in a dSPACE Board (real time simulator), the GNC on-board software is hosted and run in a LEON Board (on-board processor).

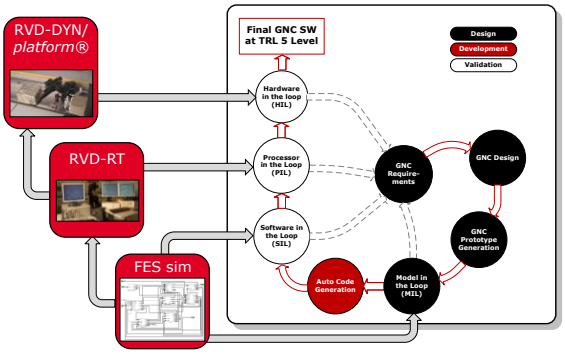

Fig. 1: HARvD development and validation chain

- The last step is the RVD-DYN Test Bench. In addition to the RT simulator, the sensor measurements are provided using real sensors stimulated through dynamic platforms fed by the dynamic and kinematics conditions (position, velocity, attitude and attitude rates) generated with the simulated real world, while the on-board software runs in the target processor.

Following the methodology used in this development and validation activity, the next natural step is the use of real flight data.

In this context, the PRISMA mission was identified as a suitable and cost-effective platform for the validation on-ground of the HARvD-GNC system using real data, and at the same time, the development, calibration and testing of a vision based optical stimulator (ViSOS by DTU) to be used for stimulation of optical sensors in on-ground testing, which will complement the current RVD-RT system used in the HARvD validation campaign.

The PRISMA mission (see [2]) consists of two satellites: Mango and Tango (see Fig. 2).

Mango is the chaser spacecraft; it is a 3-axis stabilized and has full 3D delta-V manoeuvrability independent of the spacecraft's attitude. Mango is equipped with three propulsion systems, where the main system, a hydrazine propulsion system with 6 thrusters, has approximately 120 m/s delta-V capability. The central body of Mango has exterior dimensions 750×750×820 mm. When deployed, the distance between the tips of the solar panels is 2600 mm.

Tango is the target satellite; it has a simplified, yet 3-axis stabilizing, magnetic attitude control system and no orbit manoeuvre capability. The Tango body is 570×740×295 mm.

The wet mass of the two spacecraft is approximately 190 kg. Mango is 150 kg and Tango is 40 kg.

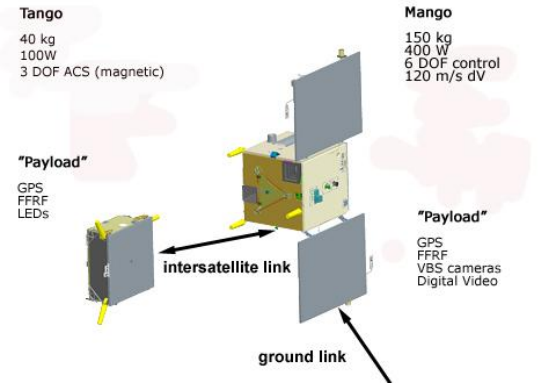

Fig. 2: PRISMA satellites

The validation of the HARvD control system with PRISMA flight data consists in the execution of MSR-like dedicated manoeuvres sequence using the PRISMA GNC/AOCS system, which is based on relative GPS for closed-loop execution of the commanded trajectories. During the scenario execution, measurements of relative and absolute sensors are acquired and downloaded to earth; they are later used off-line to feed the HARvD GNC demonstrator SW in order to validate its behaviour with real measurements. The PRISMA sensors compatible with the MSR scenario and therefore used to feed the HARvD GNC are:

- Formation Flying Radio Frequency (FFRF) sensor
- Vision Based Sensor (VBS) by DTU
- Gyroscopes
- Star Trackers
- Accelerometers

On the other hand, the data coming from the navigation filter on-board the chaser satellite (based on GPS measurements) are used as reference data for checking the HARvD navigation performance and GN(C) behaviour.

This paper is structured in the following sections:

- The first section provides details about the PRISMA HARvD experiment scenario definition
- The second section details the experiment development and execution and the flight data description
- The third section reports the validation approach using the flight data.
- The forth section describes the development, testing and calibration of the ViSOS.
- The last section provides the conclusions.

II. EXPERIMENT DEFINITION

The experiment scenario has been split in several sub-phases trying to make best use of the PRISMA spacecraft capabilities.

The first step has been to reach the experiment starting point corresponding to a distance of 20 Km between Tango and Mango on the target V-bar axis. Once achieved the starting point the experiment started with a Station Keeping (SK) and data from camera and RF sensor began to be collected for experiment purposes.

In the following ten orbits, homing manoeuvres have been carried out bringing the Main spacecraft to a closer relative position (~3000m) along the V-bar axis and maintaining it for another SK phase. The next position (around 200m from the Target) is reached by means of a couple of further homing orbits and the RF sensor is switched on low power mode.

To reach the next relative position of 50m along the V-bar axis a hopping manoeuvre during an half orbit has been executed and the position maintained with another SK period.

The long and intermediate range segments described above have then been followed by a set of Terminal RvD phases including:

- Forced motion manoeuvre up to 20m along the V-bar axis
- Forced motion manoeuvre up to 10m along the V-bar axis
- Forced motion retreat manoeuvre up to 15m along the V-bar axis
- Fly-around manoeuvre driving the Main spacecraft during 3 orbits with radius of 15m on V-bar and 7.5m on R-bar and centred on the Target spacecraft position.

The entire experiment scenario, divided in two parts (long/intermediate range up to 50m and RvD terminal part) is plotted in Fig. 3 and Fig. 4 (in along-track and radial).

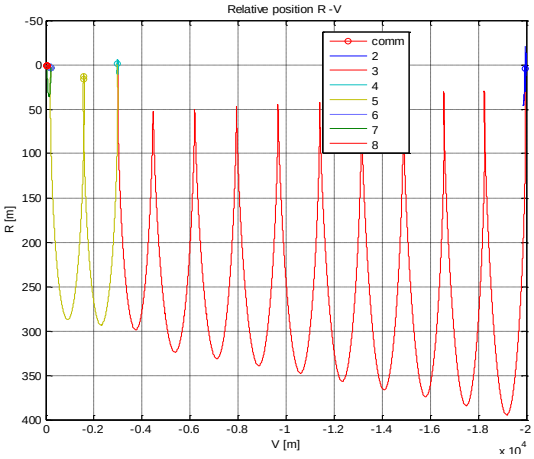

Fig. 3: PRISMA-HARvD Experiment Scenario – long/intermediate range part

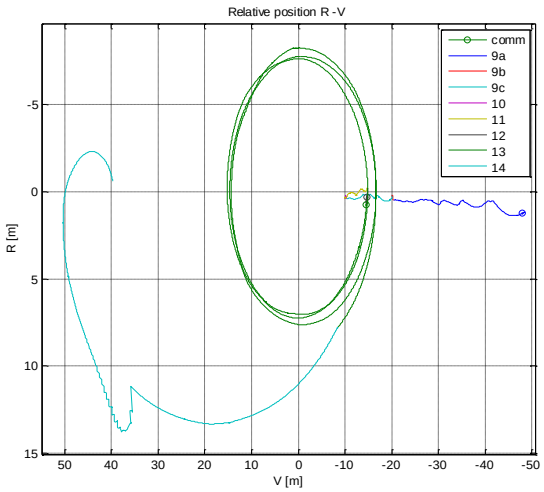

Fig. 4: PRISMA-HARvD Experiment Scenario – RvD terminal part

III. EXPERIMENT DEVELOPMENT AND EXECUTION

Table 1 sums up the experiment development including the nominal conditions of the start and the end for each phase.

N°	Step Description	Start Condition	End Condition
1	Orbit phasing. The MAIN carries out an orbital manoeuvre to achieve the experiment starting orbital phase angle wrt the TARGET	Experiment GO command	MAIN at experiment starting distance (~20 km)
2	Station keeping – Free drift Hold point. Collection of first experiment TARGET camera images and RF measurements	Experiment start command	Camera images and nominal (fine) RF mode measurements collection during 1 orbit
3	Approaching the TARGET through semi-major axis manoeuvre (homing)	RdV GO command	Estimated distance ~ 3 km
4	Station keeping – Free drift Hold point	MAIN placed at –V-bar at a distance of approx. 3 km	Ground GO command
5	V-bar approach through homing manoeuvres	Ground GO command	Estimated distance ~200 m
6	Station keeping – Free drift Hold point	MAIN placed at –V-bar at a distance of approx. 200 m	Ground GO command
7	V-bar approach through one hopping manoeuvre	Ground GO command	Estimated distance ~50 m
8	Station keeping – Free drift Hold point	Estimated distance ~50 m	Ground GO command
9a	V-bar forced motion approach	Ground GO command	Estimated distance ~20 m

Nº	Step Description	Start Condition	End Condition
9b	Station keeping – Free drift Hold point	Estimated distance ~20 m	Ground GO command
9c	V-bar forced motion approach	Ground GO command	Estimated distance ~10 m
10	Station keeping – Free drift Hold point	Estimated distance ~10 m	Ground GO command
11	V-bar forced motion retreat	Ground GO command	Estimated distance ~7.5-15 m as per free drift evolution
12	Station keeping – Free drift Hold point	Estimated distance ~15 m	Ground GO command
13	Fly around manoeuvre	Ground GO command	Ground GO command
14	Stop fly-around and end of experiment	Ground GO command	-

Table 1: Experiment Steps

It is worth mentioning here some practical aspect encountered during the experiment progress.

- The retreat phase to achieve the starting point of the experiment has been used to check the proper work of some equipment and preparing the spacecraft to the next phases. The RF sensor activation involved some difficulty, solved through parking the Main spacecraft on a fly around orbit (about 1900m from the Target) and resetting the RF sensor (see Fig. 5).

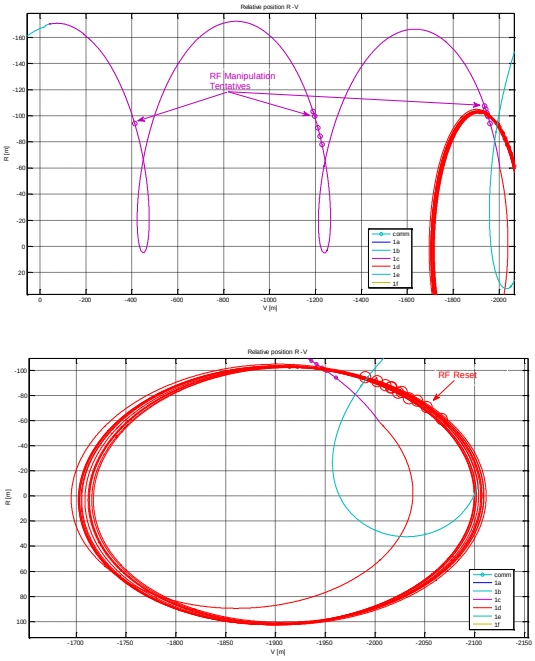

Fig. 5: Retreat phase and RF reset

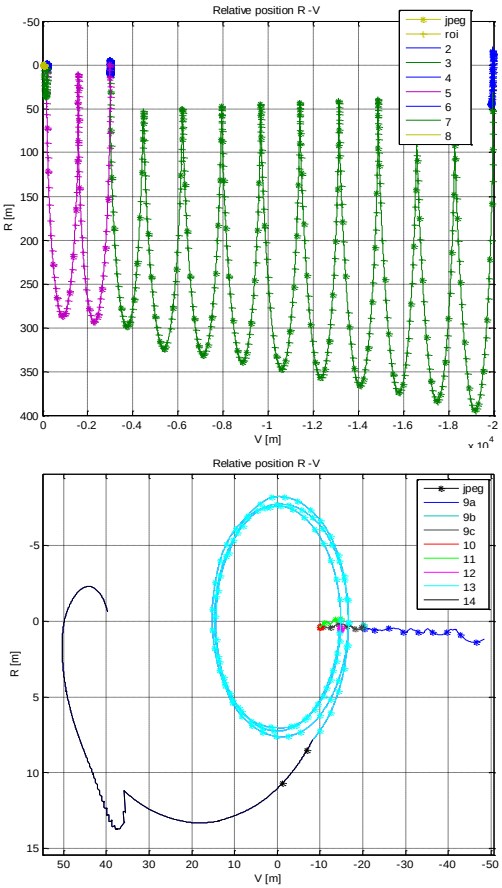

Fig. 6: Images acquisition during the experiment

- Throughout the experiment images have been acquired by means of the VBS camera in ROI format or in compressed JPEG. It is assumed that the VBS is able to distinguish the target S/C from other stellar objects and return only the ROI (reduced shots of 3x3=9 pixels) around the pixel where the target spacecraft is located. Fig. 6 shows the instants when the images are acquired, in particular the asterisk marks (*) are the JPEG images and the cross mark (+) are the ROI images. These images will be used for on-ground calibration/validation of the ViSOS system.

IV. VALIDATION APPROACH

As it has been mentioned, the PRISMA-HARvD experiment data is a cost effective way to achieve the testing and validation of some essential functions of the HARvD GNC SW demonstrator. However, due to the PRISMA mission has not been conceived taking into account the HARvD GNC design/implementation requirements, the obtained experimental data has been carefully analysed and manipulated to guarantee its

applicability to these functions of the HARvD GNC SW demonstrator.

The architecture of the HARvD GNC system is depicted in Fig. 8. From an analysis of the applicability of the validation with the PRISMA in-flight data for each function of the system, the following conclusions were extracted:

- **Navigation** function will be partially tested and validated up to TRL 6 during this activity. The Navigation module of the HARVD GNC SW Demonstrator is composed by two sub-modules:
  - Data-Pre-process: this module shall be updated to PRISMA in-flight data and cannot be considered as reaching TRL6.
  - Navigation Filters: this module is expected to achieve TRL 6 during this activity.
- **Impulsive Guidance** function: by executing the HARvD Guidance modules in open-loop using the navigation solution provided by the Navigation subsystem fed with PRISMA flight data and comparing with the PRISMA guidance outputs and dynamic evolution, it is expected to achieve TRL 6.
- **Forced motion Guidance and Control**: TRL6 level is not reachable, since this would require to execute those modules on-board in closed loop, which is not expected to be feasibly reproduced on-ground with the available PRISMA flight data.
  Nevertheless, HARvD continuous guidance and control modules will be simulated (with the PRISMA-HARvD Navigation subsystem in the loop) and the outputs will be compared with the real PRISMA dynamic evolution together with the associated information about manoeuvres triggering. The objective is TRL5.
- **Autonomous Mission Management (AMM) and Fault Detection Isolation and Recovery (FDIR)** are not considered, since AMM function will be substituted by an AMM emulator (compatible with PRISMA mission), and FDIR validation is not in the scope of this activity.

The validation approach using PRISMA in-flight data is based on the reuse as much as possible of the HARvD GNC breadboard environments and the adaptation of the HARvD GNC SW Demonstrator to make it compatible with the PRISMA sensors metrology, adapting type and number of inputs, frequencies, data formats and GNC operation modes.

However, it is needed an adaptation also of the three HARvD GNC testing environments (RVD-FES, RVD-RT and RVD-DYN –using GMV's *platform*® dynamic test bench-) in order to use the same validation methodology that the one used during the HARvD activity, which was based on three consecutive steps (see Fig. 9, for further details see [3] and [4]):

- First step based on the adjustment and preliminary GNC validation using Functional Engineering Simulator (full simulation under Matlab/Simulink/Stateflow, RVD-FES);
- Second step, the assessment of the HARvD GNC real-time performances in a Real-Time Test Bench (autocoded software demonstrator on a LEON processor board, RVD-RT); Adaptation/upgrade of the environment to the PRISMA scenario is required in order to allow the use of ViSOS and VBS sensor in the loop.
- Last step, validation considering all the effects due to the use of real hardware in an environment with real dynamic (RVD-DYN based on *platform*® dynamic test bench). Upgrade to the PRISMA scenario is required in order to permit the use of the VBS sensor. For details about the *platform*® facility see [5].

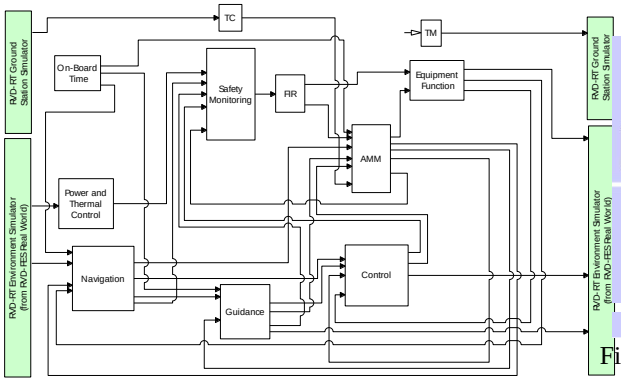

Fig. 8: HARvD GNC system high level architecture

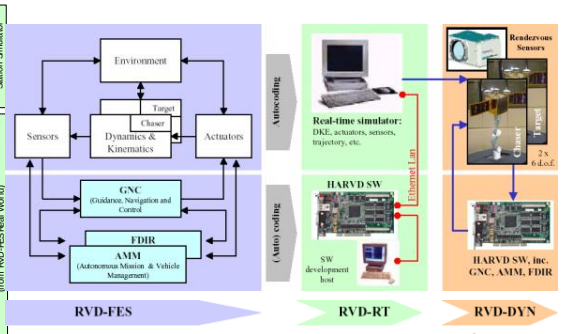

Fig. 9: HARvD Step-wise Development, Verification & Validation Approach

The in-flight metrology measurements are associated to the executed trajectories by the PRISMA on-board control. This means, that only the navigation module and some translational guidance functionalities can be directly tested with open loop execution and compared with flight results. On the other hand, forced motion guidance and control functionalities cannot be directly tested, since it implies close-loop execution. Therefore, for the validation of the full GNC system (including control module) synthetic data will be used. They are defined as ground generated data, either SW simulated or with HIL (Hardware In the Loop), and including specific flight data characteristics, such as biases, noises, and additional metrology parameters, characterized with the analysis of the in-flight data by configuring the HARvD sensor Simulink models.

For this reason the validation approach (see Fig. 10) consists of two main phases:

- Phase-1, where the HARvD GNC SW demonstrator is tested in open loop using the PRISMA experiment in-flight data.
- Phase-2, where the outputs of the PRISMA-HARvD GNC SW demonstrator, assessed with close-loop simulations, are compared w.r.t the outputs obtained during the PRISMA-HARVD experiment.

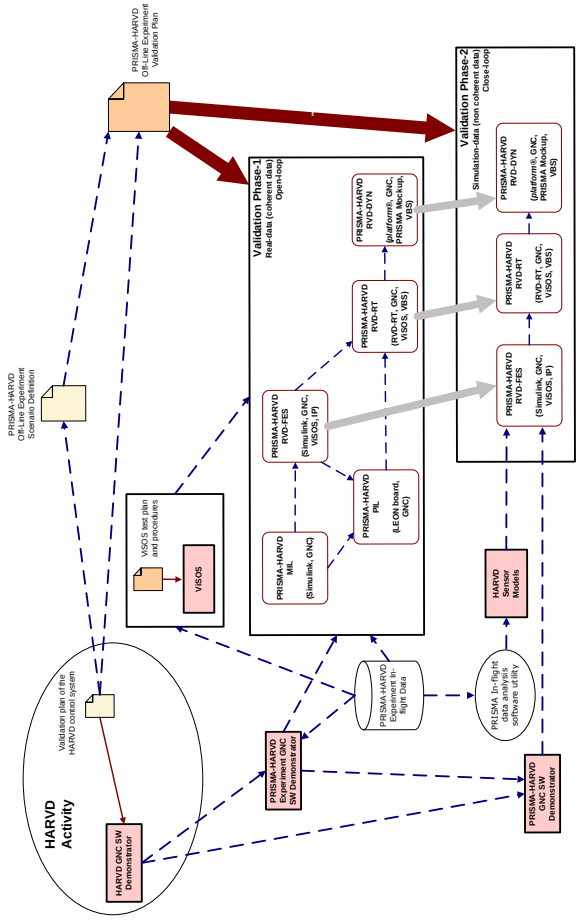

Fig. 10: HARvD validation with PRISMA flight data approach

Validation Phase 1

A modified approach of the HARvD validation methodology is used. The PRISMA-HARvD experiment on-ground reproduction will be performed in four consecutive steps:

- **MIL**: the HARvD GNC will be slightly modified at Simulink level to make it compatible with the real sensors interface and will be assessed using MIL (Model in-the loop). The experiment in-flight data will be read from file inside of Simulink and the data provided to the PRISMA-HARvD GNC. During this first step, potential changes necessary to adapt the HARvD GNC system for the on-ground reproduction experiment have been discovered and implemented. The outputs will be compared w.r.t the reference outputs (relative trajectories computed with relative GPS and delta-V executed on-board).
- **PIL**: the PRISMA-HARvD GNC will be converted to C-code using auto-coding tools. The generated GNC C-code will be assessed in a non-real time PIL (Processor In the Loop) environment, embedding it in a LEON board and feeding it with the in-flight data. The outputs will be compared w.r.t the MIL outputs and the reference outputs.
- **RVD-RT (HIL)**: the RVD-RT will be enhanced with HIL capabilities. The test bench will be upgraded with interfaces to the ViSOS and to VBS sensor in order to allow image processing validation in a real time environment. The architecture of the enhanced RVD-RT is depicted in Fig. 11. Two levels of validation will be performed:
  - The outputs of the VBS will be compared with the PRISMA-HARvD in-flight VBS data, in order to calibrate the ViSOS/VBS integration and validate its working inside the RVD-RT.
  - The outputs of the PRISMA-HARvD GNC SW will be compared w.r.t the results obtained in the MIL testing and the reference outputs. Moreover, real time performance will be assessed.

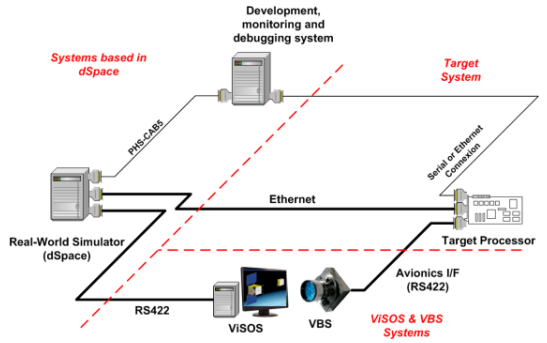

Fig. 11: High level architecture of upgraded RVD-RT

- **RVD-DYN:** the RVD-DYN will be adapted to the PRISMA experiment scenario. In this sense, it is important to take into account PRISMA mission characteristic (specially the spacecraft mock-ups and the mounting of the VBS system) and the PRISMA-HARvD experiment executed trajectories. The RVD-DYN adaptation will be performed at three levels: configuration baseline (based on the limited dynamic range); scalability of scenario to be compliant with the GMV's *platform*® operational range; set-up and calibration of the Electrical Model (EM) of VBS sensor. The architecture of the enhanced RVD-DYN is swown in Fig. 12.
  As in the previous step, the validation will be performed at two levels:
  - The outputs of the EM sensor will be compared with the PRISMA-HARvD in-flight sensor data. This also allows us to calibrate the *platform*® facility and the integration of the VBS sensor EM inside it in real dynamic conditions.
  - The outputs of the PRISMA-HARvD GNC SW will be compared w.r.t the results obtained both in the MIL and RVD-RT testing and wrt the reference outputs.

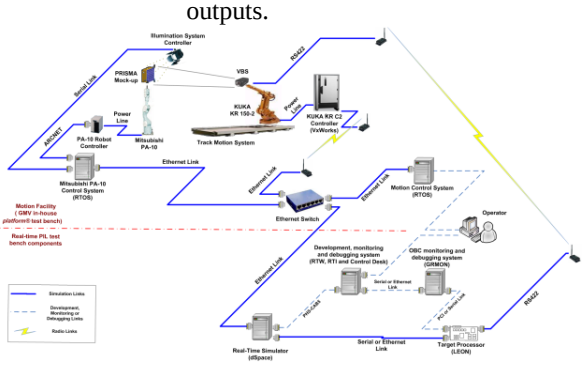

Fig. 12: High level architecture of upgraded RVD-DYN

Validation Phase 2

The validation approach used during this phase follows the same approach defined in the HARvD validation methodology. The following steps will be executed:

- **RVD-FES**: the MIL environment generated during validation phase-1 will be enhanced with the Real World model inherited from HARvD. This Real World models will include all the sensor models tuned with the PRISMA in-flight data analysis and post-processing. The PRISMA experiment scenario will be re-run using the PRISMA-HARvD GNC in close-loop and the results will be compared w.r.t the experiment in-flight data.
- **RVD-RT**: the part of the real world of the PRISMA-HARvD RVD-RT is adapted to the specific configuration of the PRISMA mission (especially the metrology set). The adapted PRISMA-HARvD RVD-FES real world is auto-coded and executed on the RT facility (based on dSpace, see [7]), but maintaining the ViSOS and VBS system in the loop (as defined in the validation phase-1). The PRISMA-HARvD experiment scenario is re-run, with the GNC in closed loop, using this enhanced RVD-RT test bench and the results are compared w.r.t the experiment in-flight data.
- **RVD-DYN**: the RVD-DYN is updated with the RT facility built in the PRISMA-HARvD RVD-RT. Note that the sensor models have been tuned using PRISMA in-flight data, therefore the spacecraft characteristics should be maintained (specially the TARGET geometry).
  Since only one mock-up is envisioned in the frame of this activity and the scalability methods for optical cameras are based on the idea of proportionally scaled mock-ups, the operational range of the dynamic scenarios (to be executed in the RVD-DYN) is dramatically reduced. This constrains the tests based on VBS to be performed in the frame of this activity (only terminal phases, < 15 m, are a priori to be assessed in the *platform*® test bench using a mock-up with scale 1:1).
  Therefore, and as it was identified in the previous validation phase, it will be very important to take into account PRISMA mission characteristic that impact on the sensor models (specially the spacecraft mock-ups – scalability issue- and the sensor set-up).
  The PRISMA-HARvD experiment will be re-run using the PRISMA-HARvD RVD-DYN test bench and the results will be compared w.r.t the experiment in-flight data.

The results of the simulation campaigns in the different test benches will be carefully analysed so as to assess the performances and behaviour of the PRISMA-HARvD GNC SW demonstrator and the traceability towards the performances and behaviour of the HARvD system.

IV. VISOS DEVELOPMENT, CALIBRATION AND TESTING

ViSOS generates calibrated images and uses them to stimulate optical sensors such as DTU's VBS.

Images are generated based on pre-defined scenes and trajectories. ViSOS allows stimulation by images representing starry sky images, spacecraft and natural celestial bodies. For image generation, off-line rendering and rendering in the loop is considered. Image generation is controlled within the RVD-RT test bench.

The ViSOS system provides stable and flexible interface to VBS and other optical sensors. This flexibility allows simulation of a variety of satellite missions and manoeuvres.

The fidelity of the stimulated images is validated against real-sky images and the on-ground scene assumptions made to generate the images. In particular generic camera attitudes, real-sky images of starry sky and of spacecraft viewed by the optical sensor are considered along with camera images from an on-ground spacecraft mock-up model.

Valid calibration of the optical system and optical stability of simulated images in the field of view of the optical sensor are crucial for meaningful and repeatable analysis of the output of the optical sensor. Therefore, a mechanically stable connection between the optical sensor and the stimulator is realised and the long-term stability is tested. Repeated system calibration assisted by calibration software and DTU's VBS as the optical sensor is carried out.

In this way, the optical sensor can be used in the loop and the effects of the optical sensor on TM data are accounted for. The use of DTU's VBS as the optical sensor in the loop therefore increases the performance and the realism of on-ground RVD-RT test bench.

The ViSOS system will be tested by simulating SC attitude determination based an the VBS's star tracker capabilities as well as RvD manoeuvres at distances ranging from a few kilometres to near close-up. The simulation will include a variety of different light condition with SC, sun and planetary objects at different relative positions.

Therefore, ViSOS is a important tool to simulate to simulate, study and train complex flight conditions in space.

Acknowledgement:
The use of data from DTU's VBS onboard the PRISMA mission is acknowledged.

V. CONCLUSIONS

This paper has presented the use of PRISMA in-flight data for the increase of the validation level of the HARvD GNC system, and the development, calibration and testing of a visual optical stimulator, which is a useful tool for on-ground validation of optical sensors and navigation function based on them.

This type of on-ground validation, thanks to the use of real sensors measurements in the loop, leads to increase the Technology Readiness Level up to 6, as per ESA definition.

Consolidated results of the HARvD GNC using PRISMA in fling data will be available at the end of 2012.

VI. REFERENCES

[1] L. Strippoli et al., *Advanced GNC solutions for Rendezvous in Earth and Planetary exploration scenarios*,59th International Astronautical Congress 2008, Glasgow, Scotland

[2] http://www.ohb-sweden.se/Prisma

[3] Colmenarejo, P. et Al., (2012).*Autonomous GNC Rodmap for Mars Sample Return Mission*. Global Space Exploration Conference 2012, 22-24 May 2012,Washington DC, USA.

[4] Colmenarejo, P. et al., *HARVD Development, Verification and Validation Approach (from Traditional GNC Design/V&V Framework Simulator to Real-Time Dynamic Testing)*. 7th International ESA Conference on Guidance, Navigation & Control Systems, 2-5 June 2008, Tralee, County Kerry, Ireland.

[5] V. Barrena et al., *Integrated Development, Verification and Validation Approach for Space Systems Using Autocoding Techniques*, Data System in Aerospace Conference (DASIA 2008), 27-30 May 2008, Palma Majorca, Spain

[6] Suatoni M. et al., *Use of COTS robotics for on-ground validation of space GNC systems: Platform Dynamic Test Bench*. ESA International Symposium on Artificial Intelligence, Robotics and Automation in Space, 4-6 September 2012, Turin, Italy.

[7] http://www.dspace.com/en/pub/home.cfm

E Prisma-HARVD Off-line Experiment Summary Report

Measurement & Instrumentation Systems

National Space Institute

Technical University of Denmark

ViSOS
Prisma-HARVD Off-line Experiment
Summary Report

Prepared for: GMV Aerospace and Defence, S.A.U.
Prepared by: ASC Team

Issued by: Dirk Rößler
David A. K. Pedersen

Approved by: Peter S. Jørgensen

Ref.: HARVD-DTU-TN-3091 Issue 1.0
Date: March 10, 2014

Change Record

Version	Date	Changed paragraphs	Remarks	Author
1.0	10/03/2014		New Release	D. Rößler D. A. K. Pedersen

Table of Contents

1 Scope

This document provides the summary report describing the conducted activities and the results obtained by DTU during the Prisma-HARVD Off-line Experiment.

2 Documents

2.1 Applicable documents

AD 1. HARVD-DTU-RQ-3001, TN 1-5, "Requirement specifications", version 1.7, 29/11/2012
AD 2. HARVD-DTU-TN-3073, TN 1-6, " VISOS concept Review, Trade-Off and Selection", version 1.5, 29/11/2012
AD 3. HARVD-DTU-TN-3080, TN 1-7: "ViSOS Definition Report", issue 1.1, 29/10/2012
AD 4. HARVD-DTU-PL-3026, TN 1-8: "ViSOS development, testing and acceptance plan", issue 1.2, 20/12/2012
AD 5. HARVD-DTU-MA-3013, "ViSOS software manual", issue 1.3, 04/12/2012
AD 6. HARVD-DTU-TN-3081, "ViSOS mechanical assembly", issue 1.3, 19/12/2012
AD 7. HARVD-DTU-TR-3055, TR 1-4: "ViSOS acceptance test report", issue 1.2, 19/12/2012
AD 8. HARVD-DTU-TR-3056, TR 2-4: "VISOS calibration and validation test results" 1.0, 10/04/2012
AD 9. HARVD-DTU-TR-3089, TN 1-9: "Mock-ups Realisms Level Assessment" 1.0, 10/04/2012
AD 10. IoD-PANGU-SUM, PANGU, Planet and asteroid natural scene generation utility, user manual, issue 3.30, 13 December 2011.
AD 11. UoD-PANGU-VSC-TN05, "Virtual Spacecraft Image Generator, TN05: PANGU Enhancements", issue 1.0, 15/12/2011
AD 12. UoD-PANGU-VSC-TN01, "Virtual Spacecraft Image Generator, TN01: Importing Spacecraft Models", issue 1.0, 15/12/2011

2.2 Reference documents

3 Acronyms

BBO	Big Bright Object
COTS	Component Of The Shelf
dec	Declination
DPU	Data Processing Unit
EFL	Effective Focal Length
FFRF	Formation Flying Radio Frequency
GPU	Graphics Processing Unit
FoV	Field of View
HW	Hardware
Kappa	VBS lens distortion parameter
LoS	Line of Sight
mag	viewer.star_magnitudes, PANGU parameter
MDM	Micro-D Metal Miniature, D shaped connector type
NSO	Non-Stellar-Object
ra	Right ascension
ROI	Region Of Interest
rollVBS	Rotation angle computed by VBS
rollP	Roll angle considered by PANGU, rollP = 270º - rollVBS
SC	Spacecraft
SW	Software
TC	Telecommand
TM	Telemetry
VBS	Vision Based Sensor
ViSOS	Vision-based Sensor Optical Stimulator
x_0, y_0	Coordinates of principle point of camera

4 Delivery documents

An overview of the delivered documents during the Prisma-HARVD off-line experiment:

1) HARVD-DTU-RQ-3001, TN 1-5, "Requirement specifications", version 1.7, 29/11/2012

The scope of this document is to provide a review and an analysis of the system and the requirements for ViSOS and possible technological solutions.

2) HARVD-DTU-TN-3073, TN 1-6, " VISOS concept Review, Trade-Off and Selection", version 1.5, 29/11/2012

The scope of the document is to provide a review about existing system components that can be employed and integrated for building the VISOS. The documents contain a trade-off analysis of candidate conceptual VISOS designs and relate these solutions to possible applications of ViSOS. Together with the analysis of the system, we conclude on the preferred general design, define the system requirements and highlight appropriate system components.

In this document we summarize existing candidate systems scene stimulation, evaluate software solutions based on PANGU and DTU-own software solutions, study special-case applications, synthesize the findings from aforementioned studies and propose an integrated system that meet the requirements for ViSOS. The proposed system consists of both hardware and software solutions.

3) HARVD-DTU-TN-3080, TN 1-7: "ViSOS Definition Report", issue 1.1, 29/10/2012

This document describes the embedding of ViSOS within the Prisma-HARVD off-line experiment, the design setup of the VISOS HW and SW components and the ViSOS manufacturing. The document provides the part, material and process list and the performance analysis. It further provides description of the interface to the camera and an example of a camera setup.

4) HARVD-DTU-PL-3026, TN 1-8: "ViSOS development, testing and acceptance plan", issue 1.2, 20/12/2012

This document describes all HW manufacturing and SW development, the testing and acceptance plan of the VISOS hardware and software components. It provides high-level system requirements in addition to the low-level requirements in [AD 1, AD 2]. The test plan as well as the acceptance and failure criteria of all tests including the system functional performance verification, system calibration, and image and SC models realism evaluation is given therein.

5) HARVD-DTU-MA-3013, "ViSOS software manual", issue 1.6, 06/05/2013

The scope of this reference manual is to describe the operations of the ViSOS SW. The manual explains the operation of the system calibration and the manipulation of PANGU-created images in order to stimulate the camera. It further describes the timing of the image manipulation SW by the computer time or by an external PPS timing signal.

This manual enables the reader to compile and to operate the calibration and manipulation SW and to deliver the required parameters to PANGU which are specific to this application. The given input parameters to PANGU enable the user the interfacing between PANGU image generation and the image manipulation SW.

6) HARVD-DTU-TN-3081, "ViSOS mechanical assembly", issue 1.3, 19/12/2012

This document describes the mechanical assembly of the ViSOS optical stimulator.

7) HARVD-DTU-TR-3055, TR 1-4: "ViSOS acceptance test report", issue 1.2, 19/12/2012

This document describes the results of the functional tests of VISOS hardware- and software components carried out by DTU during WP3200. The document contains the limitations found during the tests.

8) HARVD-DTU-TR-3056, TR 2-4: "VISOS calibration and validation test results" 1.0, 10/04/2012

This document describes the results of the ViSOS calibration and validation test results carried out by DTU during WP6100 of the Prisma-HARVD Off-line Experiment. The document contains the limitations found during the tests.

9) HARVD-DTU-TR-3089, TN 1-9: "Mock-ups Realisms Level Assessment" 1.0, 10/04/2012

This document describes the results of the assessment of the level of realism of the PRISMA Target SC models carried out by DTU during WP6200 of the Prisma-HARVD Off-line Experiment. The document contains the limitations found during the tests.

5 List of tests

Tests have been performed for validation of the functioning and for calibration of ViSOS as well as for evaluation of the representativeness of generated scene with respect to DTU in-flight experiences. The tests are summarized in Table 1.

Table 1: Summary of tests carried out during the project in WP3200, WP6100 and WP6200. **A**: test accepted, **AL:** test partially accepted / accepted with limitations, **F:** test failed.

ID	Description	A	AL	F	Comments
WP3200					
1.1	Validity of long-term HW operation	x			
1.2	Setup of dual monitor	x			
1.3	Ethernet connection: file transfer, PPS: reception, TM/TC packages: reception, sending	x			
1.4	SW support by computer HW	X			
2.1	PANGU image realism		x		Appropriate scaling of star intensity required
2.2	PANGU image geometry		x		Adjustment of assumed EFL and image post processing (DTU SW) are required
2.3	PANGU image generation, non-cooperative SC models		x		Limitation and instabilities in PANGU image generation
2.4	PANGU image generation, cooperative SC models		x		Limitation and instabilities in PANGU image generation, low light intensity
3.1	ViSOS monitor: spectrum	x			
3.2	ViSOS monitor: pixel defects	x			
3.3	ViSOS monitor: uniformity, black	x			
3.4	ViSOS monitor: uniformity, white	x			
3.5	Temperature stabilisation	x			
4.1	ViSOS monitor: mounting	x			
4.2	Camera tower: mount	x			
4.3	Camera: mount	x			
4.4	Response to monitor	x			

	setup				
4.5	Response to warm-up	X			
4.6	Long-term stability	x			
5.1	Light cage: visual inspection	X			
5.2	Ligh cage: camera test with black image	x			
5.3	Ligh cage: camera test with white image	x			
6.1	Calibration: Focusing of camera	x			
6.2	Calibration: corner extraction	x			
6.3	Calibration: convergence	X			
6.4	Calibration: accuracy of lens distortion	x			
6.5	Calibration: accuracy of monitor pose and range	X			
6.6	Calibration: mechanical adjustment of CHU	X			
6.7	Calibration: sensitivity to calibration setup.	X			
7.1	Realism of star images	x			
WP6100					
6.8	Calibration of rotation stage	X			
6.9	Calibration of translation stage	X			
8.08	Calibration of gamma correction	X			
8.09	Calibration of star intensity	X			
8.1	Calibration of image pixel resolution for images showing stars	X			The applied oversampling in PANGU can result in images with errors.
8.2	Scene representativeness: planet in camera FoV		X		Stray light effects are not simulated.
8.3	Scene representativeness: planet in camera FoV			X	The brightness of Sun is generally not representative of in-flight images in PANGU images.
8.4	Scene representativeness: dynamic star images	X			

WP6200					
9.0	Star intensity scaling	X			
9.1	SC model evaluation		X		SC invisible beyond 1800 m, model-dependent
9.2	Calibration of image pixel resolution for image showing SC models	X			
9.3	VBS solutions: static images	X			
9.4	VBS solutions: dynamic images		x		SC invisible beyond distances of 1600 m, increased noise level above 850 m, partial loss in solutions near 600 m
WP3200					
11.1	HW practicality: setup, transportation, operation	X			
11.2	SW practicality: operation of calibration	X			
11.3	SW practicality: operation of image manipulation	X			

6 Execution Summary

ViSOS is an optical ground support equipment to optically stimulate a camera. ViSOS can be used as test bed for RvD operations with a camera in the loop for proximity operations of cooperative and non-cooperative targets as well as for proximity operations and landing on small bodies.

ViSOS has been carefully designed, developed and tested. The following execution summary reports on the outcome of these activities. The major results from testing based on the tests in Table 1 are explained.

6.1 ViSOS development, operation and calibration

6.1.1 Selection of system solution

The system shall be used to stimulate a camera with scenes in space at a high level of fidelity and representativeness of the camera system. The scenes include:

1. Distant stars, Sun, Earth, Moon and other planets in front of deep, dark space;
2. Target spacecraft illuminated by Sun and planetary albedo at camera distances between 1 and 1000 km. Stars, planets and bright objects such as Sun, Earth and Moon in front of deep, dark space;
3. Target spacecraft illuminated by Sun and planetary albedo at camera distances of up to 1 km without stars in the background. If stars are visible in other real-world situation then they should also be represented;
4. Target spacecraft illuminated by sun and planetary albedo at camera distances between 4 m and 80 m from Main (non-cooperative mode) with or without bright objects such as Sun, Earth and Moon in front of deep, dark space. Known spacecraft features are visible;
5. Target spacecraft with active feature points (cooperative mode) at camera distances of 0.2 - 60 m. Depending on view direction, bright objects such as Sun, Earth, Moon or other small objects in front of deep, dark space are visible.

In order to reach representativeness of the camera system, the stimulated camera must include the CHU and the DPU. CHUs with panchromatic CCD sensors and pixel resolution of up to 1024 x 1024 px are to be considered. Therefore, the ViSOS must stimulate the camera by an optical signal, i.e. an image. The image can be projected by a monitor or a projector and viewed by the camera.

Other solutions such as direct injection of the scene signal into the camera DPU or pure computer simulation do not involve the CHU and are not assumed.

The ideal image representing the scenes must have correct geometry with long-term stability, correct illumination and update rates which are appropriate for the considered camera. Ideally, all scene objects must be free of spatial and temporal aliasing, the optimal optical signal has a continuous spectrum such as of Sun (Figure 1), a brightness contrast of about 25000:1 and a luminous intensity of 100 to 1200 cd/m2, depending on the distance of the source of the signal to the CHU. The image projector must be free of image retention in order to enable long-time camera stimulation with static scenes.

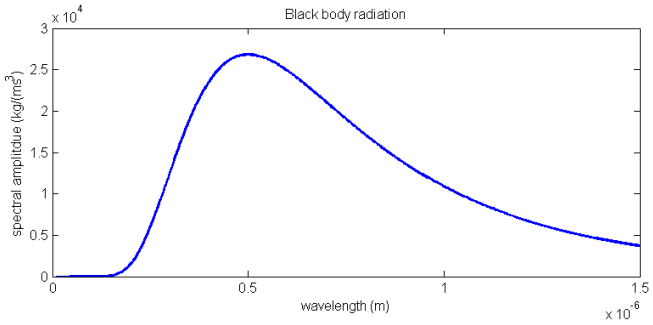

Figure 1: Black body radiation (blue line) at 5800 K (Sun) for wavelengths between 10 and 1500 nm.

The stimulator shall further be modular, reasonably sized for use in normal offices and made up of COTS that can later be replaced to account for technological advancements. For scene generation, the PANGU SW, version 3.30 [AD 10] is available and used.

COTS that are able to meet all requirements are currently unavailable. Therefore, DTU has chosen the optimum solution in which a camera is stimulated by a COTS LED monitor that is viewed by the camera CHU (Figure 2). If necessary, focusing of the CHU on the monitor screen is realized by a focusing optics in front of the CHU. The scene images are generated on an external computer (ViSOS computer).

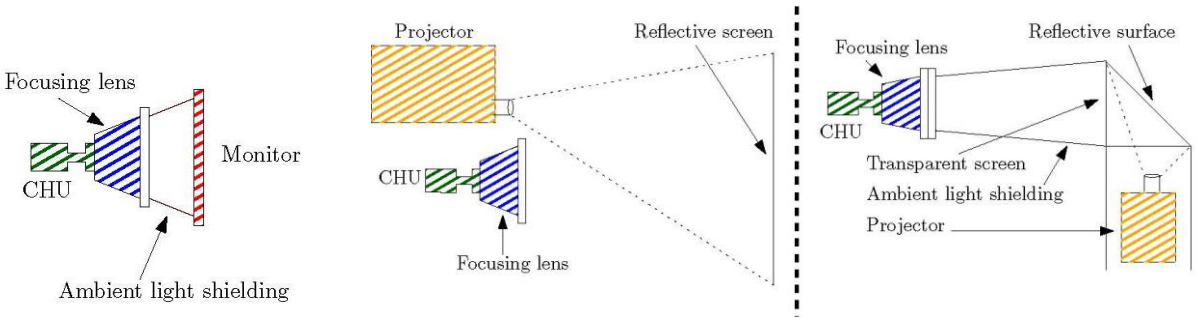

Figure 2: Candidate solutions of ViSOS with a scene generating monitor (left), a front projector with a screen (centre) or a rear projecting system (right) viewed from the CHU of a navigation sensor.

6.1.2 ViSOS system setup

ViSOS has been designed to operate in open or closed loop embedded between a Real-World Simulator and a Target Processor that connects to a camera (Figure 3). The camera is connected to ViSOS via a mechanical interface on the camera tower (Figure 6). It views the ViSOS monitor but is not a part of ViSOS.

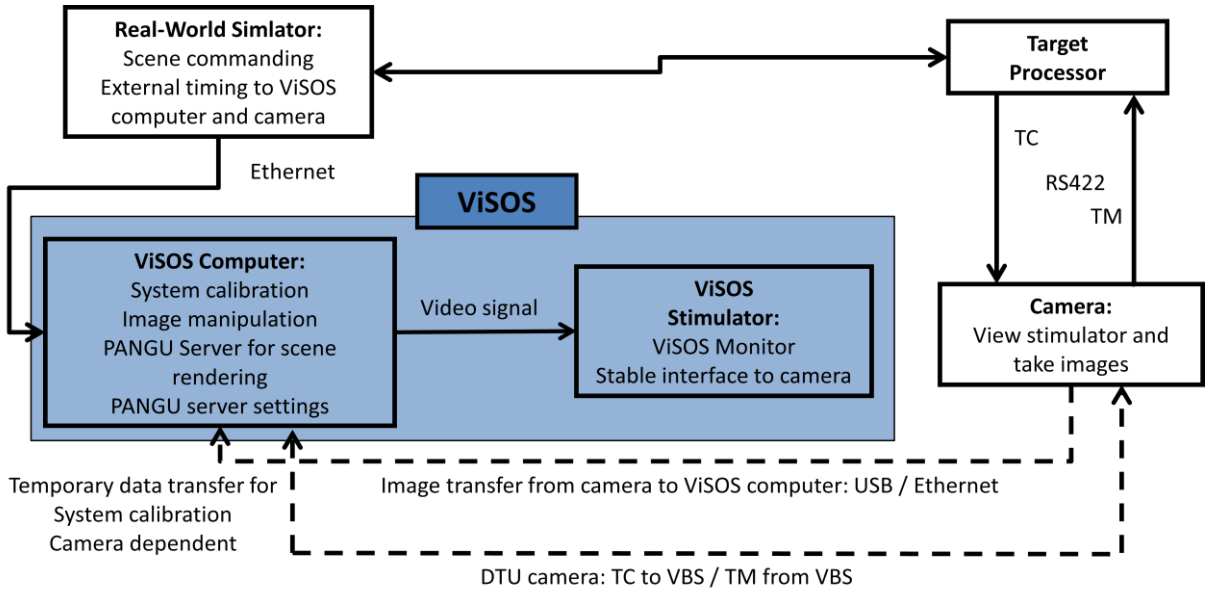

Figure 3: Embedding of ViSOS (blue).

ViSOS consists of two principle parts: the ViSOS PC and the ViSOS scene stimulator (Figure 4, Figure 5 and Figure 6).

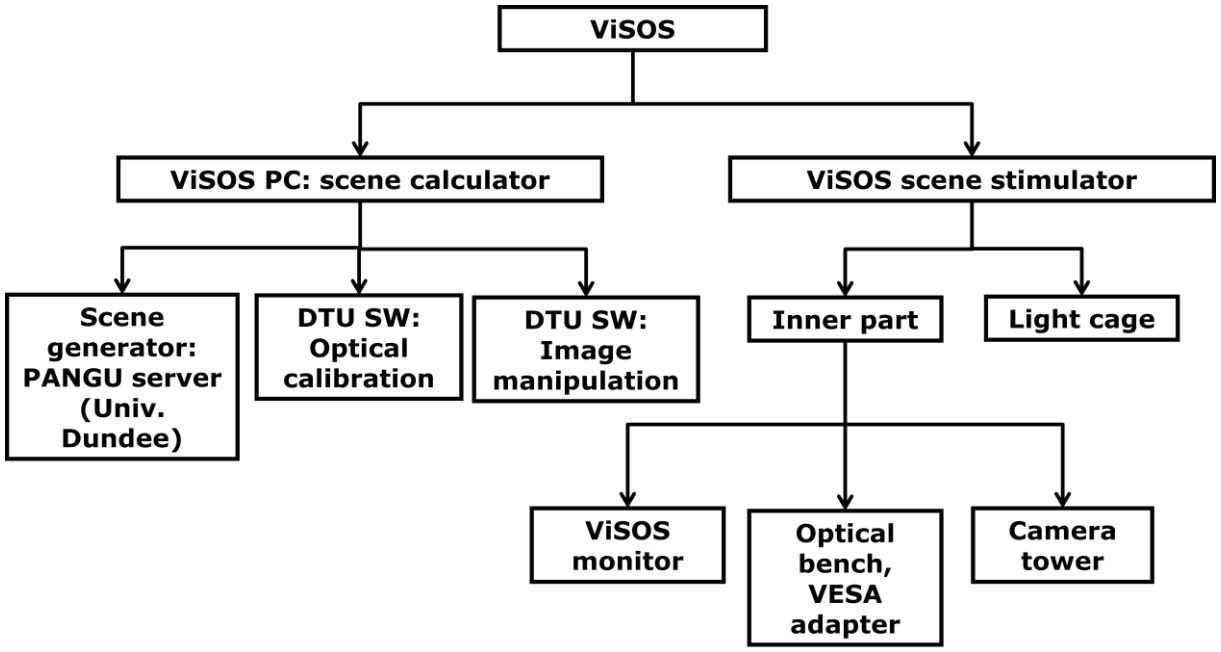

Figure 4: ViSOS principle setup and components (HW / SW).

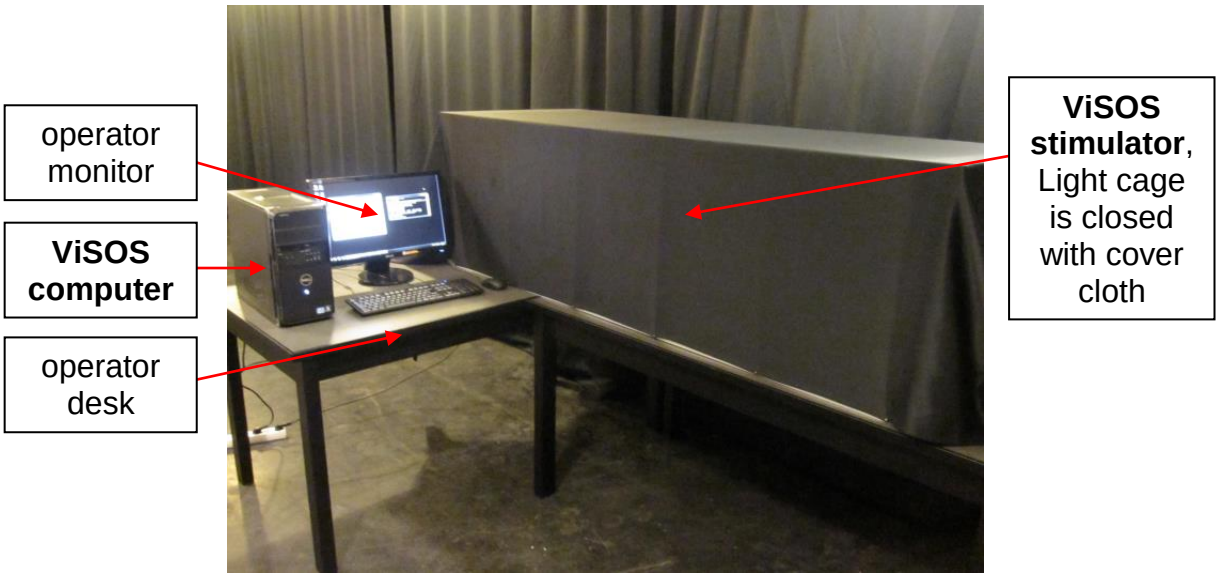

Figure 5: ViSOS example setup in the laboratory. The light cage is closed with the cover cloth.

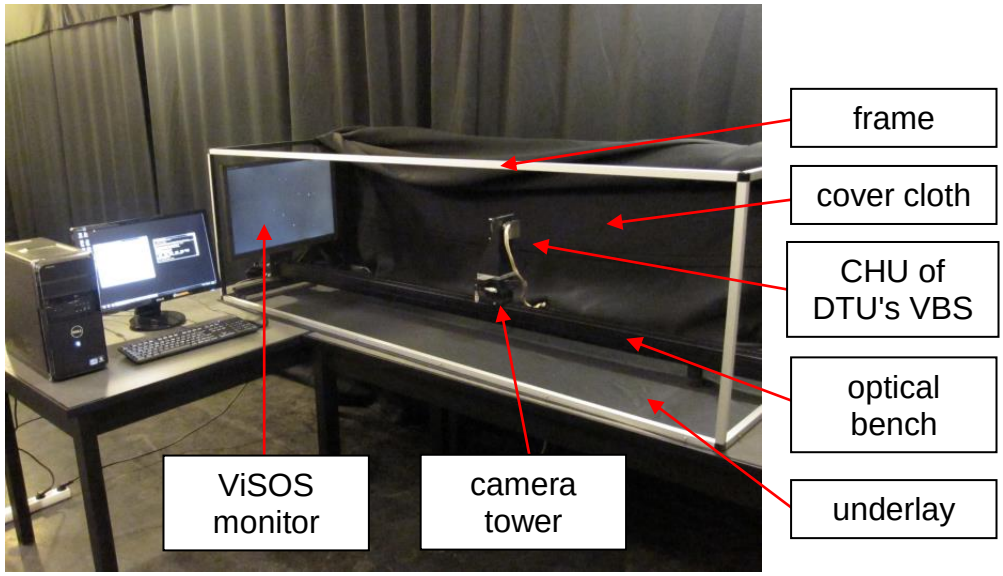

Figure 6: ViSOS example setup in the laboratory. The light cage is opened. The centre part, the frame, the underlay cloth and the CHU of DTU's VBS are visible. The DPU of DTU's VBS is not shown.

6.1.3 ViSOS HW: PC

The ViSOS PC (Figure 5) is a COTS DELL Vostro Desktop 470 computer with an additional hard disk for image file storage and an advanced GPU. The primary tasks of the ViSOS PC are the computation of the calibration parameters and generation of scene images with correct geometry that are sent to the ViSOS scene stimulator. The ViSOS PC is equipped with human interfaces, i.e. monitor, keyboard and mouse as well as USB2.0/3.0 and Ethernet/WLAN interfaces for connection to the Real-World Simulator and other devices.

6.1.4 ViSOS HW: scene stimulator

The ViSOS scene stimulator (Figure 6) is used to stimulate the camera with the image signal generated on the ViSOS PC. The ViSOS stimulator consists of the inner part and the light cage. The inner part consists of the ViSOS monitor connected to the ViSOS PC via a VESA adapter, the optical bench with the VESA adapter and the camera tower (Figure 5 and Figure 6). The optical bench is also used to position the scene stimulator on horizontal surface such as an optical table. The three feet of the optical bench provide vibration damping with maximum damping at about 15 Hz.

The light cage is independent of the inner part. It protects the inner part against light sources from other sources than the ViSOS monitor (Figure 6).

The ViSOS stimulator is designed in a modular way such that single components, e.g. the monitor can be later replaced with low effort. The system is independent of the camera HW and SW.

The ViSOS monitor is a panchromatic COTS Samsung Synchmaster SA450, with 24" screen diagonal and 1900 x 1200 px screen resolution. The monitor delivers a continuous light signal at wavelengths between approximately 420 and 780 nm (Figure 7).

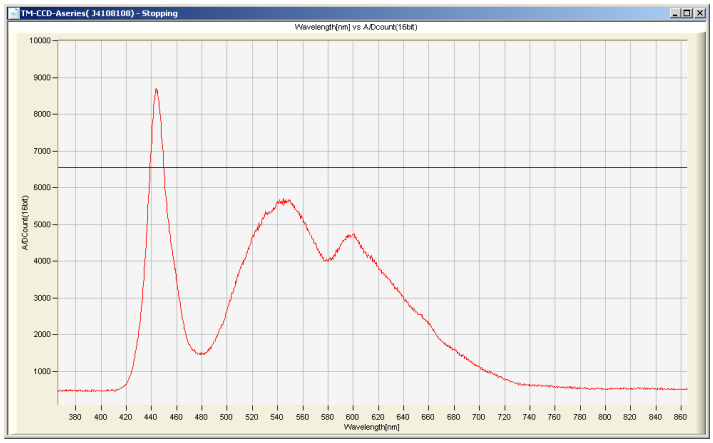

Figure 7: Light spectrum emitted from fully white monitor screen.

The camera tower is mounted on the optical bench to provide stable connection between the ViSOS monitor and the camera. With Rail carriage, Translation stage and Tilt and Rotations platform, the camera tower provides 2 DoF rotation (yaw, pitch) and 1 DoF translation facility (Table 2). It is used for adjustment of focusing and pointing of the camera. The top of the camera tower provides the mechanical interface between ViSOS and a camera [AD 3]. The calibration of the translation stage and of the Tilt and Rotations platform is provided in (Table 3), compare [AD 8].

Table 2: Calibration of micrometer screws MS1 and MS2 implemented for rotation of the mounted camera. See Figure 9 for the micrometer screws M1 and M2.

Tilt and Rotation platform			
	Rotation axis	Rotation rate	Rotation per revolution
MS1	X (pitch)	1.2º/mm	0.6º
MS2	Y (yaw)	-0.8º/mm	-0.4º
Translation stage			
	Direction	Translation rate	Translation per revolution
M3	roll axis	1.0 mm/mm	0.5 mm

Due to the size and the flexibility of the inner part and the light cage, ViSOS provides a test bed for a wide range of cameras. Cameras, not exceeding the physical limits of the scene stimulator (Figure 8) and specifically of the camera tower (Figure 9) can be mounted on the mechanical interface between ViSOS to the camera. Note that an additional camera-dependent adapter between the interface and the camera might be needed.

Depending on the camera, an additional optics in front of the camera CHU may be required to focus the camera on the ViSOS monitor screen.

An example, showing DTU's camera CHU together with the additional optics is given in (Figure 9). Both are mounted to the camera tower via a camera adapter,

Table 3: Physical limits of camera tower with Rail carriage for coarse translation, Translation stage for fine translation and Tilt and Rotation stage for 2 DoF rotation (sources: http://www.thorlabs.com, www.newport.com).

stage	range	sensitivity	Maximum vertical load
Rail carriage	0 - 1850 mm	About 1 mm	n.V.
Translation stage	13 mm	0.5 mm per revolution	90 N
Tilt and Rotation platform	Tilt (pitch): -4.3º to +7º Rotation (yaw): -2.5º to +2.5 º	2 arcsec	66 N

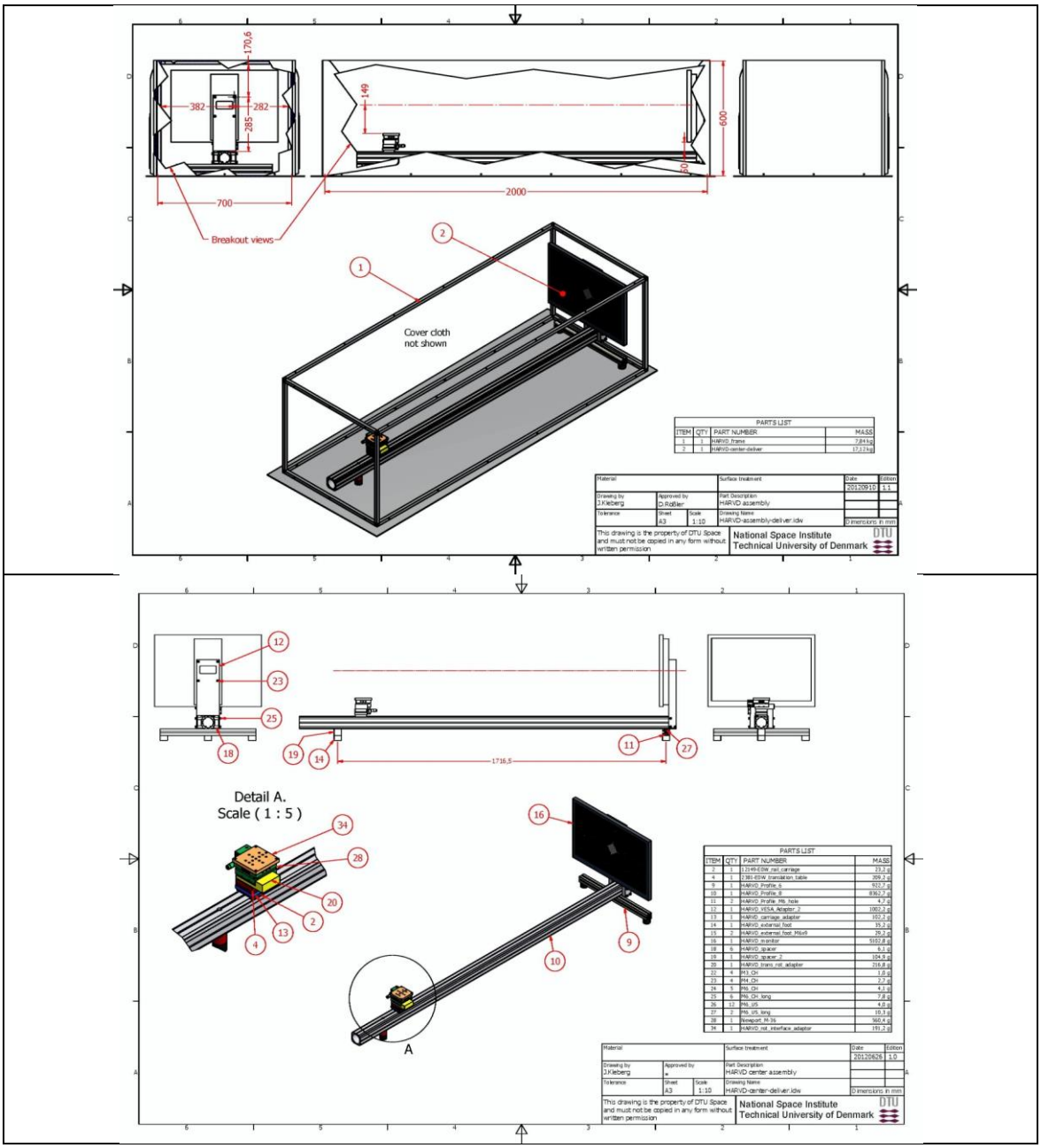

Figure 8: Physical dimensions of the ViSOS scene stimulator. Detail A shows the camera tower.

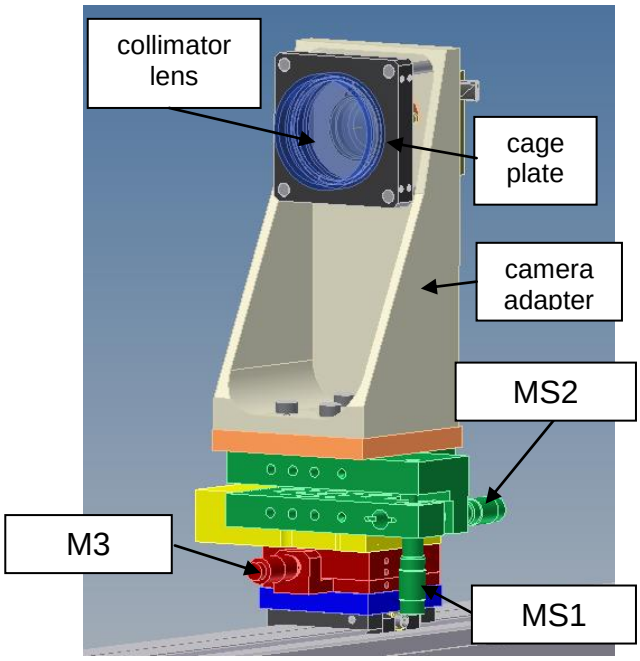

Figure 9: DTU's CHU mounted with a camera adapter to the camera interface of the camera tower. Notice the the collimator lens in front of the CHU in order to focus on the screen. The micrometer screws MS1 and MS2 of the Tilt and Rotation platform and M3 of the translation stage are labeled.

6.1.5 Practicality and environmental considerations

The ViSOS PC and the ViSOS stimulator can be assembled and set up by one person. The assembly of the stimulator and is described in detail in [AD 6].

In order to optimize the performance, the ViSOS stimulator must be installed in a thermally and mechanically stable environment on a horizontal surface such as of an optical table. Horizontally, the surface must be 700 x 2000 mm wide as a minimum.

In practice, DTU has placed the scene stimulator during operation on a concrete base or on a normal office desk in a thermally sufficiently stable room. During measurements, unauthorized staff was excluded from entering the room, walk-around of persons near the stimulator was minimized but no extra care was taken to minimize human-made noise from outside the room. Variations in room temperatures were less than ±1 K during measurements.

The functioning of the ViSOS HW including the ViSOS computer and the inner part and the light cage have been tested and verified.

6.1.6 ViSOS SW: calibration SW

The calibration SW [AD 5] delivers the calibration parameters, needed to correct generated scene images (section 6.2.2) by the image manipulation SW (section 6.1.8).

The calibration parameters describe properties of the optical system consisting of camera, focusing optics and monitor. They are calculated using calibration SW

developed by DTU and images taken by the camera of a calibration pattern shown by the calibration SW on the ViSOS monitor The calibration parameters in particular describe the geometric distortion of the FoV of the camera (lens distortion parameters) and the position and the orientation of the monitor with respect to the viewing camera or the focusing optics if applicable.

The calibration parameters are used for opto-mechanical adjustment of the camera using the functionality of the camera tower and for correction of generated scene images by image manipulation SW.

Calibration must be carried out after mechanic and thermo-elastic adjustment of the scene stimulator and the camera, i.e. every time the inner part of the scene stimulator has been assembled or moved and every time the monitor has been switched on. The reasons are mechanic uncertainties and small thermo-elastic deformations of the system due to heating by the ViSOS monitor. However, temperatures become stable within 2 hours of operation of the ViSOS monitor. Therefore, mechanic and thermo-elastic adjustment take up to 2 hours after assembly of the scene stimulator and after switching on the ViSOS monitor. After this pre-operational phase, the system can be calibrated and used for normal operation.

The system has been designed and the COTS have been selected carefully in order to optimise thermo-elastic stability. Re-calibration of the system may however be required in case of temperature or external forcing of the stimulator. The need for re-calibration can be tested using test images representing starry sky. In a thermally stable environment with temperature changes less than ±1 K, DTU has continuously used the scene stimulator for camera measurements without re-calibration for more than 21 hours and even days. During these measurements the deformation of the scene stimulator was insignificant.

The time to carry out calibration is camera dependent, i.e. dependent on the download time of an image. Considering DTU's star tracker camera[1] and 10 camera images, one system calibration takes less than 10 minutes in total.

6.1.7 ViSOS SW: PANGU image generation

PANGU, version 3.30 [AD 10] is installed on the ViSOS PC and is used for raw image generation (compare Figure 11). The viewer SW, which is part of PANGU, is started on the ViSOS PC in server mode (see [AD 10] for the SW reference and [AD 5] for a list of some parameters used by DTU) and commanded from a PANGU client. The client controls the scene generation, the transmission of image data from PANGU server to the client and storage of image files on a disk accessible to the PANGU client. The PANGU client therefore controls the timing of the image file generation. The storage of image files on disk allows direct verification of the generated images and is advantageous for analysis of the conducted experiments. A separate hard disk on the ViSOS PC (mapped as drive I:) is exclusively dedicated to

[1] Information on DTU's star tracker camera (ASC / microASC) and VBS are intellectual property of MIS at NSI DTU that may not be disclosed, distributed or reproduced without written approval by MIS at NSI DTU.

the image file storage in order to avoid interference with file i/o from other instances of the computer.

The PANGU client connects to the PANGU server through TCP/IP. It can be operated on the Real-World Simulator (Figure 3) outside of ViSOS. Alternatively, the PANGU client can operate on the ViSOS PC. In this case a SW interface must be established to the Real-World Simulator or the client must operate independently of the Real-World-Simulator. Operation of the PANGU client on the ViSOS PC is most efficient since transfer of image data between the ViSOS PC and the Real-World Simulator is avoided.

In all cases, it must be ensured, that the generated image files stored to disk are accessible to the image manipulation SW on the ViSOS PC. File storage on the drive I: of the ViSOS PC has proven to be most efficient.

In PANGU, the brightness of represented stars is related to the apparent magnitude of the stars [AD 10]. The apparent magnitude of stars associated with the maximum intensity is given by the PANGU parameter viewer.star_magnitudes [AD 10], referred to as *mag* in this document. In PANGU the brightness of stars is scaled to this *mag*-value. Using *mag* = 3.0 or 3.3, optimum results have been obtained for camera attitude determinations from stars. For some cameras, e.g. DTU's star tracker[1], dynamic scaling of the intensity of stars by modifying *mag* can be advantageous [AD 9] if non-stellar objects such as a SC are in the FoV of the camera. The modification of *mag* depends on the simulated distance between the SC and the camera r and the initial distance r_0 below which the modification is to be applied:

$$mag = mag_0 - 2.5 * log_{10}(r_0^2/r^2) \quad \forall \quad r < r_0, \tag{1}$$

where mag_0 is the initial magnitude used for scaling of star intensities in PANGU. The distance r_0 is scene dependent.

The intensity scaling by equation (1) results in variation of the number of stars visible to the camera (Figure 10) and in enhanced representativeness of the scene.

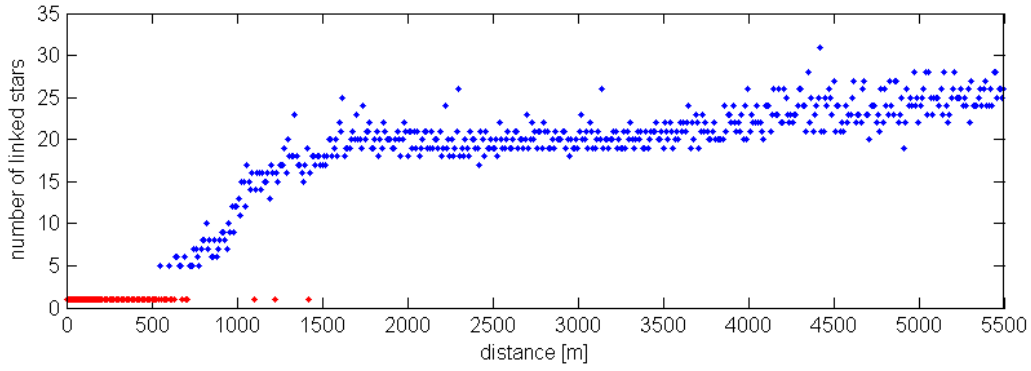

Figure 10: Number of linked stars (blue dots) as function of simulated distance between camera and a SC with constant attitude. Star-intensity scaling, compare equation (1), is applied at distances $r < r_0$ = 5000 m. Red dots mark invalid camera attitude solutions.

6.1.8 ViSOS SW: image manipulation SW, image post-processing

In the SW version available to DTU [AD 10], PANGU is unable to consider the calibration parameters delivered by the calibration SW. Therefore, the PANGU generated scene images are post-processed and shown on the ViSOS monitor (compare Figure 11) by the image manipulation SW, developed by DTU.

The manipulation SW reads the PANGU image files from disk in alpha-numerical order, starting at the lowest value, and applies the calibration parameters. All images must have identical image file format, file size and pixel resolution. Currently, the .ppm image file format, used by PANGU, is supported in order to show series of images [AD 5]. Other file formats are supported for processing a single image per SW execution.

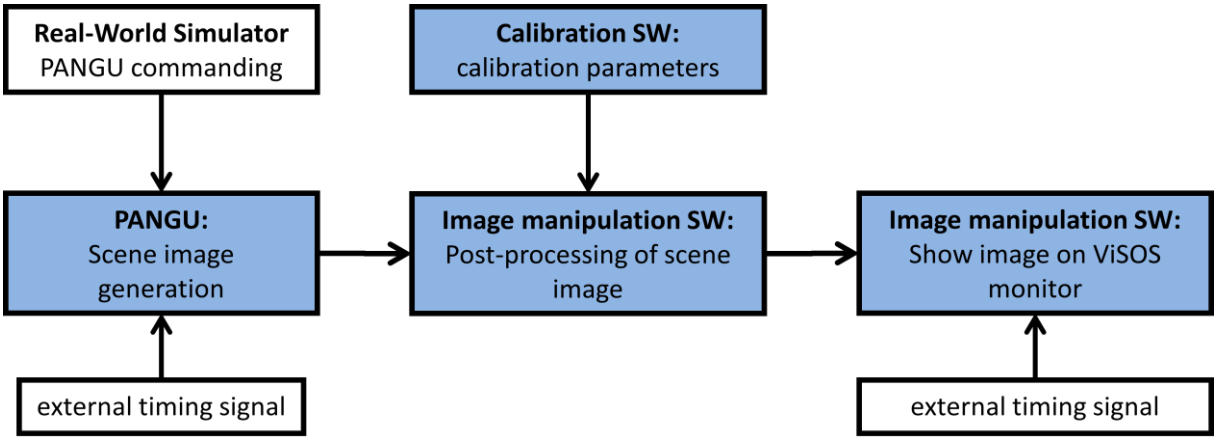

Figure 11: Monitor image generation process. Calibration SW and image manipulation SW is a DTU development. Components marked in blue are contained in ViSOS.

The pixel resolution of PANGU images can be controlled in order to optimise aliasing effects. Different image pixel resolutions are therefore supported by the image manipulation SW. The support of a particular pixel resolution is linked to the provided calibration parameters which are controlled by the pixel resolution of the considered camera. Integer multiples of the camera resolution from 1 to 10 (oversampling factor) are considered. In the tests involving DTU's star tracker oversampling factors of 1-2 have proven appropriate for optimisation of aliasing effects on SC models. However, only oversampling of 1 was meaningful due to creation of seams in images with higher oversampling factor and the apparently missing of support of non-quadratic pixel resolutions by PANGU.

6.1.9 ViSOS SW: image manipulation SW, timing of image update

Timing of the image update on the ViSOS monitor can be controlled by the computer time of the ViSOS PC or by an external PSS signal sent to the ViSOS PC via UDP. Note, that using UDP for communication facilitates real-time application of ViSOS. However, the choice of image sampling controls the achievable image update time (Figure 12). In addition, an increase in image pixel resolutions increases the computational effort and time for image file generation by PANGU. The time needed for image file generation depends additionally on the scene and on the complexity of

the considered SC and other models, see section 6.3.1. For moderate complexity and 1-3 fold oversampling, requirements on image updates of 2 Hz (for DTU star tracker[1]) and 1 Hz (otherwise), can be met.

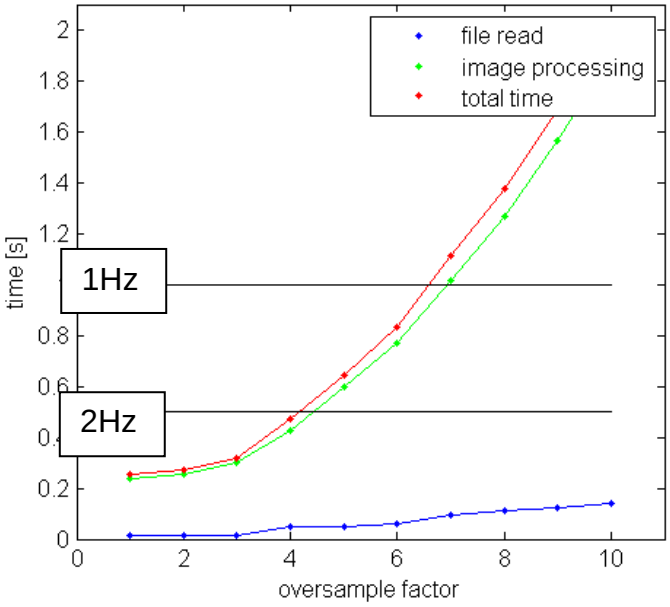

Figure 12: Time consumed by image manipulation SW for PANGU image file reading, processing and the sum of both times. Note that the times can vary with computer load. PANGU images have multiple (oversampling factor) pixel resolution of 752 x 580 px. Black lines show time limits assuming 1 and 2 Hz image update rate.

6.1.10 Light intensity scaling

The selected ViSOS monitor and GPU of the ViSOS PC apply non-linear scaling of the brightness. This scaling is controlled by the GPU using the gamma value, γ, and by the monitor using the gamma mode. The gamma value determines the relation between the intensity of the generated light *I* and the input value *V:* $I \approx V^{\gamma}$. In order to reach linearity, a correct representation of the intensity of simulated stars and other objects on the ViSOS monitor required a calibration of the parameters.

Linearity between intensities of stars in in-flight images and stars camera-take images from ViSOS generated images is found for $\gamma = 1.5$ and gamma mode 2 (Figure 13).

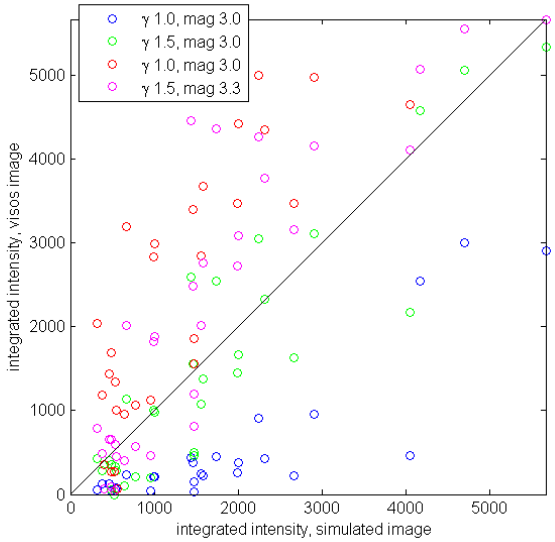

Figure 13: Integrated pixel values of PANGU generated stars in camera images vs. stars in in-flight images. Different gamma values $\boldsymbol{\gamma} = \{\mathbf{1.0}, \mathbf{1.5}\}$, $\boldsymbol{mag} = \{\mathbf{3.0}, \mathbf{3.3}\}$ and gamma mode 2 are used for PANGU image generation.

6.2 ViSOS validation and system performance

6.2.1 Focusing of the camera

Focusing of the camera on the monitor is essential for all camera operation inside of ViSOS. A camera-dependent optics in front of the CHU may be required (Figure 14). The focussing optics in front of the CHU of DTU's star tracker is a simple 1000 mm collimator with anti-reflection lens coating in the spectrum of visible light. It enables focusing of the camera on the ViSOS monitor (Figure 14).

Camera image without focusing optics	Camera image with focusing optics
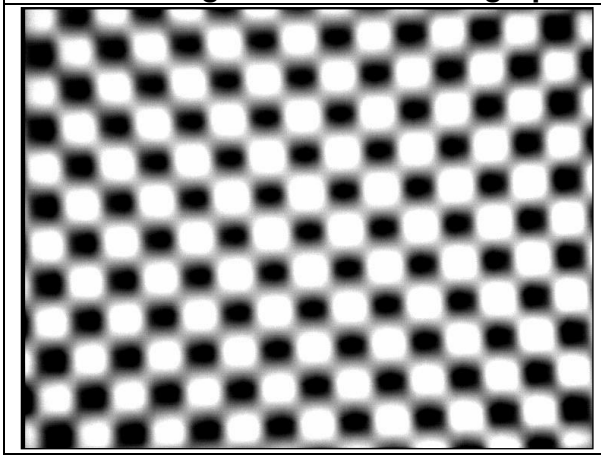	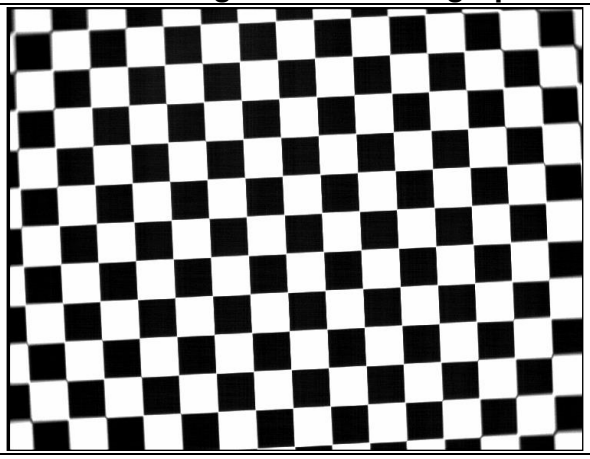

Figure 14: Effect of the focusing optics in front of the camera CHU.

6.2.2 System calibration

Optical calibration of the ViSOS monitor and the focusing lens in front of the viewing camera is applied to provide the calibration parameters to the image manipulation SW. The calibration SW is based on corner extraction of a given calibration pattern at sub-pixel accuracy (Figure 15). The calibration pattern is adjustable to the FoV of the viewing camera. Based on the extracted corners from the calibration pattern the calibration parameters are estimated (Table 4 and Figure 16).

Camera image from calibration pattern	Camera image from calibration pattern with automatically detected corners
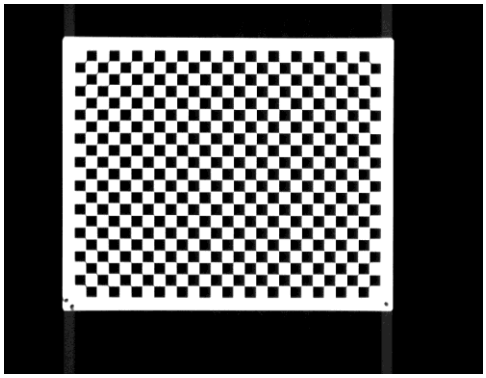	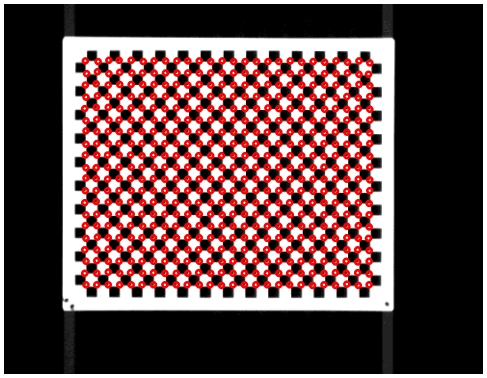

Figure 15: automatic corner extraction (red circles) of calibration pattern by calibration SW.

The calibration SW provides the extrinsic range parameters and the Euler angles describing the orientation of the monitor with respect to the viewing optics as well as the intrinsic parameters describing the geometric distortion of the image due to the viewing optics [AD 7, AD 5]. The parameters are highly reproducible (Figure 17). Outliers are detected and can be removed. Therefore, the parameters describing the range and orientation can be used by the image manipulation SW as well as for opto-mechanical adjustment of the camera by the camera tower (section 6.1.4).

Table 4: The mean and standard deviation for the calibration lens distortion parameters based on 120 images. The parameters are the principal point, radial distortion and tangential distortion.

	Cx	Cy	K1	K2	K3	P1	P2
μ	376.09	290.08	-2.5111e-8	1.0797e-13	5.1287e-19	-4.1697e-7	-2.7346e-7
σ	2.8859e-2	2.5590e-2	5.7116e-9	1.4446e-13	1.1110e-18	2.3564e-7	9.6221e-8

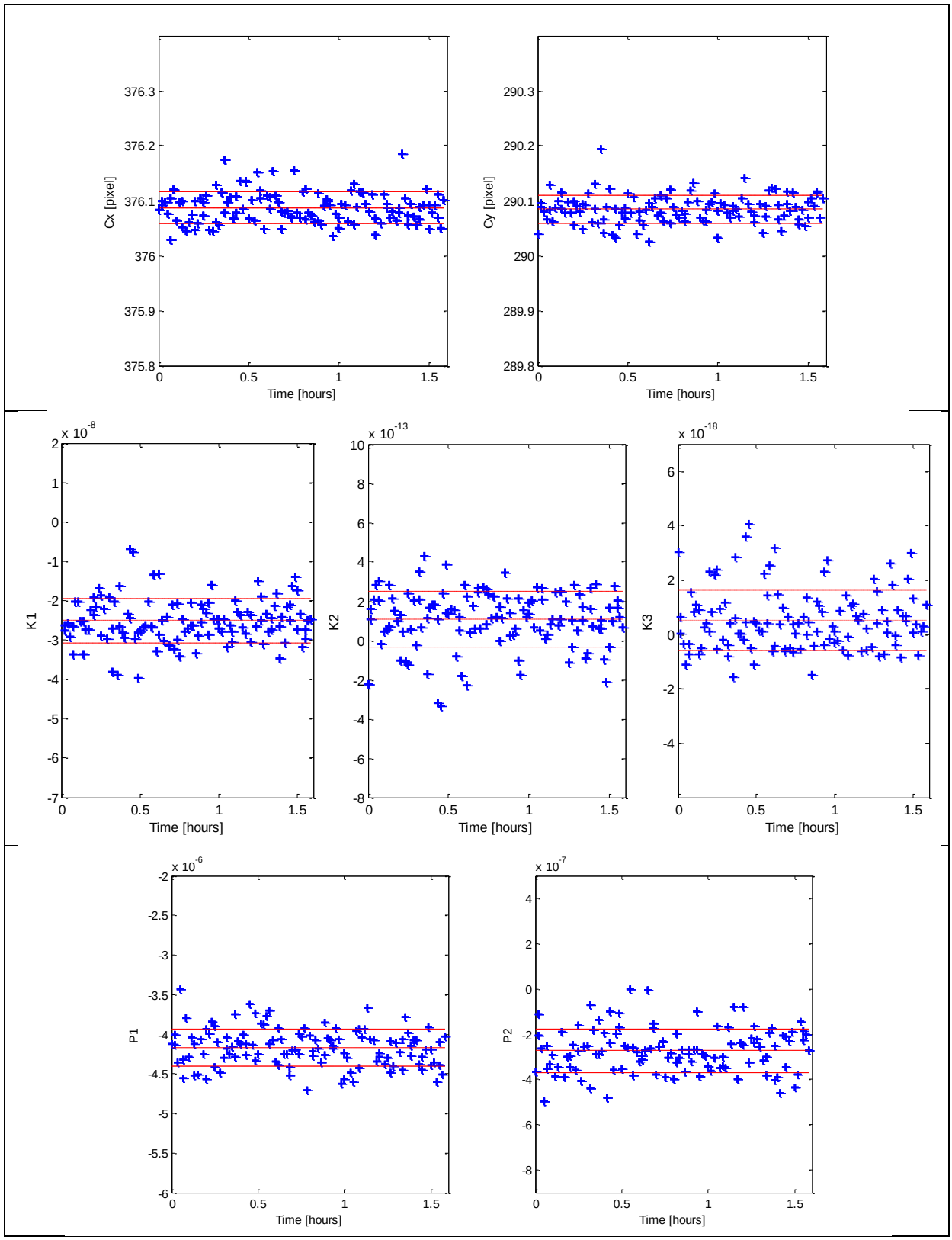

Figure 16: The intrinsic parameters. Top: principal point (Cx,Cy). Middle: radial distortion coefficients K1, K2 and K3. Below: tangential distortion coefficients P1 and P2. The three red lines indicate the mean and standard deviation.

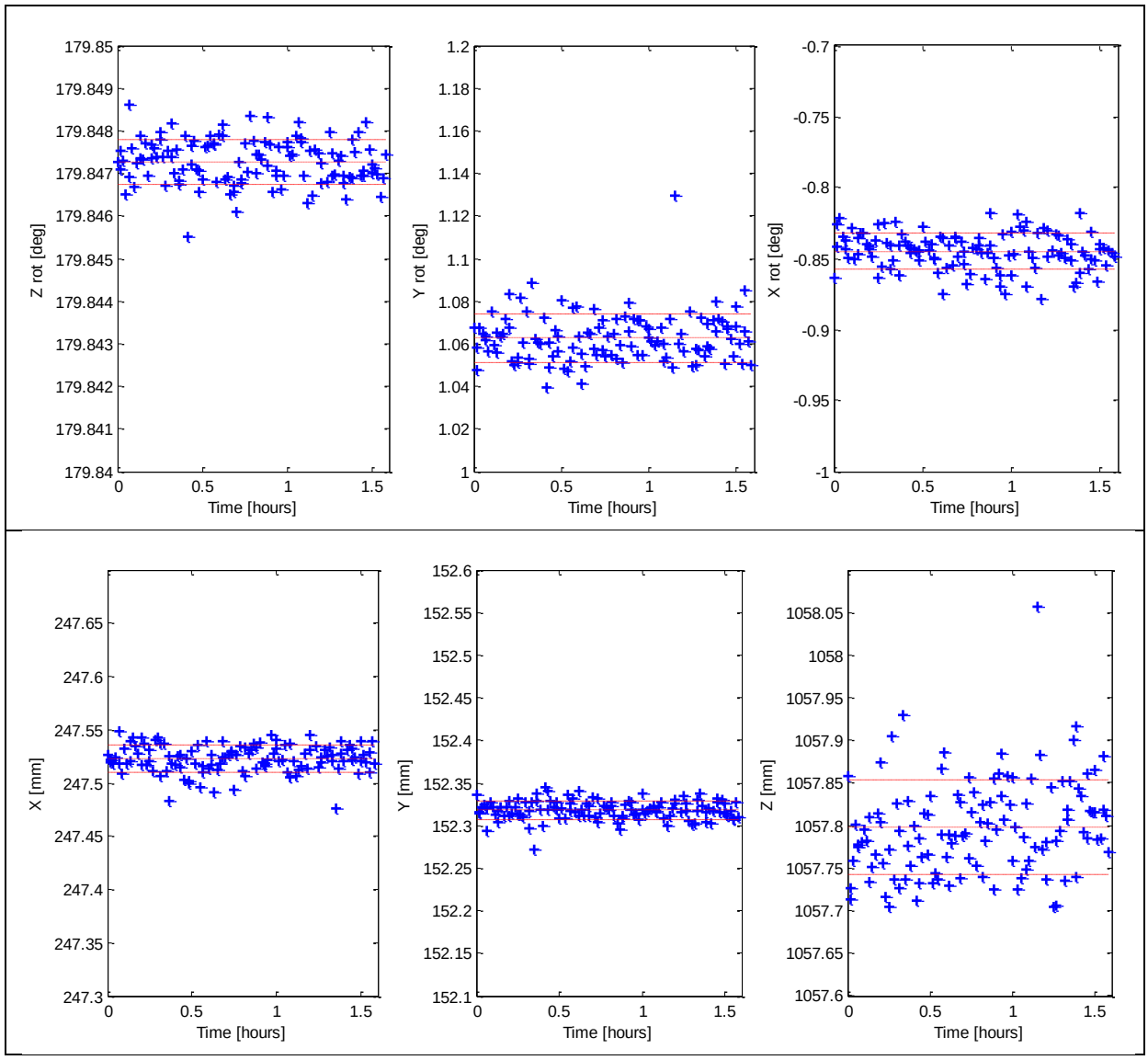

Figure 17: (Top) Orientation of the ViSOS monitor described by 3 Euler angles relative to the image frame of the CHU. (Below) Components of the range vector the image frame of the CHU to the origo of the ViSOS monitor frame. The three red lines indicate the mean and standard deviation.

6.2.3 Pre-operational phase

The system adjusts after assembly and after moving the system. The system further deforms thermo-elastically due to warm-up of the ViSOS monitor. Therefore, a pre-operational phase is required before operating ViSOS. Due to optimized mechanical design of the inner part of ViSOS and low heat production by the monitor the system stabilizes within 2 hours after assembly, moving and start of the monitor operation (Figure 18).

Calibration and operation of the system can start after the pre-operational phase.

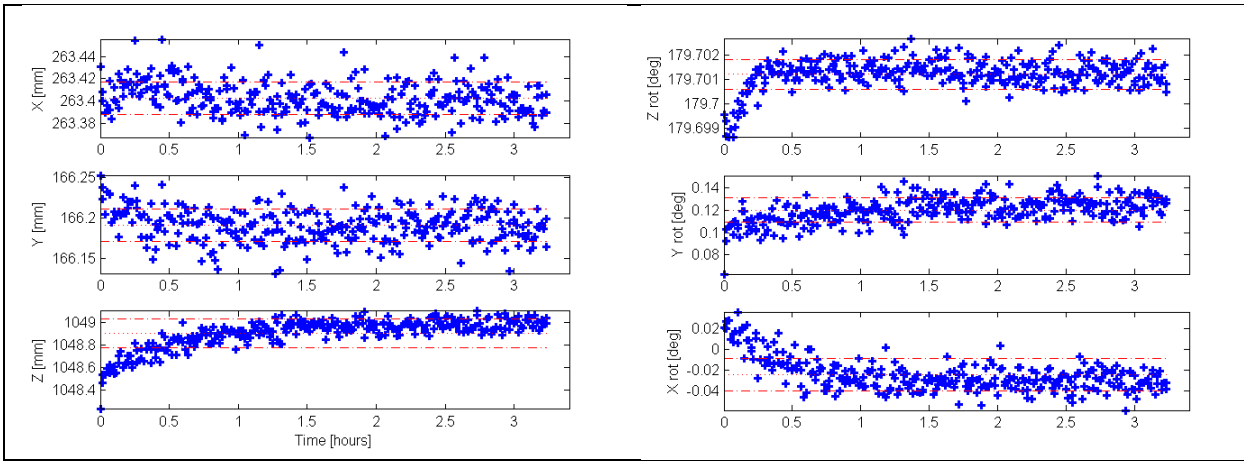

Figure 18: Range of monitor (left) and angles of rotation of calibration pattern on the monitor about x-, y,- and z- axis with respect to the camera. Measurements start immediately after mounting of the ViSOS monitor to the VESA adapter and after the monitor is switched on and warm up.

6.2.4 PANGU image generation

The image geometry of PANGU images was test based on star images from real-sky cameras (#1-#4) and camera C onboard PRISMA (#5), see Table 5.

Table 5: List of test images and camera attitudes solutions by the DPU derived from the images. Units of angles are degree.

#	Image	ra [º]	dec [º]	rollVBS [º]	Stars	Res
1	B111129_21173851.unc	11.3208	37.7121	179.6145	14	1
2	B111129_21195689.unc	349.6704	28.5571	112.9336	11	1
3	B111129_21282901.unc	32.1295	29.4660	238.0622	13	1
4	B111129_21370079.unc	24.4702	38.4952	263.7736	13	2
5	IMC_997924488.877609.png	223.7160	-46.3727	348.4073	32	1

PANGU image representing starry sky were generated based on attitudes from images #1 - #4 in Table 5. The image resolution equals the resolution of DTU's star tracker camera. For image generation EFL = 19961, corresponding to the calibrated value of the assumed camera, was used. Two sets of images with different geometry were generated by assuming 2 different values for the PANGU parameter viewer.aspect_ratio. This parameter controls the FoV geometry. It was set to 1.032 (corresponding to the cameras FoV[1] and to 8.6/8.3 (corresponding to the pixel ratio[1]). The images were uploaded to the DPU of DTU's star tracker camera bypassing the CHU.
The attitudes from PANGU generated images were determined (Table 6) but unsatisfactory values were obtained, assuming EFL = 19961. However, increasing EFL from 19961 to EFL = 20041, optimum attitude solutions with low residual and low deviation from values assumed for image generation were obtained.

Table 6: Results from attitude determination assuming different EFL for attitude determination. PANGU images are uploaded to the DPU of the VBS camera. Values related to optimum solutions are in bold.

Assumed values for attitude determination		**PANGU parameter** viewer.aspect_ratio **assumed for image generation**									
		1.0322					**8.6/8.3**				
		Determined values from generated images uploaded to the camera									
#	EFL	ra [º]	dec [º]	rollVBS [º]	Stars [#]	res	ra [º]	dec [º]	rollVBS [º]	Stars [#]	res
1	19961	11.3207	37.7314	179.6305	23	17	11.3230	37.7137	179.6114	21	23
	20041	11.3220	37.7138	179.6177	24	5	**11.3219**	**37.7128**	**179.6121**	**21**	**0**
2	19961	349.7028	28.5651	112.8578	12	8	349.6758	28.5624	112.9302	16	17
	20041	349.6753	28.5594	112.9298	12	3	**349.6716**	**28.5578**	**112.9329**	**16**	**0**
3	19961	32.1218	29.4720	238.0535	22	18	32.1218	29.4700	238.0658	21	13
	20041	32.1287	29.4679	238.0456	22	4	**32.1307**	**29.4664**	**263.7721**	**21**	**0**
4	19961	24.4533	38.4961	263.7235	19	19	24.4634	38.4924	263.7788	22	19
	20041	24.4639	38.5035	263.6951	19	1	**24.4719**	**38.4956**	**263.7721**	**21**	**0**

We conclude that PANGU is able to create fidelity star images but assumptions on the image geometry must tested.

6.2.5 Static scenes representing starry sky

The ability of ViSOS to stimulate a camera with fidelity using the monitor is tested. Therefore, PANGU images are created based on attitudes from images #1 - #4,Table 5. The PANGU images are projected on the ViSOS monitor as still images using the image manipulation SW.

For attitude determination by the camera, EFL = 19961 µm and EFL = 20041 µm are used. The results (Figure 19, Figure 20 and Table 7) show high accuracy and high stability of the solutions with respect to the attitudes used for image generation. In order to reach optimum accuracy, the EFL used for attitude solution of the camera had to be adjusted to EFL = 20041 µm. In this way, the accuracy and the stability of the camera solutions were improved.

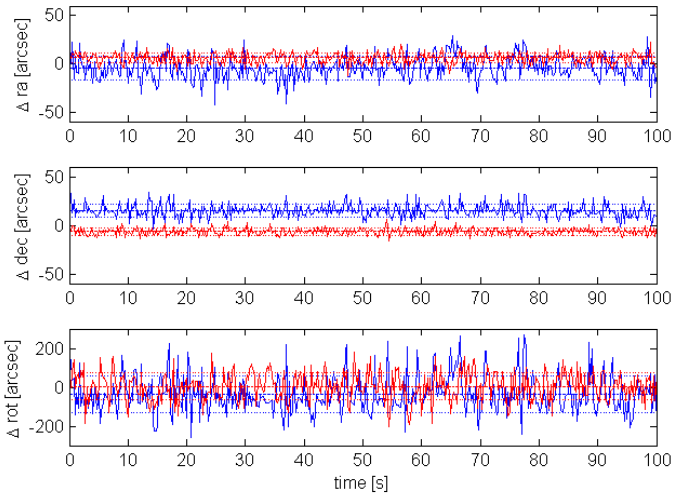

Figure 19: Series of attitude solutions using the DTU's star tracker camera and image #1 in Table 5. For image generation in PANGU, viewer.aspect_ratio=8.6/8.3 is used. Different EFL are considered: blue: EFL=19961µm, red: EFL= 20041µm and constant camera shutter.

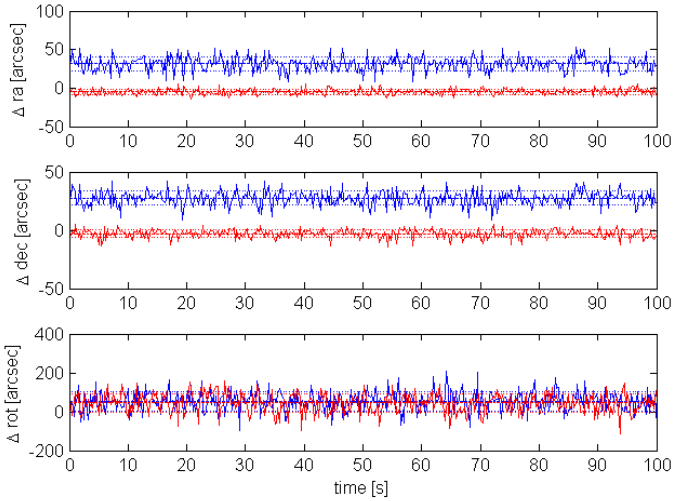

Figure 20: Series of attitude solutions using the VBS camera and image #2 in Table 5. For image generation in PANGU, viewer.aspect_ratio=8.6/8.3 is used. Different EFL are considered: blue: EFL=19961µm, red: EFL= 20041µm.

Table 7: Results from attitude solutions for PANGU images generated based on attitude values in Table 5. Images are shown to DTU's star tracker camera by the ViSOS stimulator. For image generation in PANGU, viewer.aspect_ratio=8.6/8.3 and EFL = 20041 µm are used. Attitude angles values refer to the mean deviation of the solution from the original value assumed for PANGU image generation. δ is the standard deviation. Best solutions are highlighted in bold. Measurement, #1, marked with * was conducted with fixed camera shutter. All other measurements where made with automatic camera shutter.

#	EFL [µm]	ra [']	δ(ra) [']	dec [']	δ(dec) [']	rollVBS [']	δ(rollVBS) [']	Stars [#]	δ(stars) [#]	res	δ(res)
1	19.961	-4	12	15	7	-34	95	11	1	18	3
	20.041	**7**	**6**	**-4**	**4**	**78**	**90**	**11**	**1**	**2**	**1**
	***20.041**	***6**	***6**	***-7**	***3**	***4**	***69**	***14**	***1**	***2**	***1**
2	19.961	31	9	27	6	55	51	9	1	12	2
	20.041	**-5**	**3**	**-3**	**3**	**45**	**49**	**9**	**1**	**1**	**1**
3	19.961	15	8	-32	10	-35	53	12	1	15	5
	20.041	**17**	**2**	**1**	**3**	**-11**	**34**	**12**	**1**	**1**	**0**
4	19.961	-34	6	-13	4	-80	48	11	1	11	1
	20.041	**6**	**4**	**-11**	**4**	**-86**	**49**	**11**	**1**	**1**	**1**

The resulting deviations with respect to values used for image generation are smaller than 20 arcsec for right ascension and declination and smaller than 100 arcsec the roll angle. For the four given static scenes, the uncertainties are smaller than 10 arcsec for right ascension and declination and smaller than 100 arcsec the roll angle (Table 8). Using a wider range of scenes in dynamic images, the deviations at zero velocity diminish even further (Table 8).

Table 8: Deviations in ra, dec and rollVBS between attitude solutions of a camera viewing the ViSOS monitor and values used for image generation. δ is the standard deviation from at least 100 seconds measurement. Values in brackets are deviations from dynamic images at zero velocity (quantity n in Table 9).

ra [']	δ(ra) [']	dec [']	δ(dec) [']	rollVBS [']	δ(rollVBS) [']
< 20 (< 2)	< 10	< 20 (< 1)	< 10	< 100 (< 14)	< 100

Therefore it is concluded that ViSOS is able to stimulate the camera with very high accuracy.

6.2.6 Oversampling

DTU has experienced challenges in using PANGU to create images with non-quadratic pixel resolution and oversampling with respect the camera resolution. Images created with oversampling had geometry issues related to seams or obscured FoV [AD 8]. The geometry issues result in deterioration of camera attitude solutions of a camera viewing the ViSOS monitor screen (Figure 21).

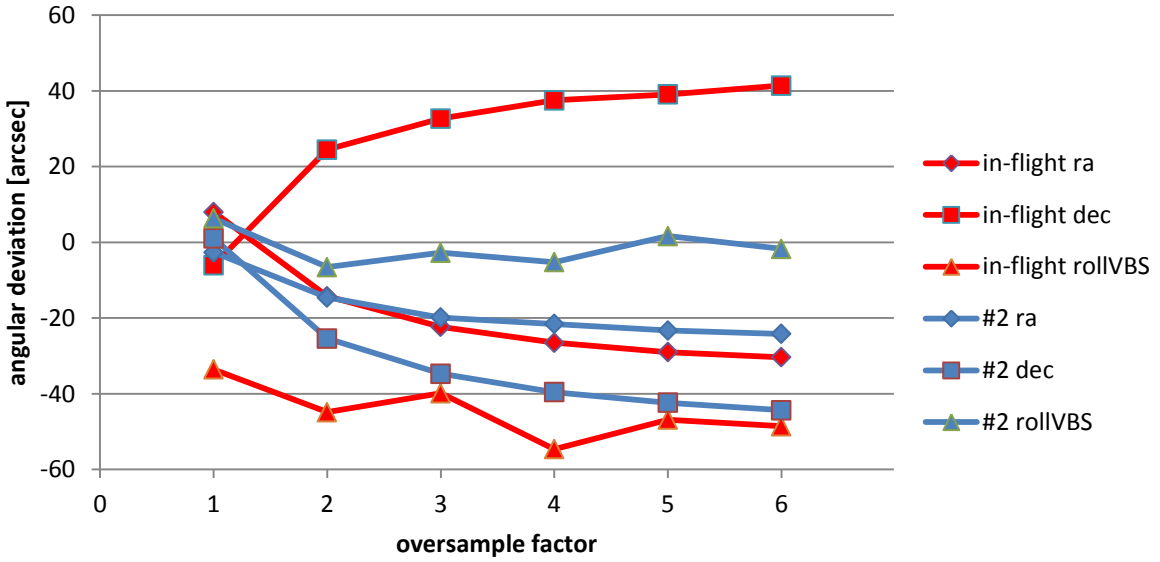

Figure 21: Mean values of angular deviation in ra, dec, rollVBS for image #2(blue) and #5(red), given in Table 5, as function of the oversampling factor. The angular deviations are calculated as the difference between camera attitude solutions of a camera viewing the images in ViSOS and the values used for PANGU image generation.

Therefore, PANGU images are generated with pixel resolutions equal to the camera resolution. Given the high image fidelity and pointing accuracy of the camera reached in this way, the avoidance of oversampling does not state a limitation. However, it is expected that oversampling, if applicable, can further enhance the system fidelity.

6.2.7 Dynamic scenes

ViSOS is able to stimulate the camera with dynamic scenes where a camera flight trajectory is simulated. The ability is validated by simulation of a flight trajectory of camera C onboard Prisma MAIN SC (Figure 22). The in-flight attitudes and timestamps are used for PANGU image generation. Linear interpolation was applied for doubling of the image update rate to 4 Hz. PANGU images are processed and shown to the camera at 4 Hz.

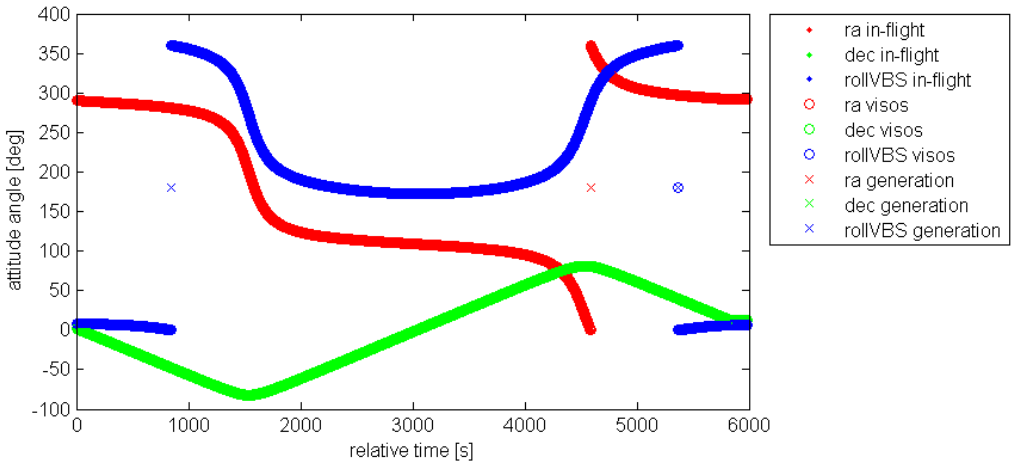

Figure 22: Attitude angles (ra, dec, rollVBS) from in-flight data (dots: in-flight), from attitude file generated by the camera viewing the ViSOS monitor (circles: ViSOS) and from interpolated attitudes used for scene generation (crosses: generation). Due to very high similarity, separation of data is difficult in this image for most cases.

The resulting camera attitudes (Figure 22) and angular rates (Figure 24) show great accuracy and similarity with in-flight values and values used for scene generation as well as perfect correlation for attitudes as well as residuals and number observed stars (Table 9). As expected from DTU's in-flight experiences, the uncertainties scale with rotation rate (Figure 23 and Table 9). Therefore, the mean values in angular differences are elevated with respect to static images. However, the intercept of the differences at zero velocity can be used to compare the difference values with values from static values. It shows that these intercept values agree well and even outperform the values found from static images by up to a factor of 20, compare Table 8.

Therefore it is concluded that ViSOS is a powerful tool to stimulate a camera with dynamic images at very high accuracy and sufficient image update rate.

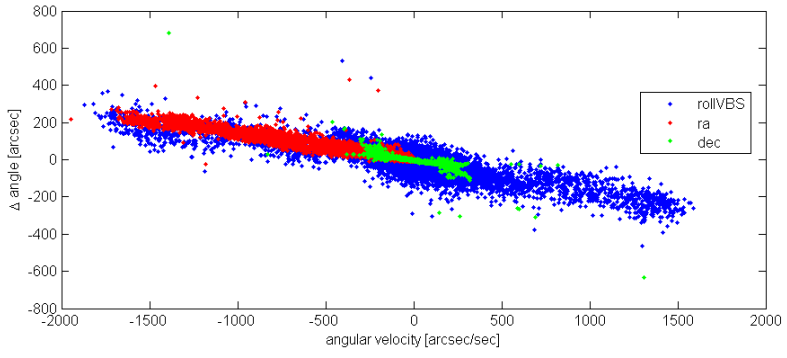

Figure 23: Differences in angular velocities between ViSOS attitudes and in-flight attitudes as function of angular velocity of the considered angle.

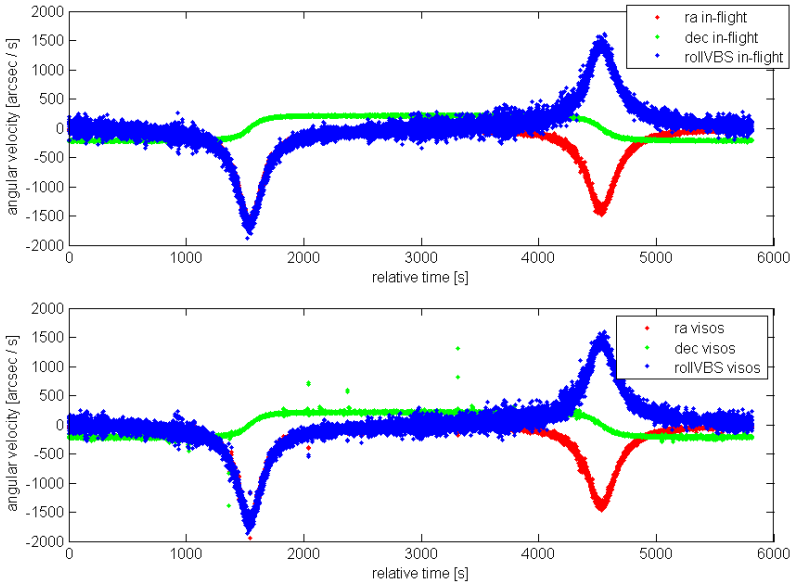

Figure 24: Attitude rates (angular velocities) for ra, dec and rollVBS in flight (top) and from ViSOS (bottom) attitude solutions. Velocities are calculated for times when in-attitudes are valid. Outliers, e.g. near 2000 s and 3300 s are related to image generation near gaps in in-flight data.

Table 9: Differences in attitudes, residuals and number of linked stars between ViSOS and in-flight attitude solutions. The parameters m and n represent fit of a linear function, y=mx+n to the relation between the angular differences and attitude rates. M and n describe the slope and intercept, respectively at zero angular velocity (Figure 23). Parameter Rxy is the correlation coefficient between the number of linked stars in ViSOS and in-flight solutions.

Quantity	Mean absolute difference	δ	m	n	R_{xy}	lag
ra	34.8’’	52.8’’	-0.14’’/’’/s	1.4’’	1.00	0
dec	27.1’’	13.8’’	-0.14’’/’’/s	0.8’’	1.00	0
rollVBS	57.0’’	58.0’’	-0.15’’/’’/s	-13.3’’	1.00	0
rate(ra)	0.010 ''/s	0.016 ''/s			1.00	0
rate(dec)	0.008 ''/s	0.004 ''/s			0.99	0
rate(rollVBS)	0.016 ''/s	0.017 ''/s			1.00	0
Residual	-1.8	0.9			0.86	6
number of stars	-5.0 (-14.9%)	4.6 (13.7%)			0.99	0

6.2.8 Long-term stability

DTU has performed a number of long-term tests of ViSOS in order to evaluate the stability of the system during operation and in order to give advice on the need of system re-calibration. Therefore, the camera CHU was stimulated using static PANGU images representing starry sky.

During these tests, no re-calibration was performed, the room temperature variations were below ±1 K.

The linear drift is negligible during these measurements. In the given example (Table 10) the total linear drift in attitudes was less then 1 arcsec for each ra, dec and rollVBS. The given examples are representative of the tests and show that ViSOS could be operated continuously for several days with acceptable linear drift.

Table 10: Linear drift of camera angles during two tests with more than 20 hours of continuous operation for each test. The camera was stimulated with starry-sky PANGU image based on attitudes from image #3 in Table 5.

	Linear drift [arcsec/sec] / [arcsec/day]		
	ra	dec	rollVBS
test 1	5.7e-06 / 0.5	7.8e-06 / -0.7	1.3e-05 / 1.1
test 2	4.8e-06 / 0.4	-1.7e-06 / -1.4	-2.0e-06 / -0.17

The spectrum of the rotation angles in the tests is flat to periods of about 20,000 s (Figure 25). However, the rise at longer periods is considered low. Therefore, the ViSOS stimulator is also stable with respect to periodic changes.

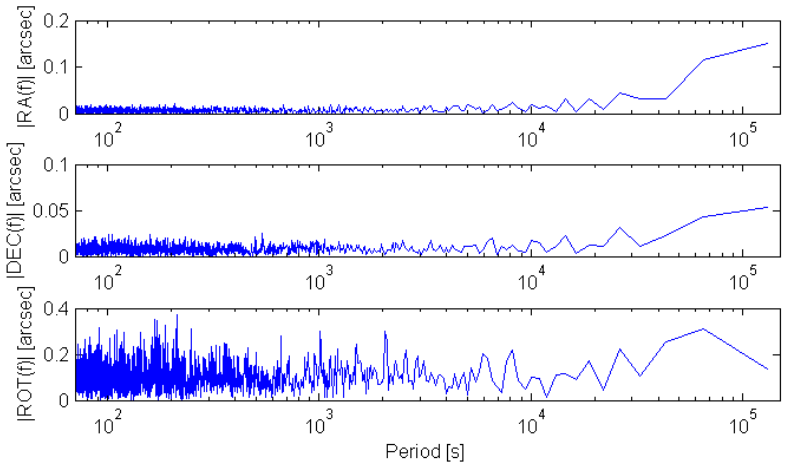

Figure 25: Amplitude spectrum of test 2 in Table 10.

ViSOS can therefore be continuously used during at least 20 hours without re-calibration of the system.

6.3 SC models analysis

Generic models of SC with different level of complexity and representativeness of the Prisma TARGET SC have been considered for analysis of the performance of the ViSOS system and of camera images taken from ViSOS images. SC models 1, 2 and 4 (Figure 26) have proven meaningful for analysis.

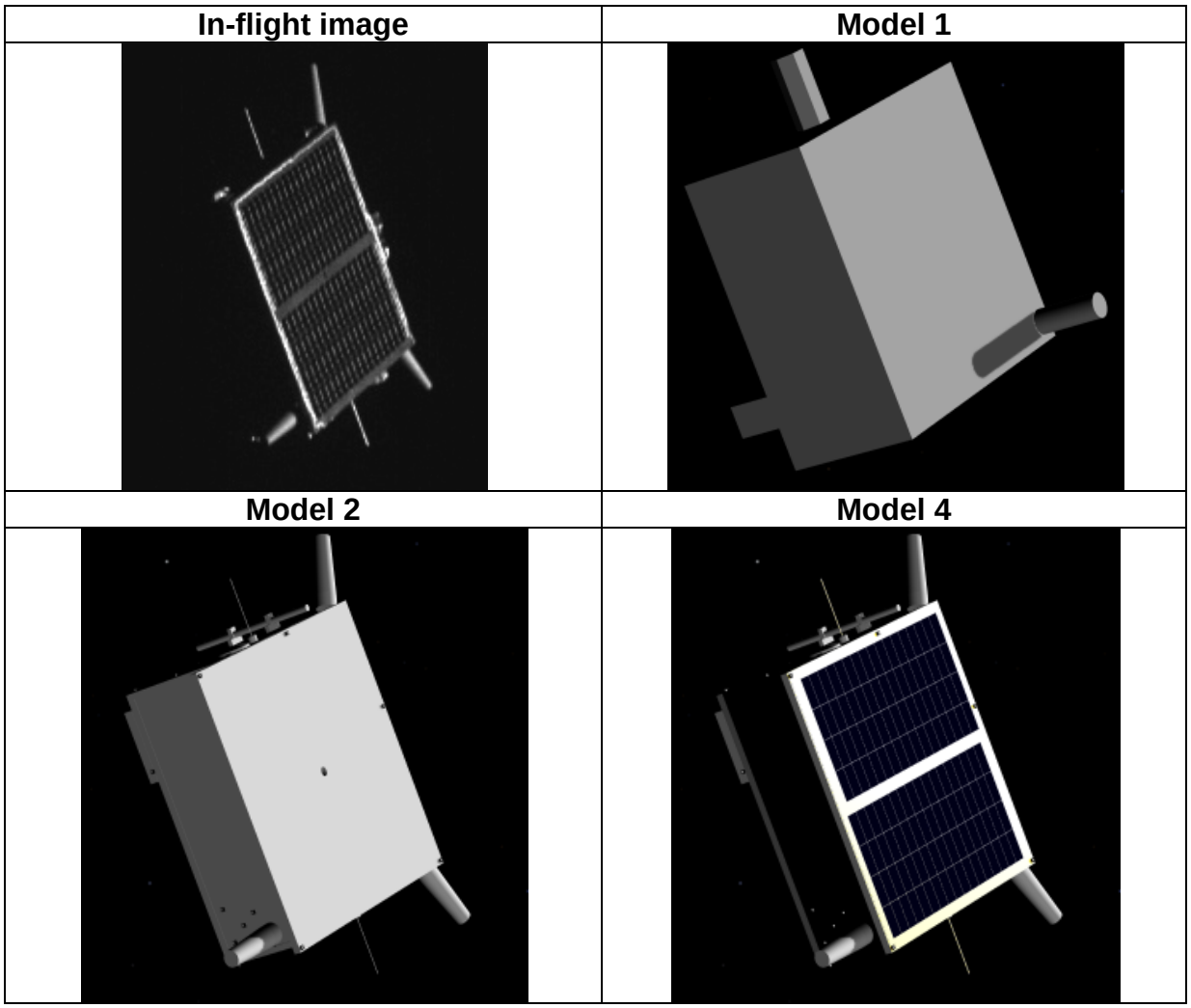

Figure 26: In-flight image of Prisma TARGET SC and PANGU SC models 1, 2 and 4.

6.3.1 Scene update rates

The time consumed for updating a scene image by PANGU depends on the complexity of the SC model. Considering SC models with moderate complexity, sufficiently high scene update rates such as 1 Hz and 2 Hz can be achieved (Figure 27).

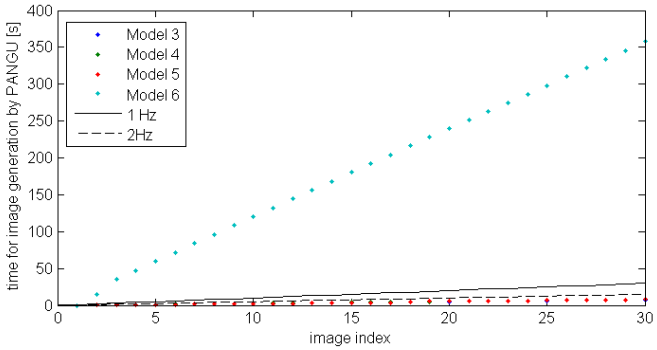

Figure 27: Time required for PANGU image generation considering models 3 – 6, image resolution of 752 x 580 px and 30 images. For image generation, PANGU server and client are located on the same computer generated. Files are stored on the same computer. The measured times include times for scene update (moving of SC) and image storage. Black lines show margins for image generation assuming 1 and 2 Hz image update frequency.

6.3.2 SC models representativeness

When stimulating DTU's VBS camera optically with generated images the considered SC models (Figure 26 and Figure 28) have comparable representativeness in terms of the visibility of edges and the LoS solutions. Camera images from the most complex model 4 show most details of surface features such as solar panels at 200 m distance and below. They are therefore most representative of in-flight images. However, the simpler model 2 is visible at larger simulated distances between SC and camera.

At distances above approximately 900 m, the representation of the SC by PANGU is limited. The limitation is indicated by green high lightening of the SC in PANGU when activating the debug mode for imposters. The limitation results in model-dependent invisibility of the SC.

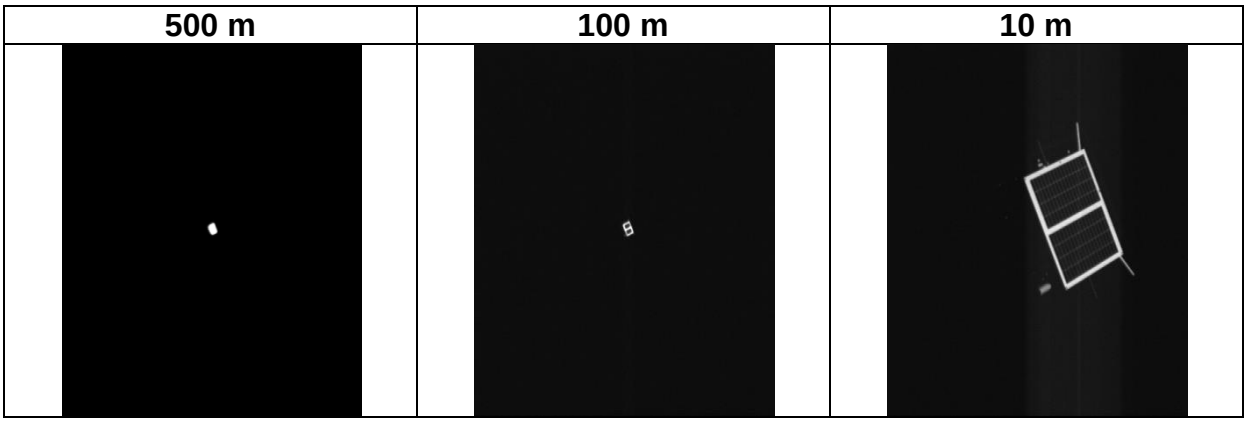

Figure 28: SC model 4 simulated at distances of 500, 100 and 10 m to the camera view by DTU's VBS camera inside ViSOS.

In PANGU images all represented images appear in focus. The distance between the ViSOS monitor and the viewing camera is considered to be constant. Therefore, variable distance-depending focusing and defocusing of the camera cannot be simulated with ViSOS. This limitation is independent of the SC model.

6.3.3 Oversampling with SC in FOV

Increased pixel resolution of SC scene images does not increase the visibility of the SC to the camera nor the quality or the representativeness of SC in ViSOS images taken with DTU's VBS camera. Therefore, the requirement to generate scene images with hyper-accuracy is not indicated.

6.3.4 Line-of-Sight solutions

ViSOS can be used to track SC in front of the camera (Figure 29) and to determine the LoS. At short distances below 100 m the increased variability of the solution is caused by the complexity of the SC model and is representative of in-flight experiences. In this example, the simulated SC is not represented in scene image at distance larger than 1600 m. Apparently erroneous images of the SC are generated near 600 m distance. These challenges result in partial loss of LoS solutions near 600 m. The SC is not represented at distances larger than 1600 m. Up-scaled or simplified SC models can be considered to overcome this issue.

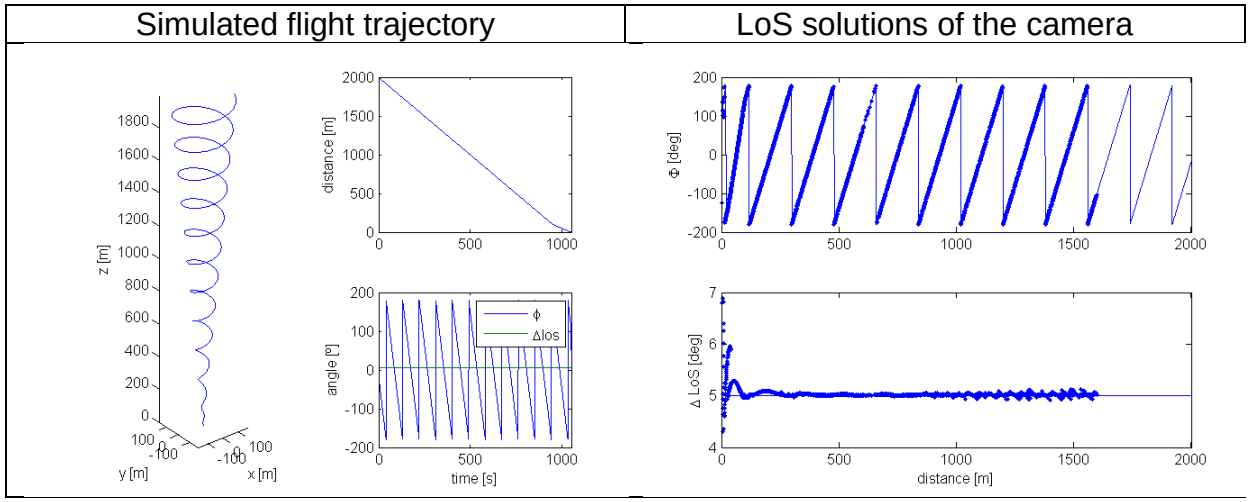

Figure 29: (Left) Simulated flight trajectory of the viewing camera in the reference frame of the considered SC model 4. ϕ is the azimuth angle in the camera CCD plane and Δlos is the angle to the boresight. Below 100 m distance, the approach velocity is reduced by a factor 2. The flight starts at 2000 m distance. (RIGHT**)** LoS solutions obtained in the reference frame of DTU VBS camera (blue dots) and values used for scene generation in PANGU (blue lines) as function of simulated distance between the SC and the viewing camera.

7 Conclusion

The developed ViSOS system is an efficient tool to stimulate a camera with scenes consisting of starry images and rendezvous and proximity maneuvers with SC in FOV of the camera.

The ViSOS system offers flexible operation with cameras of different physical size and optics. The system is modular and includes a computer as scene image generator and a monitor stimulating a camera with generated images that are projected with correct geometry. The monitor is linked to the camera CHU through a mechanically stable optical bench. The camera CHU views the monitor. Focusing of

the CHU on the monitor is realized by external optics which is specific to the considered camera. Opto-mechnical adjustment of the camera is possible with 3 DoF. The individual computer HW components are COTS and can be replaced in order to adjust the system to changing requirements.

Due to the involvement of the camera optics, CHU, in the image processing chain, ViSOS reaches a higher level of realism than other simulators without a camera in the loop such as pure computer simulation or direct scene injection into the DPU of the camera.

The HW and SW system have been verified, and calibrated. The accuracy of the geometry of the projected image, the long-term stability of the system and the representativeness of generated SC models with respect to the PRISMA Target SC have been tested.

ViSOS reaches a high level of scene accuracy, in-flight representativeness and high long-term stability. Due to system calibration and scene image manipulation by SW, the accuracy of projected images as given by the pointing of DTU's star tracker is better than 20 arcsec for ra and dec and better than 200 arcsec for roll. Typically, these are better than 10 arcsec and 100 arcsec, respectively. In thermally stable environments the system has been continuously operated without significant loss of accuracy for more than 20 hours without re-calibration. The requirement to perform re-calibration can be tested by stimulation of the camera with star images.

8 Perspectives

Future improvements of the system can be reached by optimization to one single camera model. Such optimization may result in adjustment of the shape and reduction of the size of the ViSOS system.

In the near future, monitor systems based on OLED/AMOLED with higher maturity level, sufficiently high pixel resolution and low size comparable to tablet PCs or will enter the marked. Such monitors may be alternatively considered to significantly reduce level of background illumination of the monitor and to reduce the size of the optical ViSOS system.